

# **ULTRASOUND-ASSISTED SYNTHESIS, CHARACTERIZATION, AND APPLICATIONS OF HALLOYSITE-POLYMER NANOCOMPOSITES**

**Thesis**

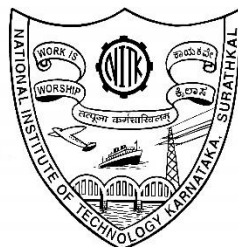
Submitted in partial fulfillment of the requirements for the degree of

**DOCTOR OF PHILOSOPHY**

**By**

**BURUGA KEZIA**

**(Reg. No. 138015CH13F05)**



**DEPARTMENT OF CHEMICAL ENGINEERING**

**NATIONAL INSTITUTE OF TECHNOLOGY KARNATAKA,**

**SURATHKAL, MANGALORE-575025**

**April, 2019**

*My thesis is dedicated*

*....to my parents for their encouragement and support*

*....to my sisters for their affection*

*.... to my good friends for being with me in all ways*

*.... and to my teachers for his moral guidance*

*during work*

## DECLARATION

I hereby *declare* that the thesis entitled “**ULTRASOUND-ASSISTED SYNTHESIS, CHARACTERIZATION, AND APPLICATIONS OF HALLOYSITE-POLYMER NANOCOMPOSITES**” which is being submitted to the **National Institute of Technology Karnataka, Surathkal** in partial fulfillment of the requirements for the award of the Degree of **Doctor of Philosophy** in Chemical Engineering is a *bonafide report of the research work carried out by me*. The material contained in this Research Synopsis has not been submitted to any University or Institution for the award of any degree.

**Buruga Kezia**

**Reg. No. 138015CH13F05**

**Department of Chemical Engineering**

**Place: NITK, Surathkal**

**Date:**

## CERTIFICATE

This is to *certify* that the thesis entitled “**ULTRASOUND-ASSISTED SYNTHESIS, CHARACTERIZATION, AND APPLICATIONS OF HALLOYSITE-POLYMER NANOCOMPOSITES**” submitted by **Buruga Kezia (Register Number: 138015CH13F05)** as the record of the research work carried out by her, *is accepted as the Research Thesis submission* in partial fulfillment of the requirements for the award of degree of **Doctor of Philosophy**.

**Research Guide**

**Dr. Jagannathan. T. K.**

**Assistant Professor**

**Dept. of Chemical Engineering**

**NITK, Surathkal**

**Chairman- DRPC**

**Dr. Hari Mahalinga**

**Head of the Department**

**Dept. of Chemical Engineering**

**NITK, Surathkal**

## ACKNOWLEDGEMENT

*First and foremost, I express my sincere heartfelt thanks and deepest gratitude to my beloved research guide **Dr. Jagannathan. T. K, Department of Chemical Engineering** for his esteemed guidance and kind cooperation throughout the project, which has helped me to complete this project satisfactorily. Apart from the technical guidance, it was his constant encouragement, affection, support and solace during the moments of despair that have been behind the successful completion of this report. This project would not have been possible without his guidance and valuable suggestions.*

*I am extremely thankful to Research Progress Assessment Committee members, **Dr. Uday Kumar Dalimba, Department of Chemistry** and **Dr. P. E. Jagadeesh Babu, Department of Chemical Engineering, NITK**, for their insightful comments and critical suggestions.*

*I acknowledge my thanks to **Dr. Vidya Shetty, Dr. Raj Mohan Bala** and **Dr. Hari Mahalingam**, Head of Department of Chemical Engineering from 2013-2015, 2015-2017, and 2017-current respectively, for extending administrative facility for tranquil progress of my Ph.D. work. I express my heart full thanks to the Director of NITK, Surathkal for providing the grants/funds to carry out this research work. I also thank all the teaching and supporting staff of the Metallurgical and Materials Engineering and Chemistry Departments, NITK for their help and support provided during the research work.*

*I would like to thank my dearest friends for their help during the research work. I would also like to thank research scholars of various departments for continuous encouragement, help and support during the course of my research work.*

*I lovingly acknowledge my parents, sisters and my relatives for their invaluable cooperation and support during every single day of my life. They have always been a source of inspiration for me. Finally, I am grateful to everybody those, who have helped and encouraged me during this research work.*

**- BURUGA KEZIA**

## **ABSTRACT**

Nanocomposites have been receiving growing interest in research as these materials display unique and attractive properties. Halloysite nanotubes are naturally occurring clay minerals and offers an inexpensive, low-tech alternative that is morphologically similar to multiwalled CNTs. In this work, ultrasound-assisted synthesis of HNT-polymer nanocomposites using three different routes i.e., solution blending, emulsion polymerization and mini-emulsion polymerization is presented. The interaction of HNTs with the polymer and their dispersion in the polymer matrix are vital in enhancing the properties of polymers. To achieve better interaction between HNTs and polymers the surface of HNTs was chemically modified with surfactant (Cetyl trimethylammonium bromide) and silane ( $\gamma$ -MPS) coupling agent. To achieve better dispersion of HNTs into polymer matrix ultrasound-assistance was utilized. HNT-polymer nanocomposites were characterized using different characterization techniques to understand their structure, morphology, functional, mechanical and thermal properties. It was observed that the surface modification of HNTs along with use of ultrasound for the process resulted in improvement in the properties of nanocomposites. HNT-polymer nanocomposites were used for two types of applications. Firstly, they were applied as protective coatings to different types of soda-lime glasses. These coatings displayed good thermal stability, mechanical strength, and hydrophobicity. They ensured better protection of the surface and the increased durability of the soda-lime glass. Next, the HNT-polymer nanocomposites was used for the fabrication of membranes for treatment of water. Two stage filtration unit comprised of nanoporous and microporous membrane was developed. The fabricated membranes displayed high water flux, great solute rejection, long-term stability of water flux, good rejection, and excellent mechanical and thermal properties. Overall, HNT-based polymer nanocomposites have greater potential for various applications in environmental construction and automobile industries.

**Keywords: Nanocomposite, Halloysite nanotubes (HNTs), Ultrasound, Coatings, Membranes**

## Table of Contents

<b>ABSTRACT</b> .....	<b>i</b>
<b>LIST OF FIGURES</b> .....	<b>xii</b>
<b>LIST OF TABLES</b> .....	<b>xxiiiv</b>
<b>NOMENCLATURE</b> .....	<b>xxvi</b>
<b>ABBREVIATIONS</b> .....	<b>xxvii</b>
<b>CHAPTER 1</b> .....	<b>1</b>
<b>INTRODUCTION</b> .....	<b>1</b>
<b>1.1 NANOCOMPOSITES</b> .....	<b>1</b>
<b>1.2 POLYMER MATRIX NANOCOMPOSITES</b> .....	<b>2</b>
<b>1.3 POLYMER NANOCOMPOSITES</b> .....	<b>3</b>
<b>1.4 HALLOYSITE NANOTUBES</b> .....	<b>4</b>
<b>1.5 METHODS FOR SYNTHESIS OF POLYMER NANOCOMPOSITES</b> .....	<b>6</b>
1.5.1 Synthesis of PNCs by solution blending method .....	6
1.5.2 Synthesis of PNCs by emulsion polymerization method.....	7
1.5.3 Synthesis of PNCs by mini-emulsion polymerization .....	8
<b>1.6 ULTRASONICATION</b> .....	<b>8</b>
1.6.1 Acoustic cavitation.....	8
1.6.2 Acoustic streaming.....	9
1.6.3 Ultrasound-assisted synthesis of PNCs.....	10
<b>1.7 APPLICATION OF HNT-POLYMER NANOCOMPOSITES</b> .....	<b>11</b>
1.7.1 HNT-based polymer nanocomposites as protective coating to glasses .....	11
1.7.2 HNT-based polymer membranes for water purification .....	12

<b>CHAPTER 2 .....</b>	<b>14</b>
<b>REVIEW OF LITERATURE .....</b>	<b>14</b>
<b>2.1 HALLOYSITE NANOTUBES (HNTs) .....</b>	<b>14</b>
<b>2.2 SURFACE MODIFICATION OF HNTs.....</b>	<b>16</b>
<b>2.3 SYNTHESIS OF HNT-POLYMER NANOCOMPOSITES .....</b>	<b>18</b>
2.3.1 Solution blending method.....	19
2.3.2 Emulsion polymerization and copolymerization .....	20
2.3.3 Miniemulsion polymerization.....	22
<b>2.4 APPLICATION OF HNT-POLYMER NANOCOMPOSITES.....</b>	<b>23</b>
<b>2.5 SCOPE OF THE PRESENT WORK &amp; OBJECTIVES .....</b>	<b>24</b>
2.5.1 Research Gaps.....	24
2.5.2 Aim.....	25
2.5.3 Objectives .....	25
<b>CHAPTER 3 .....</b>	<b>26</b>
<b>RESEARCH METHODOLOGY.....</b>	<b>26</b>
<b>3.1 MATERIALS AND METHODS .....</b>	<b>26</b>
<b>3.2 SURFACE MODIFICATION OF HNTs.....</b>	<b>28</b>
3.2.1 Surface modification of HNTs with surfactant CTAB .....	28
3.2.2 Surface modification of HNTs with $\gamma$ -MPS .....	29
<b>3.3 SYNTHESIS OF HNT-POLYMER NANOCOMPOSITES USING ULTRASOUND ASSISTED SOLUTION INTERCALATION METHOD .....</b>	<b>29</b>
3.3.1 Initial solvent screening for the blending of HNTs and polymer .....	29



3.3.2 Synthesis of HNT-polymer nanocomposites by ultrasound-assisted solution blending method.....	30
<b>3.4 SYNTHESIS OF PNCs USING ULTRASOUND-ASSISTED EMULSION POLYMERIZATION .....</b>	<b>30</b>
<b>3.5 SYNTHESIS OF PNCs USING ULTRASOUND ASSISTED MINI-EMULSION POLYMERIZATION .....</b>	<b>33</b>
<b>3.6 APPLICATION OF PNCs FOR COATING THE SURFACE OF GLASS.....</b>	<b>34</b>
3.6.1 Dip coating technique .....	34
3.6.2 Spin coating technique .....	35
<b>3.7 FABRICATION OF PNCs MEMBRANES FOR WATER PURIFICATION ...</b>	<b>36</b>
<b>3.8 CHARACTERIZATION OF PNC's USING ANALYTICAL TECHNIQUES..</b>	<b>36</b>
<b>CHAPTER 4.....</b>	<b>39</b>
<b>SURFACE MODIFICATION OF HNTs .....</b>	<b>39</b>
<b>4.1 INTRODUCTION.....</b>	<b>39</b>
<b>4.2 SURFACE MODIFICATION OF HNTs USING CETYL TRIMETHYLAMMONIUM BROMIDE .....</b>	<b>40</b>
4.2.1 Studies on structure of HNTs and CHNTs.....	41
4.2.2 Studies on surface morphology of HNT and CHNT .....	42
4.2.3 Studies on functional groups of HNT and CHNT .....	42
<b>4.3 SURFACE MODIFICATION OF HNTs WITH <math>\gamma</math>-MPS .....</b>	<b>43</b>
4.3.1 Studies on the structure of HNTs and MHNTs .....	43
4.3.2 Studies on surface morphology of HNT and MHNT .....	44
4.3.3 Studies on functional groups of HNTs and MHNTs .....	45
<b>4.4 SUMMARY.....</b>	<b>46</b>

<b>CHAPTER 5 .....</b>	<b>47</b>
<b>ULTRASOUND-ASSISTED SYNTHESIS OF HNT-PS AND HNT-PMMA NANOCOMPOSITES BY SOLUTION BLENDING METHOD .....</b>	<b>47</b>
<b>5.1 INTRODUCTION .....</b>	<b>47</b>
<b>5.2 INITIAL SOLVENT SCREENING FOR BLENDING OF HNTs AND POLYMER.....</b>	<b>48</b>
5.2.1 Effects of solvents on structure of HNT-polymer nanocomposites .....	49
5.2.2 Effects of solvents on the morphology of HNT-polymer nanocomposites .....	51
5.2.3 Effects of solvents on functional groups of HNT-polymer nanocomposites ..	51
5.2.4 Effects of solvents on thermal stability of HNT-polymer nanocomposites .....	52
<b>5.3 ULTRASOUND-ASSISTED SYNTHESIS OF HNT-POLYSTYRENE (HNT-PS) NANOCOMPOSITES BY SOLUTION BLENDING METHOD.....</b>	<b>54</b>
<b>5.3.1 Studies on the structure of HNT-PS, CHNT-PS and MHNT-PS nanocomposite.....</b>	<b>54</b>
5.3.2 Studies on the morphology of HNT-PS, CHNT-PS and MHNT-PS nanocomposite .....	55
5.3.3 Studies on functional groups of HNT-PS, CHNT-PS and MHNT-PS nanocomposites .....	568
5.3.4 Studies on thermal stability of HNT-PS, CHNT-PS and MHNT-PS nanocomposites .....	59
<b>5.4 SYNTHESIS OF HNT-POLYMETHYLMETHACRYLATE (HNT-PMMA) NANOCOMPOSITES .....</b>	<b>61</b>
5.4.1 Studies on the structure of HNT-PMMA, CHNT-PMMA and MHNT-PMMA nanocomposites .....	62

5.4.2 Studies on morphology of HNT-PMMA, CHNT-PMMA and MHNT-PMMA nanocomposites .....	63
5.4.3 Studies on functional groups of HNT-PMMA, CHNT-PMMA and MHNT-PMMA nanocomposites .....	64
5.4.4 Studies on thermal stability of HNT-PMMA, CHNT-PMMA and MHNT-PMMA nanocomposites .....	66
<b>5.5 SUMMARY.....</b>	<b>69</b>
<b>CHAPTER 6.....</b>	<b>70</b>
<b>ULTRASOUND-ASSISTED SYNTHESIS OF HNT-PS, HNT-PMMA, HNT-(PS-co-PMMA) NANOCOMPOSITES BY EMULSION POLYMERIZATION .....</b>	<b>70</b>
<b>6.1 INTRODUCTION .....</b>	<b>70</b>
<b>6.2 SYNTHESIS OF HNT-POLYSTYRENE (HNT-PS) NANOCOMPOSITES.....</b>	<b>71</b>
6.2.1 Studies on the structure of HNT-PS, CHNT-PS and MHNT-PS nanocomposites	
72	
6.2.2 Studies on the morphology of HNT-PS, CHNT-PS and MHNT-PS nanocomposites .....	74
6.2.3 Studies on functional groups of HNT-PS, CHNT-PS and MHNT-PS nanocomposites .....	77
6.2.4 Studies on thermal stability of HNT-PS, CHNT-PS and MHNT-PS nanocomposites .....	79
<b>6.3 SYNTHESIS OF HNT-POLYMETHYLMETHACRYLATE (HNT-PMMA) NANOCOMPOSITES.....</b>	<b>82</b>
6.3.1 Studies on structure of HNT-PMMA, CHNT-PMMA and MHNT-PMMA nanocomposites .....	82
6.3.2 Studies on the morphology of HNT-PMMA, CHNT-PMMA, and MHNT-PMMA nanocomposites .....	84

6.3.3 Studies on functional groups of HNT-PMMA, CHNT-PMMA, and MHNT-PMMA nanocomposites.....	86
6.3.4 Studies on thermal stability of HNT-PMMA, CHNT-PMMA, and MHNT-PMMA nanocomposites.....	88
<b>6.4 SYNTHESIS OF POLY(STYRENE-CO-METHYLMETHACRYLATE)-HNT [HNT-(PS-co-PMMA)] NANOCOMPOSITES .....</b>	<b>90</b>
6.4.1 Studies on the structure of [HNT-(PS-co-PMMA)], [CHNT-(PS-co-PMMA)] and [MHNT-(PS-co-PMMA)] nanocomposites .....	90
6.4.2 Studies on morphology of [HNT-(PS-co-PMMA)], [CHNT-(PS-co-PMMA)] and [MHNT-(PS-co-PMMA)] nanocomposites .....	92
6.4.3 Studies on functional groups of HNT-(PS-co-PMMA), CHNT-(PS-co-PMMA) and MHNT-(PS-co-PMMA) nanocomposites.....	95
6.4.4 Studies on thermal stability of [HNT-(PS-co-PMMA)], [CHNT-(PS-co-PMMA)] and [MHNT-(PS-co-PMMA)] nanocomposites.....	96
6.4.5 Studies on particle size and zeta potential analysis of [HNT-(PS-co-PMMA)] copolymer with different.....	98
<b>6.5 SUMMARY.....</b>	<b>99</b>
<b>CHAPTER 7 .....</b>	<b>101</b>
<b>ULTRASOUND-ASSISTED SYNTHESIS OF HNT-PS, HNT-PMMA, [HNT-(PS-co-PMMA)] NANOCOMPOSITES BY MINIEMULSION POLYMERIZATION ....</b>	<b>101</b>
<b>7.1 INTRODUCTION .....</b>	<b>101</b>
<b>7.2 SYNTHESIS OF HNT-POLYSTYRENE (HNT-PS) NANOCOMPOSITES ...</b>	<b>103</b>
7.2.1 Studies on structure of HNT-PS and MHNT-PS nanocomposites synthesized by ultrasound-assisted miniemulsion polymerization.....	104
7.2.2 Studies on morphology of HNT-PS, and MHNT-PS nanocomposites synthesized by ultrasound-assisted miniemulsion polymerization.....	105

7.2.3 Studies on functional groups of HNT-PS, and MHNT-PS nanocomposites synthesized by ultrasound-assisted miniemulsion polymerization.....	106
7.2.4 Studies on thermal stability of HNT-PS, and MHNT-PS nanocomposites synthesized by ultrasound-assisted miniemulsion polymerization .....	107
7.2.5 Studies on particle size and zeta potential of HNT-PS and MHNT-PS of nanocomposites synthesized by ultrasound-assisted miniemulsion polymerization.....	109
<b>7.3 SYNTHESIS OF HNT-POLYMETHYLMETHACRYLATE (HNT-PMMA) NANOCOMPOSITES.....</b>	<b>110</b>
7.3.1 Studies on structure of HNT-PMMA, and MHNT-PMMA nanocomposites synthesized by ultrasound-assisted miniemulsion polymerization .....	110
7.3.2 Studies on morphology of HNT-PMMA, and MHNT-PMMA nanocomposites by ultrasound-assisted miniemulsion polymerization .....	112
7.3.3 Studies on functional groups of HNT-PMMA, and MHNT-PMMA nanocomposites synthesized by ultrasound-assisted miniemulsion polymerization.....	113
7.3.4 Studies on thermal stability of HNT-PMMA, and MHNT-PMMA nanocomposites synthesized by ultrasound-assisted miniemulsion polymerization.....	114
7.3.5 Studies on zeta potential of HNT, MHNT, and MHNT-PMMA of nanocomposites synthesized by ultrasound-assisted miniemulsion polymerization.....	116
<b>7.4 SYNTHESIS OF POLY(STYRENE-CO-METHYLMETHACRYLATE)-HNT [HNT-(PS-co-PMMA)] NANOCOMPOSITES .....</b>	<b>117</b>

7.4.1 Studies on structure of [HNT-(PS-co-PMMA)], and [MHNT-(PS-co-PMMA)] nanocomposites synthesized by ultrasound-assisted miniemulsion polymerization.....	117
7.4.2 Studies on morphology of [HNT-(PS-co-PMMA)], and [MHNT-(PS-co-PMMA)] nanocomposites synthesized by ultrasound-assisted miniemulsion polymerization.....	117
7.4.3 Studies on functional groups of [HNT-(PS-co-PMMA)], and [MHNT-(PS-co-PMMA)] nanocomposites synthesized by ultrasound-assisted miniemulsion polymerization.....	119
7.4.4 Studies on thermal stability of [HNT-(PS-co-PMMA)], and [MHNT-(PS-co-PMMA)] nanocomposites synthesized by ultrasound-assisted miniemulsion polymerization.....	120
<b>7.5 SUMMARY.....</b>	<b>121</b>
<b>CHAPTER 8.....</b>	<b>123</b>
<b>8.1 INTRODUCTION.....</b>	<b>123</b>
<b>8.2 HNT-BASED PS AND HNT-BASED PMMA COATINGS USING DIP COATING.....</b>	<b>124</b>
8.2.1 Spectral properties of polymer coated glass substrate .....	124
8.2.2 Effect of sonication time on morphology of HNT-polymer coatings.....	131
8.2.3 Surface wetting behavior of coated and uncoated glass substrates.....	132
8.2.4 Thermal behavior of HNT-PS and HNT-PMMA nanocomposites .....	134
8.2.5 Mechanical behavior of HNT-PS and HNT-PMMA nanocomposites .....	138
<b>8.3 HNT BASED PS-co-PMMA COATINGS USING SPIN COATING .....</b>	<b>141</b>
8.3.1 Spectral properties of HNT based co-polymer coated glass substrate.....	141
8.3.2 Morphology of HNT-based co-polymer coatings.....	149

8.3.3 Surface wetting behavior of coated and uncoated glass substrates .....	152
8.3.4 Thermal behavior of HNT based PS-co-PMMA nanocomposites .....	154
8.3.5 Mechanical properties of HNT based PS-co-PMMA nanocomposites .....	157
<b>8.4 SUMMARY.....</b>	<b>160</b>
<b>CHAPTER 9.....</b>	<b>162</b>
<b>APPLICATION OF HNT-BASED PS MEMBRANES FOR WATER TREATMENT</b> <b>.....</b>	<b>162</b>
<b>9.1 INTRODUCTION.....</b>	<b>162</b>
<b>9.2 HNT-PS MEMBRANES FOR WATER PURIFICATION .....</b>	<b>163</b>
9.2.1 Morphology of HNT-PS membranes by SEM and EDAX.....	163
9.2.2 HNT-PS nanocomposites synthesized using tetrahydrofuran (THF) and N-methyl-2-pyrrolidone (NMP) as solvents .....	164
9.2.3 Morphology of HNT-PS membranes by atomic force microscopy (AFM)..	168
9.2.4 Studying the functional groups of HNT-PS membranes .....	170
9.2.5 Studying the structure of HNT-PS membranes.....	172
9.2.6 BET analysis of HNT-PS membranes .....	172
9.2.7 Studying the thermal properties of HNT-PS membranes .....	174
9.2.8 Studying the tensile strength of HNT-PS membranes (tensile strength analysis)	176
9.2.9 Application of HNT-PS membranes for water treatment .....	177
9.2.10 Performance evaluation of this study.....	179
9.2.11 Characterization of wastewater .....	189
<b>9.3 HNT-PS MEMBRANES FOR TREATING WATER RECEIVED FROM</b> <b>VARIOUS SOURCES.....</b>	<b>190</b>
9.3.1 HNT-PS membranes for treating water collected from Sea.....	190

9.3.2 HNT-PS membranes for treating Tap water .....	191
9.3.3 HNT-PS membranes for treating water from effluent .....	192
<b>9.4 SUMMARY .....</b>	<b>194</b>
<b>CHAPTER 10 .....</b>	<b>196</b>
<b>CONCLUSIONS.....</b>	<b>196</b>
<b>SCOPE FOR FURTHER RESEARCH .....</b>	<b>202</b>
<b>REFERENCES.....</b>	<b>203</b>
<b>APPENDIX.....</b>	<b>225</b>
<b>RESEARCH PUBLICATIONS .....</b>	<b>226</b>
<b>BIO-DATA.....</b>	<b>228</b>



## LIST OF FIGURES

Figure 2.1 A survey of publications related to HNTs in the last two decades.....	15
Figure 3.1 Modification of HNTs with surfactant CTAB.....	28
Figure 3.2 Surface modification of HNTs with $\gamma$ -MPS.....	29
Figure 3.3 Synthesis of PNCs by solution blending method.....	30
Figure 3.4 Experimental set-up for ultrasound assisted emulsion polymerization.....	31
Figure 3.5 Synthesis of PNCs by emulsion polymerization.....	32
Figure 3.6 Experimental setup for ultrasound-assisted miniemulsion polymerization....	33
Figure 3.7 Synthesis of PNCs by miniemulsion polymerization.....	34
Figure 3.8 Detailed procedure for coating glass substrate.....	35
Figure 4.1 X-Ray diffraction of HNT and CHNT.....	41
Figure 4.2 Scanning Electron Microscopy of (a) HNT and (b) CHNT.....	42
Figure 4.3 FT-IR analysis of HNT, CTAB, and CHNT.....	43
Figure 4.4 X-ray diffraction patterns of HNT and MHNT.....	44
Figure 4.5 SEM micrographs (a) HNT, (b) MHNT and TEM images of (c) HNT (d) MHNT.....	45

Figure 4.6 FT-IR spectra from $500\text{ cm}^{-1}$ to $4000\text{ cm}^{-1}$ of (a) HNT and MHNT (b) FT-IR spectra from $1450\text{ cm}^{-1}$ to $3100\text{ cm}^{-1}$ of MHNT.....	46
Figure 5.1 Solvent screening experiment using various solvents.....	49
Figure 5.2 XRD of HNT-polymer nanocomposites synthesised using various solvents...50	
Figure 5.3 Basal spacing of nanocomposites with and without ultrasound.....	51
Figure 5.4 SEM portraits of HNT-polystyrene nanocomposites synthesized using (a) toluene (b) benzene (c) chloroform (d) THF (e) DCM (f) $\text{CCl}_4$ .....	52
Figure 5.5 FT-IR analysis of HNT-polymer nanocomposites synthesized using various solvents.....	53
Figure 5.6 Difference in glass transition temperature ( $\Delta T_g$ ) of HNT-polymer nanocomposites synthesized using different solvents.....	54
Figure 5.7 XRD plots of HNT-PS, CHNT-PS and MHNT-PS nanocomposites.....	55
Figure 5.8 SEM images of (a) HNT-PS without sonication, (b) HNT-PS with sonication (c) CHNT-PS without sonication, (d) CHNT-PS with sonication, (e) MHNT-PS without sonication, and (f) MHNT-PS with sonication.....	57
Figure 5.9 FT-IR of HNT, PS, HNT-PS, CHNT-PS, MHNT-PS nanocomposites.....	58
Figure 5.10 DSC traces of (a) HNT-PS, (b) CHNT-PS, and (c) MHNT-PS with different HNT content ( $\text{wt}\%$ ).....	61

Figure 5.11 X-Ray diffraction patterns of HNT-PMMA, CHNT-PMMA and MHNT-PMMA nanocomposites.....	62
Figure 5.12 SEM images of (a) HNT-PMMA without sonication, (b) HNT-PMMA with sonication (c) CHNT-PMMA without sonication, (d) CHNT-PMMA with sonication, (e) MHNT-PMMA without sonication, and (f) MHNT-PMMA with sonication.....	64
Figure 5.13 FT-IR analysis HNT, PMMA, HNT-PMMA, CHNT-PMMA, and MHNT-PMMA.....	65
Figure 5.14 DSC images of (a) HNT-PMMA with different HNT content (wt%), (b) CHNT-PMMA with different HNT content (wt%) (c) MHNT-PMMA with different HNT content (wt%).....	68
Figure 6.1 XRD analysis of (a) HNT-PS, (b) CHNT-PS, and (c) MHNT-PS nanocomposites synthesized by ultrasound-assisted emulsion polymerization.....	73
Figure 6.2 SEM images of (a) HNT-PS without ultrasound, (b) HNT-PS with ultrasound, (c) CHNT-PS without ultrasound, (d) CHNT-PS with ultrasound, (e) MHNT-PS without ultrasound and (f) MHNT-PS with ultrasound.....	76
Figure 6.3 FT-IR of HNT, PS, HNT-PS, CHNT-PS, and MHNT-PS nanocomposites...	78
Figure 6.4 Thermal properties of (a) HNT-PS, (b) CHNT-PS and (c) MHNT-PS nanocomposites with different HNT content.....	81
Figure 6.5 XRD analysis of HNT-PMMA, CHNT-PMMA, and MHNT-PMMA nanocomposites.....	83

Figure 6.6 SEM images of (a) HNT-PMMA without sonication, (b) HNT-PMMA with sonication, (c) CHNT-PMMA without sonication, (d) CHNT-PMMA with sonication, (e) MHNT-PMMA without sonication, and (f) MHNT-PMMA with sonication.....	85
Figure 6.7 FT-IR analysis a) HNT b) PMMA, c) HNT-PMMA d) CHNT-PMMA e) MHNT-PMMA.....	86
Figure 6.8 Thermal properties of (a) HNT-PMMA, (b) MHNT-PMMA nanocomposites with different HNT content ( <b>wt</b> %).	89
Figure 6.9 XRD analysis of (a) HNT (b) PS-co-PMMA (c) [HNT-(PS-co-PMMA)] synthesized without ultrasound (d) [HNT-(PS-co-PMMA)] synthesized with ultrasound.....	91
Figure 6.10 SEM images of (a) HNTs (b) PS-co-PMMA (c) [HNT-(PS-co-PMMA)] without ultrasound (d) [HNT-(PS-co-PMMA)] with ultrasound for <b>30 min</b> (e) [HNT-(PS-co-PMMA)] with ultrasound for <b>60 min</b> .....	92
Figure 6.11 SEM images of (a) [HNT-(PS-co-PMMA)] without ultrasound, (b) [HNT-(PS-co-PMMA)] with ultrasound, (c) [CHNT-(PS-co-PMMA)] without ultrasound, (d) [CHNT-(PS-co-PMMA)] with ultrasound, (e) [MHNT-(PS-co-PMMA)] without ultrasound, and (f) [MHNT-(PS-co-PMMA)] with ultrasound.....	94
Figure 6.12 FT-IR analysis of, PS-co-PMMA, [HNT-(PS-co-PMMA)], [CHNT-(PS-co-PMMA)], and MHNT-(PS-co-PMMA).....	95
Figure 6.13 DSC analysis of [HNT-(PS-co-PMMA)], [CHNT-(PS-co-PMMA)] and [MHNT-(PS-co-PMMA)] nanocomposites.....	97

Figure 7.1 XRD image of (a) HNT-PS, and (b) MHNT-PS nanocomposites synthesized by ultrasound-assisted miniemulsion polymerization.....	104
Figure 7.2 SEM portraits of (a) HNT-PS without ultrasound, (b) HNT-PS with ultrasound, (c) MHNT-PS without ultrasound, and (d) MHNT-PS with ultrasound.....	105
Figure 7.3 FT-IR analysis of HNT, HNT-PS and MHNT-PS nanocomposites synthesized by ultrasound-assisted miniemulsion polymerization.....	106
Figure 7.4 DSC thermograms of (a) PS, HNT-PS, and MHNT-PS (b) PS with different <i>wt%</i> HNT nanocomposites synthesized by ultrasound-assisted miniemulsion polymerization.....	108
Figure 7.5 $\zeta$ -potential of HNTs, MHNTs, and MHNT-PS latex synthesized by ultrasound-assisted miniemulsion polymerization.....	109
Figure 7.6 XRD patterns of (a) HNT-PMMA, and (b) MHNT-PMMA nanocomposites synthesized by ultrasound-assisted miniemulsion polymerization.....	111
Figure 7.7 SEM portraits of (a) HNT-PMMA nanocomposites without ultrasound, (b) HNT-PMMA nanocomposites with ultrasound, (c) MHNT-PMMA nanocomposites without ultrasound, and (d) MHNT-PMMA nanocomposites with ultrasound.....	112
Figure 7.8 FT-IR spectrum of HNT, MHNT, HNT-PMMA, and MHNT-PMMA nanocomposites by ultrasound-assisted miniemulsion polymerization.....	114
Figure 7.9 DSC thermograms of (a) PMMA, HNT-PMMA, and MHNT-PMMA and (b) PMMA with different content of HNT nanocomposites synthesized by ultrasound-assisted miniemulsion polymerization.....	115

Figure 7.10 $\zeta$ -potential of HNTs, MHNTs, and MHNT-PMMA latex synthesized by ultrasound-assisted miniemulsion polymerization.....	116
Figure 7.11 XRD pattern of (a) [HNT-(PS-co-PMMA)] nanocomposite with and without sonication (b) [HNT-(PS-co-PMMA)] and [MHNT-(PS-co-PMMA)] nanocomposites synthesized by ultrasound-assisted miniemulsion polymerization.....	117
Figure 7.12 SEM analysis of (a) [HNT-(PS-co-PMMA)], and (b) [MHNT-(PS-co-PMMA)] nanocomposites synthesized by ultrasound-assisted miniemulsion polymerization.....	119
Figure 7.13 FT-IR spectrum of nanocomposites synthesized on using HNT and MHNT by ultrasound-assisted miniemulsion polymerization.....	120
Figure 7.14 DSC thermograms of [HNT-(PS-co-PMMA)] and [MHNT-(PS-co-PMMA)] nanocomposites with different HNT loading ( <b>wt%</b> ).....	121
Figure 8.1 Spectral properties of HNT-PS coated glass samples:(a) transmittance (b) reflectance and (c) absorptance of single side coated glass samples, and (d) transmittance (e) reflectance and (f) absorptance of double side coated glass samples. Suffixes 1 and 2 indicate single side and double side coated glasses, respectively. The dotted lines represent the corresponding properties of uncoated glass samples.....	125
Figure 8.2 Spectral properties of HNT-PMMA coated glass samples: (a) transmittance (b) reflectance and (c) absorptance of single side coated glass samples, and (d) transmittance (e) reflectance and (f) absorptance of double side coated glass samples. Suffixes 1 and 2 indicate single and double side coated glasses, respectively. The dotted lines represent the corresponding properties of uncoated glass samples.....	126

Figure 8.3 Spectral properties of (a) HNT-PS coated and (b) HNT-PMMA coated glass samples in UV and visible regions. Suffixes 1 and 2 represent single and double side coated glasses, respectively.....	127
Figure 8.4 Spectral properties of (a) HNT-PS coated and (b) HNT-PMMA coated glass samples in IR region. Suffixes 1 and 2 represent single and double side coated glasses, respectively.....	128
Figure 8.5 SEM image of HNT-PS coated glass portraying thickness of coating.....	130
Figure 8.6 Morphology of a thin film of HNT-PS coatings obtained at different sonication times: (a) without sonication, (b) <b>30 min</b> , and (c) <b>60 min</b> of sonication.....	131
Figure 8.7 Morphology of a thin film of HNT-PMMA coatings obtained at different sonication times: (a) without sonication, (b) <b>30 min</b> , and (c) <b>60 min</b> of sonication...	131
Figure 8.8 Images show contact angles of Clear (C), Bronze (Br), Green (G) and Grey (Gr) glass samples without coat, with only PS coat, HNT-PS coat with PMMA coat, and with HNT-PMMA coat.....	133
Figure 8.9 Thermogravimetric (TGA) plots of (a) HNT-PS and (b) HNT-PMMA nanocomposites. The corresponding TGA curves of respective neat polymers are presented for comparison.....	135
Figure 8.10 Glass transition temperature of (a) HNT-PS and (b) HNT-PMMA nanocomposites. The corresponding $T_g$ values of respective neat polymers are given for comparison.....	137

Figure 8.11 Tensile strength HNT-PS and HNT-PMMA nanocomposites along with their corresponding neat polymer values.....	138
Figure 8.12 Spectral behavior of [HNT-(PS-co-PMMA)] coated Bronze glass. (a) transmission (b) absorption of <b>3 wt%</b> HNT content coating coated glass; (c) transmission (d) absorption of <b>5 wt%</b> HNT content coating coated glass; (e) transmission (f) absorption of <b>7 wt%</b> HNT content coating coated glass; (g) transmission (h) absorption of <b>10 wt%</b> HNT content coating coated glass; Different coating thicknesses of samples are indicated by different colors ( <b>Bz<sub>0</sub> – uncoated, Bz<sub>1</sub> – 65 μm, Bz<sub>2</sub> – 110 μm, Bz<sub>3</sub> – 230 μm</b> ).....	142
Figure 8.13 Spectral behavior of [HNT-(PS-co-PMMA)] coated Green glass. (a) transmission (b) absorption of 3 wt% HNT content coating coated glass; (c) transmission (d) absorption of 5 wt% HNT content coating coated glass; (e) transmission (f) absorption of 7 wt% HNT content coating coated glass; (g) transmission (h) absorption of 10 wt% HNT content coating coated glass; Different coating thicknesses of samples are indicated by different colors ( <b>GG<sub>0</sub> – uncoated, GG<sub>1</sub> – 65 μm, GG<sub>2</sub> – 110 μm, GG<sub>3</sub> – 230 μm</b> ).....	144
Figure 8.14 Effect of different HNT content and coating thickness on (a) Transmission of bronze glass (b) Absorption of bronze glass (c) Transmission of bronze glass (d) Absorption of green glass (e) SSPF of bronze and green glass (f) SMPF of bronze and green glass.....	148
Figure 8.15 SEM images of cross-section of <b>5 wt%</b> [HNT-(PS-co-PMMA)] nanocomposite coatings on Bronze (Bz) glass having different coating thickness: (a) <b>65 μm, (b) 110 μm, (c) 230 μm</b> .....	150



Figure 8.16 Atomic Force Microscope images of surface of coated bronze glass with a thickness of **110 μm**. The content of HNTs in the coatings are **(a) 3 wt%** **(b) 5 wt%** **(c) 7 wt%** **and (d) 10 wt%**..... 151

Figure 8.17 (a) Effect of HNT content of coatings on contact angles measured with water droplet coated glass with coating thickness of **110 μm**. Contact angle value at **0 wt%** HNT is measured using a neat PS-co-PMMA coated glass, and (b) Images of a water droplet on glass samples coated with neat PS-co-PMMA and [HNT-(PS-co-PMMA)] nanocomposite coatings containing **3, 5, 7, and 10 wt%** HNTs, respectively. The direction of the arrow indicates the increasing content of HNTs in coatings..... 153

Figure 8.18 Thermal stability of [HNT-(PS-co-PMMA)] nanocomposite containing different amounts of HNT (a) The solid black line represents the TGA curve of neat PS-co-PMMA polymer and it is given for comparison to show the enhanced thermal stability. The corresponding DTG curves are presented in (b) FT-IR spectra of PS-co-PMMA copolymer with **5 wt %** HNT at different temperatures (c)..... 156

Figure 8.19 Effect of HNT content on mechanical properties [HNT-(PS-co-PMMA)] nanocomposite. The values at **0 wt%** of HNT correspond to neat PS-co-PMMA polymer..... 157

Figure 9.1 Results of the HNT image analysis: (a) SEM and (b) TEM.....163

Figure 9.2 HNT-PS microporous membrane (a) dried in an oven at **40 °C** for **24 h** (b) **25,000x** magnification (to view the structure inside the pore) (c) dried at room temperature for **24 h** (d) **10,000x** magnification and (e) HNT-PS nanoporous synthesized using NMP as a solvent membrane (f) **20,000x** magnification (to view the structure inside the pore).....165

Figure 9.3 EDAX of HNT-PS: (a) Microporous membrane and (b) Nanoporous membrane.....	167
Figure 9.4 Statistical approach to assess the distribution of pore size: (a) microporous and (b) nanoporous membranes.....	168
Figure 9.5 AFM image of HNT-PS (a) microporous membrane 2D (left) and 3D (right) and (b) nanoporous membrane 2D (left) and 3D (right).....	169
Figure 9.6 Contact angle of HNT-PS: (a) Microporous membrane and (b) Nanoporous membrane.....	170
Figure 9.7 FT-IR spectra of PS, HNT-PS, and HNT.....	171
Figure 9.8 XRD data of HNT and HNT-PS membranes.....	172
Figure 9.9 The structural analysis of microporous and nanoporous membranes (a) nitrogen adsorption–desorption isotherms at <b>77.4 K</b> and (b) their respective pore size distribution.....	174
Figure 9.10 Thermal properties of PS and HNT-PS membranes: (a) Glass transition analysis and (b) Thermogravimetric analysis.....	175
Figure 9.11 Detailed description of the HNT-based water purification procedures: (a) Experimental setup for water treatment; (b) Compartments for water purification; (c) Purified water collected in the bottom compartment; and (d) HNT-PS membrane used for purifying water.....	178

Figure 9.12 (a) Cross-sectional view of membrane and (b) Image of membrane after passing pure water.....179

Figure 9.13 Evaluation of the performance efficiency of Pure water flux, Rejection %, and Recovery % of HNT-PS membranes..... 185

## LIST OF TABLES

Table 2.1 Physical properties of HNTs.....	16
Table 3.1 Materials used for the synthesis of HNT-polymer nanocomposites .....	26
Table 3.2 Physical properties of HNTs as prescribed by Sigma Aldrich.....	28
Table 6.1 Chemical composition of emulsion.....	71
Table 6.2 Chemical composition of emulsion.....	82
Table 6. 3 Particle size and zeta potential of nanocomposites .....	98
Table 8.1 SSPF and SMPF values of coated and uncoated glasses .....	130
Table 8.2 Contact angles of coated and uncoated glasses .....	134
Table 8.3 Scratch test results of all four types of glass samples .....	140
Table 8.4 Effect of HNT content present in coatings on scratch resistance of [HNT-(PS-co-PMMA)] nanocomposite coatings on soda-lime glass.....	159
Table 9.1 BET analysis of both microporous and nanoporous structures of HNT-PS membrane.....	173
Table 9.2 Mechanical properties on HNT-PS membranes with different HNT content .	176
Table 9.3 Evaluation of % solvent content of microporous and nanoporous membranes using different HNT content and solvents .....	190

Table 9.4 Evaluation of porosity of microporous and nanoporous membranes using different HNT content and solvents .....	183
Table 9.5 Evaluation of shrinkage ratio using different HNT content and solvents .....	184
Table 9.6 Comparison of membrane properties with previous reports.....	189
Table 9.7 Comparison of wastewater properties between before and after passing through HNT-PS membrane filters.....	190
Table 9.8 Characterization of Sample – 1 (Sea Water).....	191
Table 9.9 Characterization of Sample -II (Tap water) .....	1922
Table 9.10 Characterization of Sample – III (Effluent water).....	1933

## NOMENCLATURE

### LIST OF SYMBOLS, UNITS AND GREEK WORDS

Symbol	Description
atm	Atmospheres
Å	Angstrom, unit
ζ	zeta potential
nm	Nanometer
μg	Microgram
mg	Milligram
g	Gram
kg	kilogram
kDa	kilo Dalton
mL	milli-litre
μg/L	microgram/litre
g/L	gram/litre
M	metre
h	Hour
min	minute
s	second

<b>wt %</b>	<b>weight%</b>
<b><math>\Delta</math></b>	<b>Delta, temperature difference</b>
<b><math>\lambda</math></b>	<b>lamda, wavelength</b>
<b><math>\Theta</math></b>	<b>theta, contact angle</b>
<b>%</b>	<b>Percentage</b>
<b>V</b>	<b>Volume</b>
<b>mS</b>	<b>milli Siemens, Conductivity</b>
<b>MPa</b>	<b>Megapascal</b>
<b>GPa</b>	<b>Gigapascal</b>

## **ABBREVIATIONS**

<b>HNT</b>	<b>Halloysite Nanotubes</b>
<b>PS</b>	<b>Polystyrene</b>
<b>PMMA</b>	<b>Polymethylmethacrylate</b>
<b>PS-co-PMMA</b>	<b>Poly(styrene-co-methylmethacrylate)</b>
<b>HNT-PS</b>	<b>Halloysite-polystyrene nanocomposite</b>
<b>HNT-PMMA</b>	<b>Halloysite-polymethylmethacrylate nanocomposite</b>
<b>PNCs</b>	<b>Polymer nanocomposites</b>
<b>CTAB</b>	<b>Cetyl trimethylammonium bromide</b>
<b><math>\gamma</math>-MPS</b>	<b><math>\gamma</math>-methacryloxypropyltrimethoxysilane</b>

<b>CHNT</b>	<b>CTAB modified HNT</b>
<b>MHNT</b>	<b><math>\gamma</math>-MPS modified HNT</b>
<b>THF</b>	<b>Tetrahydrofuran</b>
<b>DCM</b>	<b>Dichloromethane</b>
<b><math>CCl_4</math></b>	<b>carbon tetrachloride</b>
<b>NMP</b>	<b>N-Methyl-2-pyrrolidone</b>
<b>SDBS</b>	<b>Sodium dodecylbenzenesulfonate</b>
<b>KPS</b>	<b>Potassium persulfate</b>
<b>AIBN</b>	<b>Azobisisobutyronitrile</b>
<b>SEM</b>	<b>Scanning electron microscopy</b>
<b>TEM</b>	<b>Transmission electron microscopy</b>
<b>AFM</b>	<b>Atomic force microscopy</b>
<b>FTIR</b>	<b>Fourier transform and infrared</b>
<b>DSC</b>	<b>Differential scanning calorimetry</b>
<b>TGA</b>	<b>Thermogravimetric analysis</b>
<b>DTA</b>	<b>Differential thermal analysis</b>
<b>DTG</b>	<b>Differential thermal gravimetric analysis</b>
<b><math>T_g</math></b>	<b>Glass transition temperature</b>
<b>MW</b>	<b>Molecular weight</b>



<b>GPC</b>	<b>Gel permeation chromatography</b>
<b>XRD</b>	<b>X-ray diffraction</b>
<b>BET</b>	<b>Brunauer–Emmett–Teller analysis</b>

# CHAPTER 1

## INTRODUCTION

*This chapter introduces the important class of materials, polymer nanocomposites. It also covers a brief introduction of polymer-clay nanocomposites, different methods used for the synthesis of nanocomposites, ultrasound-assisted processes and their significance, and applications of polymer-clay nanocomposites.*

### 1.1 NANOCOMPOSITES

Nanotechnology is an art of working at the molecular scale for creating structures with the fundamentally unique molecular organization. It has been sighted to be promising for technological development as it accomplishes the fabrication of high-performance composite materials at low cost. Materials in the scale of nanometers function differently compared to their macroscale counterparts. Specifically, nanocomposites have been recognized to be of great significance in the field of nanotechnology. Fabrication of nanocomposites is expeditiously emerging as a multidisciplinary research interest as this could widen the application of nanotechnology.

Nanocomposites generally comprise of two or more materials in which one of the components shows dimensions in the nanometer range in at least one dimension ( $1\text{ nm} = 10^{-9}\text{m}$ ) (Roy et al. 1986). These materials have come to light as convenient substitutes to overthrow the limitations associated with micro and monolithic composites and can be fabricated using elementary and inexpensive techniques. They can overcome preparatory challenges related to the control of stoichiometry and elemental composition in nanoscale. They are considered to be the materials of the 21<sup>st</sup> century in the prospects of possessing property combinations and design uniqueness that are absent in conventional composites (Camargo et al. 2009). These materials often exhibit properties which are distinguished from conventional composites in terms of their strength and stiffness, thermal, chemical and oxidative stability as well as barrier properties. Additionally, these materials lack the

tradeoff of properties which is another unique and appealing aspect, and due to this, materials with excellent characteristics can be designed without any compromises. Hence, nanocomposites are widely used in aerospace, automotive, electronics, food packing, tissue engineering, biotechnology applications and various other applications.

Nanocomposites can be classified into three broad categories based on their matrix material which they are composed of. They are metal matrix (M-MNC), ceramic matrix (C-MNC) and polymer matrix nanocomposites (P-MNC). M-MNCs are composed of a matrix made up of alloy or ductile metal and reinforced with nanosized metals or ceramics. These materials display the combined features of metal and ceramic in terms of toughness and ductility with high strength and modulus. Therefore, M-MNCs are materials with superior compression/shear and thermal strength, and hence, they find applications in areas such as aerospace, automobiles, and structural/construction materials (Tjosng et al. 2005). C-MNCs are composed of a ceramic matrix with nanosized ceramics or metals particles incorporated into it. Ceramics display excellent wear resistance, extremely high chemical and thermal stability but, these materials are brittle, and hence their application is restricted in many fields. This can be tackled by the incorporation of energy dissipating materials such as fibers, whiskers, platelets, and particles into the ceramic matrix which can improve fracture toughness. This indeed will lead to the fabrication of advanced nanocomposites which displays high toughness (She et al. 2000). P-MNCs are materials in which nanosized organic or inorganic particles or both uniformly dispersed in the polymer matrix (thermoplastics, thermosets or elastomers) with an intention to dramatically enhance the polymer performance.

## **1.2 POLYMER MATRIX NANOCOMPOSITES**

Polymeric materials are extensively used in industry due to their inherent exciting and attractive properties such as ease of production and handling, lightweight and ductile nature. However, they lack properties such as strength and modulus as that of metals and ceramics. This limitation can be dealt by incorporating nanoparticles into polymer matrix. Polymers are reported to be filled with various inorganic compounds to enhance

mechanical strength, flame retardancy, heat and impact resistance, and to reduce electrical conductivity and gas permeability (Fischer 2003). Additionally, reinforcing polymer matrix with metal and ceramic leads to the formation of composites with unique magnetic, electronic, optical or catalytic properties, processability and film forming capability (Athawale et al. 2003). This approach improves polymer properties while restoring their lightweight and ductile nature (Akita and Hattori 1999; Jordan et al. 2005).

Polymer nanocomposites are particle-filled polymers in which at least one dimension of the dispersed phase has nanoscale dimensions, i.e., lesser than 100 *nm* (Alexandre and Dubois 2000). Consequently, nanoparticles have relatively large surface areas ( $L/h > 300$ ) and interact strongly with a polymer matrix and hence possess unique properties that cannot be found in their traditional composite counterparts. It can be highlighted that even at low volume fractions, the reinforcing efficiency of the composites is improved by 40 – 50% when compared to microcomposites (Ray and Bousmina 2005). Also, these reinforcements cause a drastic improvement in the biodegradability characteristics of polymers, making these composites promising in many fields (Kickelbick 2003). Polymer nanocomposites have attracted extensive interest in research as it offers many advantages such as improved mechanical properties (Arora et al. 2011; Hasegawa et al. 1999), improved dimensional stability (Zeng and Lee 2001), decreased water, gas and hydrocarbon permeability (Ahmadi et al. 2004), increased thermal stability (Xie et al. 2001), flame retardancy and low smoke emission (Kong et al. 2008; Ma et al. 2011), better chemical resistance and transparency, reduced weight etc. They are reported to be widely used for transportation, construction, electronics products and many other applications (Carastan and Demarquette 2007).

### **1.3 POLYMER NANOCOMPOSITES**

Polymer nanocomposites (PNCs) can be divided into different classes depending upon the reinforcing materials. Polymers may be reinforced with 3-D structures like zeolites, 2-D structures like clays, metal phosphates, oxides of metals, and 1-D and 0-D

structures like  $(\text{Mo}_3\text{Se}_3)_n$ , chains, and clusters. Among them, clay displays attractive properties such as high surface area, chemical composition, layered structure, size, etc. Clay nanoparticles have been used as inorganic additives in polymers for enhancing the performance of polymers. Polymer-clay nanocomposites have gained tremendous research interest as these materials greatly improve various physical and engineering properties of polymers at a very economical price and low filler addition. Multiple types of clays such as smectites, kaolinites, illites, chlorite group, sepiolite, attapulgite, modified (Cloisite grades) and unmodified (Na-MMT) montmorillonites are widely employed as fillers in polymer nanocomposites (Gao and He 2013; Lakshmi et al. 2008). Blending of polymer together with clay resulted in drastic improvements in mechanical (Lan and Pinnavaia 1994; Lebaron et al. 1999; Liu et al. 1999), optical (Alexandre and Dubois 2000; Koo et al. 2002), barrier properties (Ke and Yongping 2005; Messersmith and Giannelis 1995; Yano et al. 1997) and flame resistance (Blumstein 1965; Gilman 1999; Zanetti et al. 2001). Therefore, polymer-clay technology has been used to fabricate various multifunctional materials at a reasonable price which show up their applications in electronics, optics, construction, transportation and many other fields.

#### **1.4 HALLOYSITE NANOTUBES**

The mineral was named ‘Halloysite nanotubes (HNTs)’ by Berthier in 1826. It was named after Omalius d’Halloy, who recognized the mineral in Angleur, Liège, Belgium (Berthier 1982). Considerable research on HNTs commenced in the 1940’s (Brindley and Goodyear 1948; Macewan 1946; Douglas. 1947; McDowall and Vose 1952). Recently, HNTs have resumed research attention due to outpouring interest on tube-alike nanoparticles in fields of materials research and technology. HNTs are 1:1 phyllosilicate consisting of one layer of tetrahedral and one layer of octahedral sheets and display hollow microtubular and nanotubular morphology. They are excavated from naturally occurring deposits in countries like China, New Zealand, America, Brazil, and France. The molecular formula for HNTs is  $(\text{Al}_2\text{Si}_2\text{O}_5(\text{OH})_4 \cdot \text{H}_2\text{O})$  which is comparable to kaolinite but contains molecules of water in its interlayers. They also display a hollow nanotubular structure with

excellent aspect ratio. It is in contrast to kaolinite that has a stacked-plate structure (Hendricks 1938).

HNTs layered silicates and their crystal structure are made up of two building blocks, i.e., (i) octahedral sheets of edge sharing  $[AlO_6]$  and (ii) tetrahedral sheets of corner sharing  $[SiO_4]$ . In the  $[SiO_4]$  sheets the three corners are shared by tetrahedral and the remaining unbounded tetrahedral apices all point towards the same direction. Within the octahedral sheet, only two third of the existing octahedral sites are occupied by aluminium which is termed as dioctahedral layer. The layers that build up the final structure consists of each of these sheets, and hence the structure of HNTs is classified as 1:1 dioctahedral layer silicate. The water molecules exist between two consecutive layers creating a slight difference in the relative orientation between adjoining layers and results in differences in the symmetry of the final structure. The structure of HNTs annotates close similarity with the structure of kaolinite. HNTs are usually hydrated consisting of a layer of water in their interlayers. On heating, the HNTs (interlayer spacing of  $10 \text{ \AA}$ ) under the water in their interlayers vanish, causing an irreversible reduction in the interlayer spacing of HNTs (interlayer spacing  $7 \text{ \AA}$ ). Morphologically, HNTs are inorganic multi-walled nanotubes, exhibiting a layered structure containing tetrahedrally coordinated  $Si^{4+}$  and octahedrally coordinated  $Al^{3+}$  in a 1:1 stoichiometric ratio (Joussein et al. 2005). The outer and inner diameter of HNTs range between  $40 \text{ to } 70 \text{ nm}$  and  $10 \text{ to } 40 \text{ nm}$ , respectively and its length ranges between  $0.2 \text{ to } 2 \text{ }\mu\text{m}$ . Unlike other clays, in HNTs the aluminols are arranged in the interior of the HNTs, and primary siloxanes are located on the outside surface of the HNTs. Some silanols/aluminols are directed towards the ends of the layers. Thus, the interior and exterior surfaces of the HNTs exhibit positive and negative charges, respectively. HNTs find wide applications as adsorbents, raw materials for ceramics, nanocapsule for active compounds, catalysts, nanofiller in polymers and various other purposes. In comparison with nanocomposites synthesized using other clays such as MMT, Laponite, Bentonite etc, use of HNTs resulted in better thermal and mechanical properties

due to its composition and structure (Kim et al. 2003; Qutubuddin et al. 2002; Zhao and Liu 2008).

## **1.5 METHODS FOR SYNTHESIS OF POLYMER NANOCOMPOSITES**

Fabrication of PNCs can be carried out in different ways depending on the filler material, and processing technique. These techniques are broadly classified as i) Intercalation of the pre-polymer or polymer from solution (Jeon et al. 1998; Li and Ishida 2003; Lin and Otaduy 2005; Morgan and Harris 2004) ii) In-situ intercalative polymerization (Messersmith and Giannelis 1993; Mohammad and Yeum 2008) iii) Melt intercalation (Wang et al. 1998) iv) Direct mixing of particulates and polymer; v) Template synthesis; vi) In-situ polymerization, where intercalation of one or more suitable monomers takes place followed by polymerization (Noh and Lee 1999; Qutubuddin et al. 2002; Sedláková et al. 2009) and vii) Sol-gel process (Chiang and Ma 2002; Novak 1993).

### **1.5.1 Synthesis of PNCs by solution blending method**

Solution blending is a straightforward, simple and effective method for synthesis of polymer nanocomposites. It requires polymer, filler and a solvent that can serve as an intermediate between both. Solvent plays a crucial role in this method. It must dissolve the polymer and also be capable of swelling and dispersing the clay uniformly in the polymer matrix. Generally, this technique offers better distribution of the nanofiller in comparison with other methods and yields superior properties of PNCs. It can adopt processing techniques (injection and extrusion molding). It enables appropriate control on the uniformity of the components which helps in having a detailed understanding of the intercalation process and also the morphology of nanocomposites. Solution blending method aids in having good knowledge of the dynamics and structure of the intercalated polymers. It offers molecular comprehension and guide in designing materials with anticipated properties (Carastan and Demarquette 2007).

In solution blending technique, clay is dispersed in a solvent to exfoliate clay into single layers followed by the inculcation of the polymer into clay layers. The clay platelets

are generally held together by weak van der Waals forces and readily disperse in the solvent due to the escalation in entropy due to their disorganization. The polymer is subsequently adsorbed onto the delaminated clay layers to fill the layers before the reorganization, forming an intercalated followed by exfoliated nanocomposite structure (Anadão et al. 2010; Ghaemi et al. 2011).

### **1.5.2 Synthesis of PNCs by emulsion polymerization method**

Emulsion polymerization is a kind of free radical polymerization that employs water, monomer, and surfactant. The general type of emulsion used is oil-in-water emulsion, in which monomer (the oil) droplets are emulsified with surfactants in water (continuous phase). In some cases, water-soluble polymers, i.e., certain hydroxyethyl celluloses or polyvinyl alcohols, can also be employed as stabilizers/emulsifiers. A dispersion that is formed from emulsion polymerization is termed as latex (particularly if derived from a synthetic rubber) or an emulsion (in case the dispersion is immiscible in water). In this technique, polymerization occurs among the latex particles that are spontaneously formed within initial few minutes of the process. These latex particles have sizes in nano or micrometer scale and consist of many individual polymer chains. The latex particles do not coagulate with each other as the surfactant borders each particle, and the charges present on the surfactant electrostatically repels other particles. In cases where water-soluble polymers are used as stabilizers/emulsifiers instead of surfactants, water-soluble polymers tend to form a 'hairy layer' around a particle which repels it from other particles, because pushing particles together could cause compressing the chains. This technique is an essential industrial approach for the manufacture of polymer latex which finds applications as adhesives, paints, paper coatings, textile coatings, varnishes, etc. It displays advantages such as good control over reaction conditions and results in narrow particle size distribution in contrast to the solution and bulk polymerization techniques.



### **1.5.3 Synthesis of PNCs by mini-emulsion polymerization**

Mini-emulsions are relatively stable aqueous dispersions that are dispersed as mini-droplets with a size ranging from 50 to 500 nm. They are fabricated at high mixing rates in a reactor loaded with oil, water, and surfactants. An hydrophobe such as cetyl alcohol or hexadecane is employed as co-surfactant in an attempt to overpower Ostwald ripening of the droplets, which assists in achieving particles in preferred sizes. The composition of the oil phase and incorporation of hydrophobic compounds are the prominent features of mini-emulsion polymerization. Mini-emulsion polymerization has the potential to create nanoparticles which can be continuously dispersed in the aqueous phase for encapsulation and hence, it is considered advantageous over other methods of synthesis (Moraes et al. 2006). Mini-emulsions widens the applications of emulsion polymerization and offers advantages in controlling the composition of the oil phase and incorporation of hydrophobic compounds (Landfester et al. 1999). Additionally, this technique does not employ volatile organic solvents for the reaction, and therefore it is environmentally benign.

## **1.6 ULTRASONICATION**

Ultrasound is a sound wave with a frequency beyond human hearing. The frequency lies amongst 20 kHz to 10 MHz. Ultrasound is described to promote reaction rates (Richards and Loomis 1927). Process intensification with the help of ultrasound is widely used for many purposes in the scientific, engineering and medical fields as advanced and novel technology. There are two prominent mechanisms associated with ultrasonic irradiation in liquids, i.e., acoustic cavitation and acoustic streaming.

### **1.6.1 Acoustic cavitation**

On projection of ultrasonic wave in the liquid, a negative pressure is created that fractures the liquid, which is generally referred to as cavitation (Suslick 1990b). High-intensity ultrasonic wave has the potential to exceed the forces of molecular attraction and ionize concentrated H<sup>+</sup> and OH<sup>-</sup> free radicals in water. Consequently, a number of

cavitation bubbles are formed and these cavitation bubbles oscillate in the projected ultrasonic wave. When these cavitation bubbles captivate vapor or gas from the liquid medium, they tend to grow with a continuous projection of ultrasonic waves. As they grow larger in size, they become unsteady and eventually collapse implosively. These bubbles are known as “hot spots.”

According to “hot spot” theory, each bubble remains as a hot spot in the liquid medium. On implosion of the bubble, an elevated temperature of thousands of Kelvin (K) and pressure of hundreds of atmospheres (atm) are produced. These implosions give rise to highly-powerful shockwaves that repeatedly dissipate at a rate of 25 – 30 thousand times per second. As a result, ultrasound induces physical alterations of mass transfer, surface cleaning, emulsification, and thermal heating which are beneficial in the fields of nanoscale materials, environmental science, etc. The two dominant mechanisms responsible for the fragmentation of a particle in the presence of ultrasonic cavitation are mentioned below (Gopi and Nagarajan 2008):

- 1) Particle-particle interaction takes place when the sizes of particles are too small to agitate in the ultrasonic field. The intense shock waves generated accelerates the particles at the speed of about 500 *kmph* in liquids. During this, particles tend to collide with each other, which gives rise to intense chemical and structural alterations to the solid.
- 2) Particle-cavity interaction takes place when the size of the particles is large enough (agglomerates). The liquid jet travels with at a speed of roughly 500 *kmph* and strikes the surface with the intensity as the solid projectiles do. This jet causes severe damage at the point on the surface where it hits.

### **1.6.2 Acoustic streaming**

Acoustic streaming is a uni-directional, time-averaged flow developed in the liquid medium on exposure to a high-intensity ultrasonic wave. It is the steady flow generated in the viscous medium due to the proliferation of acoustic waves. Lighthill (1978) reported acoustic streaming motion arises due to the creation of gradients in momentum flux as a

consequence of the dissipation of acoustic energy flux. It takes place as a result of energy and momentum transfer of acoustic field to the fluid, through its attenuation coefficient (Madelin et al. 2006). During acoustic streaming, there is a bulk movement of fluid, due to which particles present in the sonicated system are taken along by the acoustic stream. This stream is capable of penetrating across the boundary layer of motionless fluid in the ultrasonic tank. Both acoustic cavitation and streaming work collectively in all sonication processes. At lower ultrasonic frequencies cavitation dominates, and the motion of fluid is randomized and becomes omnidirectional. Whereas at higher frequencies  $> 200 \text{ kHz}$ , acoustic streaming predominates, and flow becomes highly directional.

Ultrasound is utilized for carrying various applications such as crystallization, cleaning surfaces, degassing, extraction, emulsification, nanoparticle fabrication via sono-fragmentation, cleaning in microelectronic industry, remediation of soil contamination, dye-degradation, particles size reduction, promoting chemical reactions, enhancing the rate of reactions, etc. (Horst et al. 1996; Kass et al. 1996; Mason et al. 2004; Okitsu et al. 2005).

### **1.6.3 Ultrasound-assisted synthesis of PNCs**

In the field of polymer science, the rigorous environment created by ultrasonic waves are reported to enact as a special initiator which aids in breaking up of chemical bonds and enhance polymerization. The rate of initiation strongly relies on certain parameters like temperature, solvent properties and intensity of ultrasound (Zhang et al. 2009). Sonochemical techniques display attractive features such as faster polymerization, lower reaction temperatures, and high molecular weight of polymers. Also, sonochemistry activates and accelerates chemical reactions which reduces reaction time, enhances production rates, and can achieve some reactions that are not accomplished using conventional methods. Ultrasound-mediated processes dictate a new way of fabricating different types of polymer nanocomposites, not only for accomplishing dispersion of fillers in the matrix but also for carrying out polymerization reactions. As a unique tool, sonochemistry is attracting widespread attention around the world for the synthesis of nanocomposites.

Use of ultrasound for carrying out emulsion polymerization can further extend the advantages of this technique in terms of better polymerization rate, organized particle size distribution, and greater monomer conversion with minute quantities of initiator (Teo et al. 2008; Wang et al. 2005b). On the passage of ultrasound through the aqueous medium, a large number of micro-bubbles are produced which expand due to inconsistent pressure fields and finally explode (within a few microseconds). This cavity explosion generates enormous magnitudes of energy, extreme local temperatures  $> 10000\text{ K}$  and pressures  $> 1000\text{ atm}$  and also creates free radicals due to decomposition of monomer, surfactant, and water, these radicals aid in initiation and propagation of polymerization reactions. It has also been reported that emulsion polymerization that has been initiated by only ultrasound generates only a small quantity of radicals ( $\text{OH}^-$  and  $\text{H}^+$ ) and most of these radicals recombine to form water and  $\text{H}_2\text{O}_2$  (Bhanvase et al. 2012a; Cao et al. 2008). Therefore, it is recommended to add a minute quantity of initiator in the course of ultrasound-assisted emulsion polymerization for an industrially feasible process in terms of achieving better rates of polymerization.

## **1.7 APPLICATION OF HNT-POLYMER NANOCOMPOSITES**

### **1.7.1 HNT-based polymer nanocomposites as protective coating to glasses**

Variety of surface coatings for glass substrates have been tried in the past decades for protecting glasses from environmental degradation, physical damage, and also to improve their performance, functionality, mechanical, thermal, spectral and various other properties. However, glasses performing at high temperatures and other extreme conditions for industrial and domestic applications require the development of new coating materials to sustain such an extreme environment. Polymer-based nanocomposite coatings have achieved considerable research interest as they exhibit excellent mechanical properties such as toughness, hardness, and excellent tribological properties such as friction and wear. For the fabrication of organic-inorganic coatings, various inorganic nanoparticles such as nanoclay, carbon nanotube (CNT), nanoalumina/metals, graphite, etc. are reinforced into polymers and these coatings are used for application in aerospace, agriculture, catalysis,

cosmetics, food packaging, medicine, optics, optoelectronic devices, semiconductor devices and textiles (Hou et al. 2015; Nkeuwa et al. 2017; Sun et al. 2017; Wang et al. 2017; Zhang et al. 2017).

Among the diverse coating materials available, polymer-clay nanocomposites display advantages that may not be available in others, in terms of hardness, thermal and abrasion resistance, thermal resistance (Malas and Das 2017), good mechanical strength (Leite et al. 2010), lubrication and friction control and so, they can be used as coatings to serve diverse purposes. These coatings are made up of hard material (clay) surrounded by polymers. Including a small amount of clay in the polymer matrix significantly improves polymer behavior and properties such as strength, stiffness, and flexibility, electrical and thermal conductivities, etc.

HNTs have been reported to be reinforced into different polymer matrices, and as a result, considerable improvement in mechanical properties, structure, degradability, thermal and flame resistant properties of the polymers was observed. The enhancement in properties achieved by HNTs is comparable to that of carbon nanotubes (Deen and Zhitomirsky 2014; Erpek et al. 2017; Hedicke-höchstötter et al. 2009; Joshi et al. 2016).

### **1.7.2 HNT-based polymer membranes for water purification**

Clay based polymer nanocomposites have been identified as potential materials for the production of membranes with desirable functionalities, especially in water purification. Clays are microporous, thermally stable, chemically resistant, economical, and readily available. Clays have been used for water purification since ancient times; they have porous structures with various surface functional groups. Clays are also known to have significant antibacterial abilities due to their exclusive combination of chemical, physical and microbial properties, which enhance antimicrobial activity (Maryan and Montazer 2015). Nanocomposites consisting of polymer molecules and clays can be designed and fabricated by controlling the interaction of clay minerals with organic species at the molecular level or by adjusting the interaction enthalpy of the components (Fischer 2003). The exceptionally high surface area and aspect ratio cause property improvements

of the nanocomposites (Hong et al. 2008). As such, highly useful hybrid nanostructured materials can be generated by using polymers as a matrix to assemble clays at the nanometer scale.

This study reports ultrasound assisted synthesis of HNT-polymer nanocomposites. Various routes for synthesis of HNT-polymer composites were carried out i.e., solution blending, emulsion polymerization, and mini-emulsion polymerization in order to understand the effect of synthesis methods on properties of the synthesized composites. The surface of HNTs were functionalized using surfactant (CHNTs) and silane (MHNTs) to improve their compatibility with the polymer. The synthesized HNT-polymer nanocomposites were applied as protective coats to different types of soda lime glasses to prevent them from external damage, and enhance hydrophobicity, mechanical and thermal properties of glass without altering its inherent spectral. Two types of coating techniques were practiced i.e., spin coating and dip coating and effect of coating techniques on properties of glass were studied. The effect of thickness of coating and HNTs loading on the properties of coatings were studied in detail. Also, the synthesized HNT-polymer composites were used for fabrication of membranes and used for treatment of water. The effect of solvent on the properties of membranes was studied in detail. The membranes were characterized using different characterization techniques to understand their structure, morphology, functional, mechanical and thermal properties. Two stage filtration unit comprised of nanoporous membrane and microporous membrane was developed. Water collected from different sources (Sea water, Tap water and effluent water) were filtered in this unit. The samples were scrutinized before and after filtration to study the efficiency of membranes.

## CHAPTER 2

### REVIEW OF LITERATURE

*This chapter presents a brief examination of the literature with respect to the origin, potential applications and properties of HNTs. Synthesis of polymer-clay nanocomposites by different techniques and their applications are described. The outline, scope of the work and main objectives of the present work conclude this chapter.*

#### 2.1 HALLOYSITE NANOTUBES (HNTs)

HNTs are novel 1D natural nanomaterials with a unique combination of tubular nanostructure, large aspect ratio, natural availability, rich functionality, good biocompatibility, and high mechanical strength (Du et al. 2010). These characteristics generate exceptional mechanical, thermal, and biological properties that are available at the low cost for HNTs-polymer nanocomposites (Lvov and Abdullayev 2013). HNTs offer an inexpensive, low-tech alternative that is morphologically similar to multiwalled CNT's. They are hydrated polymorph of the 1:1 phyllosilicate clay, specifically the kaolin group (Joussein et al. 2005). A survey of publications related with HNTs during the past two decades is given in Fig. 2.1. The data were obtained based on science direct database. It is evident that the HNTs have been gaining growing research attention.

Typical analysis data of HNTs is shown in Table 2.1 obtained from previously published reports (Pooria Pasbakhsh 2015). Over the past two decades, HNTs find applications in various fields due to its novel properties. HNTs displayed potential as a viable nanoscale container for the encapsulation of biologically active molecules such as biocides and drugs as well as for their controlled release (R. Price, B. P. Gaber, Y. Lvov et al. 2001). They find high tech applications such as nanocontainers (Shchukin et al. 2008; Shchukin and Möhwald 2007). HNTs can also be used as cosmetics (Suh et al. 2011), nanoreactors (Shchukin et al. 2005; Tierrablanca et al. 2010), and catalyst support (Liu and Zhao 2009; Wang et al. 2011; Zatta et al. 2011). They can be used for controlled or sustained-released capsules which could be advantageous for various purposes such as lubricants, as paints and sealants, herbicides, household, pest

repellents, food and personal products, cosmetics, pharmaceuticals, and other agents (Levis and Deasy 2002; Lvov and Price 2008; Shchukin et al. 2008; Suh et al. 2011). HNTs can be coated with metallic and other materials to design a variety of electrical, chemical, and physical properties, which can find applications in electronic fabrication, radiation absorbing materials (RAM), and high-tech ceramic composite applications (Baral et al. 1993; Cavallaro et al. 2011; Zhang and Yang 2012). They can be utilized as molecular sieves for purposes such as water purification in refining industries, separation of liquids and gaseous mixtures, and the remediation of acid mine drainage (Li et al. 2011). HNTs are also reported to be functional as filler in polymer composite industries and reinforced into various plastics and rubbers (Ismail and Shaari 2010; Lecouvet et al. 2011; Tang et al. 2012). They are widely used for the synthesis of polymer-clay nanocomposites (Du et al. 2006). On the whole, HNTs can find potential applications in many fields such as filler in polymers, carrier for the loading and controlled release of guest molecules, adsorbent for pollution remediation, and nanoreactor/nanotemplate for the synthesis of functional materials.

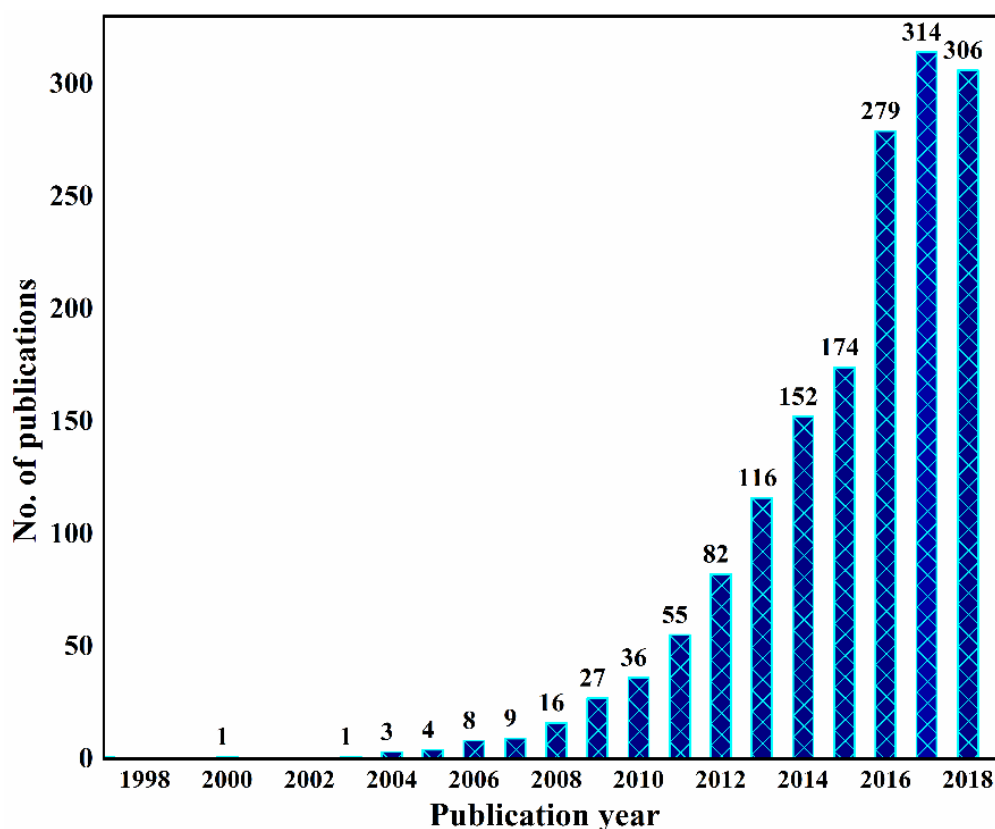


**Figure 2.1** A survey of publications related to HNTs in last two decades



Table 2.1 Physical properties of HNTs

<b>Parameter</b>	<b>Value</b>
Chemical Formula	$Al_2Si_2O_5(OH)_4 \cdot nH_2O$
Length	0.2 – 2 $\mu m$
Outer Diameter	40 – 70 $nm$
Inner Diameter	10 – 40 $nm$
Aspect ratio (L/D)	10 – 50
Elastic modulus (theoretical value)	140 $GPa$
Mean particle size in aqueous solution	143 $nm$
Particle size range in aqueous solution	50 – 400 $nm$
BET surface area	22.1 – 81.6 $m^2/g$
Pore space	14 – 46.8 %
Lumen space	11 – 39 %
Density	2.14 – 2.59 $g/cm^3$
Average pore size	79.7 – 100.2 $\text{\AA}$
Structural water release temperature	400 – 600 $^\circ C$

## 2.2 SURFACE MODIFICATION OF HNTs

Two crucial factors determine the performance of HNT-polymer nanocomposites: a good dispersion of the HNTs in the polymer matrix and a desirable interfacial affinity between the HNTs and the polymer (Du et al. 2010; Liu et al. 2014). Although HNTs display good dispersion in aqueous solutions due to the negatively charged hydrophilic external surface, achieving an exceptional dispersibility and controlled particle size in polymers remains a challenge. This is because HNTs in the polymer matrix readily form micron-sized aggregates. Therefore, to enhance the dispersion of HNTs in the polymer matrix and the interfacial interactions, it is suggested

to modify the surface of HNTs. Use of various surfactants to achieve the compatibility of clay and polymer matrix to yield a better dispersion of the clay platelets in the polymer matrix have been reported (Cavallaro et al. 2014, 2015; Laus, et al. 1998; Yang 2017). However, the effective dispersion of HNTs into the polymer matrix remains a problem.

Du et al. (2006) studied thermal stability and flame retardant effects of methacryloxypropyltrimethoxysilane modified HNTs on polypropylene nanocomposites. They reported the temperature at 5% weight loss of the nanocomposite filled with 10 phr modified HNTs was 60 °C higher than that of neat PP, and temperature at maximum weight loss rate of the nanocomposites filled with 10 phr modified HNTs was 74 °C higher than that of neat PP.

Guo et al. (2008) used Methacrylic acid (MAA) as a coupling agent to enhance the compatibility between HNTs and Styrene-butadiene-rubber by direct blending. It resulted in excellent mechanical and vulcanization properties of rubber.

Mu et al. (2008) grafted hyperbranched (co) polymers via surface-initiated self-condensing vinyl (co) polymerization and observed that surface-initiated self-condensing vinyl polymerization (SCVP) strategy via atom transfer radical polymerization (ATRP) technique was successfully used to graft hyperbranched macromolecules with different components on the surface of HNTs.

HNTs were modified with ethylenebis(stearamide) (EBS) and reinforced into poly(lactic acid). Modification of HNTs resulted in noticeable improvement in thermal behaviors as well as mechanical properties of HNT-reinforced poly(lactic acid) (Deng et al. 2009).

Liu et al. (2010) modified polymer along with HNTs with benzothiazole sulfide which showed improved mechanical and thermal properties of polypropylene-HNTs nanocomposites.

Pasbakhsh et al. (2010) grafted  $\gamma$ -methacryloxypropyl trimethoxysilane on the surface of HNT which increased its degree of dispersion in EPDM leading to the improvement of the tensile strength.

Tang et al. (2011) observed the effects of unfolded and intercalated HNTs on mechanical properties of HNTs–epoxy nanocomposites. They reported phenylphosphonic acid (PPA) could successfully unfold and intercalate HNTs, resulting in an increase of *d – spacing* from 7.2 Å to 15.1 Å, accompanied by the morphology change of most particles from nanotubes to nano-platelets.

The effect of HNTs modification with hexadecyl-tri-methyl-ammonium-bromide (HEDA), 3-aminopropyltrimethoxysilane and urea combined with in-situ matrix modification was done and intercalated into polypropylene matrix. This modification resulted in excellent improvement in the mechanical properties. This was due to increased polarity of matrix and which increased the affinity of the PP matrix for the HNTs (Khunova et al. 2013).

The surface of HNTs was modified with N,N-dimethylaminoethyl methacrylate (DMAEMA) and 2-hydroxyethyl methacrylate (HEMA) through surface-initiated atom transfer radical polymerization (SI-ATRP). They investigated on the drug release from neat and copolymer grafted HNT. It was observed drug release from coated HNT was retarded in comparison to uncoated. This indicated that the polymer brushes around the HNTs surface slowed diffusion of drug molecules from pores of nanotubes (Noein et al. 2017).

### **2.3 SYNTHESIS OF HNT-POLYMER NANOCOMPOSITES**

One of the easiest methods to achieve a nanostructured polymeric composite is to incorporate nanosized fillers into the polymer matrix. However, in this matter, the key challenge is to accomplish a well-dispersed structure of nanofillers in the polymeric matrix. The dispersion of fillers in polymers generally depends on the structure of filler, structure of the polymer, and the mixing method. Well-dispersed nanofillers provide a much higher surface to volume ratios, in comparison with conventional fillers. So incorporation of small amounts of nano-sized particles can enhance the properties of polymer matrixes dramatically. Primarily, the synthesis of HNT-polymer

nanocomposites can be carried out in three ways, solution blending, melt mixing and in-situ emulsion polymerization.

### **2.3.1 Solution blending method**

In solution blending method, a homogenous three-component mixture of polymer, clay, and solvent is prepared using heating and mechanical or ultrasonic mixing for reinforcement of filler into the polymer matrix in the presence of solvent. Once the composites are synthesized, the solvent is allowed to evaporate. During evaporation of the solvent, the clay platelets tend to rearrange into tactoids and get intercalated with the polymer. In solution-blending method, the selection of solvent plays a significant role. The solvent selected must be such that it should dissolve the polymer, should be capable of swelling the clay, should disperse clay uniformly in the polymer matrix, and it should also have a lesser affinity for the organically modified silicate surface, compared with the polymer chains. Also, the choice of solvent and cationic clay surfactant depend on the polymer studied, as sometimes the solvent adsorbs to the clay surface preferably over the polymer, preventing intercalation.

The reports on synthesis of polymer-clay nanocomposites by solution blending are mentioned here. Different polymer matrices along with clay were used for the synthesis of nanocomposites. The first report on synthesis of polyethylene oxide (PEO)-MMT nanocomposites by this method was reported by Aranda and Ruiz-Hitzky (1992). Wu and Lerner (1993) intercalated PEO into Na<sup>+</sup>-MMT and Na<sup>+</sup>-hectorite using acetonitrile as solvent. Choi et al. (2001) reported the fabrication of PEO/MMT nanocomposites using chloroform as a solvent. Jeon et al. (1998) reported nanocomposite comprised on high-density polyethylene (HDPE) and montmorillonite (MMT). MMT was modified with dodecylamine using a combination of solvents xylene and benzonitrile. Tseng et al. (2001) changed clay with cetyl pyridinium chloride and intercalated it into syndiotactic polystyrene by this method and obtained nearly exfoliated structured nanocomposites. Nanocomposite based on polysulfone and organoclay was reported by Sur et al. (2001) and obtained well-exfoliated nanocomposites. Ogata et al. (1997) developed nanocomposites comprised of polylactide (PLA) or poly( $\epsilon$ -caprolactone) but could not achieve intercalated nor

exfoliated structure but the clay existed in the form of tactoids consisting of several stacked silicate monolayers. Exfoliated nanocomposites of polyimide/MMT nanocomposites were prepared using solutions of poly(amic acid) precursors and dodecyl-MMT using N-methyl-2-pyrrolidone as a solvent by Magaraphan et al. (2001).

### **2.3.2 Emulsion polymerization and copolymerization**

Emulsion polymerization is an efficient technique for the fabrication of HNT-polymer composite. It is capable of generating monodispersed polymer nanoparticles with controlled molecular weight and uses water as the dispersion medium. Use of water is advantageous as it results in widening of the galleries of layered silicates and avoids the need for any chemical treatment. It also aids in the encapsulation of materials, if the inorganic particles employed display hydrophobic nature. However, the intensity of shear in the reactor and the type of the clay modification is significant in exfoliation of clay platelets in the organic phase (Borthakur et al. 2010). Several researchers have studied the ultrasound-assisted emulsion polymerization of various monomers such as methyl methacrylate, butyl acrylate, styrene, etc. (Kruus 1987; Ooi and Biggs 2000; Price 1996; Teo et al. 2008).

Ooi and Biggs (2000) synthesized polystyrene latex by ultrasonically initiated emulsion polymerization and reported the effect of acoustic intensity on the monomer conversion rate.

Polymer-clay nanocomposites were prepared by ultrasound assisted free radical polymerization in the presence of organically modified clay. Subsequently, melt-mixing of the product was carried out in an ultrasonically assisted mixer (Ryu et al. 2004). They reported improvement in nanoscale dispersion during melt mixing of monomer, polymer and organically modified clay as a result of employing ultrasound.

Lee et al. (2000) studied dispersion enhancement in nanocomposites by preparing polypropylene/clay nanocomposites in-situ (polymerization within the mixture) in melt phase by ultrasound application. They concluded this method could be an effective method to enhance the dispersion of fillers in thermoplastic-based nanocomposites.

Yin and Chen (2004) have also used ultrasound as a polymerization initiating mechanism for the emulsion copolymerization process. Ultrasound-assisted emulsion polymerization for one-pot synthesis of montmorillonite–exfoliated polystyrene nanocomposite was carried out and it was observed that the nanocomposite grew in one direction to form a bundle during the ultrasonic irradiation. This report indicated the noncontact directional control of certain materials by ultrasound. It has also been reported that ultrasonic irradiation successfully generates exfoliated nanocomposite with sufficient interaction between monomer and organic chains of the interlayer (Wang et al. 2005b).

High intensity ultrasound was utilized for the synthesis of intercalated polystyrene/Na<sup>+</sup>-MMT nanocomposites by intercalating hydrophobic polystyrene into the hydrophilic silicate layers. The in-situ emulsion polymerization was initiated using ultrasound. They reported that the use of ultrasonic irradiations initiates polymerization reaction of monomer. This eliminates use of additional chemical initiator and modification of layered silicates. They also reported that there was enhancement in the breakup of layered silicate bundle and reduction in the size of dispersed phase with better homogeneity on using ultrasound relative to conventional in situ emulsion polymerization. Furthermore, ultrasonic irradiation can not only initiate polymerization at room temperature and disperse clay layers at the nanoscale, but can also shorten the polymerization time. Therefore, the ultrasonically initiated in situ emulsion polymerization can be considered as a novel, simple, and fast approach to preparing polymer /layered inorganic nanocomposites (Wang et al. 2005a).

In particular, Teo et al. (2008) have presented a comparison of ultrasound initiated emulsion polymerization of methyl methacrylate (MMA), n-butyl methacrylate (BMA) and 2-ethylhexyl methacrylate (2EHMA) in the presence of sodium dodecyl sulfate as a stabilizer. The obtained latex particles were of 70 – 110 nm in size with molecular weights of the order of  $2 - 6 * 10^6 g mol^{-1}$ . It has also been reported that the rates of polymerization of the methacrylate monomers are dependent on the physicochemical properties of the monomers.

PA6/clay nanocomposites were synthesized with the help of ultrasound, and it was observed that usage of ultrasound helped in getting good dispersion of nanoparticles in the matrix without the use of any chemical modification. They reported good improvement in mechanical, rheological and structural properties (Swain and Isayev 2009).

Core-shell nanocomposite comprised of poly(styrene-co-methyl acrylate)-bentonite was fabricated via miniemulsion process assisted by ultrasound. They reported the application of ultrasound only in the stage one, i.e. during emulsion formation and observed reduction in particle size to 700 nm. Hence, ultrasonic irradiations that can be applied during emulsification (stage one) resulted in formation of core and shell structure (Borthakur et al. 2010).

Bhanvase et al. (2012) synthesized exfoliated poly(styrene-co-methyl methacrylate)/montmorillonite nanocomposites using ultrasound-assisted in-situ emulsion copolymerization. Their work highlighted the role of ultrasonic irradiations for effective dispersion of clay into the polymer matrix based on the intensified shear and turbulence levels in the reactor. It was reported that the high levels of shear generated in the reaction mixture by ultrasonic irradiation helped in the separation of a layered silicate bunch (tactoids) during the initial stage and ultimately yielded exfoliated structures.

### **2.3.3 Miniemulsion polymerization**

Nanocomposites comprised of polymer-clay can be synthesized by miniemulsion polymerization. Miniemulsion technique has shown to be an efficient method for the synthesis of nanoclay/polymer nanocomposites. Mirzataheri et al. (2009) synthesized core-shell nanocomposite of poly(styrene-co-butyl acrylate)/Cloisite 30B. Poly(styrene-methylmethacrylate)/Al<sub>2</sub>O<sub>3</sub> by mini-emulsion polymerization technique was reported by (Mahdavian et al. 2009). Hu et al. (2011) highlighted the synthesis of organic-inorganic nanocomposites by miniemulsion polymerization. Large amounts of clay have been loaded in the polymer matrix by miniemulsion polymerization (Zengeni et al. 2012). Encapsulation of organomodified montmorillonite by PMMA through ATRP in miniemulsions led to hybrid

nanoparticles with uniform size distribution. Capek (2012) investigated the kinetics of photo-initiated miniemulsion polymerization of butyl acrylate (BA) in the presence of clay. Hatami et al. (2013) examined the nucleation type, kinetics, and polymerization control of ATRP miniemulsion copolymerization of styrene (St) and methyl methacrylate (MMA) in the presence of nanoclay. Asymmetric saponite/PS nanoparticles have been synthesized via miniemulsion polymerization using nanosaponites with a size larger than the equilibrated droplet size of the miniemulsion (Tong and Deng 2013). Further, the preparation of hybrid nanoparticles in miniemulsions is reported by other reviews (Cao and Ziener 2013; van Herk 2010).

#### **2.4 APPLICATION OF HNT-POLYMER NANOCOMPOSITES**

HNTs have been recognized to have the potential for treatment of water and hence reported to be reinforced into various polymers for the synthesis of membranes for water treatment. These membranes have been reported to display various advantages in terms of holding antimicrobial, antifungal, antifouling properties and also had excellent flux rate and purifying efficiency. Chen et al. (2012) fabricated polyethersulfone (PES) ultrafiltration membrane reinforced with HNTs, these membranes display excellent antibacterial ability against *E. coli* (Gram-negative) and *S. aureus* (Gram-positive) bacteria. Polyethersulfone (PES) ultrafiltration membranes reinforced with HNT-chitosan-Ag nanoparticles were fabricated, these membranes display effective biofouling control along with antibacterial activity rates of 94% and 92.6 % against *E. coli* and *S. aureus*, respectively (Chen et al. 2013). Zhu et al. (2014) reported grafting of HNTs with sodium 4-styrene sulfonate via surface-initiated atom transfer radical polymerization (SI-ATRP) and these membranes were used for desalination of textile industry. Also, polyethersulfone (PES) ultrafiltration membrane with the improved antifouling property was prepared via traditional phase inversion method through the incorporation of dextran grafted HNTs (Yu et al. 2014). Organized arrays of halloysite clay nanotubes on polyacrylonitrile porous membrane were prepared via a facile evaporation-induced method which demonstrated great fouling resistance for dye accumulation and bovine serum albumin adsorption (Qin et al. 2016). Zeng et al. (2017) reported the functionalization of HNTs with dopamine and



reinforced into polyvinylidene fluoride (PVDF) membranes; they were able to demonstrate their possible use for dye removal.

## **2.5 SCOPE OF THE PRESENT WORK & OBJECTIVES**

### **2.5.1 Research Gaps**

Numerous studies have been carried out on fillers like carbon nanotubes (CNTs) and boron nitride nanotubes (BNNTs), because of their excellent properties. However, these materials are technologically demanding to be produced in bulk and expensive. HNTs offer an inexpensive, low-tech alternative to CNTs that is morphologically similar to multiwalled CNTs. Large-scale preparation of nanocomposites is not realized yet due to the absence of cost-effective methods for controlled dispersion of nanoparticles in the polymer matrix. Nanoparticles have a strong tendency to agglomerate, which will nullify any advantages which could be obtained as a result of the lower dimension of particles. Currently, there is great difficulty in obtaining nanocomposites with acceptable homogeneity. Even though various physical and chemical methods are reported in the literature, there is a need to develop the best routes for synthesizing PNCs that accurately control their dimension, properties and reaction mechanism. It is also essential to explore the possible uses of PNCs for various applications. The fundamental structure and property relationships of nanocomposites prepared by different methods have to be studied to develop novel HNTs-related hybrid materials for high-efficiency applications.

Dispersion of clays in the polymer matrix plays a vital role in enhancing the properties of resultant nanocomposites. Moreover, uniform dispersion constructs interfacial coupling between the clays and the polymer matrix facilitating the stress transfer to the reinforcement phase which reduces the weak points present in conventional polymer composites. Hence, there is a need to functionalize as well as use advanced techniques for achieving the uniform dispersion of HNTs in the polymer matrix. Ultrasound aids to achieve better dispersion of HNTs, and accelerates the rate of polymerization. The primary aim of this research work is to synthesize HNT-polymer nanocomposites through facile approach assisted by ultrasound and to explore the potential applications of HNT-polymer nanocomposites. Ultrasound facilitates to

overcome any preparatory challenges and enhance the properties of resultant nanocomposites. Polystyrene (PS) is a thermoplastic which is commercially available and has attractive physical properties such as extremely good dimensional stability, acceptable strength and satisfactory electrical and thermal properties and hence is used for a variety of purposes. On the other hand, Poly methymethacrylate (PMMA) is a glassy polymer and is often preferred due to its moderate properties, very high transmissivity, significantly inert to various chemical reactions, higher fracture energy, easy handling and processing, and low cost. Due to these attractive properties both PS and PMMA were used in this study.

### **2.5.2 Aim**

Synthesis of HNT-polymer nanocomposites using different preparatory methods, to investigate their properties using various characterization techniques and use them for potential applications.

### **2.5.3 Objectives**

- I. To study the surface modification of HNTs for improving the compatibility and interactions of HNTs with polymer
- II. To synthesize and characterize HNT-polymer nanocomposites by ultrasound assisted solution blending method, emulsion, and mini-emulsion polymerization.
  - (a) To study the effect of various solvents on morphology and properties of nanocomposites.
  - (b) To study the effect of sonication on the properties of nanocomposites.
  - (c) To examine the effect of surface modification and the content of HNTs on the properties of nanocomposites.
- III. To study the application of HNT-polymer nanocomposites for the protection of glass surface.
- IV. To study the application of HNT-polymer nanocomposite membranes for the treatment of wastewater.

## CHAPTER 3

### RESEARCH METHODOLOGY

*In this chapter, brief descriptions of the general chemicals employed in this study are listed; protocols followed for surface modification of HNTs, experimental procedures for synthesis of polymer-clay nanocomposites, development of these nanocomposites for coating the surface of the soda-lime glass and for fabrication of membranes are described. This chapter also includes the analytical and physical methods used for the characterization of functionalized HNTs and synthesized HNT-polymer nanocomposites.*

#### 3.1 MATERIALS AND METHODS

Table 3.1 Materials used for the synthesis of HNT-polymer nanocomposites

Sl. No.	Chemicals	Quantity	Used as
1	Polystyrene ( <i>MW</i> – 280 <i>kDa</i> )	Sigma Aldrich	Matrix
2	Polymethylmethacrylate ( <i>MW</i> – 120 <i>kDa</i> )	Sigma Aldrich	Matrix
3	Halloysite nanotubes (Properties given in Table 3.2)	Sigma Aldrich	Reinforcing material
4	Cetyl trimethylammonium bromide (CTAB)	Sisco Research Laboratories	Surfactant for modification of HNTs
5	$\gamma$ -methacryloxypropyltrimethoxysilane ( $\gamma$ -MPS)	Sigma Aldrich	Silane for modification of HNTs
6	Styrene (Sty)	Sigma Aldrich	Monomer
7	Methylmethacrylate (MMA)	Sigma Aldrich	Monomer
8	Sodium dodecyl sulphate (SDS)	Nice chemicals	Emulsifier
9	Span-60	CDH	Emulsifier

10	Sodium dodecyl benzene sulfonate (SDBS)	Rolex	Emulsifier
11	Potassium per sulfate (KPS)	Himedia	Initiator
12	2,2-azo-isobutyronitrile (AIBN)	Kemphasol	Initiator
13	Hexadecane	Sigma Aldrich	Co-surfactant
14	Toluene	Merck	Solvents
15	Benzene	Merck	Solvents
16	Carbon tetrachloride (CCl <sub>4</sub> )	Merck	Solvents
17	Tetrahydrofuran (THF)	Merck	Solvents
18	Dichloromethane (DCM)	Merck	Solvents
19	Chloroform	Merck	Solvents
20	N-methyl-2-pyrrolidone (NMP)	Merck	Solvents
21	Hydroquinone	Lobachem	Inhibitor

**Table 3. 2 Physical properties of HNTs as prescribed by Sigma Aldrich**

<b>Physical properties</b>	<b>Values</b>
Inner diameter	30 – 50 <i>nm</i>
Outer diameter	50 – 80 <i>nm</i>
Length	1 – 3 $\mu$ <i>m</i>
Aspect ratio	18
Refractive index	1.54
Specific surface area	64 <i>m</i> <sup>2</sup> / <i>g</i>
Specific gravity	2.53

All the materials used in the experiments of this work have been listed in Table 3.1. Water samples for treatment using the membranes synthesized were collected from the effluent treatment plant at the West Coast pulp and paper mill, Dandeli, India. Millipore water was used for all experiments, and all the reactions were carried out

under N<sub>2</sub> atmosphere. Sonics vibra-cell sonicator containing titanium horn with 20 kHz frequency and 500 W maximum power input was used.

### 3.2 SURFACE MODIFICATION OF HNTs

#### 3.2.1 Surface modification of HNTs with surfactant CTAB

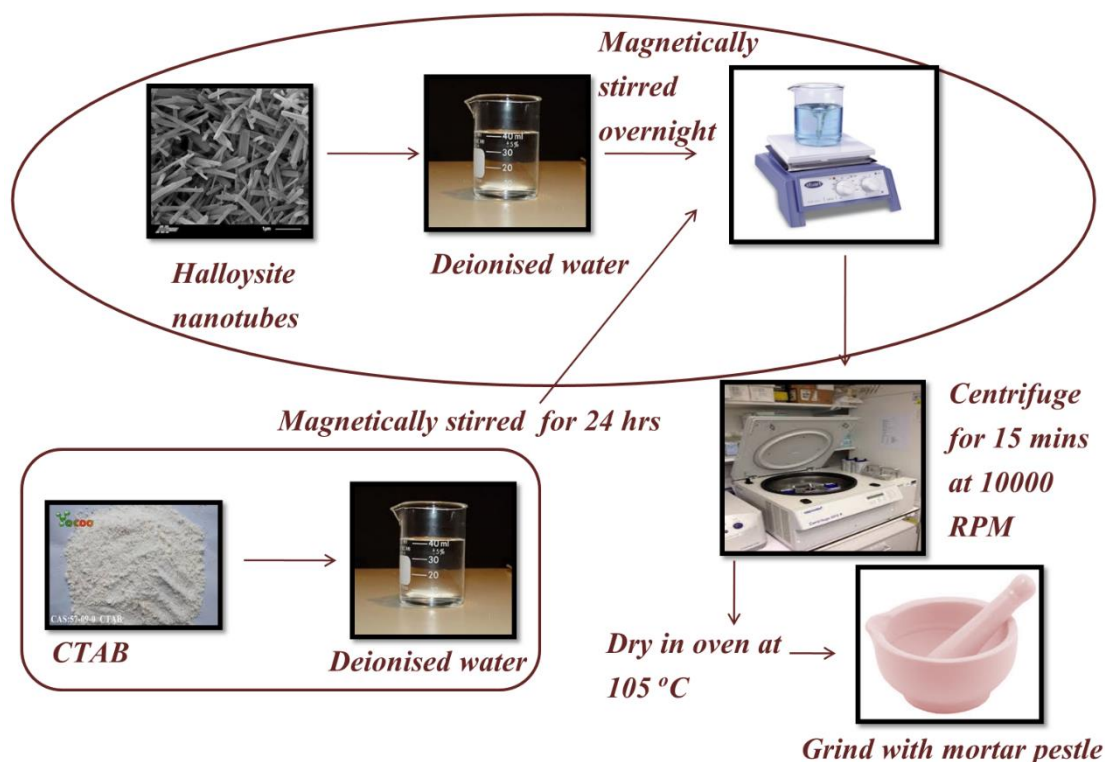


Figure 3.1 Modification of HNTs with surfactant CTAB

CHNTs was prepared by an ion-exchange method using a CTAB solution as depicted in Fig 3.1. 10 g of HNTs was dispersed in 1000 mL of deionized water and was vigorously stirred overnight using a magnetic stirrer. 5 g of CTAB was dissolved in 100 mL of deionized water and was slowly added to HNT mixture. The mixture was magnetically agitated for 24 h at room temperature. The suspension was centrifuged at 10000 RPM for 15 min and washed with distilled water to remove excess Br<sup>-</sup>. The product was dried at 105 °C until constant weight loss was obtained and labeled as CHNTs.

### 3.2.2 Surface modification of HNTs with $\gamma$ -MPS

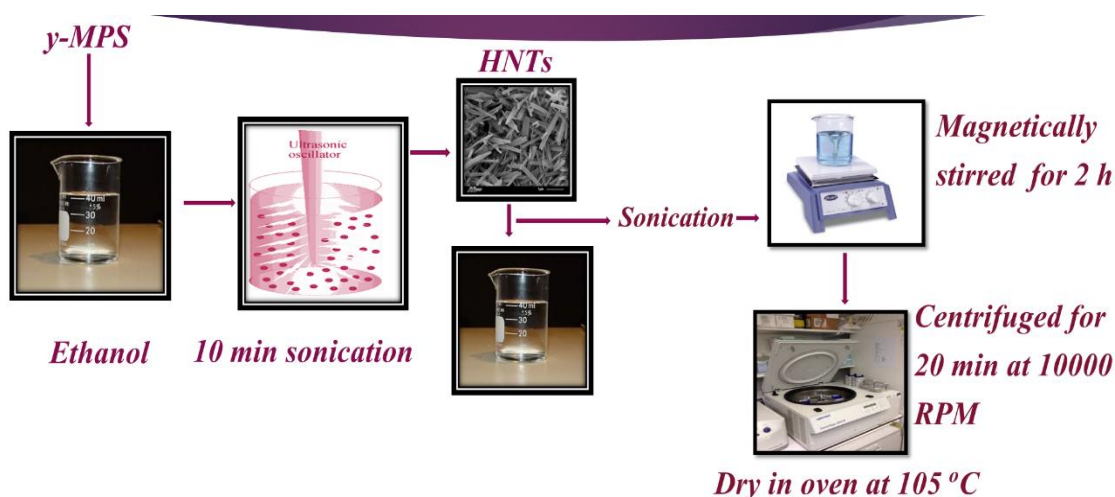


Figure 3.2 Surface modification of HNTs with  $\gamma$ -MPS

The protocol followed to modify the surface of HNTs with  $\gamma$ -MPS is displayed in Fig. 3.2. For modification of HNT, 40 mL ethanol was poured into 100 mL beaker, 4 mL  $\gamma$ -MPS was added to it and was sonicated for 10 min at 50% amplitude and a pulse time of 3s on and 2 s off. 10 g of HNT was added to this and sonicated again for 30 min. The suspension was then magnetically stirred for 30 min and centrifuged for 20 min at 10000 RPM. The supernatant was separated, and the precipitated was dried in a hot-air oven at 40 °C overnight to obtain  $\gamma$ -MPS-modified HNTs (MHNTs).

## 3.3 SYNTHESIS OF HNT-POLYMER NANOCOMPOSITES USING ULTRASOUND ASSISTED SOLUTION INTERCALATION METHOD

### 3.3.1 Initial solvent screening for the blending of HNTs and polymer

Various aromatic and non-aromatic solvents which were known to dissolve PS, PMMA were investigated to find a suitable solvent which would disperse HNTs best. 0.15 g of HNTs was added to different test-tubes, followed by addition of 5 mL of various solvents with stirring to determine the best solvent(s). Once solvent was added to the HNTs, the material was stirred and allowed to sit for 24 h to observe settling. Non-aromatic solvents tetrahydrofuran dispersed the HNTs well, but aromatic solvents provided better dispersion of HNTs. Based on these observations, toluene, tetrahydrofuran (THF), benzene, carbon tetrachloride (CCl<sub>4</sub>), chloroform,

dichloromethane (DCM) prevented precipitation of HNTs after 24 h and hence were chosen as the solvent for the solution intercalation experiments.

### 3.3.2 Synthesis of HNT-polymer nanocomposites by ultrasound-assisted solution blending method

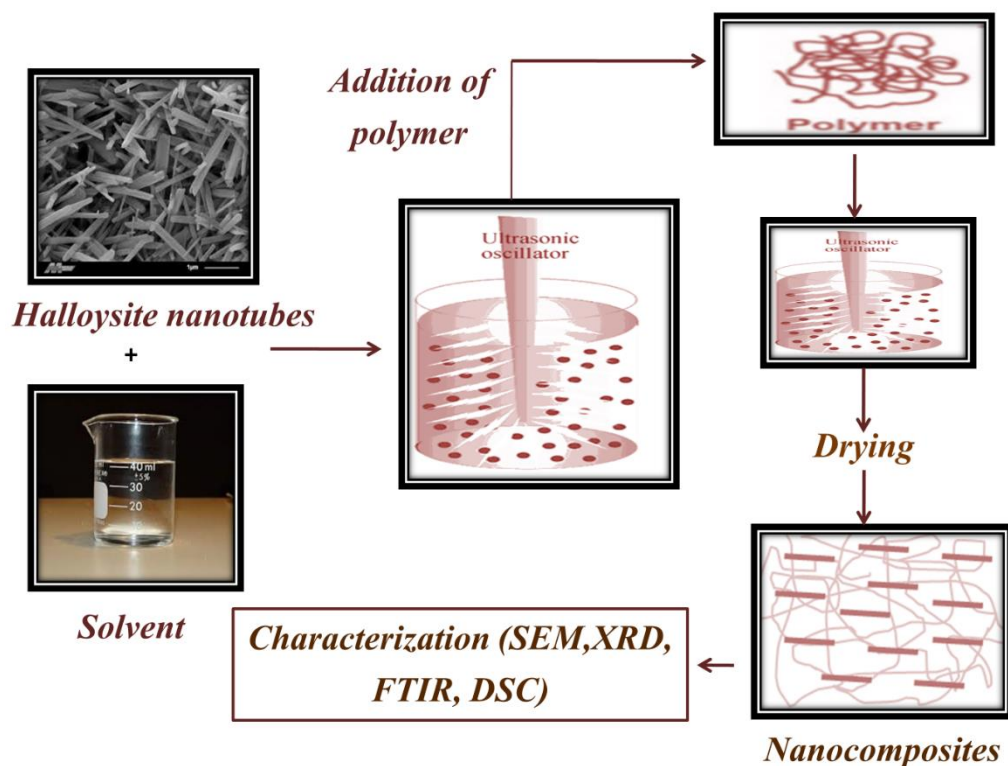


Figure 3.3 Synthesis of PNCs by solution blending method

HNT-polymer composites of polystyrene matrix were prepared by addition of different *wt%* of HNTs in 20 mL of various solvents. The suspension was stirred magnetically for 1 h and sonicated for 1 h. Then, 2 g of polymer was added and again stirred magnetically for 1 h and sonicated for 0.5, 1, 1.5, and 2 h to study the effect of sonication time on properties of composites. The mixture was cast into Petri dishes and allowed to dry for 24 h at room temperature, during which solvent got evaporated, and thin films were obtained. These composites were labeled as HNT-polymer. Virgin polymer sample without addition of HNTs was also prepared for comparison. The detailed procedure can be seen in Fig. 3.3.

### 3.4 SYNTHESIS OF PNCs USING ULTRASOUND-ASSISTED EMULSION POLYMERIZATION

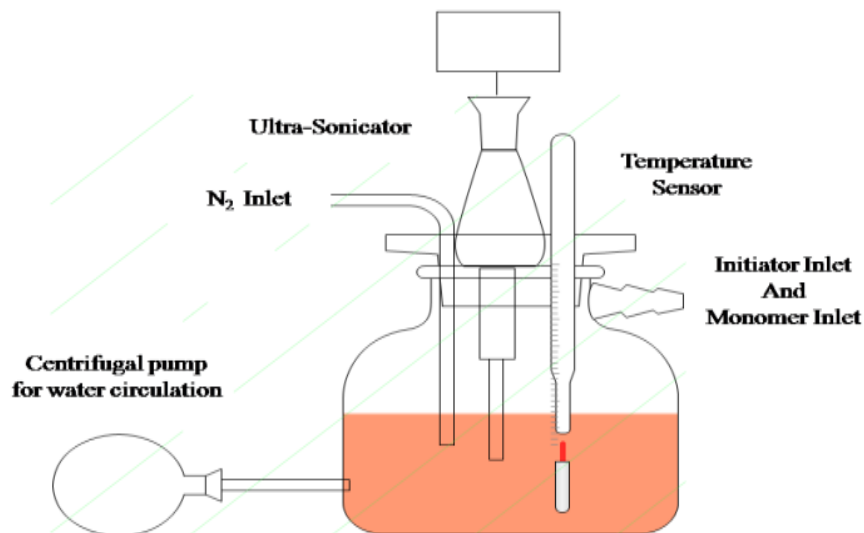


Figure 3.4 Experimental set-up for ultrasound assisted emulsion polymerization

PNCs synthesis was carried out in the emulsion polymerization reactor as shown in Fig. 3.4 and operated in semi-batch mode. The experimental setup consists of a reactor which is a jacketed glass vessel of 500 *mL* volume capacity equipped with a 13 *mm* stainless steel probe connected to an ultrasonic generator (Sonics Vibra-cell, USA). The ultrasonic horn operates at a frequency of 20 *kHz*, and the rated output power was 500 *W*. In the experiment, the ultrasonic horn is operated at different amplitudes, meaning that the supplied power to the system was varied to study the effect of acoustic intensity on synthesized nanocomposites. The actual power dissipation by the probe sonicator was measured using a calorimetric method. All the experiments were carried out in the presence of a nitrogen atmosphere to avoid contact of the reaction mass with the external oxygen.



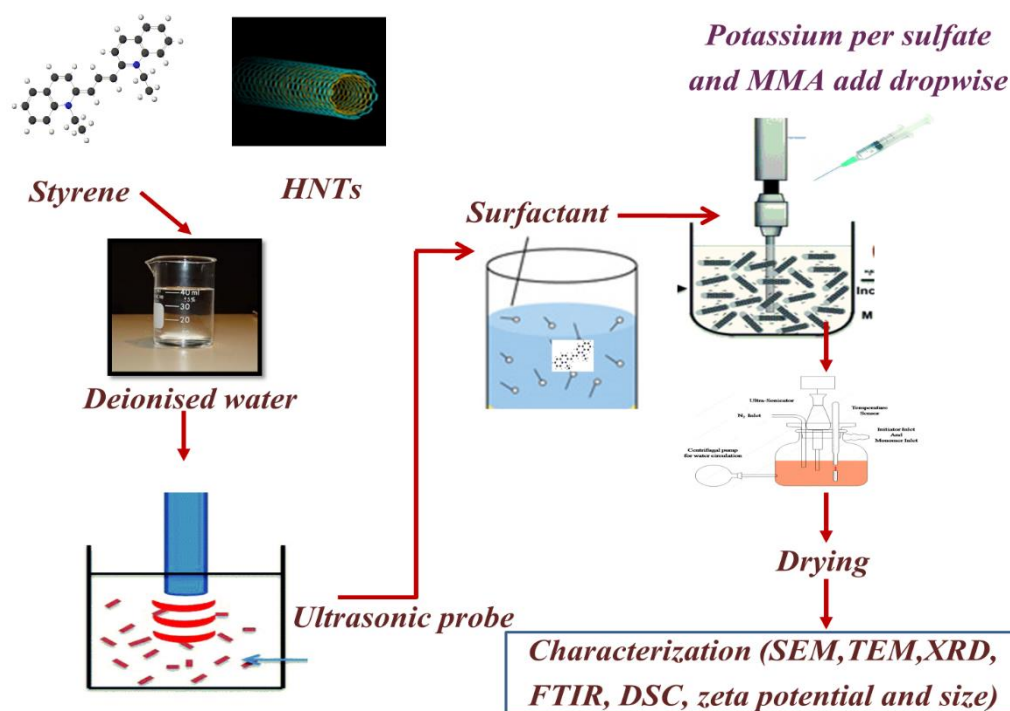


Figure 3.5 Synthesis of PNCs by emulsion polymerization

In a typical run, the surfactant solution was prepared initially by adding 1.08 g of SDS in 100 mL of distilled water and was transferred to the ultrasound probe reactor. 11.9 mL of monomer was added to the ultrasound probe reactor along with HNTs (0.5 – 5 wt % of the monomer quantity to study effect of clay loading) and irradiated for 15 min using ultrasound to exfoliate HNTs into the organic phase droplets. Reaction mixture was heated after addition of styrene, and the temperature was maintained at  $60 \pm 1$  °C throughout the duration of the experiment. In a separate beaker, initiator solution was prepared by dissolving 0.86 g of KPS in 20 mL water and then added dropwise into the reactor. The complete reaction was carried over a period of 60 min in the presence of the ultrasonic irradiation to ensure complete exfoliation of the HNTs in the polymer latex. Samples were withdrawn at regular intervals to monitor the percentage conversion by gravimetric analysis. These samples were dried in an oven at 150 °C until constant weight is obtained so that all the water and unreacted monomer are removed. The sequence of the experiment is clearly depicted in Fig. 3.5.

### 3.5 SYNTHESIS OF PNCs USING ULTRASOUND ASSISTED MINI-EMULSION POLYMERIZATION

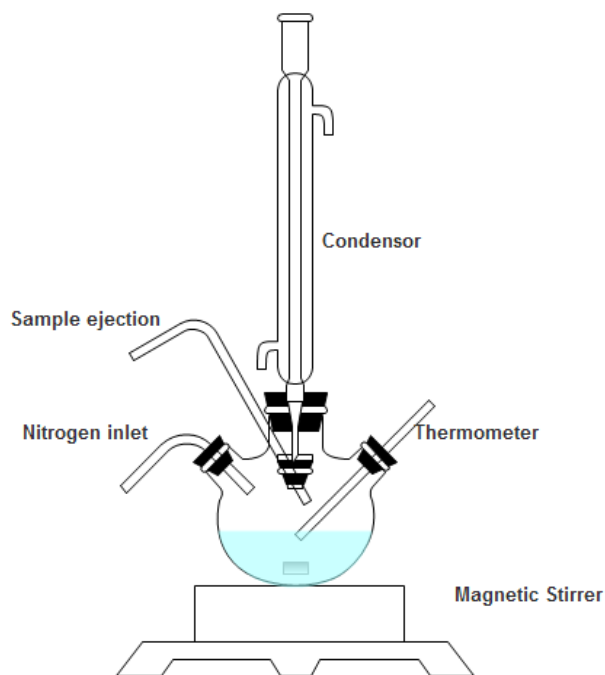


Figure 3.6 Experimental setup for ultrasound-assisted miniemulsion polymerization

Polymerization was carried out in a jacketed beaker as shown in Fig. 3.6. It is equipped with a condenser, a mechanical stirrer, a thermometer and a nitrogen inlet. Mini-emulsion was prepared by taking monomer and HNT in a 100 mL beaker and stirred magnetically for one hour and cooled to 0 °C; it was then ultrasonicated for 30 min (Phase-I). Phase-II was prepared by taking water, span-60, SDBS, and hexadecane under simple stirring at room temperature for 30 min. Phase-I and phase-II were mixed under vigorous magnetic stirring for 30 min. Then the mixture was homogenized by sonication. This mini-emulsion was used for subsequent polymerization and transferred to this reactor and subsequently degassed by N<sub>2</sub> at room temperature for 30 min. When the temperature of the system reaches 70 °C 0.14 g of AIBN (1% of the monomer) was added to initiate polymerization. The polymerization was conducted at this temperature for seven hours under continuous mechanical stirring. The reaction was terminated by adding 1 mL of 1% hydroquinone solution into the latex sample. When the reactor reaches room temperature, the concentrated milky mini-emulsion latex was collected and filtered to remove any coagulum present. A

series of nanocomposite particles were prepared by incorporating different percentage (with respect to the total monomer content) of clay in the mini-emulsion. A detailed explanation of mini-emulsion polymerization is explained in Fig. 3.7.



Figure 3.7 Synthesis of PNCs by miniemulsion polymerization

### 3.6 APPLICATION OF PNCs FOR COATING THE SURFACE OF GLASS

#### 3.6.1 Dip coating technique

The detailed procedure for coating glass substrate is explained in Fig. 3.8. The test coupons (substrate) used for the study were clear (C), bronze (Bz), green (G) and grey (Gr) glasses having dimensions of 30 mm x 30 mm x 5 mm. HNT is used as filler and its properties are given in Table 3.2. For the synthesis of HNT-polymer nanocomposites, 30 mL of toluene was poured into a 100 mL beaker containing 0.15 g HNTs (5 wt%). The mixture was stirred magnetically for 60 min followed by sonication for 30 min to achieve a uniform dispersion of HNTs in toluene. After that 3 g of polystyrene or PMMA was added to toluene containing well-dispersed HNTs for the synthesis of HNT-PS or HNT-PMMA nanocomposites, respectively. The mixture was again stirred magnetically for 60 min followed by sonication for 60 min to ensure dissolution of the polymer in the solvent and for a uniform dispersion of HNTs in the polymer solution. The polymer solution containing well-dispersed HNTs was used for

coating the glasses. The glass coupons were cleaned initially by immersing them in an ultrasonic cleaner for about 10 *min* to remove the surface impurities as well as surface non-homogeneities. Then the coupons were cleaned using detergent followed by water wash and dried in an oven at 105 °C for about 30 *min*. Finally, the coupons were wiped with acetone to make them ready for dip-coating. The cleaned glass coupons were immersed in the prepared HNTs-dispersed polymer solution for a minute and then they were dried in an oven at 150 °C for 1 *h*. One set of the glass samples was coated on single side by wrapping tape on the other side whereas another set of samples was coated on both sides. The single and double-side coated glass samples were subjected to different analyses and the results were compared with that of corresponding uncoated glass samples.

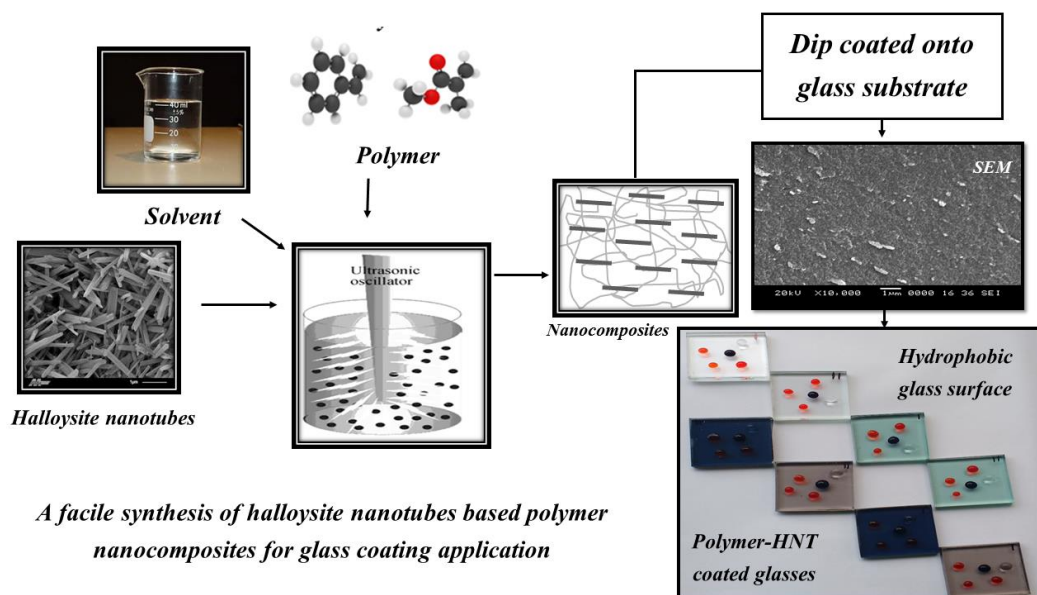


**Figure 3.8 Detailed procedure for coating glass substrate**

### 3.6.2 Spin coating technique

For spin coating, both type of glass substrates i.e., Bz and GG were immersed in water in a bath-type sonicator for about 10 *min* to ensure the substrate is free from surface impurities and non-homogeneity. These substrates were wiped with acetone and dried before using them for spin coating. The HNTs dispersed copolymer solution was spin coated onto each substrate and dried in an oven at 150 °C for 1 *h*. The time for spin coating was varied for each substrate to vary the thickness of coatings. These

coated glass samples varying in HNT wt% and thickness were investigated by different characterization techniques to study their effect on the spectral, morphological, mechanical, scratch resistance and thermal properties of glasses.

### **3.7 FABRICATION OF PNCs MEMBRANES FOR WATER PURIFICATION**

PNCs with a polystyrene matrix were prepared by the addition of 1, 3, 5, and 10 wt% of HNTs into 20 mL of solvent. The suspension was homogenized magnetically for 1 h and sonicated for 1 h using a 13 mm stainless steel probe connected to an ultrasonic generator (Sonics Vibra-cell, USA). Different amounts of HNT loading were added to 20 mL of different solvents, magnetically homogenized for 1 h, and sonicated for 1 h. Then, 2 g of polystyrene was added, and the solutions were again homogenized magnetically for 1 h and sonicated for 1 h. Mixtures were cast onto glass petri dishes, immediately dipped in a beaker containing water for 1 min, and then de-moisturized for 24 h at room temperature. Finally, the solvent was allowed to evaporate to obtain thin films. These composites were labelled as HNT-PS. A virgin polystyrene sample (labelled as PS) was also prepared for comparison purposes.

### **3.8 CHARACTERIZATION OF PNCs USING ANALYTICAL TECHNIQUES**

Characterization is an essential part of all investigations dealing with materials. The important aspects of characterization are chemical composition and compositional homogeneity (chemical homogeneity), structure (including crystal system where possible atomic coordinates, bonding and ultra-structure) and identification and analysis of defects and impurities influencing the properties of the materials. Characterization, therefore, describes all those features of composition and structure of a material that would suffice for reproducing the material. The advances made in the last few years in characterization techniques, especially in the structure elucidation, have been stupendous and have opened new vistas in solid state materials.

The structures of nanocomposites were investigated by X-ray diffraction (XRD) using a RIGAKU Ultima-IV diffractometer. The intensity data were obtained in the  $2\theta$  range of 10–60° at a time step of 2°/s using  $Cu - K\alpha$  ( $\lambda = 1.542 \text{ \AA}$ ) radiation. The

surface morphology and elemental distribution (EDAX) of HNT-PS nanocomposites were examined using a JEOL JSM-6360LV scanning electron microscope (SEM). A small slice of the nanocomposite was placed on a sticky carbon tape on the standard Al mount and sputtered with a thin conductive layer of gold. The surface roughness of the fabricated membranes was analyzed by atomic force microscopy (AFM, Bruker Dimension Fast scan, USA). Around  $1\text{ cm}^2$  of the membranes was sliced and glued on the glass substrate for scanning. The surface roughness  $R_a$  was analyzed using Gwydion software, and the average value of at least three random locations was taken. Intercalation of HNTs into the polymer matrix was examined using a Bruker FT-IR instrument in  $4000\text{--}400\text{ cm}^{-1}$  spectrum region. The Brunauer–Emmett–Teller (BET) was carried out on Quantachrome ASiQwin Automated Gas Sorption to determine surface area. Also, Barrett–Joyner–Helanda (BJH) was carried out to analyze pore size distribution and the adsorption-desorption isotherm of the microporous and nanoporous membrane from  $N_2$  sorption isotherm. The sample was weighted and degassed prior to  $N_2$  sorption analysis. Surface wettability and contact angle measurements were performed by FTA 200 Firsten angstroms dynamic contact angle analyser using sessile drop technique. The glass transition temperature of HNT-PS was determined using differential scanning calorimetry (DSC: Model, NETZSCH DSC 404, Germany) an increase of  $10\text{ }^\circ\text{C}/\text{min}$  from  $0$  to  $300\text{ }^\circ\text{C}$  was maintained under nitrogen flow. Thermal degradation of HNT-PS was determined using a HITACHI EXSTAR TG/DTA 6300 instrument by heating at  $10\text{ }^\circ\text{C}/\text{min}$  from  $0$  to  $600\text{ }^\circ\text{C}$  in an inert nitrogen atmosphere. The stress-strain behaviour of the samples was assessed using a Shimadzu tensile testing machine. Testing was conducted according to the ASTM D638 standard method with a crosshead speed of  $4\text{ mm}/\text{min}$  at room temperature.

For characterization of wastewater, a two-stage purification system was developed which was comprised of a microporous membrane and a nanoporous membrane. The wastewater samples were analyzed for its physiochemical properties. Physical tests of water were carried to measure pH, turbidity, hardness, and conductivity using different techniques. The analysis of major chemical variables (such as alkalinity, acidity, total dissolved solids (TDS), and total suspended solids (TSS), dissolved oxygen (DO), biological oxygen demand (BOD), and chemical oxygen

demand (COD)) was carried out using various chemical techniques (Dogar et al. 2013). The water purification standard values were referenced to the World Health Organization (WHO) standards for drinking water (WHO Guidelines).

The performance and efficiency of PS-HNT membranes were also investigated. The efficiency of the fabricated membranes was determined by calculating % solvent content, porosity, shrinkage ratio, water flux, % rejection, and % recovery (Kausar 2014). Permeability, diffusion coefficients, flux decline, rejection rate, and separation factors are the significant performance-related parameters. In contrast, various chemical and physical properties (pore size, pore size distribution, membrane thickness pore shape, adsorptive/absorptive properties, and charge density) are considered as morphology-related parameters. These parameters are discussed in detail to assess the performance of membranes. The membrane was cleaned, to determine its reusability, with 0.2 wt% sodium hydroxide (NaOH) solution for 60 *min* and 0.2 wt% nitric acid (HNO<sub>3</sub>) solution for 30 *min* twice (Madaeni and Mansourpanah 2004). The detailed cleaning protocol in this study was adopted from the report by Rezaei et al. (2011). After the membrane was cleaned, it was tested to ensure its cleanliness. For this filter water was passed through the membrane, if the water after passing through the membrane was clean it indicated that the membrane is cleaned properly.

## CHAPTER 4

### SURFACE MODIFICATION OF HNTs

*In this chapter, the successful surface modification of HNTs by chemical functionalization is reported. Functionalization is carried out with an objective to increase compatibility of HNTs with the polymer. The modified HNTs were systematically characterized and the results are presented.*

#### 4.1 INTRODUCTION

All the experiments for the modification of the surface of HNTs were performed as per the procedures described in Chapter 3. Modification of HNTs is very essential for the formation of PNCs with improved properties. The surface of HNTs can be modified by the replacement of inorganic cations on the surface of HNTs by cationic surfactants or silanes. Additionally, HNTs can adsorb some organic moieties with specific functional groups, by the forming hydrogen bonds between these functional groups and hydroxyl groups of the HNTs. Hence, the surface of HNTs can be treated using organic compounds. HNTs possess  $\text{OH}^-$  polar groups on their inner lumen making them highly hydrophilic, and holds very few functional groups on their exterior structure, which aids them to separate from agglomerates and promotes their dispersion in the polymer. The inner surface of HNTs is chemically active, while the outer surface is regarded as nonreactive. However, some hydroxyl groups (Al-OH or Si-OH) present on external surfaces at edges and defects provide active sites for chemical reactions. HNTs agglomerate under the influence of van der Waals forces because of their relatively large surface energy due to their nanoscale dimension. Even though uniform dispersion of HNTs into the polymer matrix has been reported in the literature (Ismail et al. 2008; Lin et al. 2011; Liu et al. 2007), lower activity of HNTs external surface hinders interfacial interaction which lowers the HNTs efficiency for dispersion as well as reinforcement. Whereas, uniform dispersion of nanofiller and its interaction with the polymer matrix play a crucial role in determining the overall properties of nanocomposites. Surface modification of clay has become an urgent necessity as HNTs have highly hydrophilic interior and exterior surfaces that severely restrict its usage in



diverse applications. Certain surface modifications of HNTs enable intercalation of organic and inorganic compounds between HNTs layers, leading to their perpendicular expansion and thereby the opportunity to exfoliate individual layers. One of the approaches to achieve uniform distribution is to modify the surface of the filler with small organic molecules or polymers, which in turn improves the physical and chemical properties of the nanosurfaces. Surface chemistry is vital for improving the overall performance of nanoparticles. A better understanding of a filler's surface chemistry and its modification can help to improve its performance and develop new materials. Hence, in this chapter, the surface modification of HNTs using a surfactant (CTAB) and a silane ( $\gamma$ -MPS) is reported.

Experiments were carried out to modify the surface of HNTs with an objective to convert hydrophilic nanotubes to organophilic materials and hence to increase the compatibility between clay and polymer which in turn improves polymer properties. The properties and structure of nanocomposites were characterized using XRD, SEM, TEM, FT-IR, and TGA. Results are presented in the form of tables and figures wherever necessary. Detailed discussion on the results with proper justification and literature support is given.

## **4.2 SURFACE MODIFICATION OF HNTs USING CETYL TRIMETHYLAMMONIUM BROMIDE**

The surface of HNTs was modified using cetyl trimethylammonium bromide and characterized to understand their structure, morphology, and functional groups. CTAB has positively charged head group, the surfactant was selectively adsorbed onto the external surface of HNTs and forms tubular nanoparticles with a hydrophobic shell and a hydrophilic cavity.

#### 4.2.1 Studies on structure of HNTs and CHNTs

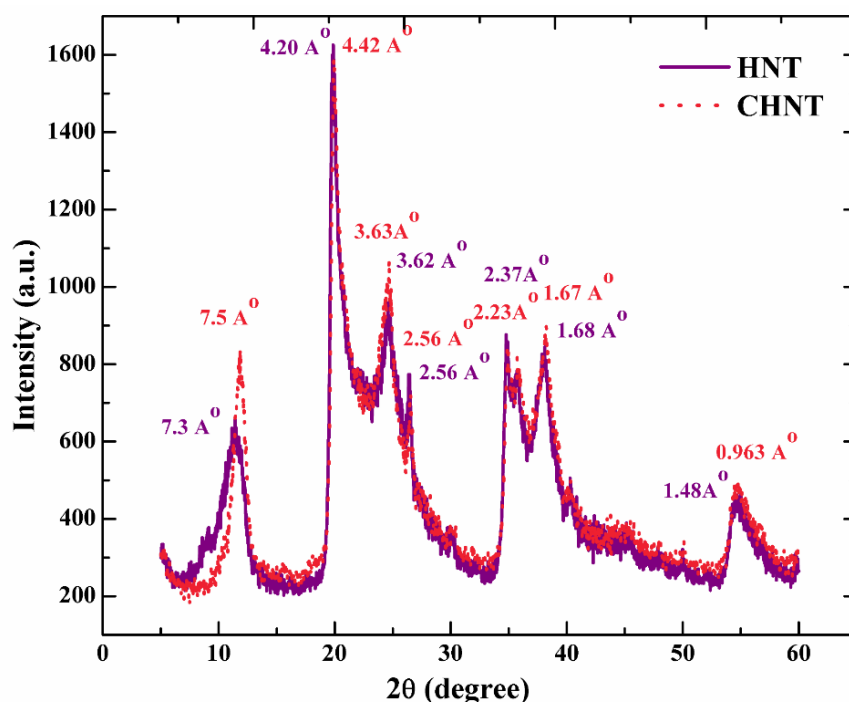


Figure 4.1 X-Ray diffraction of HNT and CHNT

XRD data provides useful insights regarding the changes that occur in the interlayer spacing of HNTs. Fig. 4.1 displays the XRD plots of pristine HNTs and CTAB-modified HNTs (CHNT), which were investigated in the range of  $2\theta$  from 5 – 65°. For pristine HNTs, the characteristic peak (001) appeared at a  $2\theta$  value of 12.11° which corresponds to the basal spacing of ( $d - spacing$ ) of 7.3 Å, as calculated using Bragg's law ( $\lambda = 2d \sin \theta$ ). In case of HNTs modified with CTAB this peak appeared at the lesser  $2\theta$  value of 11.79 corresponding to the basal spacing of 7.5 Å. This increase in interlayer spacing is chiefly due to the presence of large hydrophobic groups on the surfactant as well as due to a reduction in the surface energy of HNTs (Singla et al. 2012). Additionally, the surfactant got adsorbed onto the surface of HNTs and increased the wettability of HNTs making them hydrophobic. Hence it can be observed in Fig. 4.1 that there was an increase in the intensity of CHNT representing an increase in a number of nanoparticles and hence, decrease in agglomerates. Upon intercalation of CTAB, increase in the basal spacing was observed.

#### 4.2.2 Studies on surface morphology of HNT and CHNT

SEM analysis was done in order to determine shape, size and study morphology of HNTs and CHNTs. Fig. 4.2 displays the micrographs of pristine HNT and CHNTs. Intramolecular forces within the particles caused particle aggregation as depicted in Fig. 4.2a whereas on treatment with CTAB, i.e., Fig. 4.2b there was a decrease in agglomerates of HNTs, as the surface of HNTs was made hydrophobic due absorption of ammonium salts onto the surface of HNTs due to the ion-exchange mechanism.

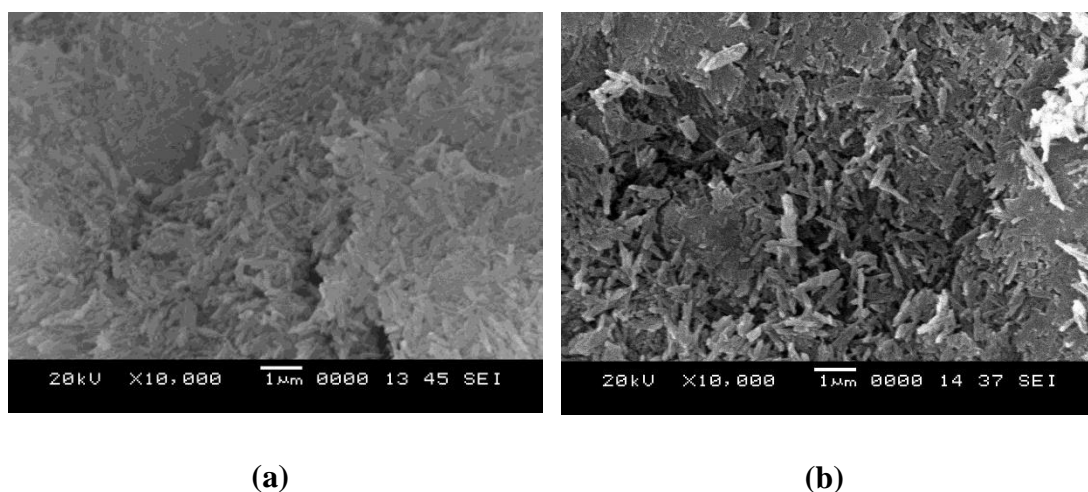


Figure 4.2 Scanning Electron Microscopy of (a) HNT and (b) CHNT

#### 4.2.3 Studies on functional groups of HNT and CHNT

Peaks at  $3692.79$  and  $3623.21\text{ cm}^{-1}$  in Fig. 4.3 of HNTs are attributed to stretching vibrations of inner surface Al-OH. Water in the interlayer is indicated by bending vibration at  $1638.39\text{ cm}^{-1}$ . The peak at  $1030.10\text{ cm}^{-1}$  is assigned to stretching mode of Si-O apical. The peak at  $909.18\text{ cm}^{-1}$  attributes to bending vibration of inner surface hydroxyl groups. Bending vibrations of Al-O-Si and Si-O-Si are observed at  $750.02$  and  $687.79\text{ cm}^{-1}$  respectively. The characteristics peaks of HNTs and CTAB can be observed at wavenumbers of  $3692\text{ cm}^{-1}$  and  $3623\text{ cm}^{-1}$  and CTAB at  $2900.3\text{ cm}^{-1}$  and  $2837.1\text{ cm}^{-1}$ , respectively (Fig. 4.3). But it can be observed from the FT-IR plot of CHNT, that there are certain additional functional groups that are formed due to the interaction of CTAB with HNTs. This confirms the adsorption of surfactant on the surface of HNTs.

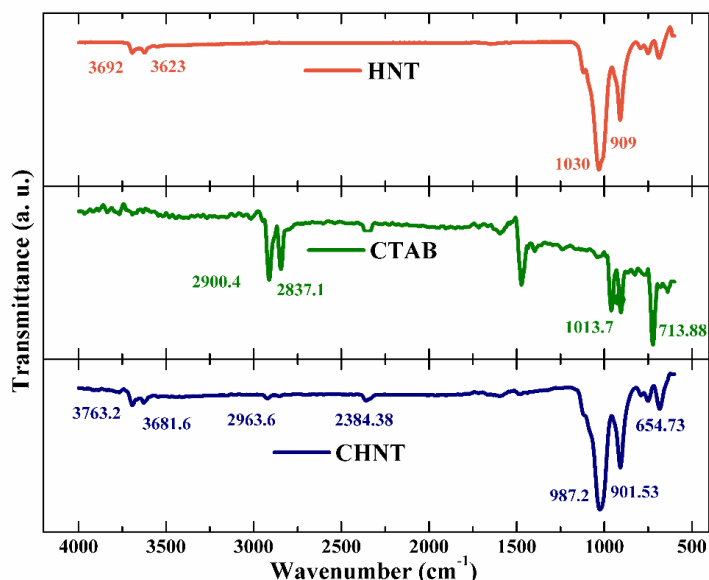


Figure 4.3 FT-IR analysis of HNT, CTAB, and CHNT

### 4.3 SURFACE MODIFICATION OF HNTs WITH $\gamma$ -MPS

HNTs were treated with  $\gamma$ -MPS to improve their interaction with the polymer. The  $\gamma$ -MPS modified HNTs (MHNTs) were characterized to confirm the surface modification of HNTs with  $\gamma$ -MPS and to analyze the structure, morphology and functional groups of MHNTs.

#### 4.3.1 Studies on the structure of HNTs and MHNTs

Figure 4.4 shows the diffraction patterns of pristine HNTs and MHNTs. Most of the interlayer inner-surface Al-OH groups of HNT were unavailable for modification as they were blocked by the strong hydrogen bonds between layers. In spite of this, it can be seen in Fig. 4.4 that there is a slight increase in the  $d$ -spacing in HNTs upon modification with  $\gamma$ -MPS which indicates slight intercalation of MPS into the interlayer of HNTs. This was possible because of sonication which generates high temperatures, high pressures and rigorous environment for intercalation to happen (Frost et al. 2001). A significant peak in HNTs appeared at a  $2\theta$  value of  $11.38^\circ$  indicating  $d$ -spacing of  $7.76 \text{ \AA}$ , whereas this peak in the MHNTs was sharp and shifted to a higher  $2\theta$  value of  $11.87^\circ$  indicating the intercalation of  $\gamma$ -MPS into the HNTs interlayers.

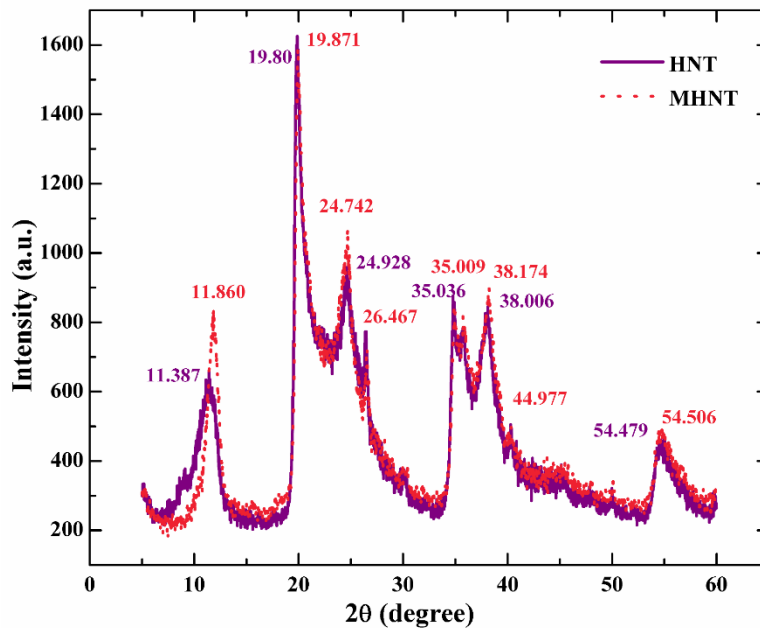
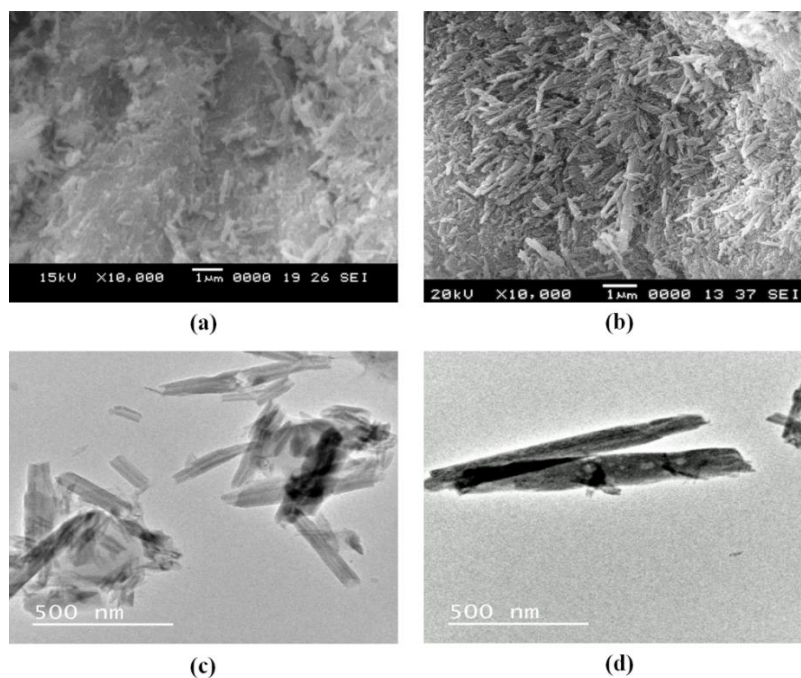


Figure 4.4 X-ray diffraction patterns of HNT and MHNT

### 4.3.2 Studies on surface morphology of HNT and MHNT

The SEM image of the untreated HNTs (Fig. 4.5a) shows a tubular nanostructure of HNTs. Whereas, upon modification with  $\gamma$ -MPS, the SEM micrographs revealed relatively fine distributed morphologies and reduction in aggregation (Fig. 4.5b). Intramolecular forces within the particles resulted in aggregation of particles whereas treatment with  $\gamma$ -MPS caused a decrease in agglomerates of HNTs, This is because the surface of HNTs was made hydrophobic due absorption of silanes onto the surface of HNTs with their surface hydroxyl groups via chemical bonds. TEM image of HNTs showed tubular nanostructure and the hollow lumen of HNTs (Fig. 4.5c). TEM image of MHNTs (Fig. 4.5d) shows the surface is rougher than that unmodified HNTs. Some irregular precipitate can be seen on the outer surface of the MHNTs, and a part of the hollow lumen of HNTs is filled. This indicates that a layer of  $\gamma$ -MPS was wrapped on the outer-surface and partially on inner-surface of HNTs.



**Figure 4.5 SEM micrographs (a) HNT, (b) MHNT and TEM images of (c) HNT (d) MHNT**

#### 4.3.3 Studies on functional groups of HNTs and MHNTs

FT-IR spectra of untreated HNTs and MHNTs samples are presented in Fig. 4.6a. The absorption bands at  $912\text{ cm}^{-1}$  and  $1031\text{ cm}^{-1}$  of HNTs can be related to the Al-OH vibrations and Si-O stretching bands. MHNT displayed a new FT-IR band at  $1476.96\text{ cm}^{-1}$  which are assigned to the scissoring of  $(\text{CH}_2)_3$ . Wavenumbers at  $1726.1$  and  $2959.96\text{ cm}^{-1}$  (Fig. 4.6b) can be assigned to C-O and C-H stretching vibration, respectively. The absence of a band at  $1700\text{ cm}^{-1}$  and the appearance of OH vibration bands at  $912, 3623.47$  and  $3693.56\text{ cm}^{-1}$  suggest that hydrogen bonds could not be formed between HNTs and  $\gamma$ -MPS as OH groups of HNTs were not easily accessible for modification. However, increase in the intensity of band from HNT to MHNT at  $912\text{ cm}^{-1}$  along with broadening and intensifying of band at  $1095\text{ cm}^{-1}$  indicated the possibility of RSi-O-Si and RSi-O-Al bonds between RSi-OCH<sub>3</sub> and RSi-OH groups of  $\gamma$ -MPS with Si-O groups at the surface, and Al-OH groups at the edges of the HNTs (Padhi et al. 2017; Pasbakhsh et al. 2010). These observations suggest a partial modification of  $\gamma$ -MPS on surface and edges of HNTs. In comparison with the FT-IR analysis of untreated HNTs, the peak at  $1726.1\text{ cm}^{-1}$  attributed to

stretching vibration of the C=O bond of MPS in the FT-IR spectrum of MHNTs. The formation of bands at  $1032\text{ cm}^{-1}$  and  $1095.96\text{ cm}^{-1}$  in MHNTs indicates the formation of Si-O-Si bonds, as silane groups of  $\gamma$ -MPS were linked to the surface of the HNTs. This confirms the successful modification of HNT with silane  $\gamma$ -MPS.

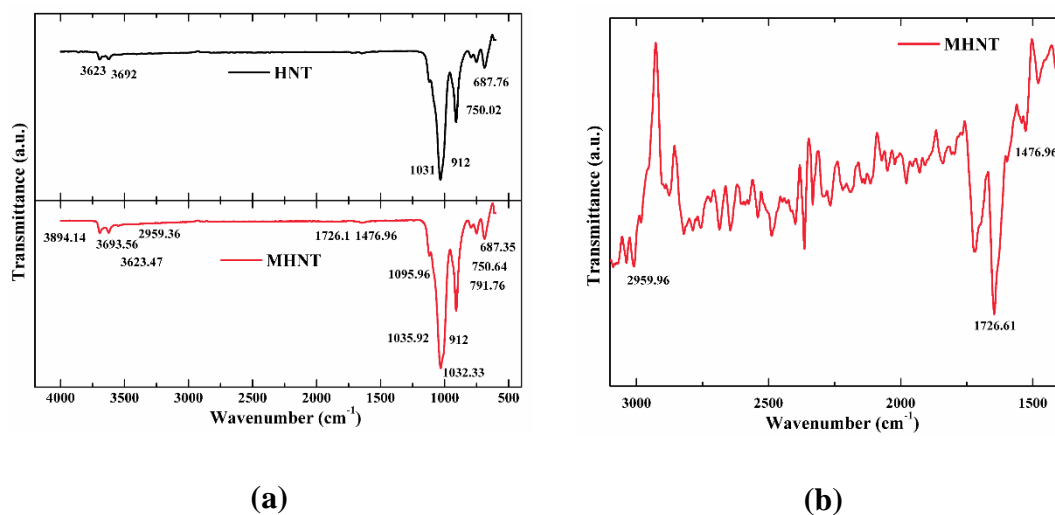


Figure 4.6 FT-IR spectra from  $500\text{ cm}^{-1}$  to  $4000\text{ cm}^{-1}$  of (a) HNT and MHNT (b) FT-IR spectra from  $1450\text{ cm}^{-1}$  to  $3100\text{ cm}^{-1}$  of MHNT

#### 4.4 SUMMARY

Modification of HNTs was done using CTAB, and its successful intercalation into the clay gallery was observed by XRD analysis. The increase in  $d$  – spacing for HNTs and CHNT was from  $7.3$  to  $7.5\text{ \AA}$ . FT-IR results confirmed successful adsorption of CTAB onto the surface of HNTs. The surface of HNTs was also favorably modified by silane  $\gamma$ -MPS. Studies on functional groups of HNTs and MHNTs by FT-IR confirmed the successful modification of the HNTs. XRD results showed that there was no prominent shift in the basal spacing, indicating that a very small amount of  $\gamma$ -MPS intercalated into the interlayers of HNTs, while the surface of HNTs was modified completely. These modified HNTs were incorporated into polymer matrix to study the effect of HNTs modification of polymer properties which is presented in the next chapter.

## CHAPTER 5

### ULTRASOUND-ASSISTED SYNTHESIS OF HNT-PS AND HNT-PMMA NANOCOMPOSITES BY SOLUTION BLENDING METHOD

*This chapter presents the results of characterization of HNT-polymer nanocomposites synthesized via ultrasound-assisted solution blending technique. Pristine HNTs and modified HNTs were used as reinforcement in polymer and the effect of surface modification and sonication on structure, morphology, functional groups and thermal stability were investigated and reported.*

#### 5.1 INTRODUCTION

In this chapter, the synthesis of HNT-polymer nanocomposites using two polymers, i.e., polystyrene (PS) and polymethylmethacrylate (PMMA) by ultrasound-assisted solution blending method is reported.

HNTs are hydrophilic, hence their dispersion into the polymer is very difficult to attain, whereas uniform dispersion of filler into the polymer matrix is significant because if the filler is not properly dispersed the properties may not improve in contrast the properties may tend to degrade. In this regard, the crucial parameters are a surface modification, solvent used, and technique followed for synthesis of nanocomposites. In solution-intercalation method, selection of solvent plays a very important role. The solvent selected must be such that it should dissolve the polymer, should be capable of swelling the clay, should disperse clay uniformly in the polymer matrix, and it should also have lesser affinity for the organically modified silicate surface, compared with the polymer chains. Also, the choice of solvent and cationic clay surfactant depend on the polymer studied, as sometimes the solvent adsorbs to the clay surface preferably over the polymer, preventing intercalation. Therefore, initially the effect of different solvents on the structure, morphology and thermal stability of the resulting nanocomposites was investigated. Among the various solvents used in this work, toluene was found to be the best solvent and it was used for the synthesis of HNT-polymer nanocomposites.

Next focus was on utilizing ultrasound for achieving uniform dispersion of the filler in the polymer matrix. Ultrasound has been reported to be intensified source for



dissipation of energy for synthesis of polymer-clay nanocomposites and yields constructive results because cavitations generated by ultrasound results in shearing action that aids in homogeneous dispersion of clay into the polymer as well as cause exfoliation (Borthakur et al. 2010; Ryu et al. 2004). Also, in polymer-clay nanocomposites systems, ultrasound has been profitably utilized to obtain fine clay dispersion and enhance the swelling of clay particles in suspending medium. Further, sonication enhances movement of clay into the polymer matrix by increasing the interlayer spacing and promotes better interaction between clay and polymer. Hence, acoustic cavitations can be effectively induced by coupling ultrasound with a liquid medium for dispersion of filler and quality control. Therefore, the effect of ultrasound on the synthesis of nanocomposites was investigated and presented.

In Chapter 3, successful modification of HNTs using a surfactant CTAB and a silane  $\gamma$ -MPS is reported. In this chapter, these modified HNTs were incorporated into the polymer matrix, and the effect of modification on polymer properties was investigated and compared to pristine HNTs. The detailed characterization of these composites was carried out to understand the structural, morphological, functional and thermal properties of nanocomposites.

## **5.2 INITIAL SOLVENT SCREENING FOR BLENDING OF HNTs AND POLYMER**

Figure 5.1 shows solvent screening using various solvents. Non-aromatic solvents tetrahydrofuran dispersed the clay well, but aromatic solvents provided better clay dispersion. Based on these observations, toluene, tetrahydrofuran (THF), benzene, carbon tetrachloride ( $\text{CCL}_4$ ), chloroform, dichloromethane (DCM) prevented precipitation of clay after 24 h and hence were chosen as the solvent for the solution intercalation experiments.

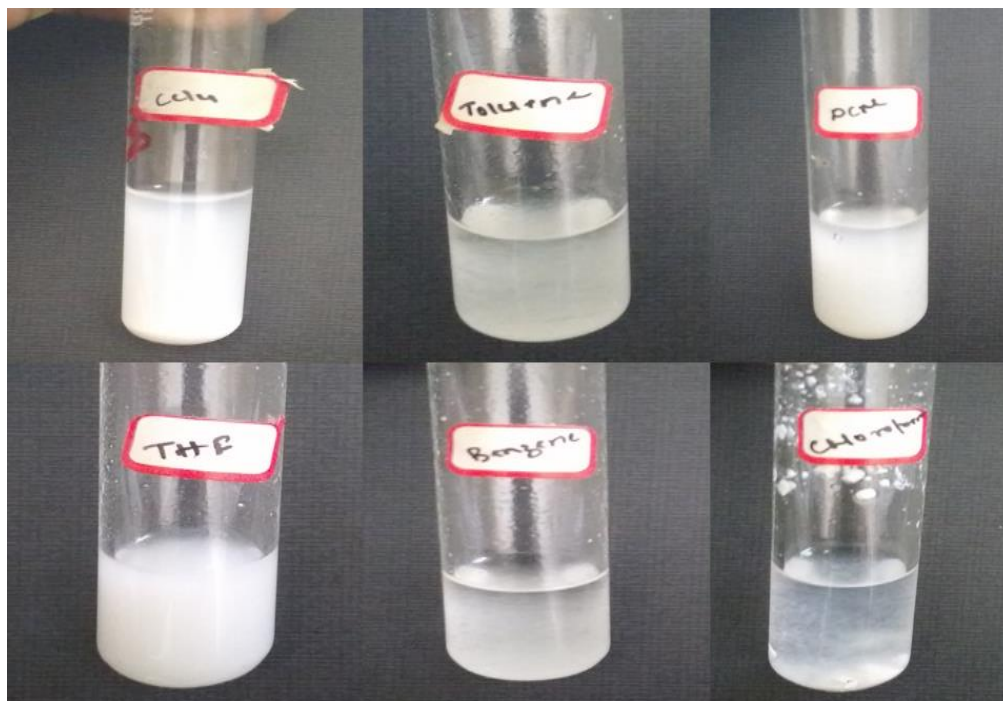


Figure 5.1 Solvent screening experiment using various solvents

### 5.2.1 Effects of solvents on structure of HNT-PS nanocomposites

The structure of nanocomposites fabricated using different solvents was scrutinized by XRD analysis. Bragg's Law was used to calculate the  $d$  – spacing of nanocomposites synthesized using various solvents. It can be analyzed in Fig. 5.2a that the nanocomposites fabricated using toluene did not show the presence of significant peak which reveals complete exfoliation of HNTs into the polymer matrix, whereas the nanocomposites synthesized using various other solvents showed significant peaks at different  $2\theta$  values. Additionally, toluene displayed highest basal spacing revealing better intercalation between polymer and HNTs. These results indicate that toluene was a suitable solvent for the synthesis of nanocomposites with good miscibility between PS and HNTs. In order to confirm the formation of exfoliated structure, XRD of HNT-PS was performed between  $5^\circ$  to  $65^\circ$  and is presented in Fig. 5.2b.

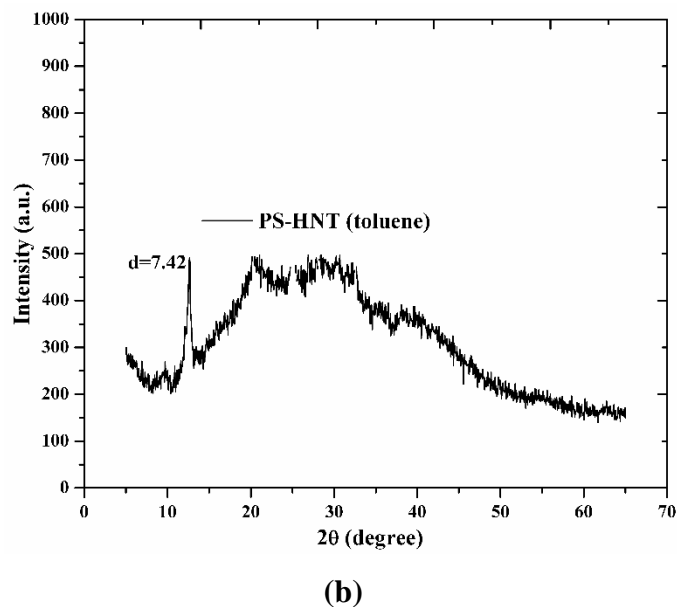
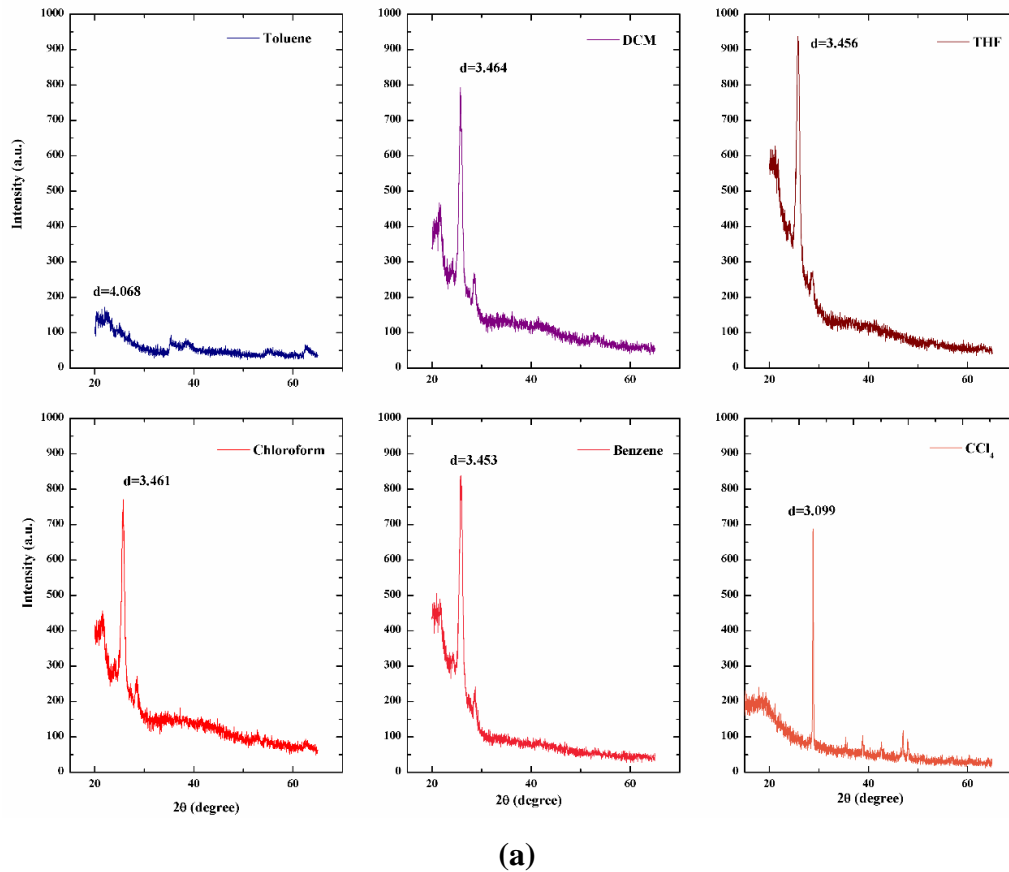


Figure 5.2 XRD of HNT-PS nanocomposites (a) Synthesised using various solvents, and (b) HNT-PS nanocomposites in the  $2\theta$  range between  $5^\circ - 65^\circ$

From Fig. 5.3, it can be analyzed that there was an increase in  $d$  – spacing on sonicating indicating better synergy between HNTs and PS. Even though all these

solvents resulted in increase in  $d$  – spacing on subjecting to ultrasound, toluene resulted in causing complete exfoliation signifying it to be the best solvent for synthesizing exfoliated HNT-polymer nanocomposites.

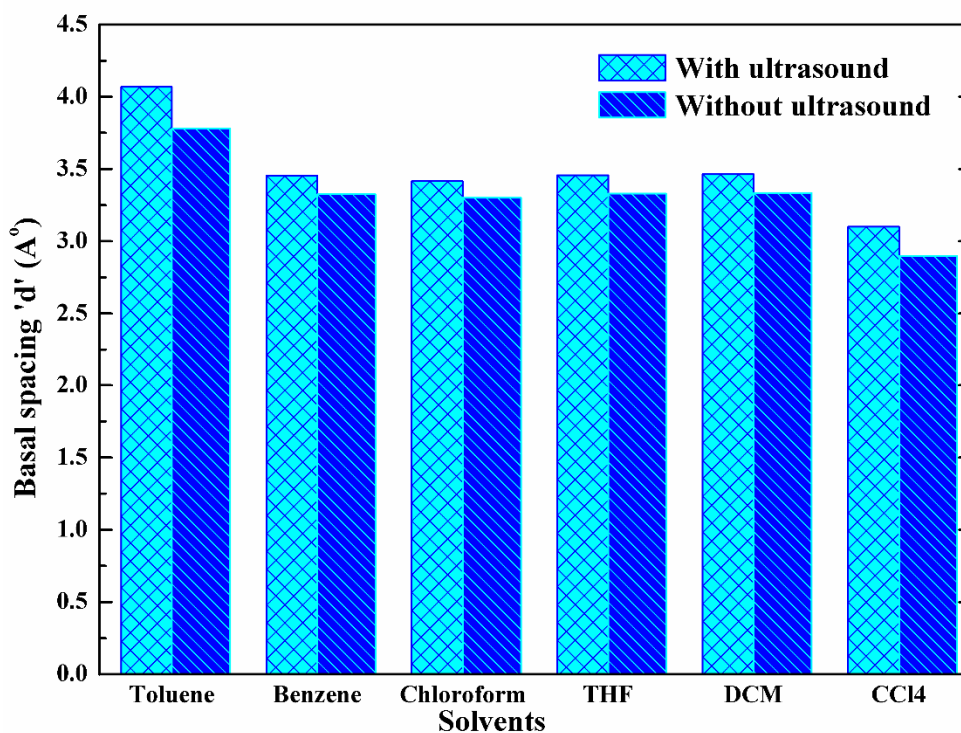


Figure 5.3 Basal spacing of nanocomposites with and without ultrasound

### 5.2.2 Effects of solvents on the morphology of HNT-PS nanocomposites

The SEM portraits of nanocomposites synthesized using various solvents are displayed in Fig. 5.4. It can be examined that the nanocomposite synthesized using toluene resulted the uniform dispersion of HNTs into the polymer. Chloroform and CCl<sub>4</sub> also caused good dispersion of fillers, however basal spacing is low in comparison with toluene, whereas the other solvents resulted in phase separated morphology. Thus, it signifies toluene to be superior over other solvents.

### 5.2.3 Effects of solvents on functional groups of HNT-PS nanocomposites

Figure 5.5 demonstrates the existence of HNTs major absorbance peaks in nanocomposites synthesized using various solvents proving the existence of clay inside the latex particles and indicates encapsulation of HNTs into nanocomposites. This confirms the intercalation of HNTs into the polymer matrix.

#### 5.2.4 Effects of solvents on thermal stability of HNT-PS nanocomposites

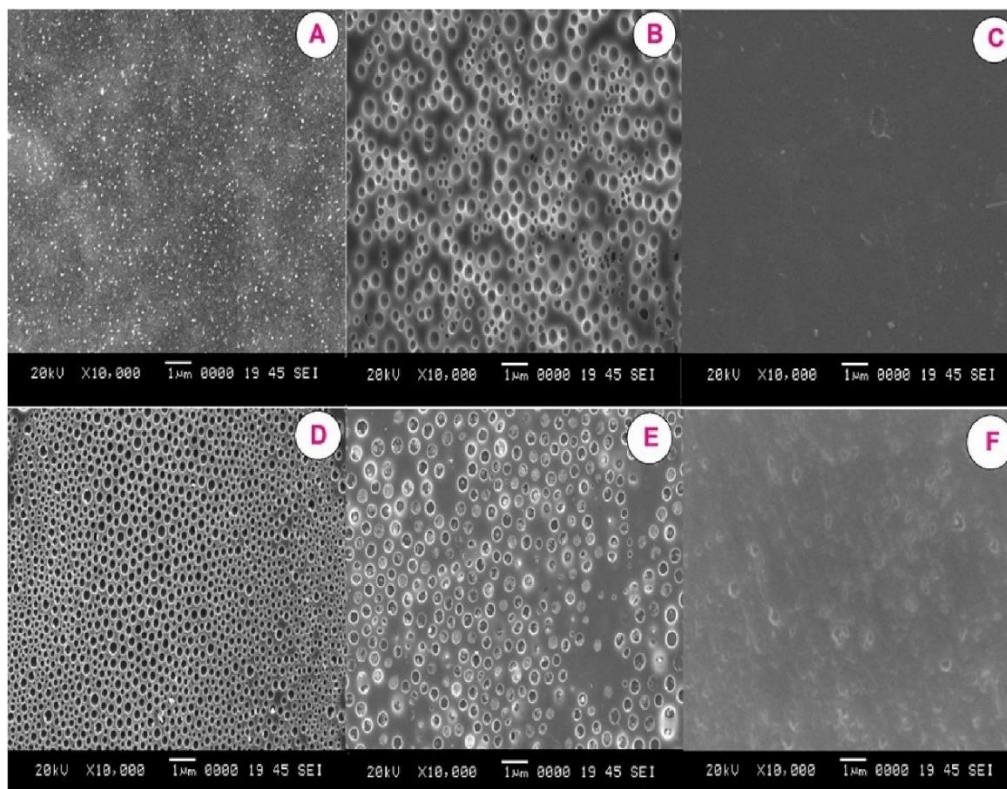


**Figure 5.4** SEM portraits of HNT-polystyrene nanocomposites synthesized using (a) toluene (b) benzene (c) chloroform (d) THF (e) DCM (f)  $\text{CCl}_4$

The effect of solvent on the synthesis of nanocomposites is significant as it affects the thermal stability of the nanocomposites. The HNT-PS nanocomposites fabricated using different solvents have been subjected to DSC analysis to observe effect of solvent on thermal properties of nanocomposites due to the type of solvent. Fig. 5.6 displays the  $\Delta T_g$  values of nanocomposites synthesized using various solvents. The glass transition temperature,  $T_g$  of nanocomposites increased significantly in comparison to a neat polymer whose  $T_g$  was 99 °C irrespective of the solvent used. However, the increase in  $T_g$  is significantly larger on using toluene in comparison with other solvents as it could disperse the filler uniformly in the polymer matrix.

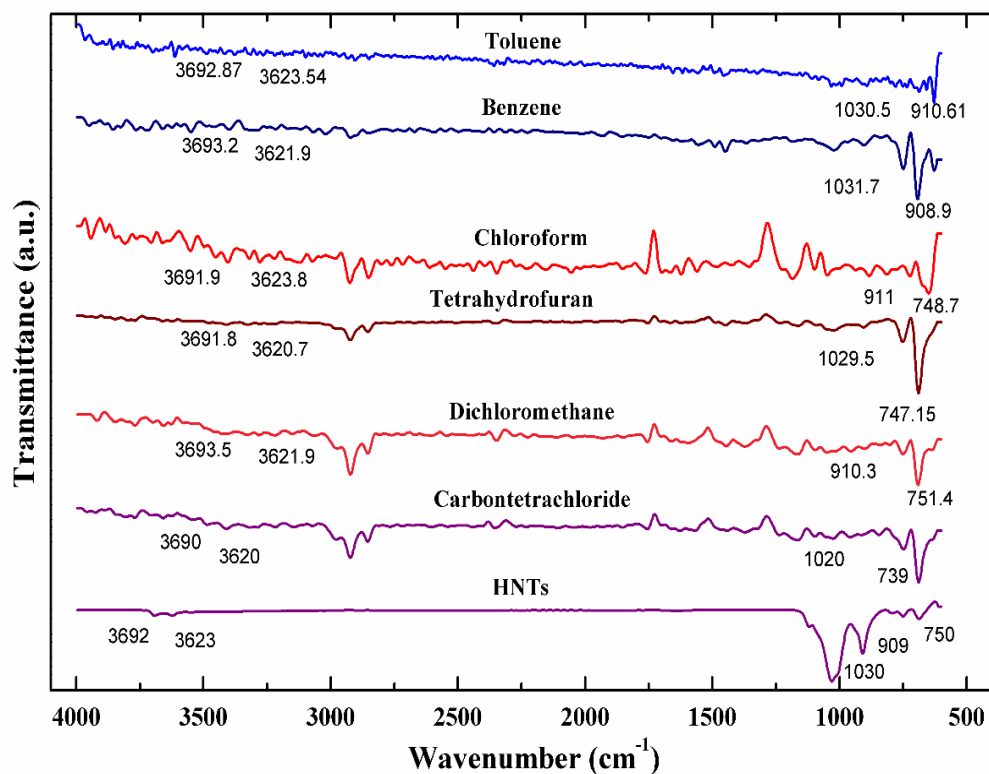


Figure 5.5 FT-IR analysis of HNT-PS nanocomposites synthesized using various solvents

Although nanocomposites could be propitiously synthesized using various solvents, toluene revealed good exfoliation, uniformly dispersed morphology and good  $T_g$  in comparison with other solvents, hence proving it to be the best solvent for HNT-PS nanocomposite synthesis. Chemical composition is the key parameter for solubility of polymer in organic solvent. The solvent chosen must be such that it should be capable of over-ruling polymer-polymer interactions in order to dissolve polymer segments. That suggests a solvent molecule should have a favorable interaction with the polymer segments. Fortunately toluene holds the required properties and polystyrene, as well as polymethylmethacrylate, exhibits strong polarizable side groups that can be dissolved by toluene. This is the reason for toluene to be suitable solvent for dissolving polystyrene. Also, toluene had the potential for dispersing HNTs, further ultrasound aided in uniform dispersion of HNTs into the polymer matrix and also caused sufficient increase in basal spacing of nanocomposites for the polymer to enter the interlayers of

clay which resulted in intercalated as well as exfoliated morphology thereby enhancing polymer properties for potential applications.

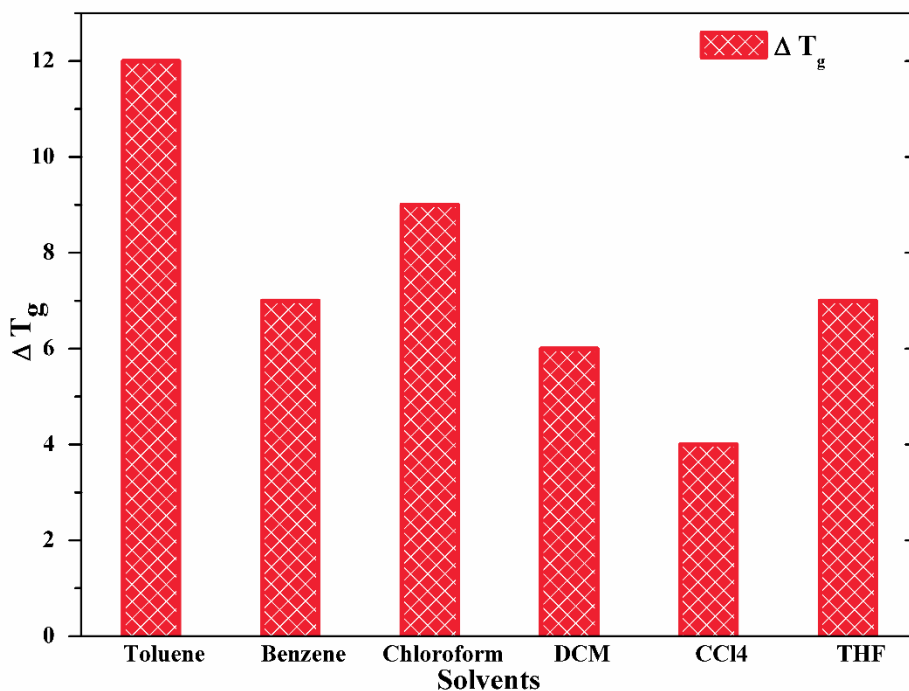
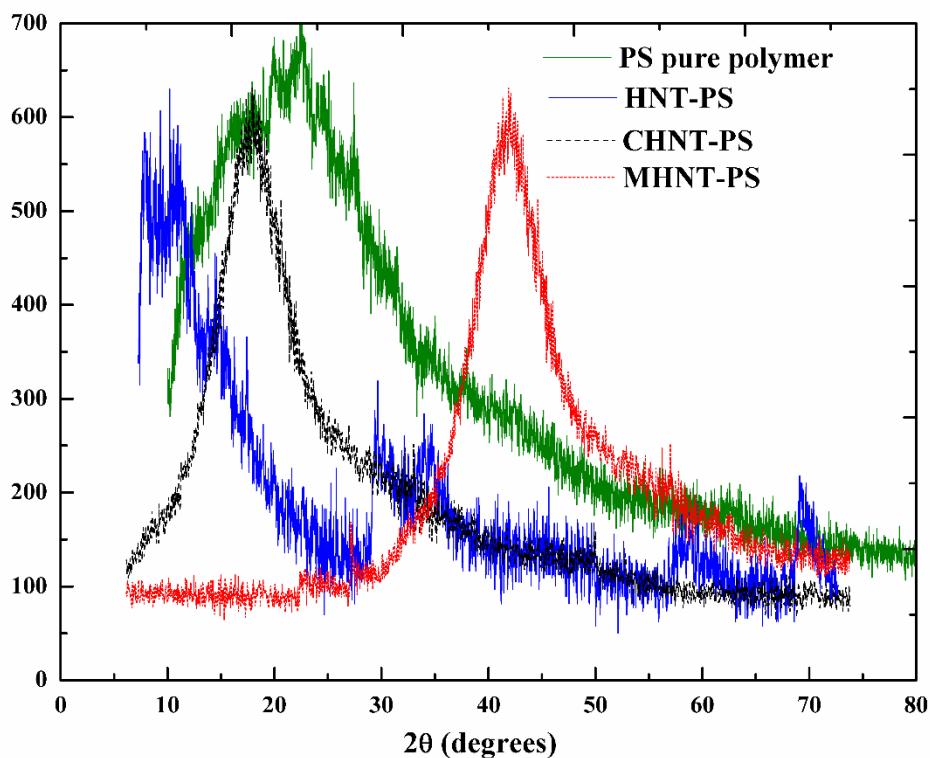


Figure 5.6 Difference in glass transition temperature ( $\Delta T_g$ ) of HNT-PS nanocomposites synthesized using different solvents

### 5.3 ULTRASOUND-ASSISTED SYNTHESIS OF HNT-POLYSTYRENE (HNT-PS) NANOCOMPOSITES BY SOLUTION BLENDING METHOD

Solution intercalation technique or solution blending method exhibits various advantages such as the ability to adopt processing techniques, good control on the homogeneity of the constituents which assists in understanding the intercalation process and morphology of nanocomposites. Also, cavitation's generated by ultrasound aids in dispersing HNTs evenly into the polymer matrix. Surface modification of HNTs increases the affinity of clay towards polymers which aids in the uniform distribution of HNTs inside the polymer matrix material which further enhances various polymer properties. Hence, synthesis of HNT-PS and HNT-PMMA using modified and unmodified HNTs was carried and by ultrasound-assisted solution casting method.

#### 5.3.1 Studies on the structure of HNT-PS, CHNT-PS and MHNT-PS nanocomposite



**Figure 5.7 XRD plots of HNT-PS, CHNT-PS and MHNT-PS nanocomposites**

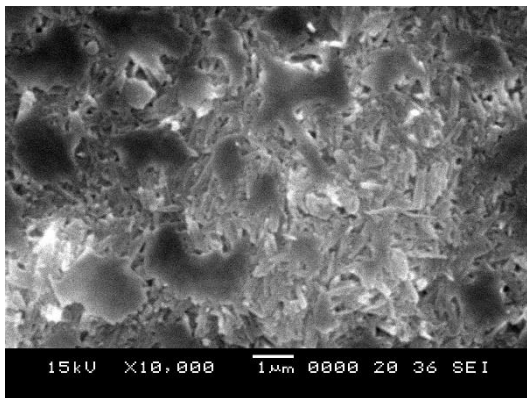
X-ray diffraction measurements were carried out to analyze the structural characteristics of PS and HNT-PS nanocomposites. Fig. 5.7 visualizes the structure of pure PS and nanocomposites synthesized using both unmodified and modified HNTs. It can be noticed that nanocomposites containing modified HNTs showed lesser significant peaks than that of unmodified HNTs. This suggests complete exfoliation of clay into the polymer matrix thus suggesting improved properties. The use of ultrasound energy further aids in exfoliating HNTs into the polymer matrix. Therefore modification of HNTs along with use of ultrasound aids is achieving uniform distribution of HNTs in polymer matrix.

### **5.3.2 Studies on the morphology of HNT-PS, CHNT-PS and MHNT-PS nanocomposite**

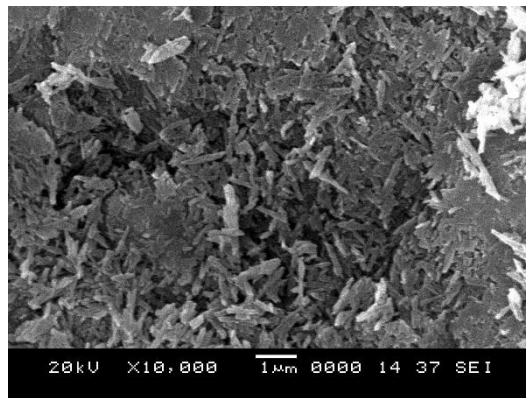
SEM analysis was done to determine shape, size and study the morphology of the nanocomposites. To observe dispersion of the particles, nanocomposites which were prepared using toluene and sonicated for 1 h were examined using SEM.



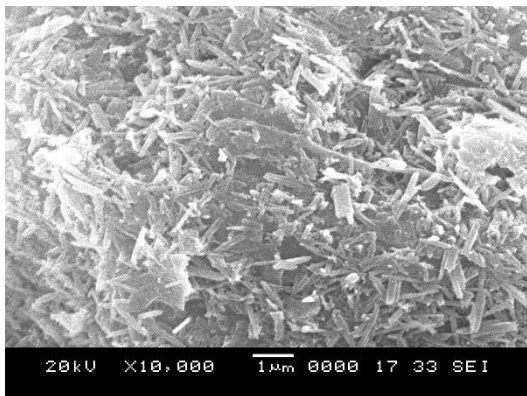
It can be observed that the particle size was substantially lower as compared to the nanocomposite synthesized using sonication. This decrease in the particle size of the nanocomposite is due to high frequency and intensity that is generated by sound waves that tear apart the agglomerations and results in uniform distribution of nanotubes, further, it could be observed there was improvement in the dispersion of HNTs in the polymer matrix due to the continuous ultrasonic irradiation.



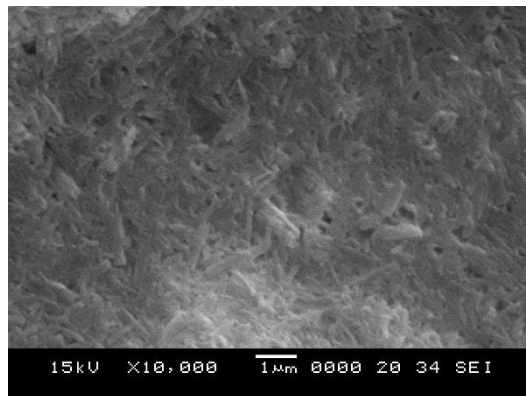
(a)



(b)



(c)



(d)

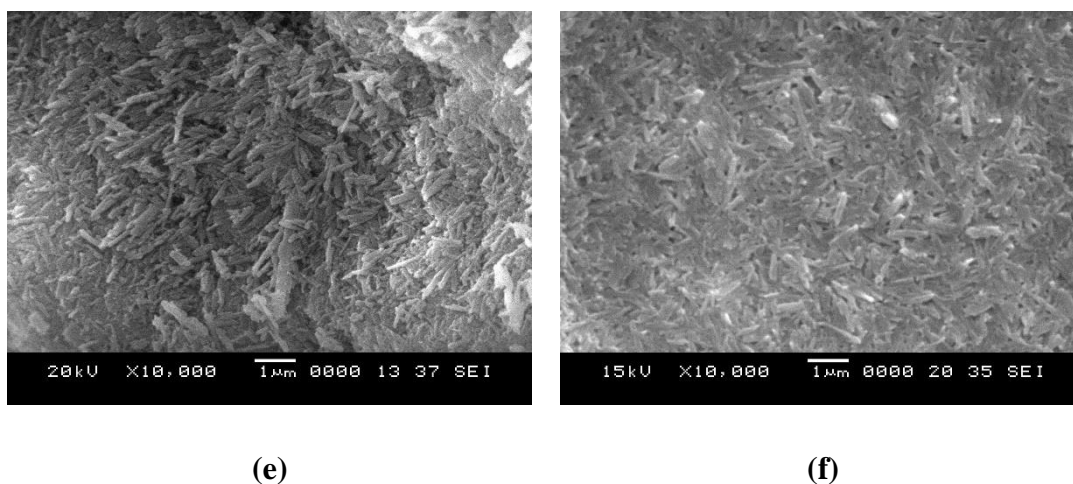


**Figure 5.8 SEM images of (a) HNT-PS without sonication, (b) HNT-PS with sonication (c) CHNT-PS without sonication, (d) CHNT-PS with sonication, (e) MHNT-PS without sonication, and (f) MHNT-PS with sonication**

### **5.3.3 Studies on functional groups of HNT-PS, CHNT-PS and MHNT-PS nanocomposites**

To examine the successful incorporation of HNT, CHNTs, and MHNTs into the polymer matrix FT-IR analysis of the nanocomposites was performed and displayed in Fig. 5.9. It can be observed that the nanocomposites which were synthesized without modification of HNTs i.e. HNT-PS clearly demonstrates the existence of HNT major absorbance peaks in polystyrene spectrum which proves the existence of clay inside the latex particles and indicates encapsulation of HNTs into the final nanocomposites. However, the peak at  $3692\text{ cm}^{-1}$  shifts to  $3694.43\text{ cm}^{-1}$  in the nanocomposite which attributes interaction of Al layer of HNT with the polymer surface. Thus from FT-IR study, we may infer successful incorporation of HNT in the polymer matrix.

The functional groups of the nanocomposites on modification of HNTs with CTAB and incorporated into PS can also be observed in Fig. 5.9. The characteristics peaks of CTAB and CHNT (Fig. 4.3) are present in the nanocomposite synthesized using PS as a matrix. The IR spectrum of PS displays bands at wavenumber  $3066\text{ and }3025\text{ cm}^{-1}$  which are assigned to the stretching vibration of aromatic C–H. The bands at  $2922\text{ and }2851\text{ cm}^{-1}$  are attributed to the stretching vibration of aliphatic

C–H. The bands between 1666 and 1945  $\text{cm}^{-1}$  dictates combination bands. The stretching vibration of aromatic C=C can be seen in 1491, 1449 and 1599  $\text{cm}^{-1}$ . The bending vibration of aliphatic C–H can be seen at 1188–1368  $\text{cm}^{-1}$ . The 1026  $\text{cm}^{-1}$  band can be assigned to the bending vibration of aliphatic C–H. Also, the bending vibration of aromatic C–H are represented at 698, 756, and 543  $\text{cm}^{-1}$ . The FT-IR spectra of the CHNT-PS clearly exhibits the characteristic absorptions bands that are attributable to PS and CHNT. All PS bands which appeared in these spectra display a slight shifting. Also, new bands that appeared in the regions of 3626, 1027, and 465  $\text{cm}^{-1}$  were attributed to OH stretching of structural hydroxyl groups (Al–OH), Si–O stretching, and bending vibrations of CHNT and indicates the existence of CHNT in the PS matrix where the polymer chain was inserted between the layers of the HNT by secondary valence forces. Also, the incorporation of CHNT into the polymer matrix was confirmed by the presence of CHNT major peaks and PS major peaks in the resultant nanocomposites as portrayed in Fig. 5.9. This confirms the reinforcement of CHNTs in PS matrix.

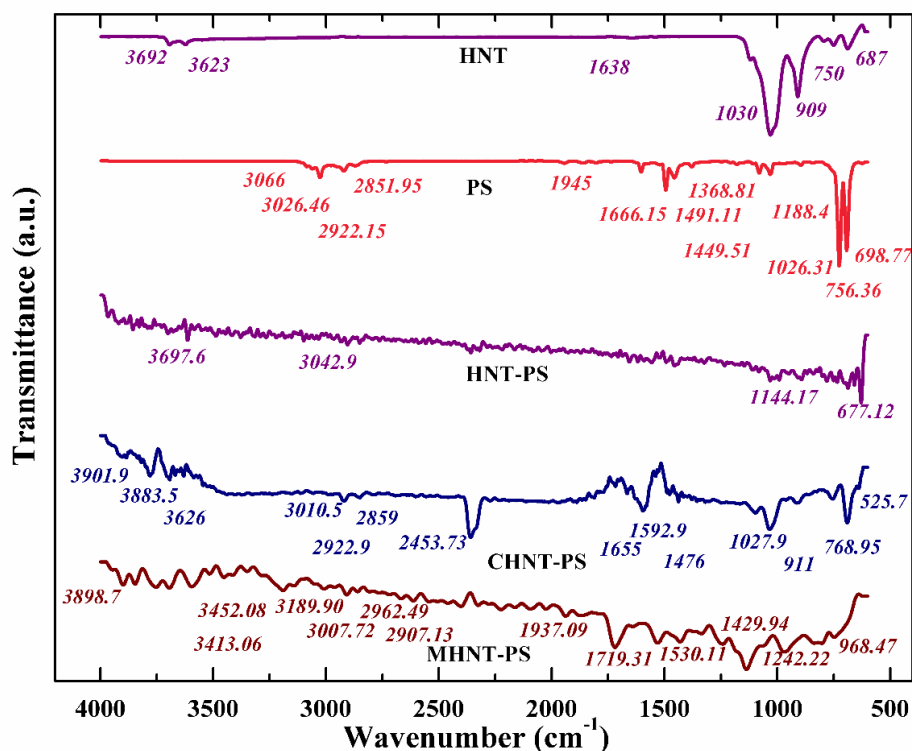
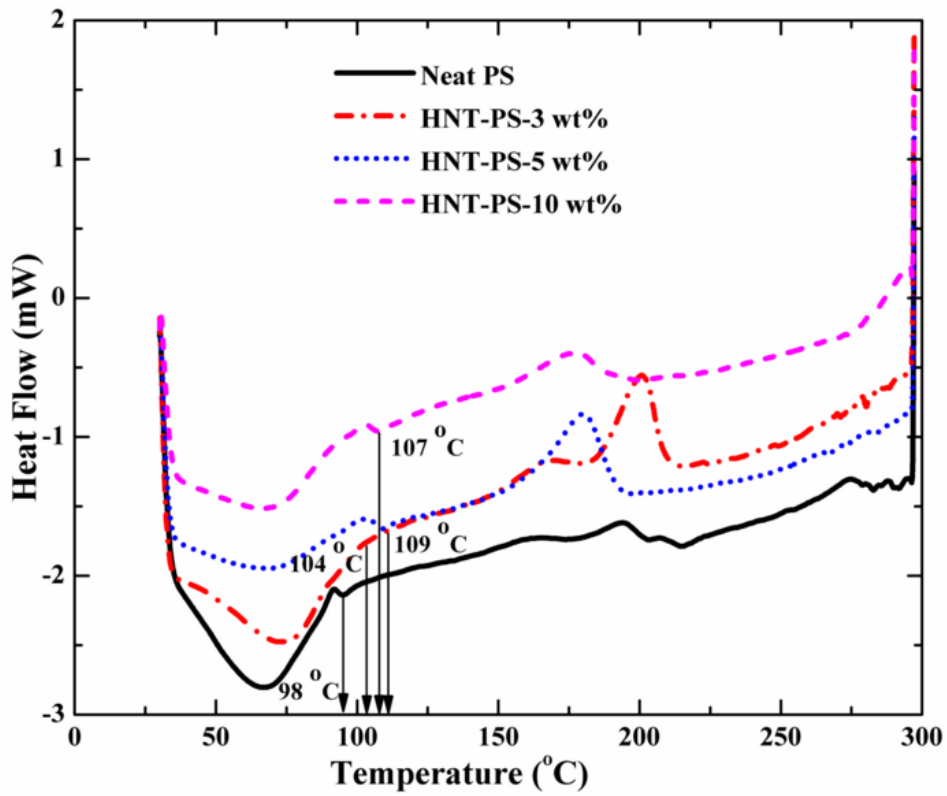


Figure 5.9 FT-IR of HNT, PS, HNT-PS, CHNT-PS, MHNT-PS nanocomposites

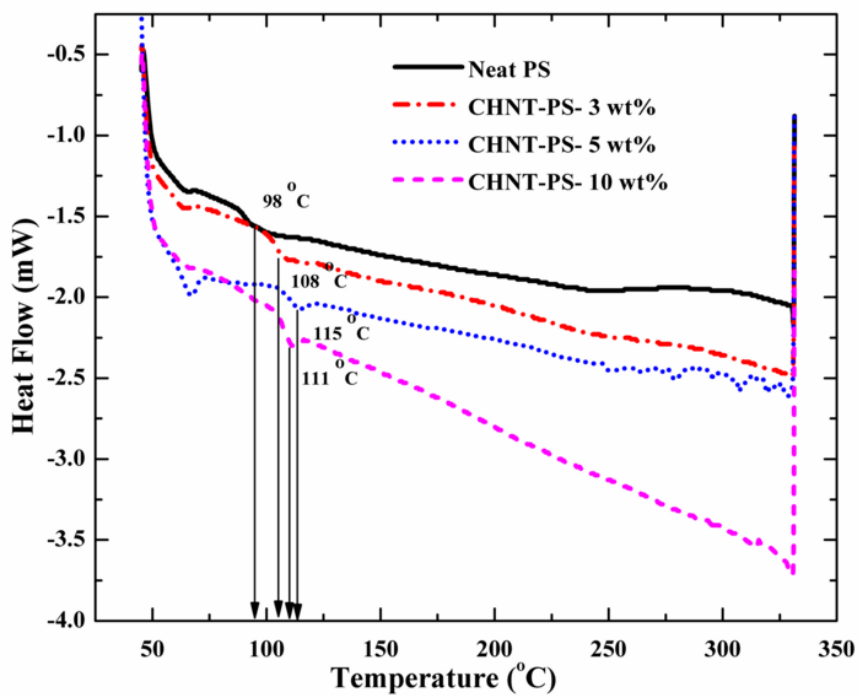
The HNTs modified with  $\gamma$ -MPS was also exfoliated into the PS matrix, and the FT-IR analysis is portrayed in Fig. 5.9. The major absorbance peaks of  $\gamma$ -MPS modified HNTs can be observed in Fig. 4.6. It can be observed that the band at  $912\text{ cm}^{-1}$  for MHNT was shifted to  $968.47\text{ cm}^{-1}$  for MHNT-PS. This can be attributed to the interaction of OH group inside the HNT lumen, indicating the penetration of  $\gamma$ -MPS into the HNT interlayers. Additionally, the considerable reduction in the intensity of the bands at  $3623.47\text{ cm}^{-1}$  and  $3693.56\text{ cm}^{-1}$  is related to the appearance of new bands at  $2962.49\text{ cm}^{-1}$  and  $2907.13\text{ cm}^{-1}$ . This indicates the reaction between hydroxyl groups inside the lumen with PS. Thus the FT-IR suggests the presence of MHNT inside the PS matrix.

#### **5.3.4 Studies on thermal stability of HNT-PS, CHNT-PS and MHNT-PS nanocomposites**

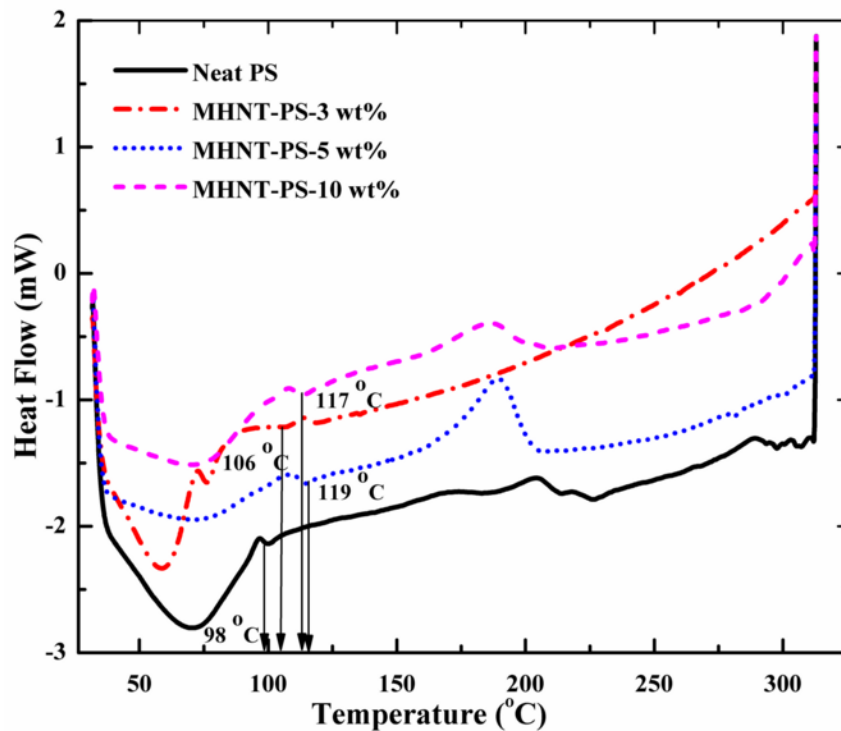
To have a detailed understanding of the thermal behavior of nanocomposites synthesized using HNT, CHNT, and MHNT. Fig. 5.10 shows DSC traces of pure PS and HNT-PS, CHNT-PS and MHNT-PS with 0, 3, 5, 10 wt% HNT loading. HNT-PS nanocomposites showed higher  $T_g$  than that of pure PS thus ensuring better thermal stability. It can also be observed that there was a further increase in the  $T_g$  of the nanocomposites on modifying with CTAB and  $\gamma$ -MPS. Additionally, it can be noted that the  $T_g$  is improved with an increase in HNT loading up to a certain % after which it reduces. The possible reason for this is the addition of HNTs in the polymer matrix is believed to restrict the intercalated polymer chains between the layers of HNT, which prevents the segmental motions of the polymer chains. On the other hand, however, a slight decrease in  $T_g$  can be observed with increase in amount of HNTs, due to difficulty in dispersion of HNTs in polymer matrix. This causes formation of agglomerates thus causing a decrease in the thermal stability. Thus it can be noted the 5 wt % HNTs is optimum to synthesis nanocomposites with good thermal properties.



(a)



(b)



(c)

Figure 5.10 DSC traces of (a) HNT-PS, (b) CHNT-PS, and (c) MHNT-PS with different HNT content ( $wt\%$ )

#### 5.4 SYNTHESIS OF HNT-POLYMETHACRYLATE (HNT-PMMA) NANOCOMPOSITES

Polymethylmethacrylate was used as the matrix material, and polymer nanocomposites were synthesized using HNT, CHNT, and MHNT as reinforcing the material. The nanocomposites were synthesized by ultrasound-assisted solution casting method using toluene as solvent. The effect of HNT modification and sonication on properties of nanocomposites were investigated and reported in the section below.

#### 5.4.1 Studies on the structure of HNT-PMMA, CHNT-PMMA and MHNT-PMMA nanocomposites

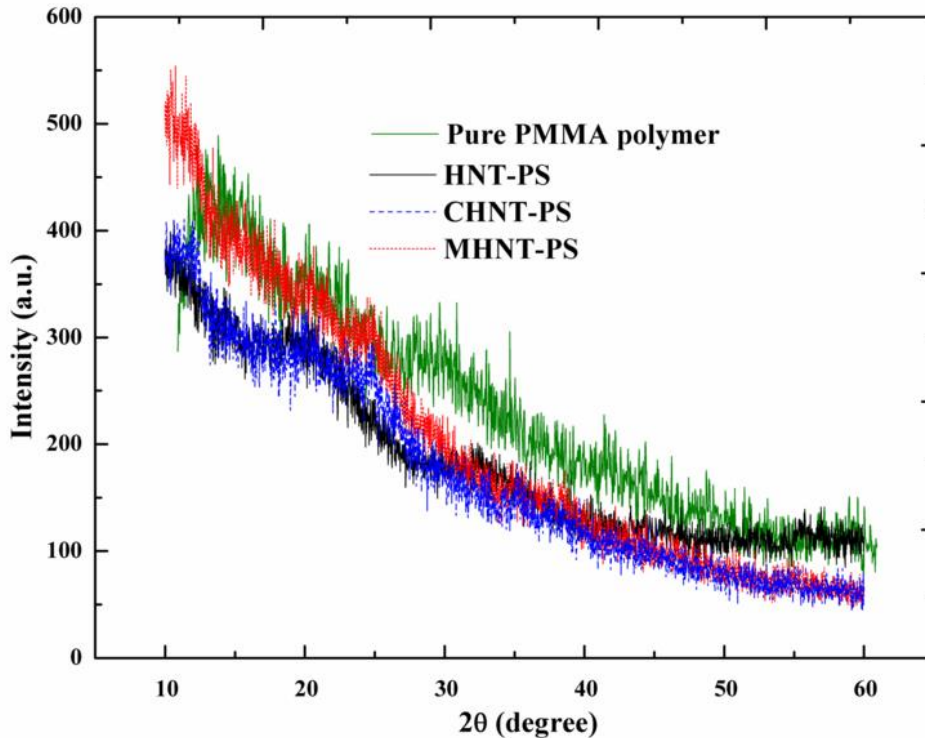


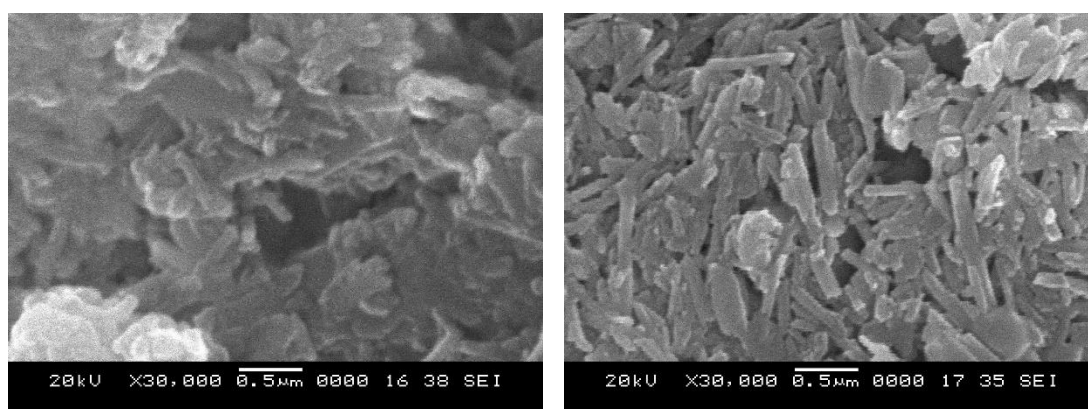
Figure 5.11 X-Ray diffraction patterns of neat PMMA, HNT-PMMA, CHNT-PMMA and MHNT-PMMA nanocomposites

XRD analysis presents important details regarding the changes that occur in the interlayers of HNTs. Generally, a decrease in  $2\theta$  values suggests an increase in d-spacing and results in the formation of intercalated structure. In case of an exfoliated structure there is a complete loss of registry between the clay layers, and hence no peaks can be observed in the XRD plot. Fig. 5.11 exhibits the structure of pure PMMA and nanocomposites synthesized using pristine HNT as well as modified HNT. It can be noted that the nanocomposites synthesised on reinforcing CHNTs and MHNT into the PMMA matrix resulted in a ordered structure without the presence of significant peaks, this confirms the exfoliation of HNTs into the polymer matrix. It can be seen that a significant peak appears at  $2\theta$  value of  $20^\circ$  in all the composites. This peak corresponds to the amorphous phase of PMMA, characterizing its arrangement of macromolecules. The presence of this peak was significant as it confirmed that the XRD analysis was sensitive to detect the presence of the HNTs in the nanocomposites. In the case of

CHNT-PMMA and MHNT-PMMA nanocomposites, it can be seen in Fig. 5.11 that some diffraction peaks of CHNT, MHNT and the broad peak of PMMA appeared in the spectra.

#### 5.4.2 Studies on morphology of HNT-PMMA, CHNT-PMMA and MHNT-PMMA nanocomposites

Figure 5.12 visualizes the SEM images of nanocomposites synthesized in the presence and absence of ultrasound. It can be observed that nanocomposites synthesized in the absence of ultrasound resulted in agglomerated morphology whereas those synthesized with ultrasound showed the uniform dispersion of nanotubes across the specimen. This is due to high frequency and intensity that is generated by sound waves that tear apart the agglomerations and results in uniform distribution of nanotubes. It can be further observed that nanocomposites synthesized on using HNTs whose surface was modified with CTAB and  $\gamma$ -MPS and utilizing ultrasound showed systematic arrangement of HNTs into the polymer matrix and reduction in agglomerates of HNTs which further aids in uniform dispersion of filler into polymer.



(a)

(b)



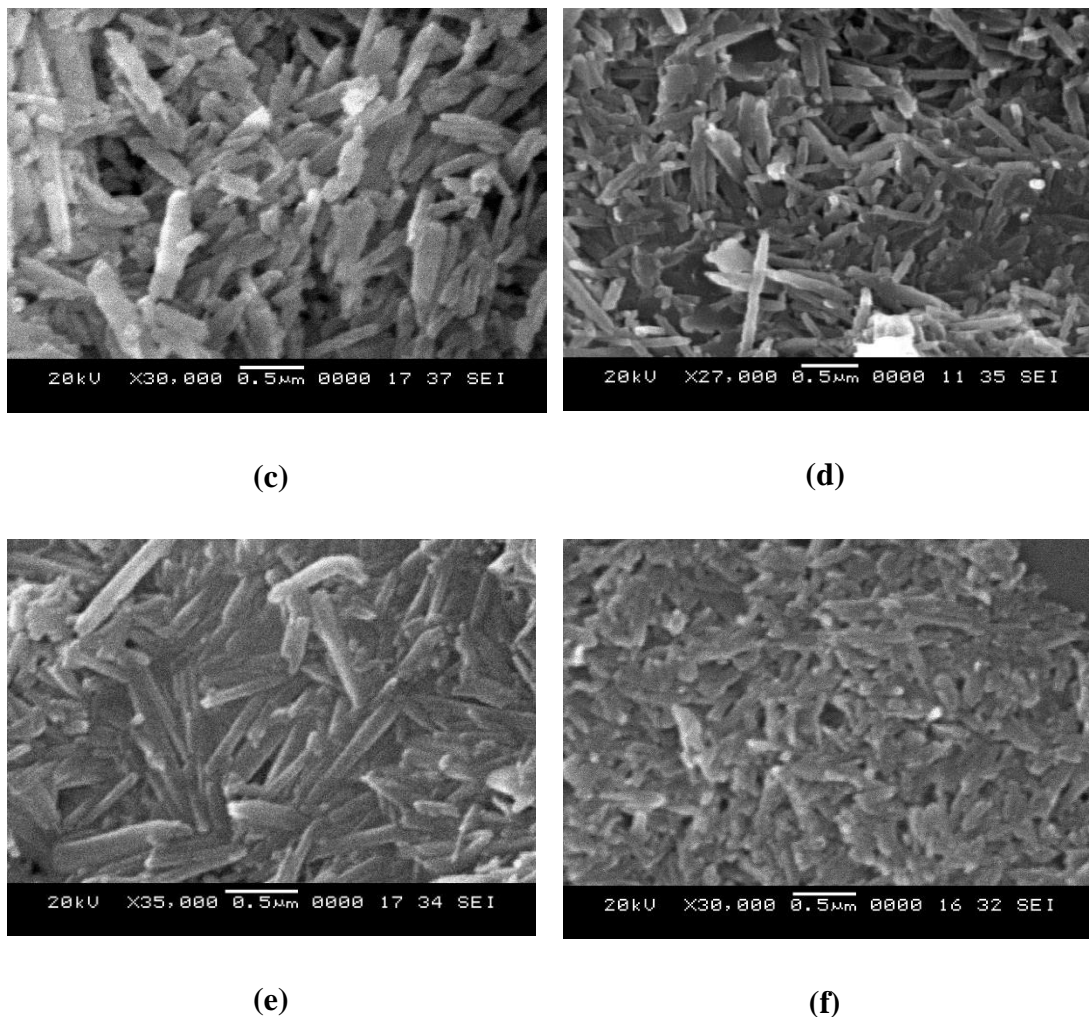


**Figure 5.12 SEM images of (a) HNT-PMMA without sonication, (b) HNT-PMMA with sonication (c) CHNT-PMMA without sonication, (d) CHNT-PMMA with sonication, (e) MHNT-PMMA without sonication, and (f) MHNT-PMMA with sonication**

#### **5.4.3 Studies on functional groups of HNT-PMMA, CHNT-PMMA and MHNT-PMMA nanocomposites**

Figure 5.13 shows the FT-IR analysis of HNTs, PMMA, HNT-PMMA, CHNT-PMMA and MHNT-PMMA nanocomposites. The most significant feature of HNTs is the presence of characteristic peaks at  $3692.79, 3623.21 \text{ cm}^{-1}$  ascribes Al-OH, and  $1030.10, 909.18 \text{ cm}^{-1}$  represents Si-O. The presence of these peaks on the synthesized nanocomposites indicated the presence of HNTs in PMMA matrix. Also, a distinct absorption peak appeared at  $1719 \text{ cm}^{-1}$  (C=O stretching) due to the characteristic

frequencies of PMMA. This result might be attributed to PMMA being intercalated and hydrogen-bond formation between the oxygen of the polymer molecules and the hydroxyl of the HNT lattice. Hence, these results indicate that the solution casting assisted by ultrasound successfully produced HNT-PMMA nanocomposites.

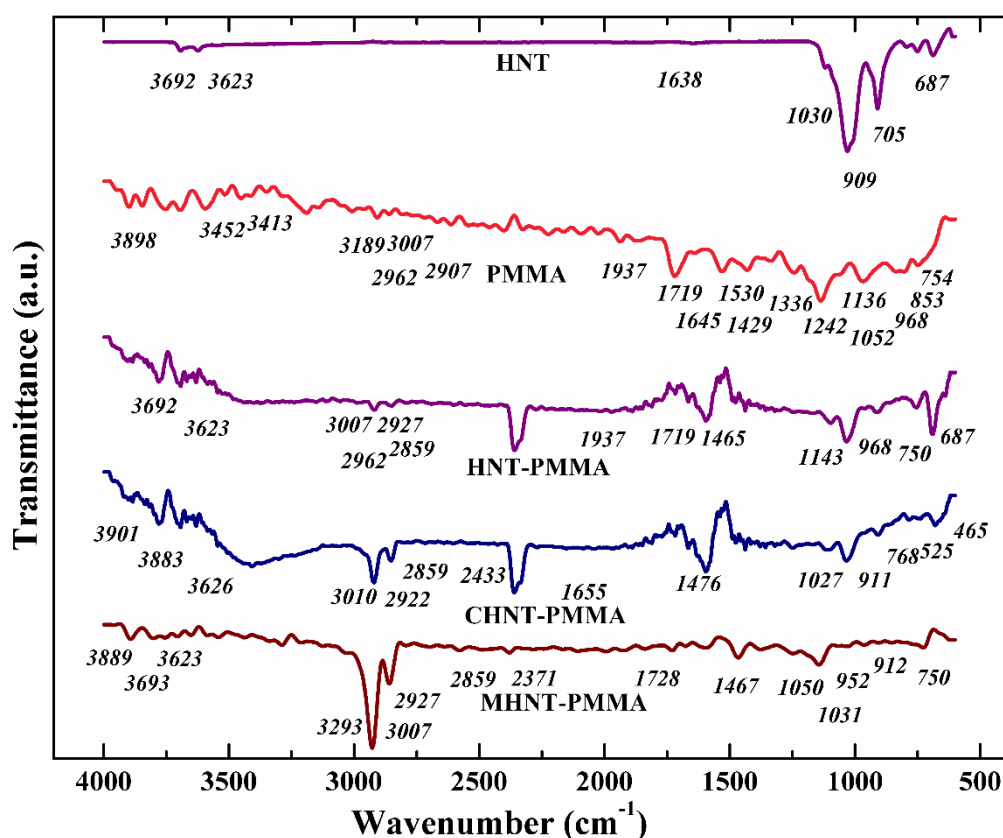


**Figure 5.12 FT-IR analysis HNT, PMMA, HNT-PMMA, CHNT-PMMA, and MHNT-PMMA**

The functional groups of the nanocomposites on modification of HNTs with CTAB and incorporated into PMMA can also be observed in Fig. 5.13. The characteristics peaks of CTAB and HNT (Fig. 4.3) are present in the nanocomposite synthesized using PMMA as a matrix. The IR spectra of PMMA exhibits distinct absorption band from  $1136\text{ cm}^{-1}$  to  $1242\text{ cm}^{-1}$ , this can be assigned to the stretching vibration of C–O–C. The two bands at  $1336\text{ cm}^{-1}$  and  $754\text{ cm}^{-1}$  can be ascribed to the  $\alpha$ -methyl group vibrations. The band at  $968\text{ cm}^{-1}$  is the characteristic absorption vibration of PMMA, along with the bands at  $1052\text{ cm}^{-1}$  and  $853\text{ cm}^{-1}$ . The two bands at  $2962\text{ cm}^{-1}$  and  $2907\text{ cm}^{-1}$  corresponds to the C–H bond stretching vibrations of the

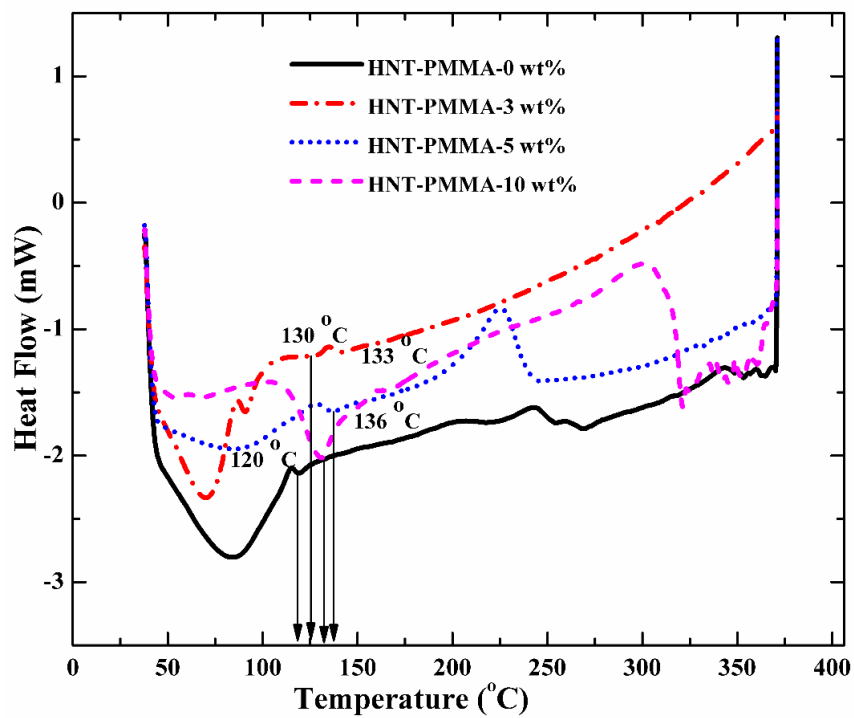
-CH<sub>3</sub> and -CH<sub>2</sub>- groups, respectively. The band at 1719  $cm^{-1}$  confirms the existence of the acrylate carboxyl group. The band at 1429  $cm^{-1}$  can be related to the bending vibration of the C-H bonds of the -CH<sub>3</sub> group. Additionally, two weak absorption bands can be seen at 3413  $cm^{-1}$  and 1645  $cm^{-1}$ ; these can be assigned to the OH group stretching and bending vibrations, respectively, of physisorbed moisture. The FT-IR spectra of the CHNT-PMMA exhibits the characteristic absorptions bands that are attributable to PMMA and CHNT. All PMMA bands which appeared in these spectra display a slight shifting. Also, new bands that appeared in the regions of 3626, 1027, and 465  $cm^{-1}$  were attributed to OH stretching of structural hydroxyl groups (Al-OH), Si-O stretching, and bending vibrations of CHNT and indicates the existence of CHNT in the PMMA matrix where the polymer chain was inserted between the layers of the HNT by secondary valence forces. Also, the incorporation of CHNT into the polymer matrix was confirmed by the presence of CHNT major peaks and PMMA major peaks in the resultant nanocomposites as portrayed in Fig. 5.13. This confirms the reinforcement of CHNTs in PMMA matrix.

The FT-IR analysis was carried out for MHNT-PMMA, and it was observed that the band at 912  $cm^{-1}$  for MHNTs was shifted to 952  $cm^{-1}$  for MHNT-PMMA. This can be attributed to interaction of OH group inside the HNT lumen, which indicates penetration of  $\gamma$ -MPS into HNT interlayers. The IR band at 1031  $cm^{-1}$  is assigned to Si-O groups at the surface of HNTs, while the band at 1050  $cm^{-1}$  for MHNT-PMMA is attributed to formation of Si-O-Si groups, indicating the interaction between  $\gamma$ -MPS and the surface of HNT. The significant reduction in intensity of the bands at 3623  $cm^{-1}$  and 3693  $cm^{-1}$  is related to the appearance of new bands at 2927  $cm^{-1}$  and 2859  $cm^{-1}$ . This decrease indicates the reaction between hydroxyl groups inside the lumen with PMMA.

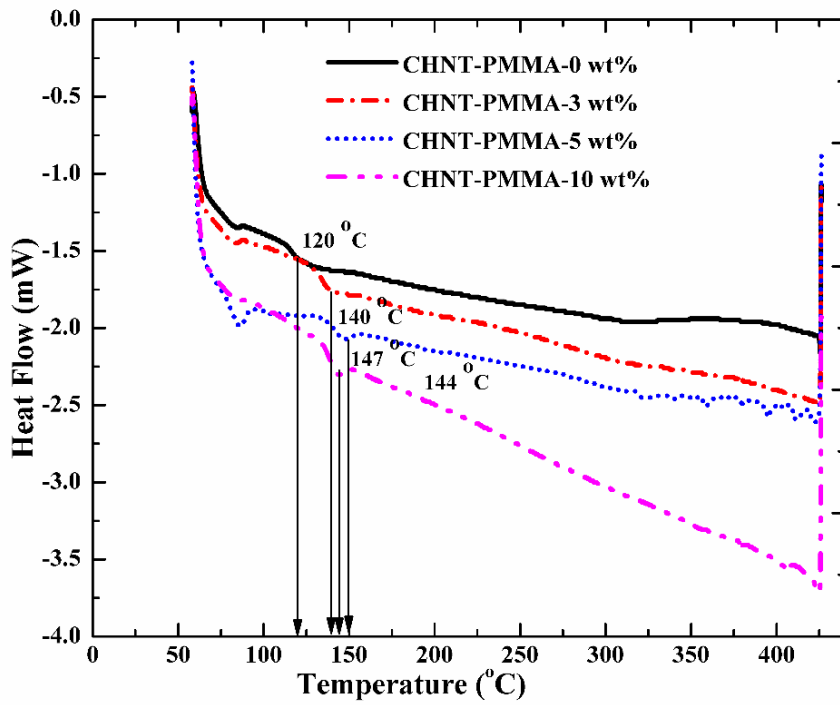
#### **5.4.4 Studies on thermal stability of HNT-PMMA, CHNT-PMMA and MHNT-PMMA nanocomposites**

The DSC traces of nanocomposites synthesized using HNT, CHNT, and MHNT with 0, 3, 5, 10 wt% HNT loading are presented in Fig. 5.13. HNT-PMMA nanocomposites was observed to display higher  $T_g$  than that of pure PMMA ensuring

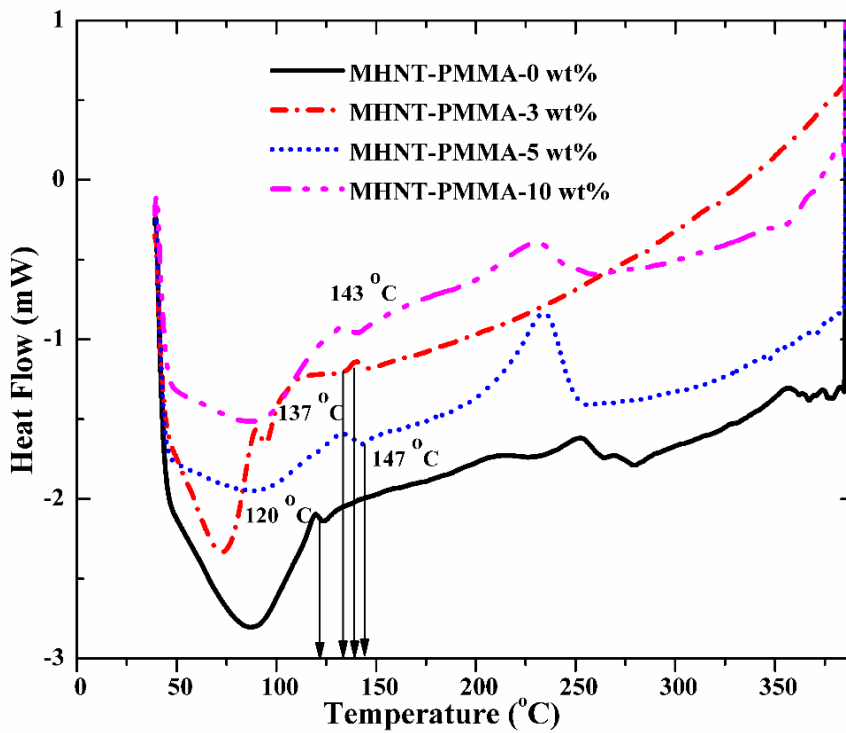
better thermal stability. A further increase in the  $T_g$  of the nanocomposites was observed on modifying HNTs with CTAB and  $\gamma$ -MPS. Additionally, it can be noted that the  $T_g$  is improved with an increase in HNT loading up to a certain % after which it reduces. The decrease in  $T_g$  with increase in amount of HNTs is due to the difficulty in dispersion of HNTs in polymer matrix. This causes formation of agglomerates thus causing a decrease in the thermal stability. Thus it can be noted the 5 wt % HNTs is optimum to synthesis nanocomposites with good thermal properties.



(a)



(b)



(c)

Figure 5.13 DSC images of (a) HNT-PMMA with different HNT content (wt%), (b) CHNT-PMMA with different HNT content (wt%) (c) MHNT-PMMA with different HNT content (wt%)

## 5.5 SUMMARY

Although nanocomposites could be propitiously synthesized using various solvents, toluene revealed good exfoliation, uniformly dispersed morphology and good  $T_g$  in comparison with other solvents, hence proving it to be the best solvent for HNT-polymer nanocomposite synthesis. Chemical composition is the key parameter for solubility of polymer in organic solvent. The solvent chosen must be such that it should be capable of over-ruling polymer-polymer interactions in order to dissolve polymer segments. That suggests a solvent molecule should have a favorable interaction with the polymer segments. Fortunately toluene holds the required properties and polystyrene, as well as polymethylmethacrylate, exhibits strong polarizable side groups that can be dissolved by toluene. This is the reason for toluene to be suitable solvent for dissolving polystyrene and polymethylmethacrylate. Also, toluene had the potential for dispersing HNTs, further ultrasound aided in uniform dispersion of HNTs into the polymer matrix and also caused sufficient increase in basal spacing of nanocomposites for polymer to enter the interlayers of clay which resulted in intercalated as well as exfoliated morphology thereby enhancing polymer properties for potential applications. HNT-PS and HNT-PMMA nanocomposites were fabricated using pristine HNTs, CHNT and MHNT with 0, 3, 5, and 10 wt % HNT content by solution intercalation method assisted by ultrasonic treatment. XRD analysis showed progressive disappearance of significant peaks which explains the good interaction between polymer and HNTs. Surface modification of HNTs further aided the formation of ordered structure. Ultrasonic treatment produced a rapid interaction of HNTs inside the polymer matrix. This is supported by SEM analysis showing a homogenous dispersion of HNTs. Surface modification of HNTs further aided in uniform dispersion of HNTs in the polymer matrix. FT-IR analysis of the nanocomposites revealed the presence of characteristic peaks of HNTs, CHNT, and MHNT in the polymer matrix. This confirms the reinforcement of HNTs in polymer matrix. DSC analysis of HNTs displayed a notable increase in the glass transition temperature of nanocomposites on the addition of HNTs into the polymer matrix. Improvement in the  $T_g$  was observed on addition of HNTs up to 5 wt%; further addition caused a decrease in  $T_g$  due to dispersion difficulties.

## CHAPTER 6

### ULTRASOUND-ASSISTED SYNTHESIS OF HNT-PS, HNT-PMMA, HNT-(PS-co-PMMA) NANOCOMPOSITES BY EMULSION POLYMERIZATION

*The characterization results of HNT-polymer nanocomposites synthesized by ultrasound-assisted emulsion polymerization technique are presented in this chapter. Pristine HNTs and modified HNTs were used as filler in polymer, and the effect of surface modification and sonication on structure, morphology, functional groups and thermal stability were investigated and reported.*

#### 6.1 INTRODUCTION

Emulsion polymerization is an essential industrial way for the manufacture of polymer latex for diverse applications such as varnishes, paints, adhesives, coatings, etc. The advantages of emulsion polymerization over the other synthesis techniques are controlled reaction conditions and narrow particle size distribution. This is because the reaction occurs in small droplets which are dispersed in a continuous phase. This leads to excellent shear stability, controlled polymerization rates and molecular weights of polymer and there is no migration of emulsifier migration during film formation (Ohtsuka et al. 1981). The final properties of synthesized nanocomposites depend on the interaction between polymer matrix and filler, the interfacial adhesions, and on the proportionate distribution of filler into the polymer matrix; this task can be accomplished in a better way by modification of HNTs and using ultrasound.

Conventional polymerization uses chemical initiators for generation of free radicals that readily decompose on heating. Apart from that additionally radicals can also be formed by degradation of water molecules, monomers, and formed polymer chains in ultrasound-assisted emulsion polymerization. This results in the formation of radicals by decomposition of water ( $\text{OH}^-$  and  $\text{H}^+$ ), surfactant, monomer or oligomer molecules. The free radicals initiate and propagate the polymerization reactions (Bhanvase et al. 2012b). High-intensity ultrasound, when coupled with liquid media, induces cavitations and streaming which indeed results in an enhancement of some

physical processes like mass transport, emulsification, bulk thermal heating, and many other chemical processes (Wang et al. 2005b). Sonochemical cavitation is a method of concentrating the diffuse energy of sound to a unique set of conditions to prepare novel materials with unusual properties (Suslick 1990a). Hence the ultrasound-assisted method of synthesizing nanocomposites is a potential way to prepare composites with unique characteristics.

In this chapter, the synthesis of HNT-polymer nanocomposites by ultrasound-assisted emulsion copolymerization with unmodified and modified HNTs has been reported. The key parameters that affect the stability of the emulsion and hence the properties of the resulting nanocomposites are sonication and HNT content. The effects of these parameters on the process were investigated in detail and reported in this chapter. The synthesized nanocomposites were characterized by scanning electron microscope (SEM), X-ray diffraction (XRD), Fourier transform and infrared spectroscopy (FT-IR), Zeta potential and particle size analysis and differential scanning calorimetry (DSC) to investigate structure, morphology, functional groups and thermal stability.

## 6.2 SYNTHESIS OF HNT-POLYSTYRENE (HNT-PS) NANOCOMPOSITES

In this section, investigation on the synthesis of nanocomposites consisting of polystyrene matrix and reinforced with pristine HNTs, on modification with surfactant (CTAB) and modification with silane ( $\gamma$ -MPS) was been reported. Emulsion polymerization was carried out by the addition of chemicals as mentioned in Table 6.1.

Table 6.1 Chemical composition of emulsion

<b>Chemicals</b>	<b>Quantity</b>
Styrene	10 mL
Halloysite nanotubes (HNTs)	0 – 5 g
Water	120 mL
Potassium per sulphate (KPS)	0.86 g
Sodium Dodecyl Sulphate (SDS)	1.06 g



### 6.2.1 Studies on the structure of HNT-PS, CHNT-PS and MHNT-PS nanocomposites

XRD analysis of the samples could provide information on changes occurred in the interlayer spacing of clay layers in nanocomposites. Fig. 6.1 compares the XRD patterns of HNT-PS, CHNT-PS and MHNT-PS nanocomposites synthesized by ultrasound-assisted emulsion polymerization. Broad peaks were observed in the XRD plots indicating that exfoliated and intercalated (partially exfoliated) structures of the nanocomposites. The XRD pattern of HNT-PS shows a broad peak centered at  $2\theta$  of  $24^\circ$ . Similarly, CHNT-PS and MHNT-PS show that peak at  $2\theta$  of  $20^\circ$ . It indicated an increase in  $d$  – *spacing* of HNT layers in nanocomposites synthesized on using surface modified HNTs. This increase in the  $d$  – *spacing* corresponds to the insertion of organic moieties between the interlayers of HNTs.

On the modification of HNTs with CTAB, it can be particularly noted that CHNT particles dispersed uniformly in the styrene monomer in comparison with pristine HNTs. And, with increase in the structural affinity among styrene monomer and organic group of CHNT, there is increase in the dispersibility of CHNT in styrene monomer. In general, the penetration of monomers into the lamellae of CHNT is facilitated by the attractive forces between the CHNT interlayers and the free monomer molecules. The solvation efficiency of the CHNT with monomer depends on the nature of the organic group intercalated in the HNT and on the chemical structure of the monomer used. With the growth of alkyl chain length of the alkyl ammonium cations in HNT, there is an increase in the basal spacing of CHNT. As the monomer penetrates into CHNT interlayer space followed by polymerization, there is an increase in the interlayer distance which depends on the structure of organic groups of CHNT rather than the chain length of the alkyl ammonium cation. With the increase in the interlayer distance of CHNT, the PS polymer chains polymerized in the interlayers (Doh and Cho 1998). Also, the presence of a double bond on the ammonium cation of the HNTs permits some amount of the monomer to attach to the HNT, and this encourages exfoliation. Therefore, modification of HNTs with CTAB resulted in better interaction between polymer and HNT and formation of mixed structures, i.e., intercalation and exfoliation.

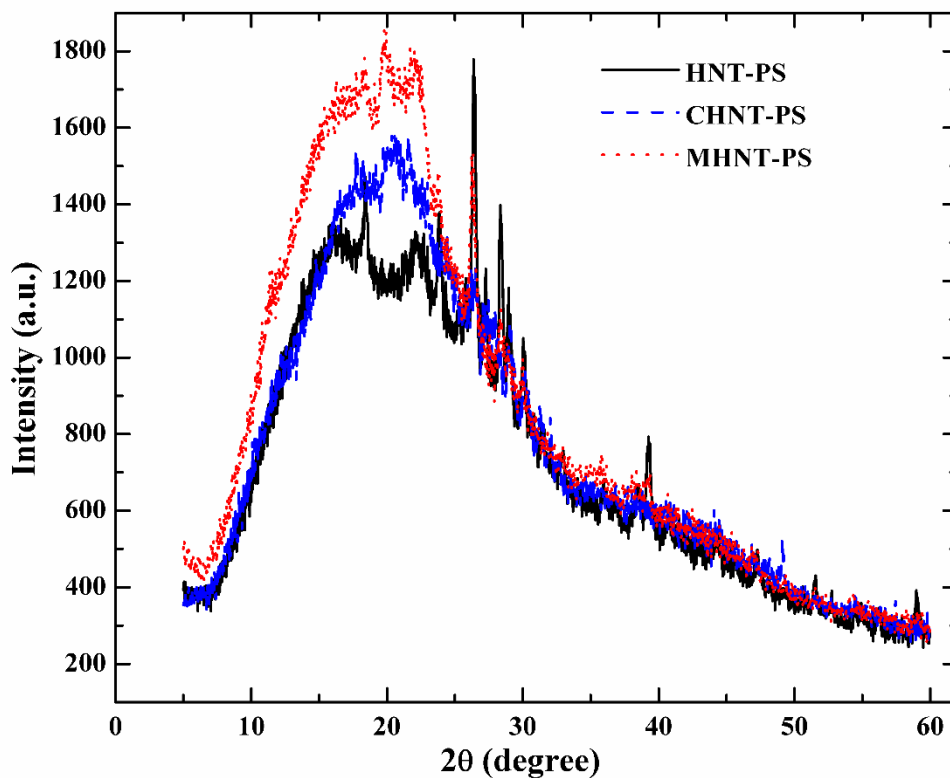


Figure 6.1 XRD analysis of (a) HNT-PS, (b) CHNT-PS, and (c) MHNT-PS nanocomposites synthesized by ultrasound-assisted emulsion polymerization

Next, studies on reinforcing MHNT in the polystyrene matrix was investigated. Generally, the grafting of silane onto HNTs occurs in two steps. In the first step, silane molecules are intercalated into the HNT interlayer, and in the second step, the condensation reaction occurs between silane molecules and the HNTs layer surface. Also, silane molecules react at the broken edges of HNTs. The condensation reaction between the surface hydroxyl groups located on the HNT edges and the alkoxy groups of the silane molecules gives rise to the formation of Si-O-Si covalent bonds. It can be noticed in Fig. 6.1 that the basal spacing of the MHNT-PS disappears progressively in X-ray diffractograms of the nanocomposites. This disappearance of basal reflections suggests the better interaction between PS and MHNTs. Also, ultrasound exerts high shearing stresses on the HNTs locally causing progressive delamination and exfoliation. The presence of a broad peak in all the nanocomposites indicates the synthesized

polymer is amorphous. The reduction in peaks in case of modified HNTs suggested better interaction between the PS and HNTs.

### **6.2.2 Studies on the morphology of HNT-PS, CHNT-PS and MHNT-PS nanocomposites**

On projection of ultrasonic probe into the liquid cavitations bubbles are generated. These bubble expand due to the fluctuations in pressure and collapse adiabatically (Gogate 2008). These severe adiabatic conditions generated within the liquid medium are responsible for the generation of radicals as a result of dissociation of the trapped water/organic molecules. The formation of extreme turbulence associated with strong liquid circulation currents leads to formation of a very fine and stable emulsion along with significant enhancement in dispersion or the mass transfer rates. Hence, ultrasound is an intensified source of energy dissipation during the synthesis of HNT-polymer nanocomposites. This is because of the following reasons.

1. As a result of shearing action generated by ultrasonic cavitation which aids in exfoliation and uniform dispersion of HNTs into the organic phase (Ryu et al. 2004). Additionally, cavitation can aid in the separation of HNTs into the number of exfoliated platelets due to microstreaming phenomena (Borthakur et al. 2010).
2. Uniform size of monomer droplet can be achieved without any agglomerations (Teo et al. 2008). The ultrasound pulses in the first few minutes of polymerization causes increase in instant free radical to monomer ratio as well as mixing efficiency, which results in smaller and more uniform particles.

Figure 6.2a illustrates typical morphology of HNT-PS nanocomposite particles prepared by emulsion polymerization without the use of ultrasound. It can be observed that the particles are in perfect spherical shape, but there is slight aggregation. Since HNTs are negatively charged on their outer surface, it may be either distributed inside monomer droplets or get adsorbed to the monomer and water interface (Huang and Brittain 2001). The dried latex particles were analyzed by SEM to understand its morphology. It can be seen that the particles are not very prominent, this is because of partial exfoliation due to less compatibility between styrene and HNT and also intercalation of styrene in HNTs. Fig. 6.2b shows the morphology of particles

synthesized by emulsion polymerization assisted by ultrasound. It can be noted that ultrasonic irradiation was effective in promoting free radical polymerization along with nanoscale dispersion of HNTs in the polymer matrix.

The morphology of composites synthesized using CHNT and MHNT was analyzed by SEM to understand the effect of HNT modification on the morphology of composites. It can be observed from Fig. 6.2 (c & e) that there was a reduction in aggregates on the use of modified HNTs. This is because pristine HNTs formed large aggregates due to van der Waal's intertube attraction and the aggregation, whereas modification results in the formation of particles with fewer aggregations. CTAB plays a major role in synthesizing nanoparticles by adsorbing onto the surface of HNTs and, forming nanoparticles, lowering its surface energy, and thus prevents aggregation. On the other hand, on modification of HNTs with  $\gamma$ -MPS, the surface of HNTs was made hydrophobic by absorption of silanes through chemical bonding with surface hydroxyl groups of HNTs.

Figure 6.2 (c & e) shows the nanocomposite which was synthesized on modification of HNTs with CTAB and  $\gamma$ -MPS respectively, without the use of ultrasound. It shows a lot of agglomerations and uneven distribution of filler particles in the polymer matrix. Fig. 6.2 (d & f) shows a sample obtained after sonication time of 60 *min*. It reveals that uniform dispersion of HNTs in the polymer is achieved as it also promotes proportionate distribution of filler into the polymer matrix. Any further increase in sonication time resulted in breaking of polymer chains due to high temperatures and pressures which may degrade the properties of nanocomposites (samples are not shown here). The nanocomposite synthesized by subjecting to ultrasound for 60 *min* had a smooth surface without any agglomerations and had mono-dispersed morphology, and hence 60 *min* seems to be optimum for in-situ synthesis of nanocomposites. Ultrasonic waves in the first few minutes of polymerization causes increase in free radical to monomer ratio and mixing efficiency, which results in smaller and more uniform particles.

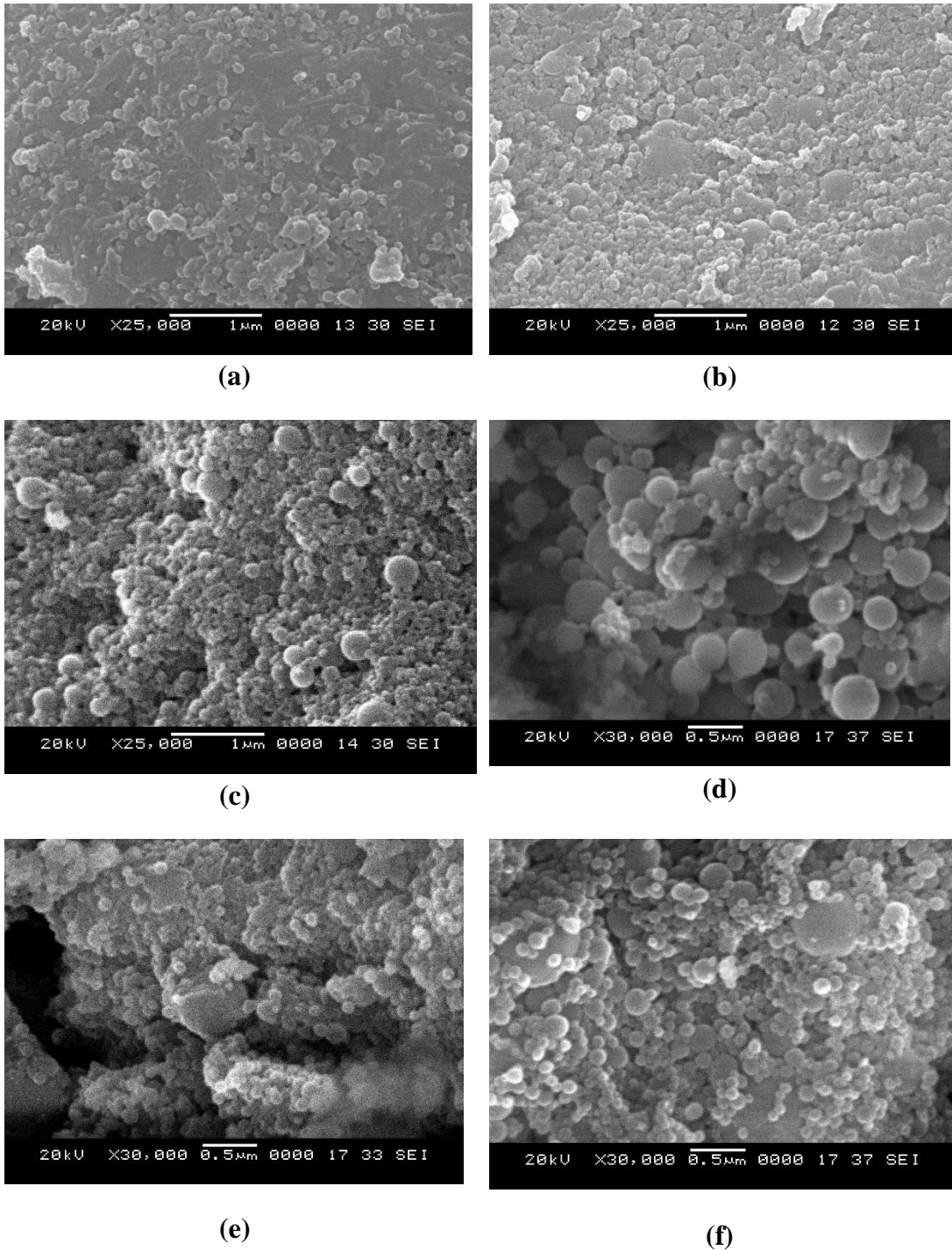


Figure 6.2 SEM images of (a) HNT-PS without ultrasound, (b) HNT-PS with ultrasound, (c) CHNT-PS without ultrasound, (d) CHNT-PS with ultrasound, (e) MHNT-PS without ultrasound and (f) MHNT-PS with ultrasound

The particle size was substantially lower as compared to the nanocomposite synthesized using conventional emulsion polymerization. This decrease in the particle

size of the nanocomposite can be attributed to the reduction in initial monomer droplet size obtained by sonication, and improvement in the dispersion of HNTs in the polymer matrix due to the continuous ultrasonic irradiation.

### **6.2.3 Studies on functional groups of HNT-PS, CHNT-PS and MHNT-PS nanocomposites**

To examine the successful incorporation of HNT, CHNTs, and MHNTs into the polymer matrix FT-IR analysis of the nanocomposites was performed and displayed in Fig. 6.3. It can be observed that the nanocomposites which were synthesized without modification of HNTs, i.e., HNT-PS demonstrates the existence of HNT major absorbance peaks in polystyrene spectrum which proves the existence of clay inside the latex particles and indicates encapsulation of HNTs into the final nanocomposites. However, the peak at  $3692\text{ cm}^{-1}$  shifts to  $3694.43\text{ cm}^{-1}$  in the nanocomposite which attributes interaction of Al layer of HNT with the polymer surface. Thus from FT-IR analysis, we may infer successful incorporation of HNT in the polymer matrix.

The functional groups of the nanocomposites on modification of HNTs with CTAB and incorporated into PS can also be observed in Fig. 6.3. The characteristics peaks of CTAB and CHNT (Fig. 4.3) are present in the nanocomposite synthesized using PS as a matrix. The IR spectrum of PS displays bands at wavenumbers  $3066\text{ and }3025\text{ cm}^{-1}$  which are assigned to the stretching vibration of aromatic C–H. The bands at  $2922\text{ and }2851\text{ cm}^{-1}$  are attributed to the stretching vibration of aliphatic C–H. The bands between  $1666\text{ and }1945\text{ cm}^{-1}$  dictates combination bands. The stretching vibration of aromatic C=C can be seen at  $1491, 1449\text{ and }1599\text{ cm}^{-1}$ . The bending vibration of aliphatic C–H can be seen at  $1188\text{–}1368\text{ cm}^{-1}$ . The bands at  $1026\text{ cm}^{-1}$  can be assigned to the bending vibration of aliphatic C–H. Also, the bending vibration of aromatic C–H are represented at  $698, 756, \text{ and }543\text{ cm}^{-1}$ . The FT-IR spectra of the CHNT-PS exhibits the characteristic absorptions bands that are attributable to PS and CHNT. All PS bands which appeared in these spectra display a slight shifting. Also, new bands that appeared in the regions of  $3626, 1027, \text{ and }465\text{ cm}^{-1}$  were attributed to OH stretching of structural hydroxyl groups (Al–OH), Si–O stretching, and bending vibrations of CHNT and indicates the

existence of CHNT in the PS matrix where the polymer chain was inserted between the layers of the HNT by secondary valence forces. Also, the incorporation of CHNT into the polymer matrix was confirmed by the presence of CHNT major peaks and PS major peaks in the resultant nanocomposites as portrayed in Fig. 6.3. This confirms the reinforcement of CHNTs in PS matrix.

The HNTs modified with  $\gamma$ -MPS was also exfoliated into the PS matrix, and the FT-IR analysis is portrayed in Fig. 6.3. The major absorbance peaks of MHNT can be observed in Fig. 4.6. It can be observed that the band at  $912\text{ cm}^{-1}$  for MHNT was shifted to  $968.47\text{ cm}^{-1}$  for MHNT-PS. This can be attributed to the interaction of OH group inside the HNT lumen, indicating the penetration of  $\gamma$ -MPS into the HNT interlayers. Additionally, the considerable reduction in the intensity of the bands at  $3623.47\text{ cm}^{-1}$  and  $3693.56\text{ cm}^{-1}$  is related to the appearance of new bands at  $2962.49\text{ cm}^{-1}$  and  $2907.13\text{ cm}^{-1}$ . This indicates the reaction between hydroxyl groups inside the lumen with PS. Thus the FT-IR suggests the presence of MHNT inside the PS matrix.

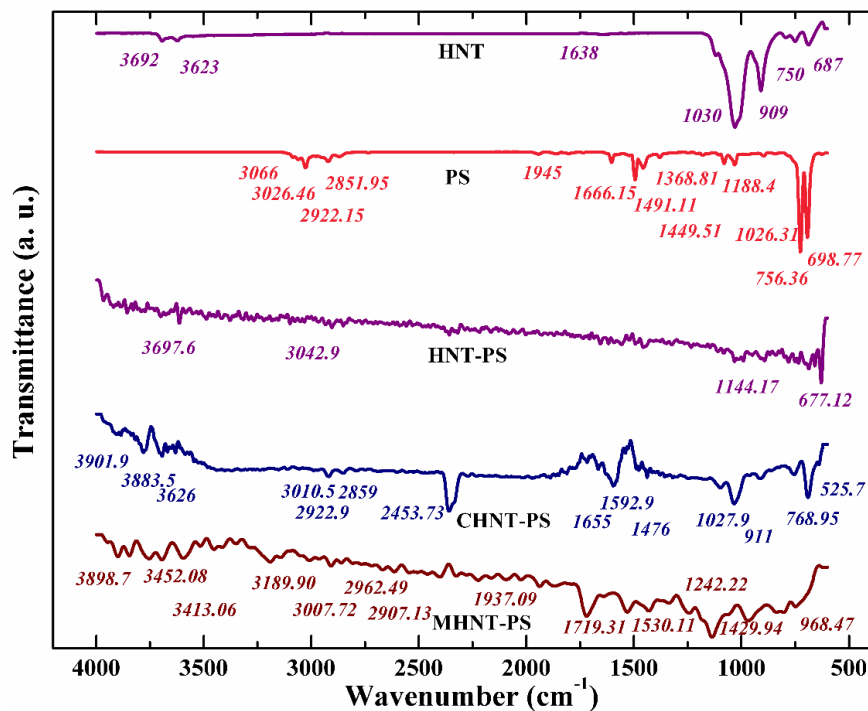


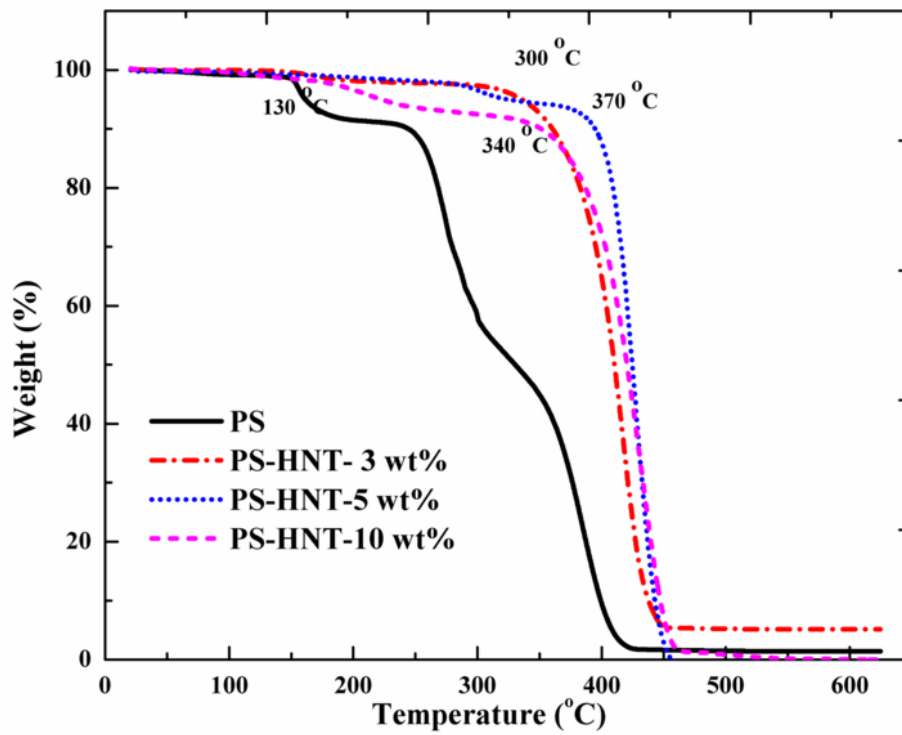
**Figure 6.3** FT-IR of HNT, PS, HNT-PS, CHNT-PS, and MHNT-PS nanocomposites

#### **6.2.4 Studies on thermal stability of HNT-PS, CHNT-PS and MHNT-PS nanocomposites**

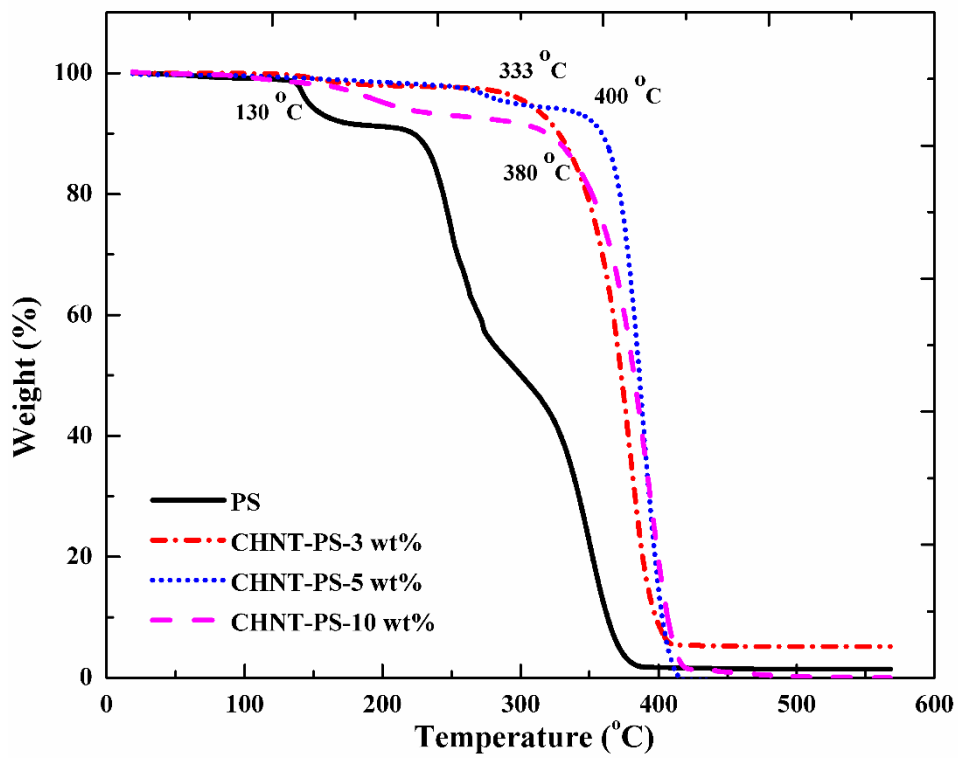
From Fig. 6.4a, it can be observed that the thermal stability of the nanocomposite is enhanced upon addition of HNT and increasing HNT content relative to that of virgin polystyrene. Typically, the onset temperature of the degradation is significantly higher for the nanocomposites than for virgin polystyrene. The increase in the thermal stability is due to the presence of HNTs is attributed to the formation of char that plays a role as mass transport barrier and an insulator between the bulk polymer and the surface, where the combustion of the polymer takes place (Wang et al. 2002). The presence of HNTs also obstructs diffusion of volatile decomposition products within the nanocomposites (Sinha Ray and Okamoto 2003). This is due to the decrease in area available for diffusion as the permeable polymers are replaced by impermeable HNTs which increases the distance that the gas has to follow a tortuous path is formed around the HNTs. Also, the enhancement of thermal stability of nanocomposites can also be due to restricted thermal motion of polymer chains inside the HNT layers. Additionally, the increment in thermal stability may also be attributed to higher molecular weight by emulsion polymerization, enhanced interaction between polymer and clay, and modification of HNTs.

The effect of loading different *wt%* of HNT into the polymer matrix on the thermal properties of the polymer was investigated. It can be observed from the thermograms that HNT content had a notable effect on thermal stability. The nanocomposites with 5 *wt%* HNT showed higher thermal stability relative to the nanocomposites with 3 *wt%* HNT. For HNT-PS, the maximum barrier properties were observed for PS with 5 *wt%* HNT. Additionally, increase in HNT content increased the gas permeability. This is because the permeability of gas depends upon the particle size and dispersion of filler. On increasing HNT content beyond 5 *wt%*, there is a reduction in dispersion of nanofiller which might occur due to agglomeration. This agglomeration leads to unequal distribution of HNT layers, thus causing a decrease in permeability.

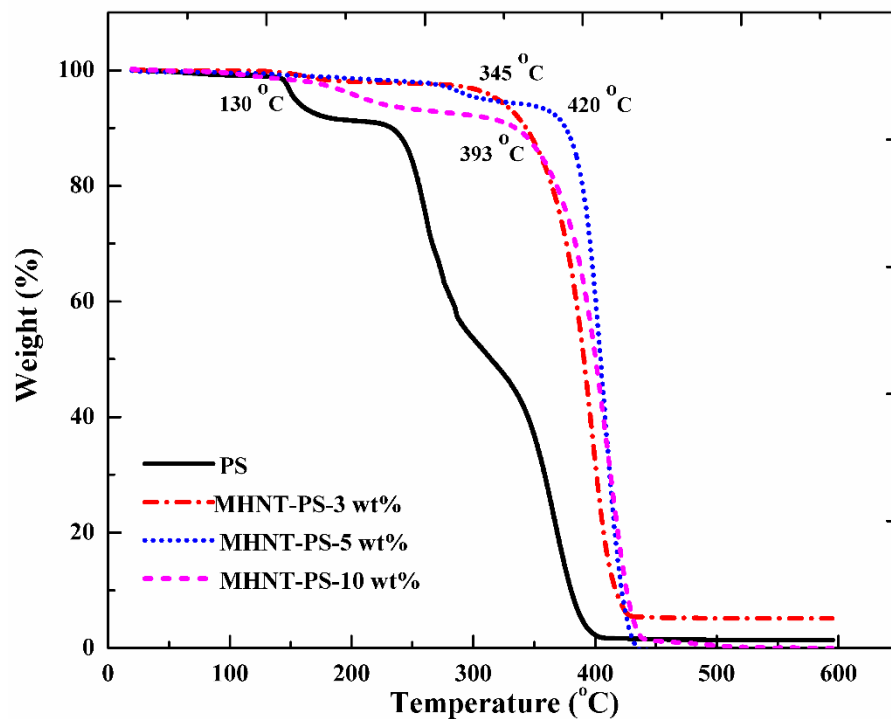




(a)



(b)



(c)

Figure 6.4 Thermal properties of (a) HNT-PS, (b) CHNT-PS and (c) MHNT-PS nanocomposites with different HNT content

Further, it can be noticed that the nanocomposites synthesized on modified HNTs showed noticeable improvement in thermal stability as seen in Fig. 6.4 (b and c). It may be attributed to the confinement of PS polymer chains between HNT layers as well as the HNT surface-polymer interactions in the nanostructured hybrid of PS and modified HNT. Therefore, the improvement in the thermal stability will lead to the better service performance of the hybrid composite at elevated temperature. This is mainly due to the improved interactions between the clay and the polymer upon a modification of HNTs that serves to stabilize the nanocomposite. Modification of clays improves their decomposition temperature. Due to this the formation of char occurs at a more appropriate time which retains the polymer from getting decomposed (Zhu et al. 2001). In the case of the unmodified HNTs char formation occurs faster and can be broken up by the time that the polymer degrades. Addition of even 3 wt% of modified HNTs into the polymer caused the onset temperature to improve significantly.

### 6.3 SYNTHESIS OF HNT-POLYMETHYLMETHACRYLATE (HNT-PMMA) NANOCOMPOSITES

PMMA is an optically clear thermoplastic, and it is usually used as a substitute for inorganic glass because of its high impact strength, lightweight, shatter-resistant, and exhibits favorable processing conditions. It exhibits outstanding properties including weather and scratch resistance. It has MMA on the adjacent methyl group (CH<sub>3</sub>) in the polymer structure which prevents it from packing closely in a crystalline fashion, and also rotating freely around the C-C bonds. Various methods have been employed for the synthesis of polymer nanocomposites with better properties such as solvent blending, in-situ polymerization, and melt-intercalation. In this section, investigation on the synthesis of nanocomposites consisting of polymethylmethacrylate matrix and reinforced with pristine HNTs, on modification with surfactant (CTAB) and modification with silane ( $\gamma$ -MPS) by emulsion polymerization is reported. Emulsion polymerization was carried out by the addition of chemicals as mentioned in Table 6.2.

Table 6.2 Chemical composition of emulsion

<b>Chemicals</b>	<b>Quantity</b>
Methylmethacrylate (MMA)	10 mL
Halloysite nanotubes (HNTs)	0 – 5 g
Water	120 mL
Potassium per sulphate (KPS)	0.86 g
Sodium Dodecyl Sulphate (SDS)	1.06 g

#### 6.3.1 Studies on structure of HNT-PMMA, CHNT-PMMA and MHNT-PMMA nanocomposites

XRD is a most useful technique for the measurement of d-spacing of ordered intercalated and exfoliated nanocomposites. MMA contains both a low polar portion (methacryl group) and a high polar portion (ester group), hence the polarity of MMA is higher than that of styrene, as verified by the dipole moment difference. MMA has a stronger compatibility with the polar clay surface than styrene.

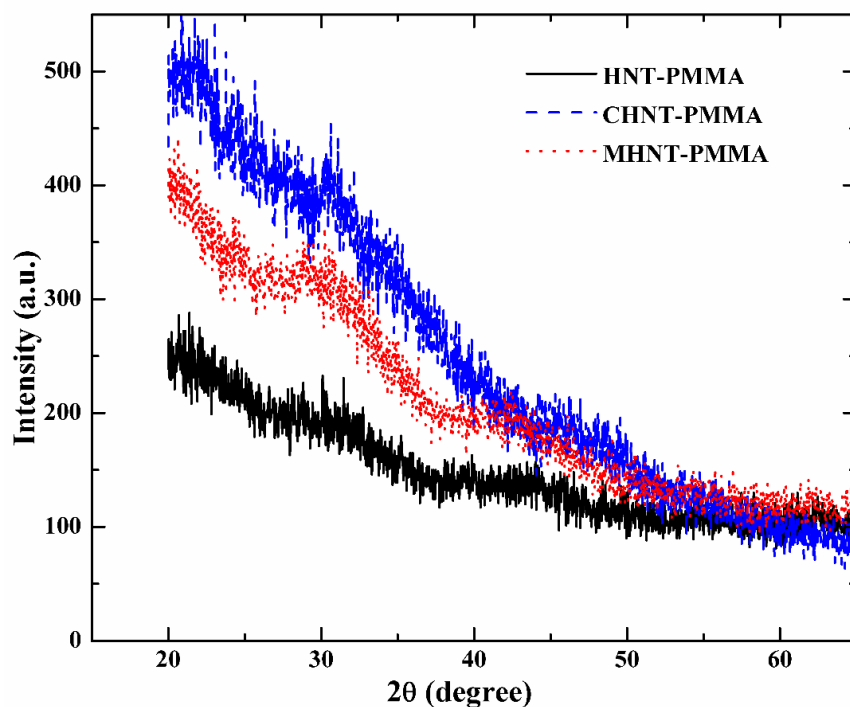


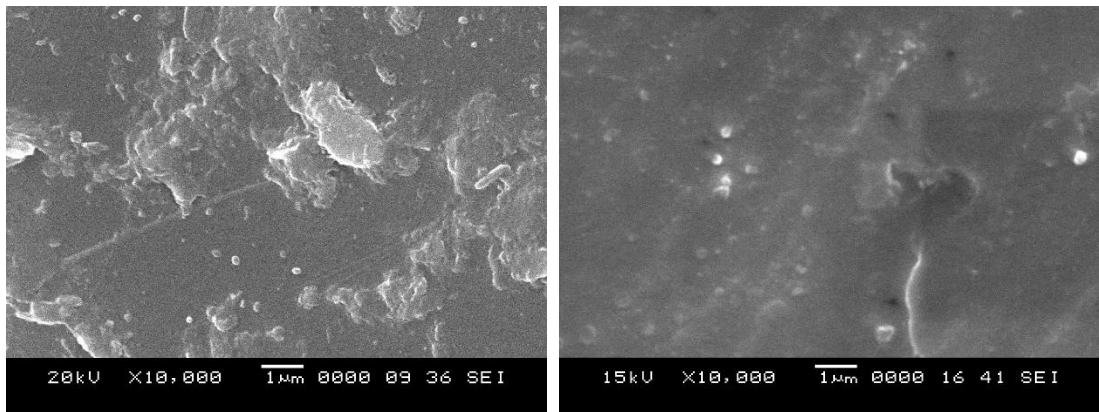
Figure 6.5 XRD analysis of HNT-PMMA, CHNT-PMMA, and MHNT-PMMA nanocomposites

The XRD pattern of HNT-PMMA, CHNT-PMMA and MHNT-PMMA in the  $2\theta$  range of  $10^\circ$ – $65^\circ$  are shown in Fig. 6.5. This clearly reveals that HNT layers have been introduced in the nanocomposites as a single polymer chain enters between the HNTs and a tactoid morphology results with alternating polymeric and HNT layers. Further, it can be observed that there is no presence of prominent peak which denotes that a considerable amount of polymer has inserted the gallery space and expanding the clay layers so far (Morgan and Gilman 2003). Also, it can be observed that there is a slight increase in the  $d$  – *spacing* of composites on using CHNTs and MHNTs relative to HNTs. The different  $d$  – *spacing* value obtained for the PMMA with HNTs and modified HNTs nanocomposite is probably due to the amount of polymer penetrated between the HNT layers and the interaction between a modified HNT with PMMA matrix. CTAB contains a positively charged ammonium head group and a nonpolar aliphatic chain. Hence on modification of HNTs with CTAB, and upon interaction with MMA, the interaction between MMA and HNTs becomes more favorable due to their polar nature. Additionally, the van der Waals interaction is also established between the

low polar methacryl group and the nonpolar alkyl chain. Hence, it can be observed in Fig. 6.5 CHNT-PMMA that there is no presence of significant peaks which confirms good interaction between PMMA and CHNT. A similar kind of observation could be seen on using MHNTs for the formation of nanocomposites in Fig. 6.5 MHNT-PMMA. Modification of HNTs with silane increased the dispersion of HNTs which ultimately increased the interaction between PMMA and HNTs. This increase is due to the formation of intercalated nanocomposite which shows that the polymer has entered into the HNT gallery.

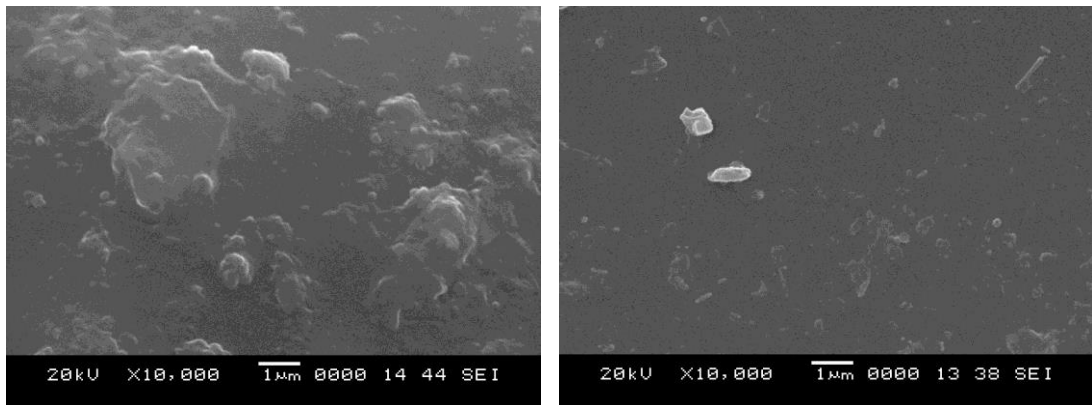
### **6.3.2 Studies on the morphology of HNT-PMMA, CHNT-PMMA, and MHNT-PMMA nanocomposites**

SEM analysis was carried out to understand the morphology of nanocomposites synthesized. Figure 6.6b shows enhanced breakup of HNT aggregates and reduction in the size of the dispersed phase with better homogeneity on utilizing of ultrasound for carrying out in situ emulsion polymerization in comparison to the conventional in situ emulsion polymerization. The shearing action produced by ultrasonic cavitation aids in the synthesis of exfoliated HNT-PMMA nanocomposite with homogeneous dispersion of HNTs in the organic phase. Additionally, sonication cannot just initiate polymerization at room temperature but can also aid in better dispersion of HNTs at nanoscales, and shorten the polymerization time. Hence, the ultrasound-assisted in situ emulsion polymerization can be considered can be advantages in the synthesis of HNT-polymer nanocomposites. Further modification of HNTs with CTAB and  $\gamma$ -MPS can ease the dispersion of HNTs into the polymer thereby leading to better interaction and better properties of nanocomposites.



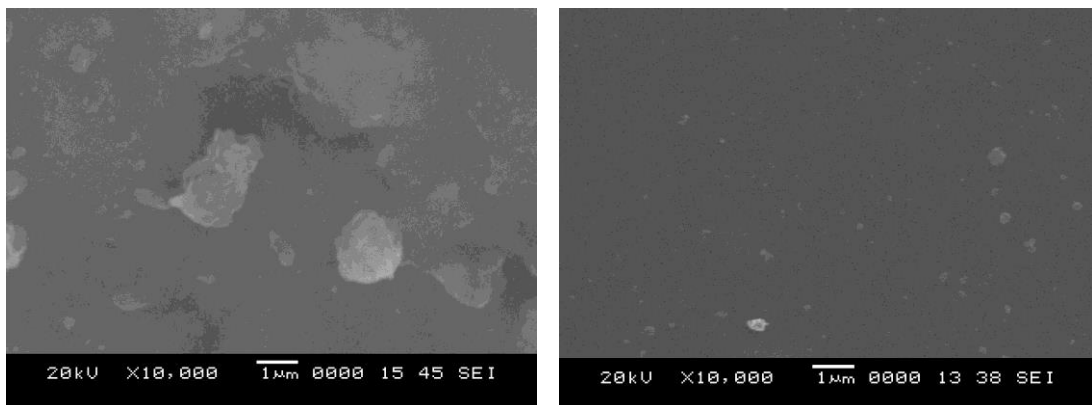
(a)

(b)



(c)

(d)



(e)

(f)

**Figure 6.6 SEM images of (a) HNT-PMMA without sonication, (b) HNT-PMMA with sonication, (c) CHNT-PMMA without sonication, (d) CHNT-PMMA with sonication, (e) MHNT-PMMA without sonication, and (f) MHNT-PMMA with sonication**

### 6.3.3 Studies on functional groups of HNT-PMMA, CHNT-PMMA, and MHNT-PMMA nanocomposites

Figure 6.7 shows the FT-IR analysis of HNTs, PMMA, HNT-PMMA, CHNT-PMMA, and MHNT-PMMA. The most significant feature of HNT is the presence of characteristic peaks at  $3692.79$ ,  $3623.21 \text{ cm}^{-1}$  ascribes Al–OH, and  $1030.10$ ,  $909.18 \text{ cm}^{-1}$  represents Si–O. The presence of these peaks on the synthesized nanocomposites indicated the presence of HNTs in PMMA matrix. Also, a distinct absorption peak appeared at  $1719 \text{ cm}^{-1}$  (C=O stretching) due to the characteristic frequencies of PMMA. This result might be attributed to PMMA being intercalated and hydrogen-bond formation between the oxygen of the polymer molecules and the hydroxyl of the HNT lattice. Hence, these results indicate that the solution casting assisted by ultrasound successfully produced HNT-PMMA nanocomposites.

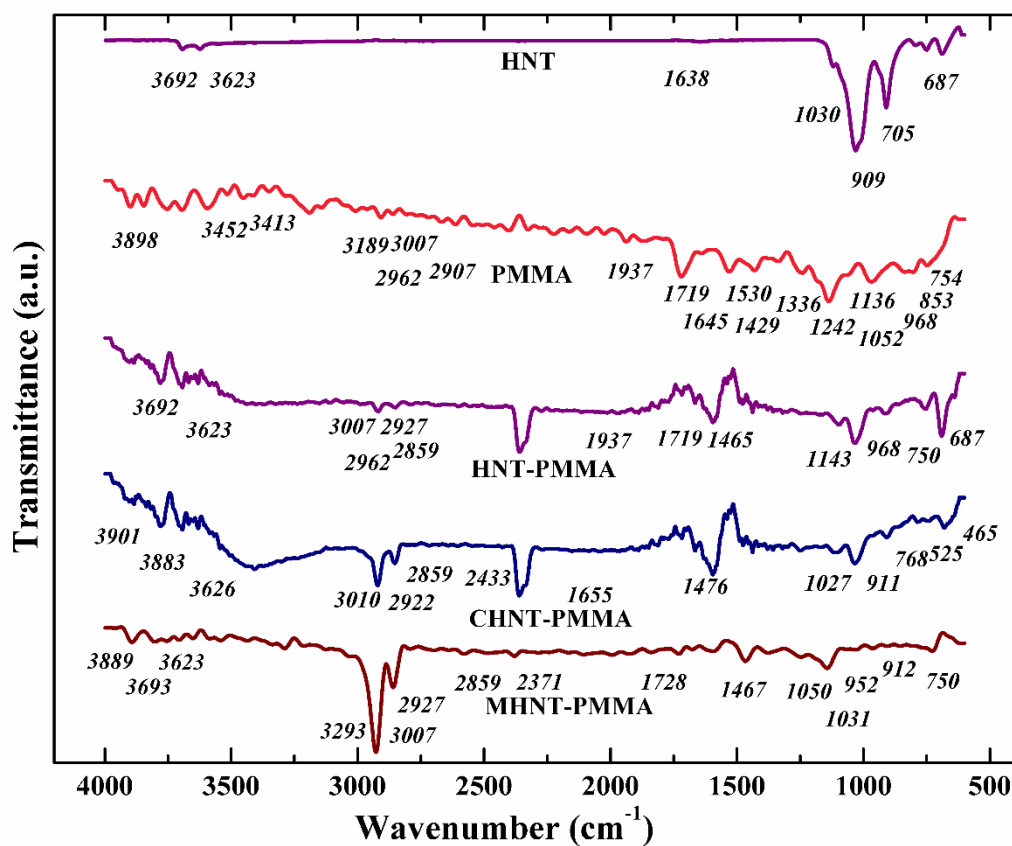


**Figure 6.6** FT-IR analysis a) HNT b) PMMA, c) HNT-PMMA d) CHNT-PMMA e) MHNT-PMMA

The functional groups of the nanocomposites on modification of HNTs with CTAB and incorporated into PMMA can also be observed in Fig. 6.7. The

characteristics peaks of CTAB and CHNT (Fig. 4.3) are present in the nanocomposite synthesized using PMMA as a matrix. The IR spectra of PMMA exhibits distinct absorption band from  $1136\text{ cm}^{-1}$  to  $1242\text{ cm}^{-1}$ , this can be assigned to the stretching vibration of C–O–C. The two bands at  $1336\text{ cm}^{-1}$  and  $754\text{ cm}^{-1}$  can be ascribed to the  $\alpha$ -methyl group vibrations. The band at  $968\text{ cm}^{-1}$  is the characteristic absorption vibration of PMMA, along with the bands at  $1052\text{ cm}^{-1}$  and  $853\text{ cm}^{-1}$ . The two bands at  $2962\text{ cm}^{-1}$  and  $2907\text{ cm}^{-1}$  corresponds to the C–H bond stretching vibrations of the  $-\text{CH}_3$  and  $-\text{CH}_2-$  groups, respectively. The band at  $1719\text{ cm}^{-1}$  confirms the existence of the acrylate carboxyl group. The band at  $1429\text{ cm}^{-1}$  can be related to the bending vibration of the C–H bonds of the  $-\text{CH}_3$  group. Additionally, two weak absorption bands can be seen at  $3413\text{ cm}^{-1}$  and  $1645\text{ cm}^{-1}$ ; these can be assigned to the  $-\text{OH}$  group stretching and bending vibrations, respectively, of physisorbed moisture. The FT-IR spectra of the CHNT-PMMA exhibits the characteristic absorptions bands that are attributable to PMMA and CHNT. All PMMA bands which appeared in these spectra display a slight shifting. Also, new bands that appeared in the regions of  $3626, 1027, \text{ and } 465\text{ cm}^{-1}$  were attributed to OH stretching of structural hydroxyl groups (Al–OH), Si–O stretching, and bending vibrations of CHNT and indicates the existence of CHNT in the PMMA matrix where the polymer chain was inserted between the layers of the HNT by secondary valence forces. Also, the incorporation of CHNT into the polymer matrix was confirmed by the presence of CHNT major peaks and PMMA major peaks in the resultant nanocomposites as portrayed in Fig. 6.7. This confirms the reinforcement of CHNTs in PMMA matrix.

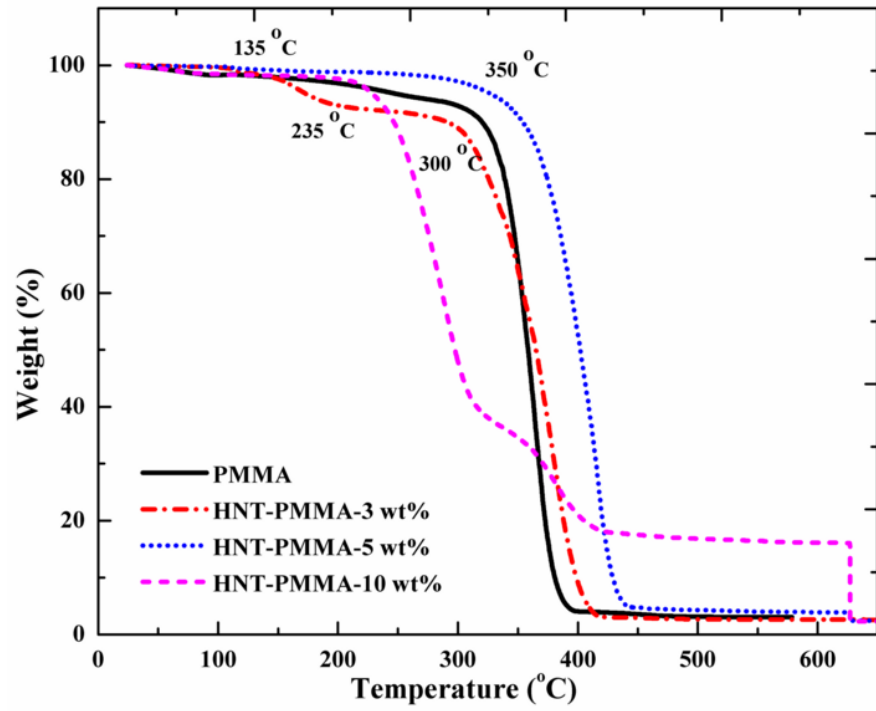
The FT-IR analysis was carried out for MHNT-PMMA, and it was observed that the band at  $912\text{ cm}^{-1}$  for MHNTs was shifted to  $952\text{ cm}^{-1}$  for MHNT-PMMA. This can be attributed to the interaction of OH group inside the HNT lumen, which indicates penetration of  $\gamma$ -MPS into HNT interlayers. The IR band at  $1031\text{ cm}^{-1}$  is assigned to Si–O groups at the surface of HNTs, while the band at  $1050\text{ cm}^{-1}$  for MHNT-PMMA is attributed to the formation of Si–O–Si groups, indicating the interaction between  $\gamma$ -MPS and the surface of HNTs. The significant reduction in intensity of the bands at  $3623\text{ cm}^{-1}$  and  $3693\text{ cm}^{-1}$  is related to the appearance of new bands at  $2927\text{ cm}^{-1}$  and



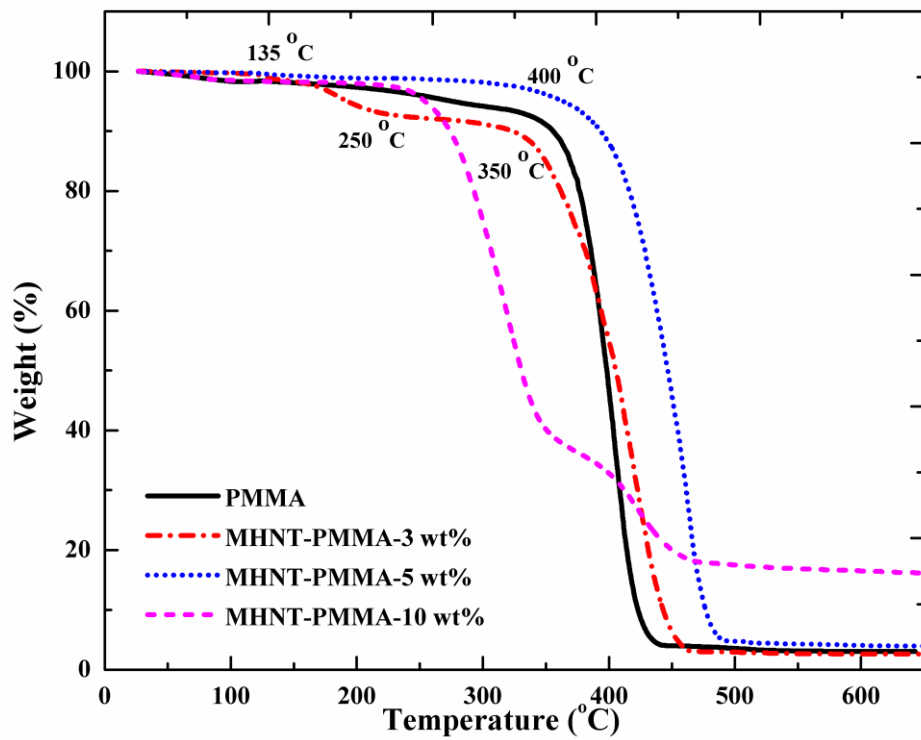
2859  $cm^{-1}$ . This decrease indicates the reaction between hydroxyl groups inside the lumen with PMMA.

#### **6.3.4 Studies on thermal stability of HNT-PMMA, CHNT-PMMA, and MHNT-PMMA nanocomposites**

The thermogram of pure PMMA, HNT-PMMA, and MHNT-PMMA nanocomposites with different HNT content has been carried out and reported in Fig. 6.8. It can be observed that the thermal stability of PMMA improved on including HNTs into the polymer matrix. The thermal stability of PMMA is seen to be increasing with increasing HNT content up to 5 wt%. This demonstrates the role of HNTs in improving the thermal stability of nanocomposites. On further increase in HNT content, the thermal properties decrease due to dispersion difficulties. It can further be noted that the TGA isotherm shows improvement in the stability of composites synthesized using MHNT. The increase in barrier property due to improved dispersion on the use of ultrasound as seen in Fig. 6.8 (b and c). This is because of improvement in the bonding between the HNT and PMMA, which results in enhanced thermal stability. This alteration is due to the presence of a high surface area of HNTs in the polymer matrix because of which there is a restriction of segmental motions at the organic-inorganic interface. The confinement of polymer chains between the HNT layers and HNT surface and polymer also improves the thermal stability significantly. Hence, the modification of HNT by  $\gamma$ -MPS combined with sonication produced HNT-PMMA nanocomposites having better dispersion of HNTs leading to better thermal properties.



(a)



(b)

**Figure 6.7 Thermal properties of (a) HNT-PMMA, (b) MHNT-PMMA nanocomposites with different HNT content (wt %)**

## **6.4 SYNTHESIS OF POLY(STYRENE-CO-METHYLMETHACRYLATE)-HNT [HNT-(PS-co-PMMA)] NANOCOMPOSITES**

Synthesis of [HNT-(PS-co-PMMA)] nanocomposites via ultrasound-assisted emulsion polymerization takes place in two steps. In the first step, modified HNTs is mixed with styrene in the presence of ultrasonic irradiations which aids in obtaining the exfoliated structure. High shear levels along with intense turbulence generated due to the cavitation result in exfoliation of agglomerated HNTs into single platelets, which eases their dispersion into the monomer (Borthakur et al. 2010). This effective blending of clay with monomer results into stable emulsion without phase separation (Sun et al. 2004). In the second step, OH group of SDS gets adsorbed on the edges of the HNT. The polar carboxyl groups of the styrene and methyl acrylate interact with the polar groups ( $\text{OH}^-$ ) present on HNTs (Landfester 2006). The interaction between the polar groups leads to a formation of stable emulsion droplets of monomers containing clay due to reduction of Oswald ripening process (Webster and Cates 1998). At the time of polymerization, radicals present either due to dissociation of the initiator at higher temperature or by adiabatic implosion of cavities due to the sonication (Cao et al. 2008). These primary radicals that are produced by the dissociation of cavitating bubbles further react with the monomer molecules at the interface between the cavitation bubble and solution interface and produce additional radicals. These radicals along with the reduced diffusion resistance as a result of turbulent conditions initiate and enhances the polymerization (Teo et al. 2008). Also, there is a reduction in diffusion resistance due to acoustic cavitation; this enhances the micro-vortex motion of ingredients leading to stirring effects in the reaction medium. Further, the polymerization of MMA with a styrene monomer takes place around the HNTs which contributes to the exfoliation of nanocomposites leading to exfoliated structure of [HNT-(PS-co-PMMA)] nanocomposite.

### **6.4.1 Studies on the structure of [HNT-(PS-co-PMMA)], [CHNT-(PS-co-PMMA)] and [MHNT-(PS-co-PMMA)] nanocomposites**

XRD analysis of the samples could provide information on changes in interlayer spacing of clay layers in nanocomposites. From Fig. 6.9 curve (a) it can be observed that a significant peak appears at  $2\theta$  value of  $11.4^\circ$  which indicates an interlayer

spacing of 7.78 Å as calculated using Bragg's law. Curve b (Fig.6.9) represents the PS-co-PMMA copolymer. Here the presence of a broad peak indicates the synthesized copolymer is amorphous. Curve (c) shows a result corresponding to nanocomposite which was fabricated without using ultrasound. In curve (c), the presence of peaks represents the filler could not be exfoliated into the polymer whereas those peaks disappears in curve (d) which correspond to nanocomposite sample prepared with ultrasound. From XRD spectra, it can be conjectured that in presence of ultrasonic irradiations at a sonication time of 60 min, complete exfoliation of HNTs into the polymer matrix is achieved. The formation of exfoliated structure is due to complete loss of registry between clay layers and hence no peak is observed in XRD trace. Therefore, the use of ultrasound plays a vital role in the dispersion and exfoliation of clay in polymer matrix.

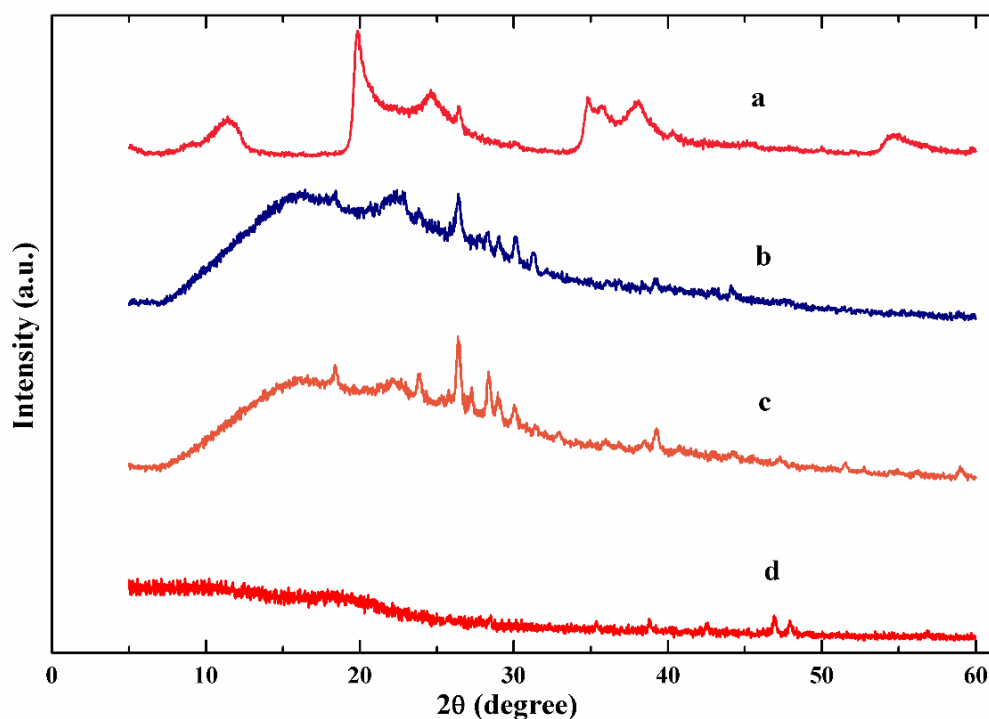


**Figure 6.8 XRD analysis of (a) HNT (b) PS-co-PMMA (c) [HNT-(PS-co-PMMA)] synthesized without ultrasound (d) [HNT-(PS-co-PMMA)] synthesized with ultrasound**

#### 6.4.2 Studies on morphology of [HNT-(PS-co-PMMA)], [CHNT-(PS-co-PMMA)] and [MHNT-(PS-co-PMMA)] nanocomposites

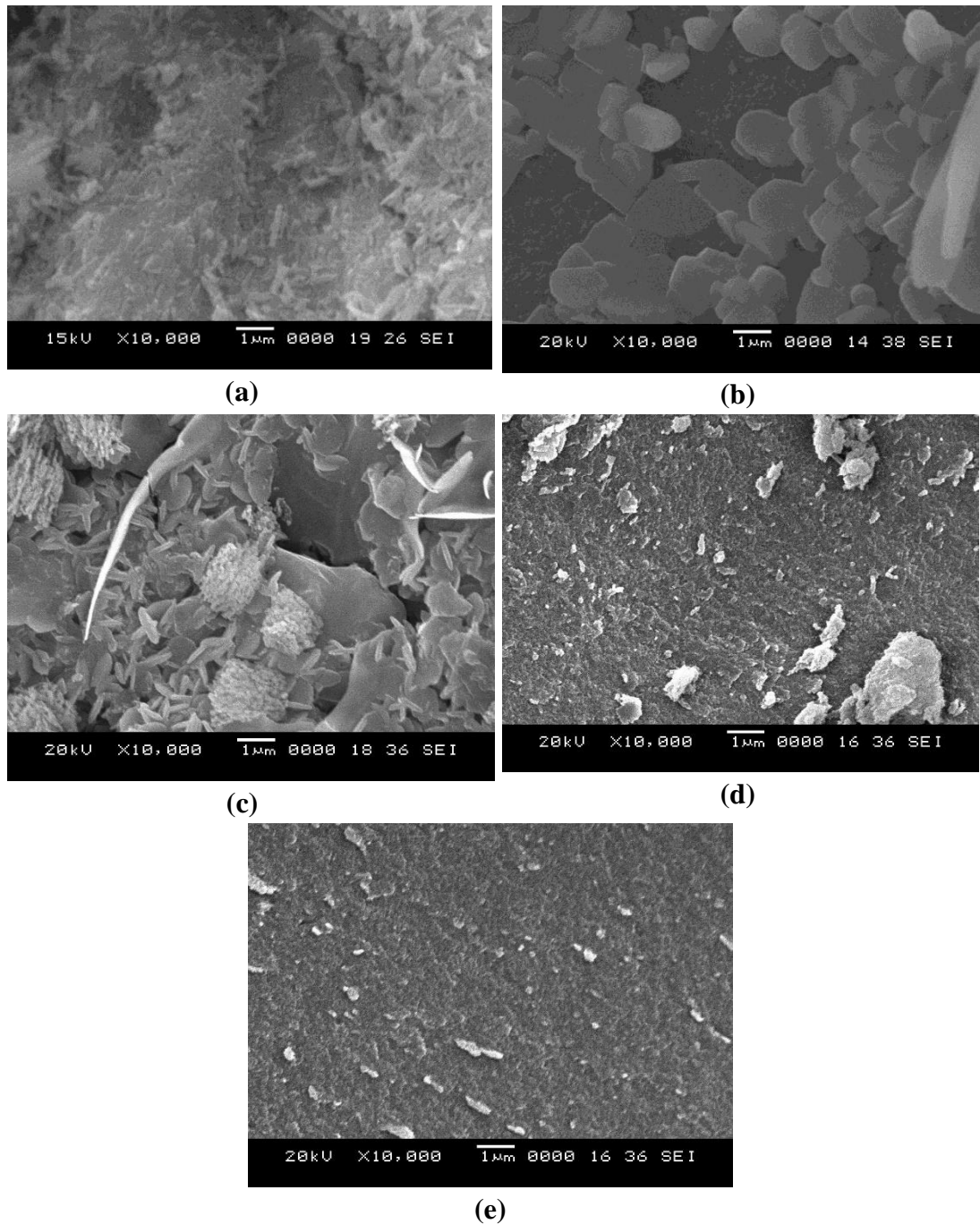
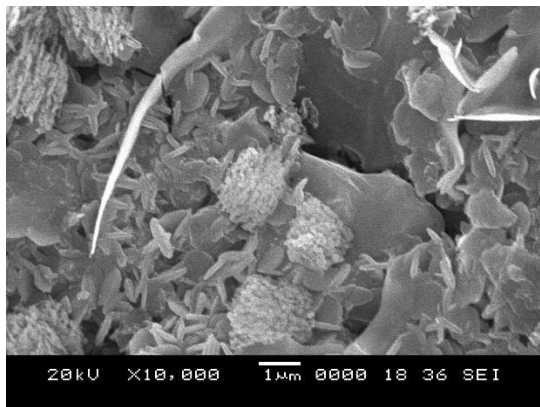


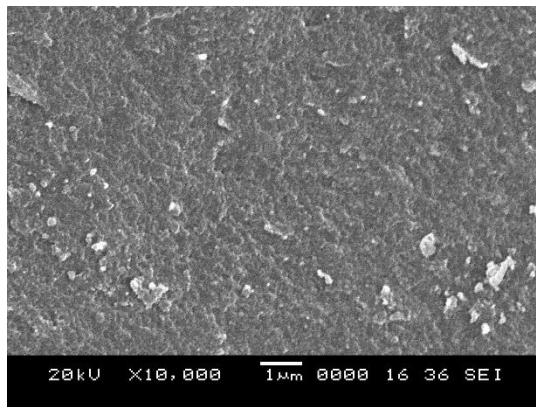
Figure 6.9 SEM images of (a) HNTs (b) PS-co-PMMA (c) [HNT-(PS-co-PMMA)] without ultrasound (d) [HNT-(PS-co-PMMA)] with ultrasound for **30 min** (e) [HNT-(PS-co-MMA)] with ultrasound for **60 min**

SEM was performed to examine the dispersion of HNT in the polymer matrix and surface morphology of the nanocomposites. Figs. 6.10 (a & b), shows the SEM image of HNTs and copolymer respectively. As shown in the picture (Fig 6.10a), the size of filler material was in nanoscale, and the particles were rod-shaped particles. Fig. 6.10c shows the nanocomposite which was synthesized without the use of ultrasound. It shows a lot of agglomerations and uneven distribution of filler particles in the polymer matrix. Fig. 6.10d shows a sample obtained after 30 *min* sonication time, in this sample, the particles are not sequenced well into polymer matrix due to insufficient sonication time. All the composite samples shown contain 5 *wt %* HNT content. Fig. 6.10e corresponds to a sample obtained after a sonication time of 60 *min*. It reveals that uniform dispersion of HNTs in polymer is achieved as it also promotes proportionate distribution of filler into the polymer matrix. The nanocomposite synthesized by subjecting to ultrasound for 60 *min* had a smooth surface without any agglomerations and had mono-dispersed morphology, and hence 60 *min* seems to be optimum for in-situ synthesis of nanocomposites.

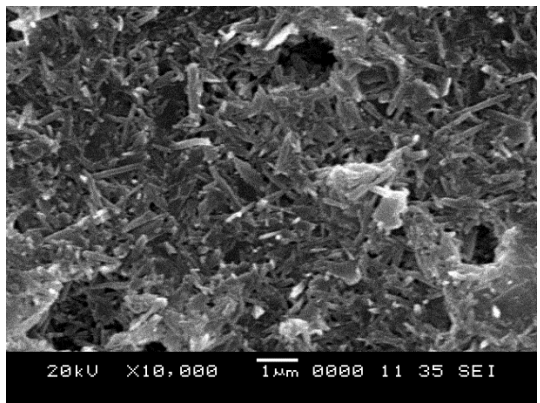
To have a detailed understanding on the effect of sonication and modification of HNTs on the morphology of nanocomposites SEM analysis was carried out and represented in Fig. 6.11 (a to f). It can be observed that incorporation of CHNTs and MHNTs into the copolymer matrix resulted in homogeneous dispersion of HNTs. This was because the modified HNTs exhibited better interaction with polymer. It can be observed that the HNT layers are finely dispersed in the PS-co-PMMA latex giving rise to the exfoliated structure of [HNT-(PS-co-PMMA)] nanocomposite. In contrast, to [HNT-(PS-co-PMMA)] nanocomposite images which were synthesized without use of ultrasound (Fig. 6.11a, c and e), which shows insufficient mesoscale HNTs distribution in the nanocomposite, possibly due to inadequate mixing, the Figs (6.11b, d, and f) show the presence of well dispersed HNTs in the polymer latex. This better dispersion can be attributed to the reduction in initial monomer droplet size obtained by ultrasonic irradiation, and improvement in the dispersion of HNTs platelets in the polymer matrix due to the continuous ultrasonic irradiation.



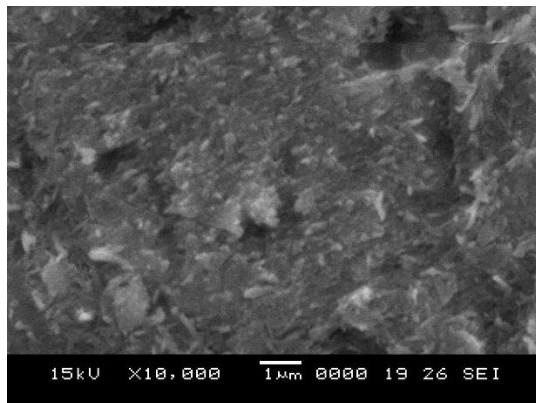
(a)



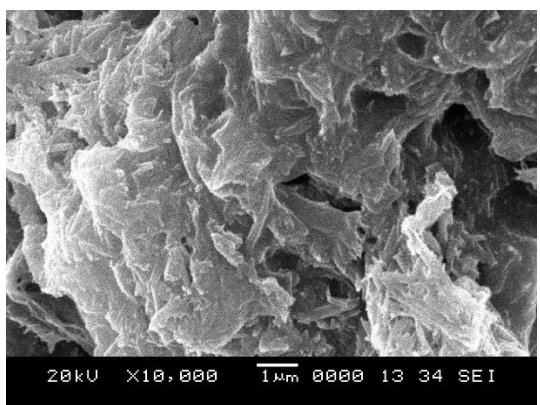
(b)



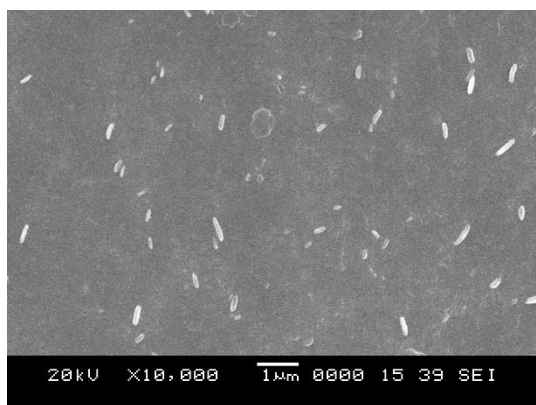
(c)



(d)



(e)



(f)

**Figure 6.10 SEM images of (a) [HNT-(PS-co-PMMA)] without ultrasound, (b) [HNT-(PS-co-PMMA)] with ultrasound, (c) [CHNT-(PS-co-PMMA)] without ultrasound, (d) [CHNT-(PS-co-PMMA)] with ultrasound, (e) [MHNT-(PS-co-PMMA)] without ultrasound, and (f) [MHNT-(PS-co-PMMA)] with ultrasound**

### 6.4.3 Studies on functional groups of HNT-(PS-co-PMMA), CHNT-(PS-co-PMMA) and MHNT-(PS-co-PMMA) nanocomposites

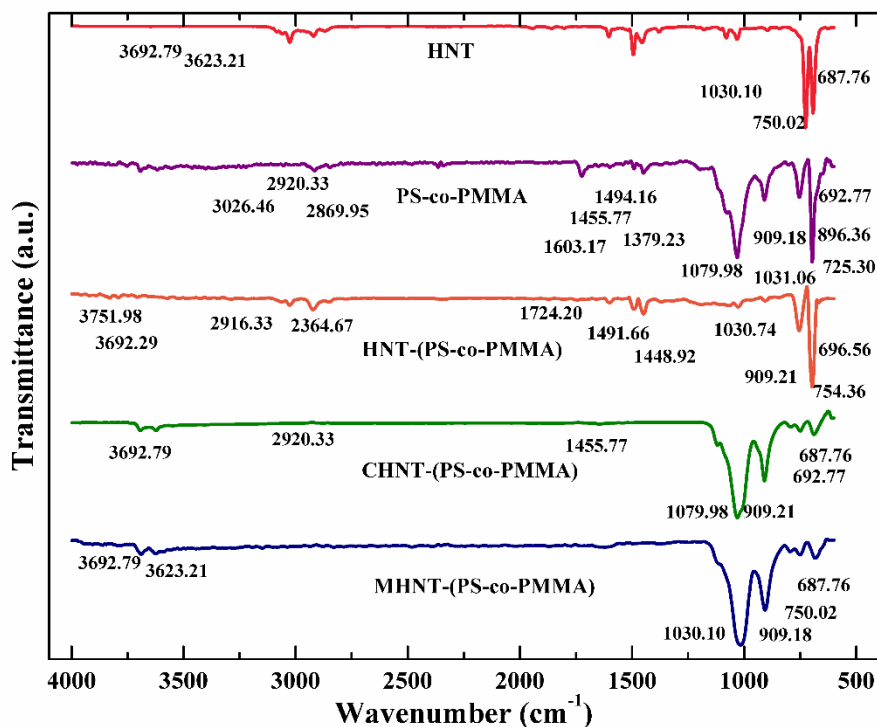


Figure 6.11 FT-IR analysis of, PS-co-PMMA, [HNT-(PS-co-PMMA)], [CHNT-(PS-co-PMMA)], and MHNT-(PS-co-PMMA)

Figure 6.12 presents the results of FT-IR analysis on HNTs, PS-co-PMMA copolymer and [HNT-(PS-co-PMMA) nanocomposite (5 wt% HNT content and 60 min of sonication) samples. The peak at  $3751\text{ cm}^{-1}$  (in both HNT and nanocomposite) corresponds to the stretching of OH in silicate layers. The Si-O stretching vibration of silicate layer is indicated by a sharp peak at  $1030.74\text{ cm}^{-1}$  (in both HNT and nanocomposite). The stretching of Al-O and bending of Si-O in nanocomposite are indicated by peaks at  $754.36\text{ and }696.56\text{ cm}^{-1}$  respectively. The presence of signature of major peaks corresponding to HNTs and copolymer in the synthesized nanocomposite indicates the presence of HNTs in the copolymer matrix, and hence, FT-IR confirms the successful incorporation of HNT into the polymer matrix. Also, the major absorption peaks of MHNT (Fig. 4.6) MHNT displayed a new FT-IR band at  $1467\text{ cm}^{-1}$  which is assigned to the scissoring of  $(\text{CH}_2)_3$ . Wavenumbers at  $2925\text{ cm}^{-1}$  can be assigned to C-H stretching vibration, respectively. The absence



of a band at  $1700\text{ cm}^{-1}$  and the appearance of OH vibration bands at  $3624$  and  $3694\text{ cm}^{-1}$  suggest that hydrogen bonds could not be formed between HNTs and  $\gamma$ -MPS as OH groups of HNTs were not easily accessible for modification. The presence of MHNT major absorbance peaks in PS-co-PMMA spectrum can be seen in Fig. 6.12 which confirms the existence of MHNT inside the latex particles and indicates encapsulation of MHNTs into the final nanocomposites. Thus from FT-IR study, we may infer successful incorporation of MHNT in the PS-co-PMMA copolymer matrix.

#### **6.4.4 Studies on thermal stability of [HNT-(PS-co-PMMA)], [CHNT-(PS-co-PMMA)] and [MHNT-(PS-co-PMMA)] nanocomposites**

The thermal properties of nanocomposites were investigated by DSC analysis. DSC investigates the effects of heat on phase transitions and chemical reactions with respect to temperature. Glass transition temperature ( $T_g$ ) of polymers is the temperature at which amorphous friable polymers gets converted to rubbery kind of material and becomes flexible. Inclusion of HNTs into the polymer matrix can enhance the thermal stability of polymers for the following reasons. Primarily, HNTs possess higher thermal stability compared to polymers as the degradation temperature of HNT starts at approximately  $400\text{ }^\circ\text{C}$ . Secondly, the uniform dispersion of HNTs into the polymer matrix makes sure an increased barrier to heat and mass transports. Lastly, the presence of lumens in the HNTs provides a room for polymer chains as well as degradation products to occupy the lumens space which results in delayed mass transport which in turn increases the thermal stability. As per the results of DSC, the  $T_g$  of synthesized copolymer was  $95\text{ }^\circ\text{C}$ , and the  $T_g$  of copolymer containing  $3\text{ wt}\%$ ,  $5\text{ wt}\%$ , and  $10\text{ wt}\%$  were  $150$ ,  $120$ , and  $109.84\text{ }^\circ\text{C}$ , respectively.

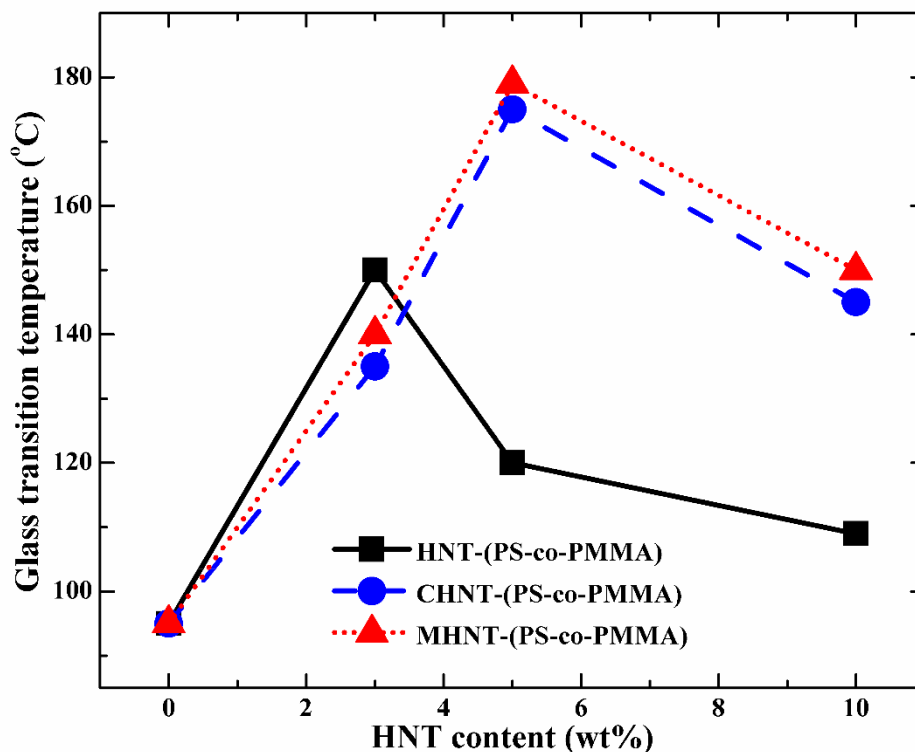


Figure 6.12 DSC analysis of [HNT-(PS-co-PMMA)], [CHNT-(PS-co-PMMA)] and [MHNT-(PS-co-PMMA)] nanocomposites

The increase or decrease in  $T_g$  of the polymer varies monotonically with increasing nanofiller content. As already mentioned the increase in  $T_g$  is believed to occur due to confinement of the intercalated polymer chains between the sheets in the interlayers of HNTs, which prevents the segmental motions of the polymer chains. As shown in Fig. 6.13, there was an increase in  $T_g$  up to 3 wt% filler loading whereas any further increase in HNT content resulted in a decrease in  $T_g$ . One of the reasons which cause decrease in  $T_g$  at higher filler loadings compared to other samples might be due to non-uniform alignment of HNTs in the polymer matrix which ended up in the aggregation of particles and hence, decreased the thermal stability relatively. From these results, the thermal properties of [HNT-(PS-co-PMMA)] nanocomposites can be considerably enhanced at 3wt % loading that seems to be optimum. It can also be seen in Fig. 6.13 that there was improvement in the thermal stability of nanocomposites of modifying the surface of HNTs. This is again attributed to the better interaction between the polymer and HNTs.

#### 6.4.5 Studies on particle size and zeta potential analysis of [HNT-(PS-co-PMMA)] copolymer with different HNT content (wt%)

Table 6. 3 Particle size and zeta potential of nanocomposites

Sample	D (nm)	L (nm)	PDI	$\zeta$ (mV)	E (cm <sup>2</sup> /Vs)	C (mS/cm)
PS-co- PMMA				-123.2	-0.000956	0.119
1 wt % HNT	50.3	204.8	0.289	-116.6	-0.000811	0.180
3 wt % HNT	69.5	258.9	0.313	-108.9	-0.000844	0.220
5 wt % HNT	93.9	1056	0.376	-86.1	-86.1	0.421
7 wt % HNT	73.9	-	0.426	-92.9	-92.9	0.541
10 wt % HNT	111.4	-	0.371	-106.4	-106.4	0.239
Without sonication	68.3	5510	1.588	-99.2	-0.000768	0.652

\*D-Diameter, L-Length,  $\zeta$ -Zeta potential, E-Electrophoretic mobility, C-Conductivity

Particle size analysis and zeta potential analysis was carried out, and the results are displayed in Table 6.3. Particle size analysis displayed two peaks representing the diameter and lengths of HNTs respectively. Nanocomposites which were synthesized with the aid of ultrasound had particles with diameters ranging between 69.5 – 111.4 nm and the length ranging from 258.9 to 1056 nm as seen in Table 6.3. Whereas composites synthesized without use of ultrasound had particles with diameter of 68.3 nm and average length of 5510.8 nm. This is due to agglomeration of particles

as these particles are hydrophilic. Also the polydispersity index is 1.544, which represents a broad range of particle distribution. Particle size analysis clearly explains the role of ultrasound in dispersion of particles in the copolymer, the acoustic cavitations generated during sonication aids in breaking agglomerates of hydrophilic particles and hence results in sequential distribution of particles without any surface modification of particles. Zeta potential provides information on the stability of emulsion; it explains the ability of emulsion to resist changes in its physiochemical properties with time, particles interact with each other according to magnitude of zeta potential.

From Table 6.3, it can be seen that the stability of copolymer was  $-123.2\text{ mV}$ , whereas on addition of HNTs into the polymer matrix there was an increase in stability of polymer latex as HNTs have charged surfaces and can aid in stabilizing the emulsion. Electrophoretic mobility is movement of dispersed particles with respect to surrounding fluid under the influence of electric field. The electrophoretic mobility increases with increase in charge and decrease in the size of particles, hence it can be seen that the electrophoretic mobility increases on addition of HNTs due to the charges present on the surface of HNTs.

## 6.5 SUMMARY

Herein, the synthesis of HNT-PS, HNT-PMMA and [HNT-(PS-co-PMMA)] using pristine and modified HNT by ultrasound-assisted emulsion polymerization is reported. It was found that the polarity and hydrophilicity of the monomers greatly affect dispersion of the HNT in polymer matrix. In comparison with conventional emulsion polymerization technique, ultrasound-assisted polymerization resulted in generation of free radical due to cavitation and also aided in fast dissociation of initiator to free radicals. Additionally, on use of ultrasound for the process, HNT particles are dispersed more uniformly. During sonication, it was observed that there was increase in the viscosity of the monomer-HNT mixture and gelation occurred which indicated network formation by the disruption and dispersion of clay aggregates.

The surface of HNT was modified successfully with surfactant (CTAB) and silane ( $\gamma$ -MPS). Modification of HNTs showed improvement in dispersion of HNT in

the polymer matrix thereby improving thermal properties of nanocomposites. Barrier properties showed increasing trend in improvement with the increase in clay loading. And better dispersion of clay due to modification improved barrier properties to a significant extent. Also, the addition of 5 wt% HNT content HNT content was optimum, and higher HNT content resulted in agglomeration. XRD results showed a slight increase in the basal spacing, and the composite was a mixture of intercalated as well as exfoliated structure for all polymers. The modification of HNTs results in better HNTs separation and a more disordered intercalated nanocomposite. This is because of favorable interactions of the HNTs with the monomer. Introducing polymerizable groups onto the HNTs surface improves the dispersion of clay significantly and mixed (intercalated and exfoliated) HNT-polymer nanocomposites were obtained. The presence of HNTs can substantially improve the dimensional stability of the polymer matrix in an exfoliated nanocomposite with uniform mesoscale clay dispersion. CTAB has been employed for surface modification of clays as it has long hydrophobic alkyl chain which shows good compatibility towards organophilic polymer. Also, along with long alkyl chain structure, sonication also plays a great role in increasing the gallery space between the HNT interlayers. There are apparently two steps of dispersion and distribution of HNTs in the polymer matrix. The first step is nanoscale dispersion, which involves layer separation of the HNTs. Here, the physical interaction, as well as chemical compatibility among modified HNT surface and intercalated compound, determines the degree of increase in layer spacing. The second step involves the mesoscale distribution of HNTs where the disruption of HNT aggregates and primary particles take place. This requires interaction of HNTs with the polymer matrix which depends on the mixing strength. The CTAB modified clay was more effective in promoting mixed structure in polymer. This depicts the role of ammonium salt (modifier) on the structure of nanocomposites.

## CHAPTER 7

### ULTRASOUND-ASSISTED SYNTHESIS OF HNT-PS, HNT-PMMA, [HNT-(PS-co-PMMA)] NANOCOMPOSITES BY MINIEMULSION POLYMERIZATION

*This chapter reports the results on characterization of HNT-polymer nanocomposites by ultrasound mini-emulsion polymerization technique. Pristine HNTs and modified HNTs were used as reinforcement in polymer, and the effect of surface modification and sonication on structure, morphology, functional groups and thermal stability were investigated and reported.*

#### 7.1 INTRODUCTION

The synergetic properties of polymer nanocomposites have attracted extensive research around the world. End properties of nanocomposites greatly rely on filler properties, preparation techniques and polymer chemistry (Zhao and Liu 2008). Therefore in this chapter, report on the synthesis of HNT-polymer nanocomposites by ultrasound-assisted miniemulsion polymerization using pristine HNTs and HNTs modified with  $\gamma$ -MPS is presented. Polymer nanocomposites produced by miniemulsion polymerization route belongs to family of heterophase polymerizations where the formation of functionalized polymers or modification of polymers occurs in stable nanodroplets (Crespy and Landfester 2010). Miniemulsion polymerization has the potential to create nanoparticles which can be continuously dispersed in aqueous phase for encapsulation and hence it is considered advantageous over other methods of synthesis (Moraes et al. 2006). Miniemulsions are relatively stable aqueous dispersions that are dispersed as mini-droplets with a size ranging from 50 to 500 nm. They are fabricated at high shears in a system containing oil, water, and surfactants. A compound which is highly insoluble in water such as hexadecane is employed as co-surfactant to impede Ostwald ripening of the droplets and aids in attaining particles in aspired size range. Composition of oil phase and incorporation of hydrophobic compounds are the prominent features of miniemulsion polymerization (Landfester et al. 1999). This method is environmentally favorable as it exempts use of volatile organic solvents.

Miniemulsion polymerization carried out with assistance of ultrasound is another way to extend the advantages of this route. In recent years, ultrasound has been widely used in polymer particle synthesis due to its outstanding contributions. High intensity ultrasound is capable of dissociating surfactant, monomer and solvent molecules and providing free radicals required for polymerization. Hence, free radical polymerization reaction rates can be enhanced by the assistance of ultrasound. Utilising ultrasound for preparation of miniemulsions is promising as the acoustic cavitations generated during sonication results in enormous high temperatures, pressures and rigorous environment and hence initiates chemical reactions (Lii et al. 1999). Under these extreme conditions, free-radicals are generated due to decomposition of monomer, water, surfactant, or rupture of polymer chains which initiates polymerization.

Uniform dispersion of nanofillers, and its interaction with the polymer matrices plays a very crucial role in determining the overall properties of nanocomposites, one way to achieve this is to modify the surface of filler with small organic molecules or polymers, which in-turn improves the physical and chemical properties of nanosurfaces (Bansal et al. 2006). Surface chemistry plays an important role in the overall performance of nanoparticles, better understanding of the surface chemistry of filler and its modification helps to improve their performance and to develop new applications. Also, the presence of covalent bonds between the nanofillers and polymer matrices could considerably improve thermomechanical properties of the resulting polymer nanocomposites. HNTs have a different structure on their outer and inner lumen surfaces. HNTs' inner lumen surface consists of Al-OH octahedral sheet, and outer surface consists of Si-O-Si groups. Therefore the inner surface of HNTs is chemically active, and the outer surface is regarded as nonreactive. However, some hydroxyl groups (Al-OH or Si-OH) existing on external surfaces within the edges and defects provide active sites for chemical reactions.

Hence, herein successful synthesizes HNT-polymer nanocomposites by ultrasound-assisted miniemulsion polymerization is presented. Styrene, methylmethacrylate, and copolymer of styrene and methylmethacrylate were used as monomers. Pristine HNTs and HNTs modified with  $\gamma$ -MPS were used as fillers in

polymers. Sonication, modification of HNTs and HNT content are the parameters which affect the stability of mini-emulsion, hence the effect of these parameters on structure, morphology, functional groups and thermal properties of the synthesized nanocomposites were studied in detail. These nanocomposites can be used for applications such as commercial packings of edibles, barrier coatings, and pharmaceutical purposes.

## **7.2 SYNTHESIS OF HNT-POLYSTYRENE (HNT-PS) NANOCOMPOSITES**

Nanocomposites synthesis techniques plays a major role in overall property enhancement. In this section the reinforcement of pristine HNT and MHNTs into polystyrene by ultrasound-assisted miniemulsion polymerization is reported. A detailed understanding on effect of surface modification on increasing interaction between polymer and HNTs and improvement in thermal stabilities of the resulting nanocomposites has been reported in this section.

HNTs are dispersed in monomer mixture with the help of sonication. These monomers are absorbed by HNT layers. Subsequently, the monomer covered HNT particles are dispersed in water in presence of Span-60 and SDBS. This stabilizes the dispersion due to non-ionic–ionic (Span-60–SDBS) surfactant mixture. When this dispersion is subjected to sonication polymerization is initiated as cavitations generated during sonication produces rigorous conditions in terms of high temperature and pressure within the cavity. Additionally the presence of the surfactant mixture exfoliates HNTs. Polymerization was conducted in the presence of AIBN initiator at 70 °C. Polymerization yields spherical shaped polymer particles in nanosize.



### 7.2.1 Studies on structure of HNT-PS and MHNT-PS nanocomposites synthesized by ultrasound-assisted miniemulsion polymerization

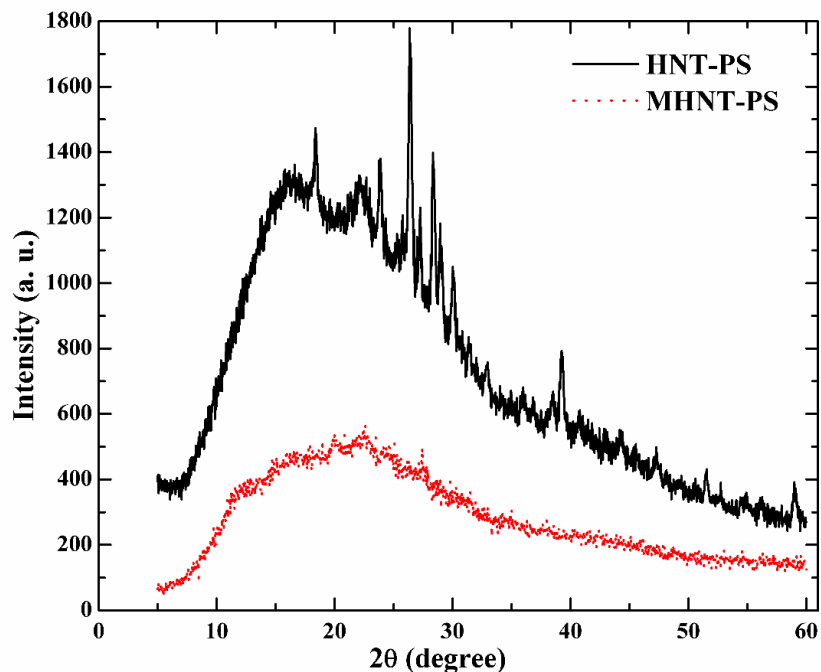


Figure 7.1 XRD image of (a) HNT-PS, and (b) MHNT-PS nanocomposites synthesized by ultrasound-assisted miniemulsion polymerization

Figure 7.1 shows the diffraction patterns of nanocomposites synthesised using HNT and MHNT. It can be observed that nanocomposites synthesised on using MHNT showed a drastic decrease in sharp peaks and intensity relative to pristine HNT. This indicates complete exfoliation of HNTs into the polystyrene matrix thus suggesting improved properties and clearly confirms the formation of nanocomposites. The better exfoliation of HNTs on modification with silane indicates a ‘polarity match’ with the HNT surface and results in favorable interaction of MHNTs and PS. This clearly explains the role of HNTs modification on formation of nanocomposites. The presence of broad peak indicated the amorphous nature of polymer. Additionally, the high shear effect of ultrasonic irradiation during polymerization aids in exfoliation of HNTs into the polystyrene. HNTs exfoliates in the polymer matrix as result of large spacing between the layers due to cavitation jet effect. Thus XRD analysis confirms that the intense energy produced during sonication along with modification of HNTs aids in forming completely exfoliated structure.

### 7.2.2 Studies on morphology of HNT-PS, and MHNT-PS nanocomposites synthesized by ultrasound-assisted miniemulsion polymerization

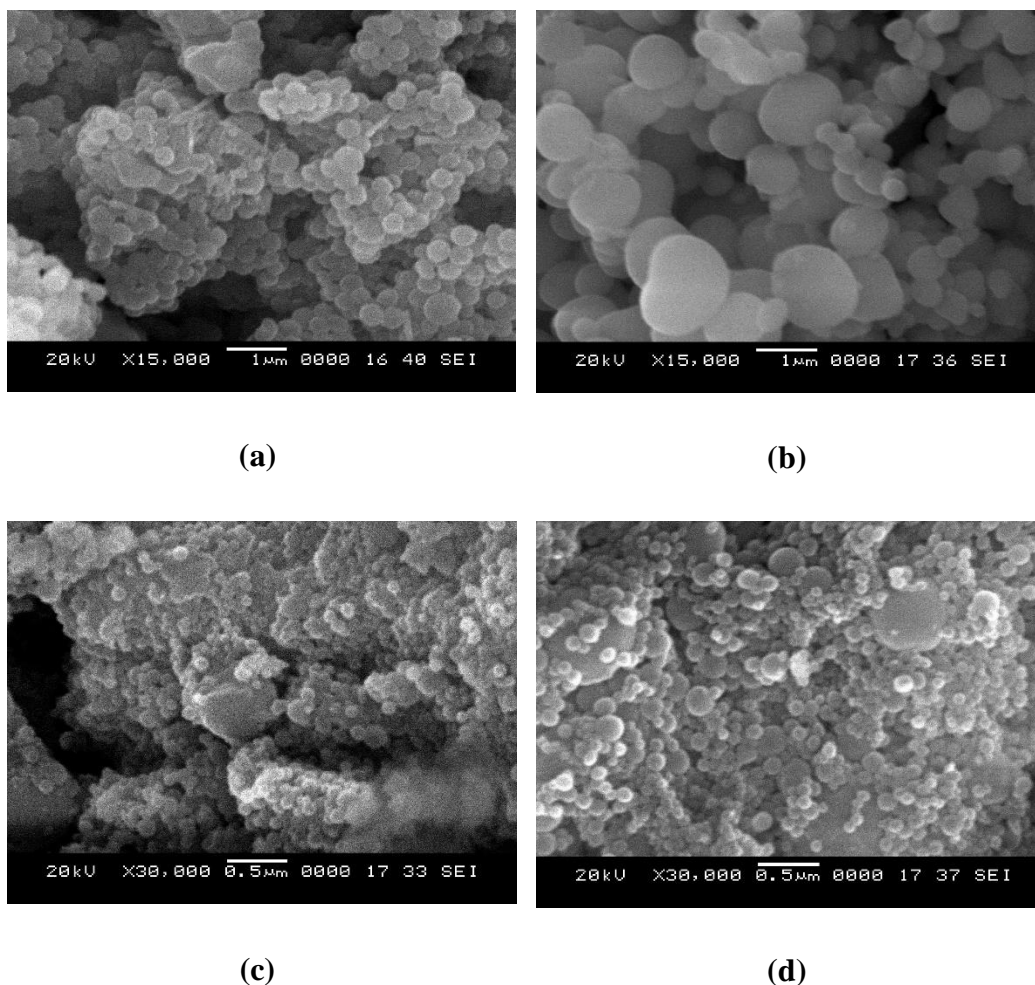


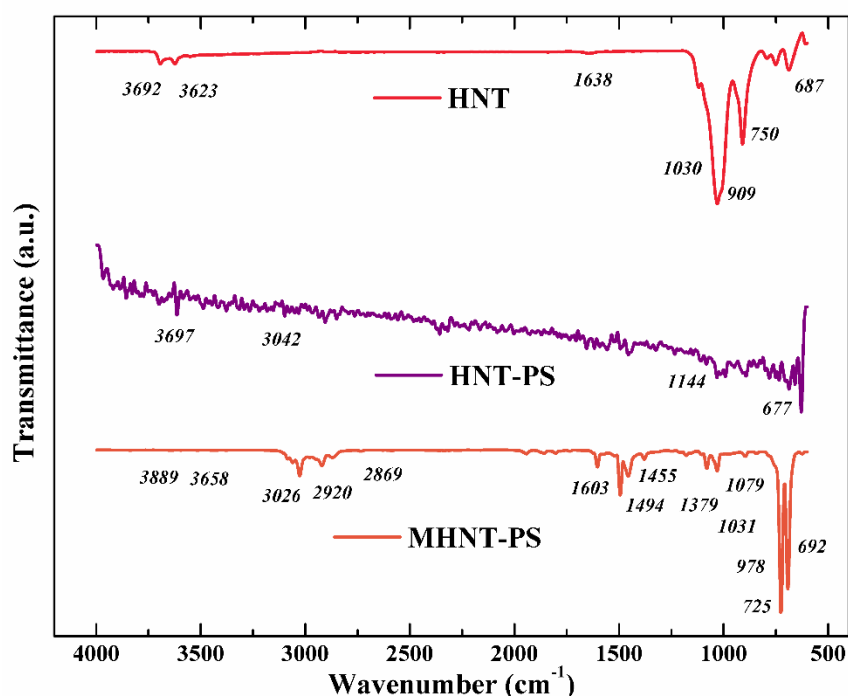
Figure 7.2 SEM portraits of (a) HNT-PS without ultrasound, (b) HNT-PS with ultrasound, (c) MHNT-PS without ultrasound, and (d) MHNT-PS with ultrasound

Figure 7.2 shows the SEM image of HNT-PS and MHNT-PS nanocomposites synthesised by miniemulsion polymerization with and without sonication to understand the effect of sonication on the morphology of synthesised nanocomposites. It could be observed from Fig. 7.2b that on using ultrasound for synthesis of particles, the number of particles will increase considerably due to the reduction in the size of droplets. This decrease in the size of the nanocomposite is due to the reduction in initial monomer droplet size as a result of sonication, and improvement in the dispersion of HNTs in the polymer matrix due to the continuous ultrasonic irradiation. Also, the rate at which

radicals are generated is directly proportional to the number of cavitation bubbles which depends on the acoustic intensity (Price et al. 1992). Therefore, it can be observed that the size of the particles as well as agglomerations has reduced on utilising ultrasound for carrying out the reaction.

It can also be further observed that on using MHNTs for fabrication of MHNT-PS nanocomposites there was further decrease in the particle size. Modification of HNTs with silane resulted in better dispersion of particles as the modification increases the interactions with the styrene monomer and the degree of dispersion of the HNTs in the polystyrene matrix. Hence, it can be seen from Fig. 7.2d that particle size as well as agglomerations have reduced.

### 7.2.3 Studies on functional groups of HNT-PS, and MHNT-PS nanocomposites synthesized by ultrasound-assisted miniemulsion polymerization



**Figure 7.3 FT-IR analysis of HNT, HNT-PS and MHNT-PS nanocomposites synthesized by ultrasound-assisted miniemulsion polymerization**

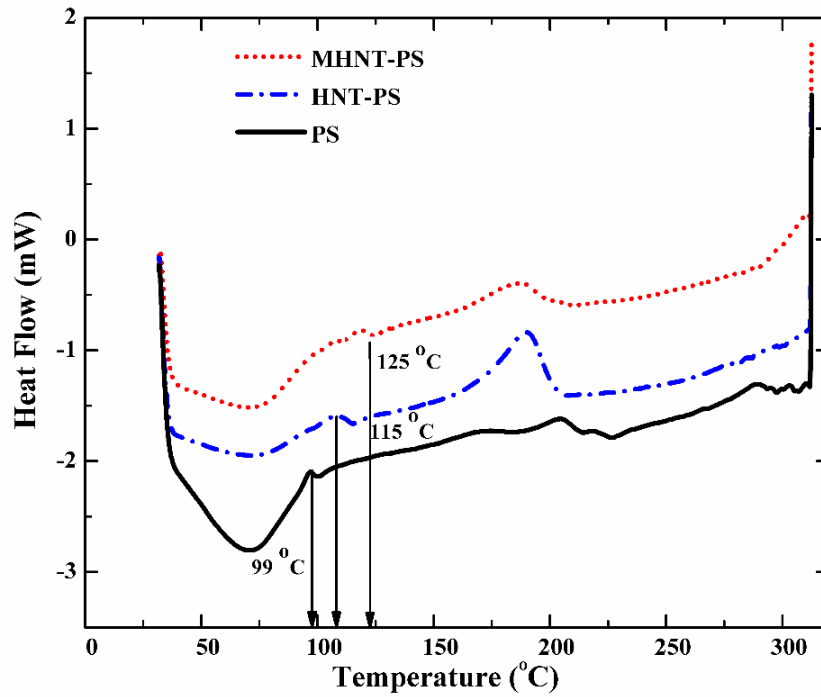
FT-IR analysis of HNT-PS and MHNT-PS was analyzed to understand about the functional groups of the nanocomposites. It was observed from Fig. 7.3 that the nanocomposites which was synthesized using pristine HNT clearly demonstrates the existence of HNT major absorbance peaks in polystyrene spectrum which proves the

existence of clay inside the latex particles and indicates encapsulation of HNTs into the final nanocomposites. However, the peak at  $3692\text{ cm}^{-1}$  shifts to  $3697\text{ cm}^{-1}$  in the nanocomposite attributes to the interaction of Al layer of HNT with the polystyrene surface. Thus from FT-IR study we may infer successful incorporation of HNT in the polymer matrix.

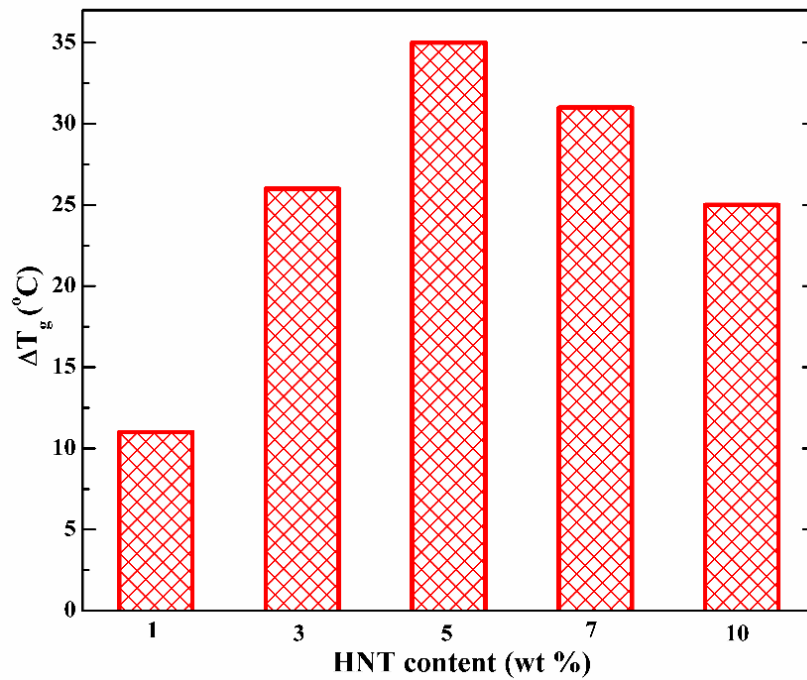
Further, the major absorbance peaks of MHNT can be observed from Fig. 4.6. It can be observed that the band at  $912\text{ cm}^{-1}$  for MHNT was shifted to  $978\text{ cm}^{-1}$  for MHNT-PS. This can be attributed to the interaction of OH group inside the HNT lumen, indicating the penetration of  $\gamma$ -MPS into the HNT interlayers. Additionally, the considerable reduction in the intensity of the bands at  $3623.47\text{ cm}^{-1}$  and  $3693.56\text{ cm}^{-1}$  is related to the appearance of new bands at  $2920\text{ cm}^{-1}$  and  $2869\text{ cm}^{-1}$ . This indicates the reaction between hydroxyl groups inside the lumen with PS. Thus the FT-IR suggests the presence of MHNT inside the PS matrix.

#### **7.2.4 Studies on thermal stability of HNT-PS, and MHNT-PS nanocomposites synthesized by ultrasound-assisted miniemulsion polymerization**

It can be seen from Fig. 7.4 that there was increase in  $T_g$  on inclusion of HNT into polymer matrix.  $T_g$  of virgin PS and HNT-PS were estimated to be  $99\text{ }^\circ\text{C}$  and  $115\text{ }^\circ\text{C}$  respectively, whereas  $T_g$  of MHNT-PS was  $124\text{ }^\circ\text{C}$ . PS-MHNT nanocomposites showed higher  $T_g$  than that of pure PS and HNT-PS, the  $T_g$  is evidently improved.



(a)



(b)

**Figure 7.4 DSC thermograms of (a) PS, HNT-PS, and MHNT-PS (b) PS with different wt% HNT nanocomposites synthesized by ultrasound-assisted miniemulsion polymerization**

Functionalization improves intercalation of polystyrene chains between the layers due to incorporation of appropriate organic links between the polystyrene matrix and the HNTs. Also, there is reduction in surface energy of silane treated clay which facilitates macromolecule access between the layers of HNTs which restricts the movement of intercalated polystyrene chains between the sheets of the HNT, which prevents the segmental motions of the polystyrene chains and increases thermal properties.

### 7.2.5 Studies on particle size and zeta potential of HNT-PS and MHNT-PS of nanocomposites synthesized by ultrasound-assisted miniemulsion polymerization

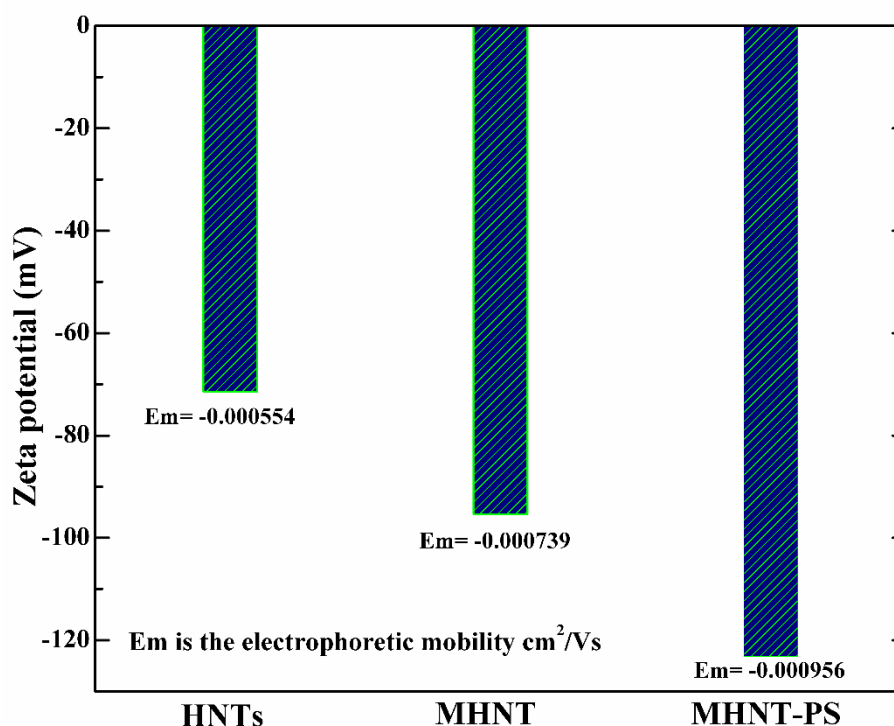


Figure 7.5  $\zeta$ -potential of HNTs, MHNTs, and MHNT-PS latex synthesized by ultrasound-assisted miniemulsion polymerization

It can be observed from Fig. 7.5 that the zeta potential value of the neat HNTs was  $-71.5$ , whereas on modification of HNTs the stability increased to  $-95.4$  mV. The synthesis of PS-MHNTs caused increase in latex stability. This is due to self-arrangement of the MHNT within the polymer particles which inturn influences the surface tension of latex and stabilizes the latex.

### **7.3 SYNTHESIS OF HNT-POLYMETHYLMETHACRYLATE (HNT-PMMA) NANOCOMPOSITES**

Polymethylmethacrylate (PMMA) nanoparticles have been widely used for various applications in the field of nanotechnology. It has excellent optical properties like clarity and transparency; it is chemically inert, easy to handle, weather resistant; it holds good mechanical and electrical properties, thermal stability, and can be easily molded (Silva et al. 2010). However, PMMA has poor heat resistance and flexural strength, brittle and susceptibility to cyclic loading which limits its applications in various fields. This limitation can be tackled by reinforcing filler into the polymer matrix. Inorganic fillers in polymer matrices has attained great research interest in recent years as these materials not only reduce the cost for polymer based products but also enhances various polymer properties.

In this section synthesis of HNT-PMMA nanocomposites by miniemulsion polymerization assisted by ultrasound is reported. The objective is to synthesize polymer nanoparticles with desired size and enhanced properties to make it compatible for various applications. Sonication, modification of HNTs and HNT content are the key parameters which can affect the properties of the resulting nanocomposites and hence, their effect was investigated and presented.

#### **7.3.1 Studies on structure of HNT-PMMA, and MHNT-PMMA nanocomposites synthesized by ultrasound-assisted miniemulsion polymerization**

Figure 7.6 shows the diffraction patterns of PMMA nanocomposites synthesized using HNTs and MHNTs. Most of the interlayer inner-surface Al-OH groups of HNT were unavailable for modification as they were blocked by the strong hydrogen bonds between layers. However, as seen in Fig. 4.4 (Chapter-4), there was a slight increase in the d-spacing of the HNTs upon modification with  $\gamma$ -MPS, indicating slight intercalation of  $\gamma$ -MPS into the interlayer of HNTs. This is possible because of the sonication, which generates high temperatures and pressures, and a rigorous environment for intercalation to occur. In addition, the intense energy produced during sonication exfoliated HNTs into the polymer. Hence, it can be observed from Fig. 7.6 that the nanocomposite synthesized using MHNTs showed a drastic decrease in peak sharpness and intensity compared with the HNT-PMMA nanocomposite. This indicates

complete exfoliation of MHNTs into the polymer and thus improved properties of the nanocomposite. Therefore, the combination of surface modification of HNTs along with sonication helped with fabrication of completely exfoliated HNT-PMMA nanocomposites. The presence of the broad peak indicates the amorphous nature of the polymer.

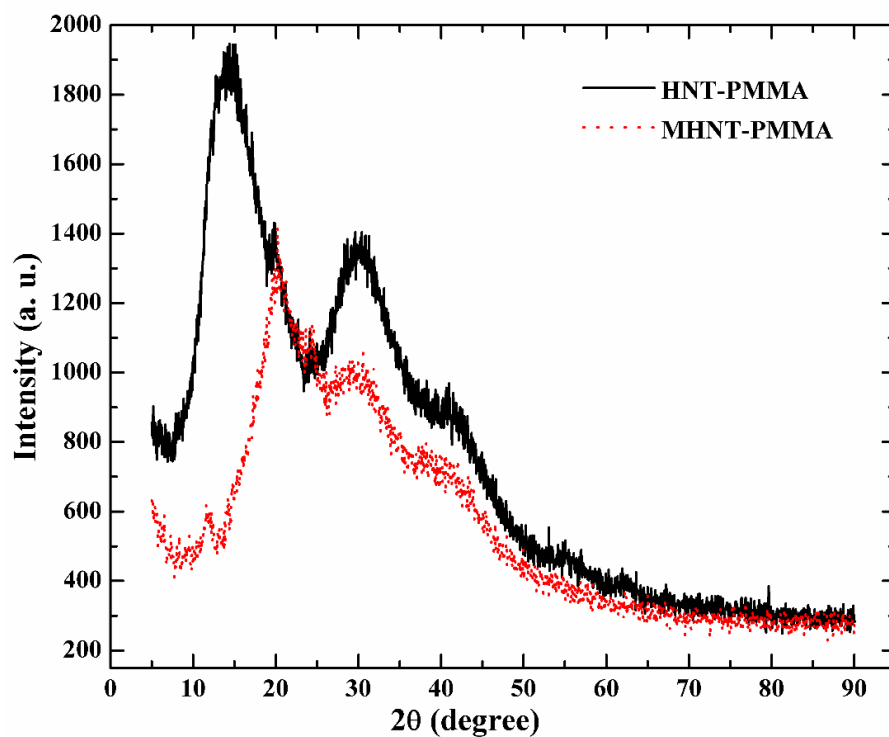


**Figure 7.6 XRD patterns of (a) HNT-PMMA, and (b) MHNT-PMMA nanocomposites synthesized by ultrasound-assisted miniemulsion polymerization**



### 7.3.2 Studies on morphology of HNT-PMMA, and MHNT-PMMA nanocomposites by ultrasound-assisted miniemulsion polymerization

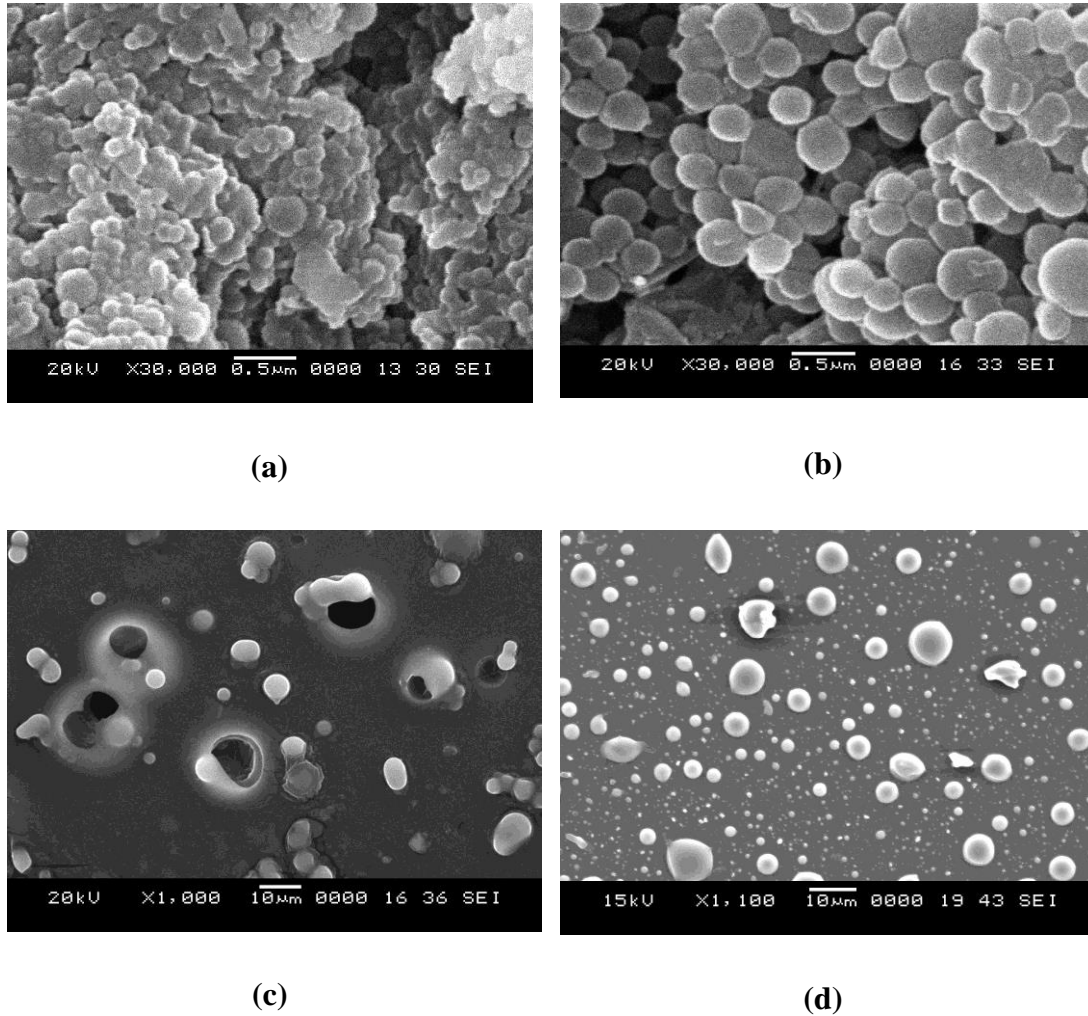


**Figure 7.7 SEM portraits of (a) HNT-PMMA nanocomposites without ultrasound, (b) HNT-PMMA nanocomposites with ultrasound, (c) MHNT-PMMA nanocomposites without ultrasound, and (d) MHNT-PMMA nanocomposites with ultrasound**

Figure 7.7 shows the SEM portraits of nanocomposites. From Fig. 7.7a it can be viewed that the nanocomposites synthesized without use of ultrasound resulted in incomplete polymerization and could not result in definite particle structure, whereas nanocomposites synthesized on subjecting to ultrasound for **60 min** (Fig. 7.7b) resulted in well-organized nanosized spherical polymer particles. Also, from the SEM image of the MHNT-PMMA nanocomposite (Fig. 7.7d), it can be observed that

mini-emulsion polymerization resulted in formation of well-organized, nanosized spherical polymer particles (300–500 nm).

### 7.3.3 Studies on functional groups of HNT-PMMA, and MHNT-PMMA nanocomposites synthesized by ultrasound-assisted mini-emulsion polymerization

Figure 7.8 depicts the FT-IR analysis of HNT, MHNT, HNT-PMMA and MHNT-PMMA. The characteristic peaks of PMMA at about  $2962.49\text{ cm}^{-1}$  and  $2907.13\text{ cm}^{-1}$  are associated with C–H stretching vibration. At  $1719\text{ cm}^{-1}$  the peak represents sharp C=O stretching vibration, and peak located at  $1429\text{ cm}^{-1}$  is attributed to the C–H bending. The presence of these significant functional groups of PMMA and HNT in the HNT-PMMA polymer matrix confirmed the embodiment of HNTs into the polymer. The absorption bands at  $912\text{ cm}^{-1}$  and  $1031\text{ cm}^{-1}$  for the HNTs can be attributed to Al-OH vibrations and Si-O stretching. MHNT displayed a new FT-IR band at  $1476.96\text{ cm}^{-1}$ , which is assigned to scissoring of  $(\text{CH}_2)_3$ . The signals at wavenumber of  $1726.1\text{ cm}^{-1}$  and  $2959.96\text{ cm}^{-1}$  can be assigned to C-O and C-H stretching vibration, respectively. The absence of a band at  $1700\text{ cm}^{-1}$  and the appearance of OH vibration bands at  $912\text{ cm}^{-1}$ ,  $3623.47\text{ cm}^{-1}$ , and  $3693.56\text{ cm}^{-1}$  suggest that hydrogen bonds could not be formed between HNTs and  $\gamma$ -MPS, as OH groups of HNTs were not easily accessible for modification. However, the increase in the intensity of the band at  $912\text{ cm}^{-1}$  from HNT to MHNT along with the broadening and intensification of the band at  $1095\text{ cm}^{-1}$  indicate the possibility of RSi-O-Si and RSi-O-Al bonds between RSi-OCH<sub>3</sub> and RSi-OH groups of  $\gamma$ -MPS with Si-O groups at the surface, and Al-OH groups at the edges of the HNTs. These observations suggest a partial modification of  $\gamma$ -MPS on the surface and edges of HNTs. In comparison with the FT-IR analysis of the unmodified HNTs, the peak at  $1726.1\text{ cm}^{-1}$  is attributed to stretching vibration of C=O bond of MPS in the FT-IR spectrum of MHNTs. The appearance of bands at  $1032\text{ cm}^{-1}$  and  $1095.96\text{ cm}^{-1}$  in the spectrum for MHNTs indicates formation of Si-O-Si bonds, as silane groups of  $\gamma$ -MPS were linked to the surface of the HNTs. This confirms successful modification of HNTs with silane. The band at  $912\text{ cm}^{-1}$  for MHNTs was shifted to  $952.46\text{ cm}^{-1}$  for MHNT-PMMA. This can be attributed to interaction of OH group inside the HNT lumen, which indicates penetration of  $\gamma$ -MPS into HNT

interlayers. The IR band at  $1031\text{ cm}^{-1}$  is assigned to Si-O groups at the surface of HNTs, while the band at  $1050.46\text{ cm}^{-1}$  for PMMA–MHNT is attributed to formation of Si-O-Si groups, indicating the interaction between  $\gamma$ -MPS and the surface of HNTs. The significant reduction in intensity of the bands at  $3623.47\text{ cm}^{-1}$  and  $3693.56\text{ cm}^{-1}$  is related to the appearance of new bands at  $2927.41\text{ cm}^{-1}$  and  $2859.27\text{ cm}^{-1}$ . This decrease indicates the reaction between hydroxyl groups inside the lumen with PMMA.

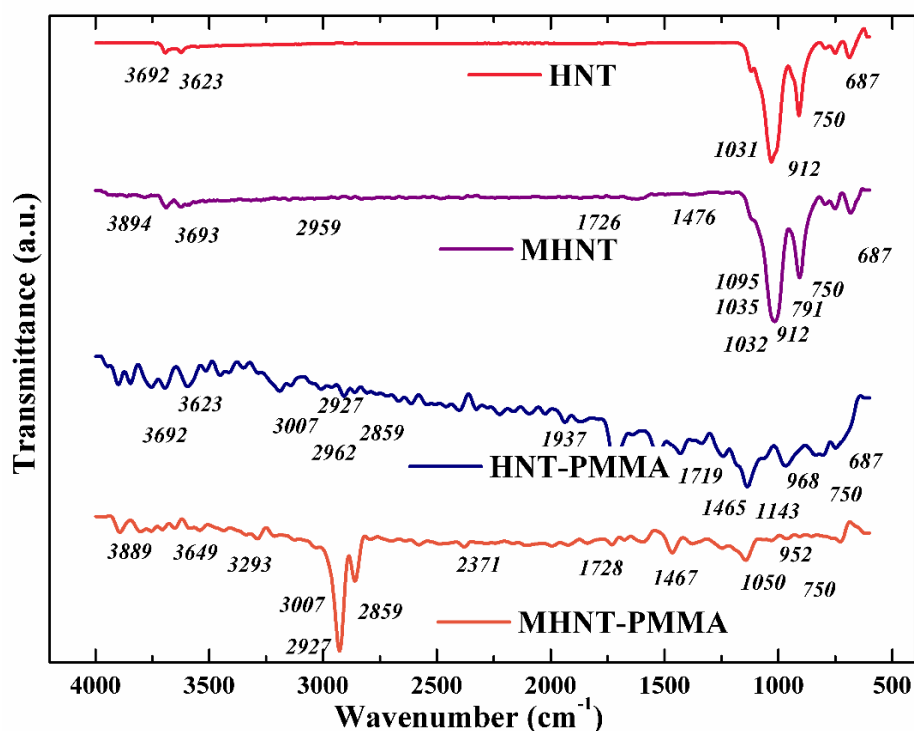
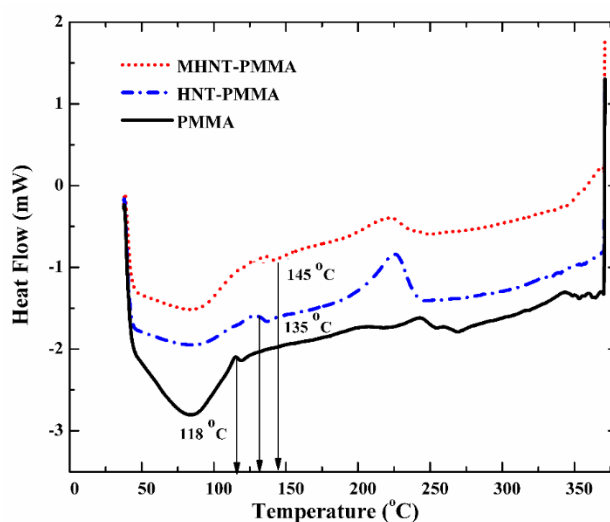


Figure 7.8 FT-IR spectrum of HNT, MHNT, HNT-PMMA, and MHNT-PMMA nanocomposites by ultrasound-assisted miniemulsion polymerization

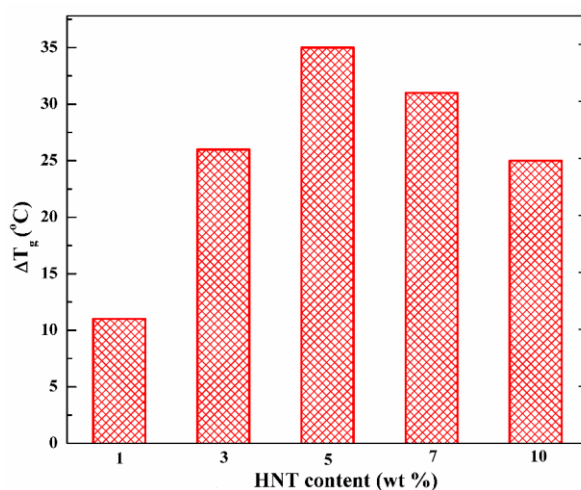
### 7.3.4 Studies on thermal stability of HNT-PMMA, and MHNT-PMMA nanocomposites synthesized by ultrasound-assisted miniemulsion polymerization

Differential scanning calorimetry analysis was carried out to investigate the glass-transition temperature ( $T_g$ ) of the nanocomposites. The DSC curves are presented in Fig. 7.9a. The  $T_g$  value for PMMA, HNT-PMMA and MHNT-PMMA nanocomposites was estimated to be 118, 135, and 145 °C, respectively. The MHNT-PMMA nanocomposite showed higher  $T_g$  compared with neat PMMA or unmodified HNT-filled PMMA, representing an evident improvement. Therefore, functionalization

of HNTs improved the intercalation of polymer chains between the HNT layers due to incorporation of appropriate organic links between the polymer matrix and HNTs. There is also a reduction in surface energy of silane-treated clay, which facilitates macromolecule access between the layers of clay, thereby restricting movement of intercalated polymer chains between the sheets of the HNTs and preventing segmental motion of the polymer chains. These results show improvement in the thermal properties of the polymer upon using MHNTs.



(a)



(b)

**Figure 7.9 DSC thermograms of (a) PMMA, HNT-PMMA, and MHNT-PMMA and (b) PMMA with different content of HNT nanocomposites synthesized by ultrasound-assisted miniemulsion polymerization**

The effect of HNT content on glass transition temperature of HNT-PMMA was also investigated. It was found that the  $T_g$  of PMMA was 118 °C on synthesizing without HNTs, whereas on addition of 1% HNTs the  $T_g$  increased by 11 °C. The corresponding increase in  $T_g$  with increasing HNT content can be viewed from Fig. 7.9b. Higher loadings impeded dispersion of HNTs into polymer matrix which resulted in clay aggregation and increase in particle size. Therefore 5 wt% HNTs addition can be said to be optimum for synthesis of HNT-PMMA nanocomposites.

### 7.3.5 Studies on zeta potential of HNT, MHNT, and MHNT-PMMA of nanocomposites synthesized by ultrasound-assisted miniemulsion polymerization

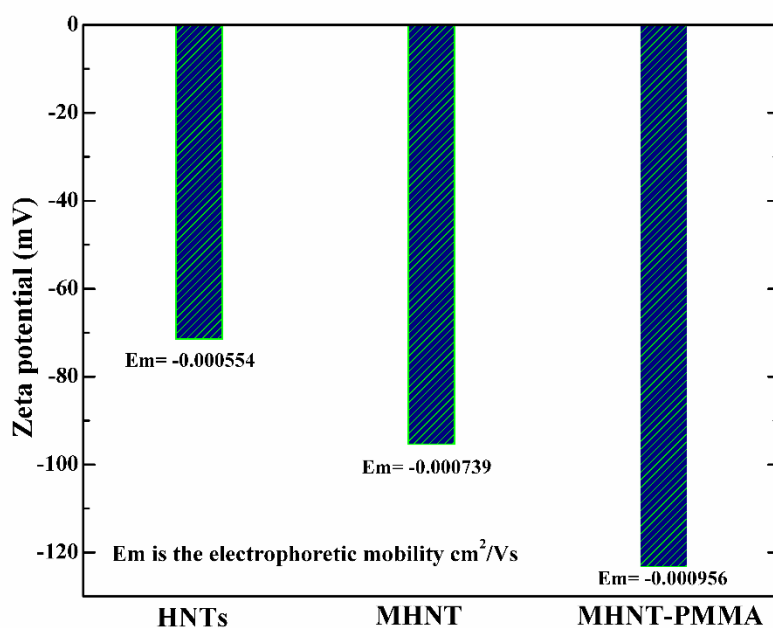


Figure 7.10  $\zeta$ -potential of HNTs, MHNTs, and MHNT-PMMA latex synthesized by ultrasound-assisted miniemulsion polymerization

The zeta potential indicates the stability and homogeneity of HNTs, MHNTs, and MHNT-PMMA latex in water. It can be observed from Fig. 7.10 that the zeta potential value of unmodified HNTs was  $-71.5\text{ mV}$ , whereas the zeta-potential of MHNTs increased to  $-95.4\text{ mV}$ . This increase in the zeta-potential for the MHNTs is due to increased surface charges after silane treatment with  $\gamma$ -MPS. Furthermore, it can be inferred that the stability of the MHNT-PMMA emulsion is high from its zeta-

potential value of  $-122.5\text{ mV}$ . Hence, addition of MHNTs aids formation of very stable emulsions, due to self-arrangement of the MHNTs within polymer particles, which reduces the interfacial tension between the two phases and stabilizes the emulsion via electrostatic or steric effects.

#### 7.4 SYNTHESIS OF POLY(STYRENE-CO-METHYLMETHACRYLATE)-HNT [HNT-(PS-co-PMMA)] NANOCOMPOSITES

In this section the synthesis of PS-co-PMMA using pristine and modified HNTs by ultrasound-assisted miniemulsion polymerization is presented.

##### 7.4.1 Studies on structure of [HNT-(PS-co-PMMA)], and [MHNT-(PS-co-PMMA)] nanocomposites synthesized by ultrasound-assisted miniemulsion polymerization

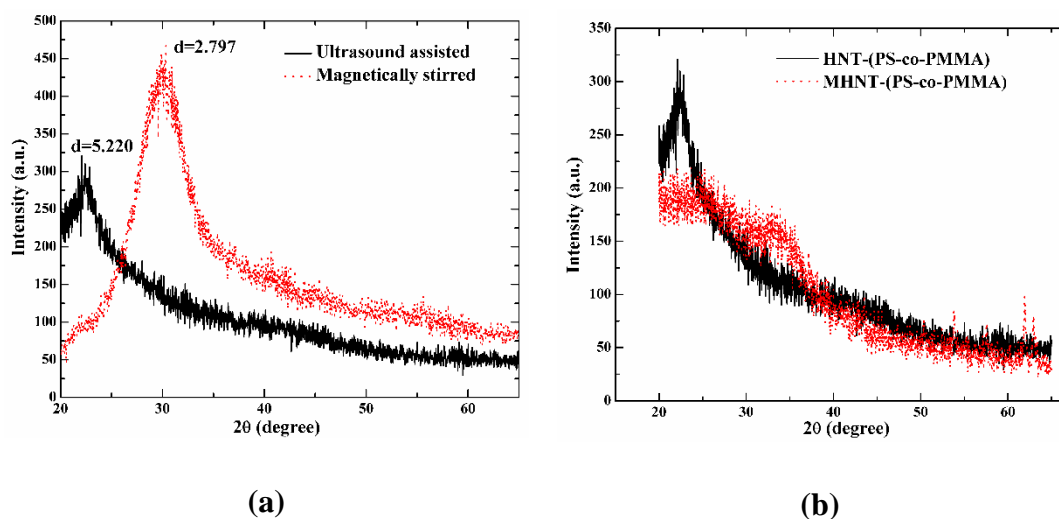


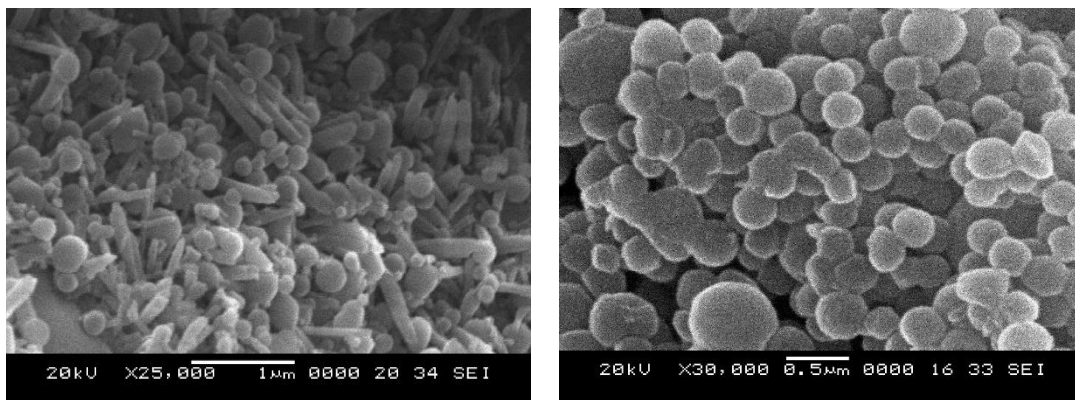
Figure 7.11 XRD pattern of (a) [HNT-(PS-co-PMMA)] nanocomposite with and without sonication (b) [HNT-(PS-co-PMMA)] and [MHNT-(PS-co-PMMA)] nanocomposites synthesized by ultrasound-assisted miniemulsion polymerization

##### 7.4.2 Studies on morphology of [HNT-(PS-co-PMMA)], and [MHNT-(PS-co-PMMA)] nanocomposites synthesized by ultrasound-assisted miniemulsion polymerization

Figure 7.11a describes interlayer structure of nanocomposites with and without sonication. A significant broad peak appeared at  $32^\circ$  on synthesising nanocomposites

without sonication, whereas on using sonication this peak appeared at  $17^\circ$ . This shows an increase in interlayer spacing upon sonication that can be made available for polymer for better interaction with HNT thereby enhancing the properties, further it can be noted that no significant peaks are observed meaning formation of completely exfoliated structure. Hence, sonication plays a vital role in dispersion quality and charges in layers. The high anionic charge density of SDBS facilitates its movement into the interlayers of HNTs due to development of ionic networks and modifier component. This increases the hydrophobicity of HNTs due to inculcation of alkyl long chains which are present in SDBS. This is the key aspect for intercalation of HNTs (Qutubuddin et al. 2002), which promotes exfoliation process by embodiment of monomer molecules followed by polymerization. Hydroxyl group present on the surface of the HNTs are absorbed by SDBS and hence there is decrease in the HNT particle hydrophobicity, resulting in enhanced colloidal stability thereby increasing exfoliation of HNTs. The high shear through acoustic irradiation aids in exfoliation, thus SDBS helps in reaching the co-monomers within the layer and they widen up the gap between the interlayers. Polar carboxyl groups present in methylmethacrylate interacts with polar groups existing in the intergalleries which further facilitates in continuous addition of styrene monomers into intergalleries and compels the clay layers to exfoliate. From Fig. 7.11b it can be observed that modification of HNTs with silane aided in better dispersion of MHNT in the polymer matrix thereby increasing the exfoliation and hence reduction in the significant peaks. This further leads to improved polymer properties.

Nanocomposites of PS-co-PMMA synthesized using HNTs and MHNTs are shown in Fig. 7.12. It can be seen that these composites display nearly mono-dispersed morphology and had smooth surface without any agglomerations in polymer-matrix.



(a)

(b)

Figure 7.12 SEM analysis of (a) [HNT-(PS-co-PMMA)], and (b) [MHNT-(PS-co-PMMA)] nanocomposites synthesized by ultrasound-assisted miniemulsion polymerization

#### 7.4.3 Studies on functional groups of [HNT-(PS-co-PMMA)], and [MHNT-(PS-co-PMMA)] nanocomposites synthesized by ultrasound-assisted miniemulsion polymerization

The effect of HNTs inclusion on polymer structure is represented in Fig. 7.13. The stretching vibrations of inner surface of Al-OH are represented by peaks at  $3692$  and  $3623\text{ cm}^{-1}$ . Bending vibrations at  $1638.39\text{ cm}^{-1}$  indicate presence of water in interlayer's of HNTs. The stretching of Si-O apical is demonstrated by the peak at  $1030.10\text{ cm}^{-1}$ . The bending vibration of inner surface hydroxyl groups can be observed by peak at  $909.18\text{ cm}^{-1}$ . Peaks at  $750.02$  and  $687.79\text{ cm}^{-1}$  represents the bending vibrations of Al-O-Si and Si-O-Si respectively. The presence of HNT major absorbance peaks in [HNT-(PS-co-PMMA)] spectrum clearly confirms the existence of HNTs inside the latex particles and indicates encapsulation of HNTs into the final nanocomposites. Also, the major absorption peaks of MHNT (Fig. 4.6) MHNT displayed a new FT-IR band at  $1467\text{ cm}^{-1}$  which is assigned to the scissoring of  $(\text{CH}_2)_3$ . Wavenumbers at  $2925\text{ cm}^{-1}$  can be assigned to C-H stretching vibration, respectively. The absence of a band at  $1700\text{ cm}^{-1}$  and the appearance of OH vibration bands at  $3624$  and  $3694\text{ cm}^{-1}$  suggest that hydrogen bonds could not be formed between HNTs and  $\gamma$ -MPS as OH groups of HNTs were not easily accessible for modification. The



presence of MHNT major absorbance peaks in PS-co-PMMA spectrum can be clearly seen from Fig. 7.13 which confirms the existence of MHNT inside the latex particles and indicates encapsulation of MHNTs into the final nanocomposites. Thus from FT-IR study we may infer successful incorporation of MHNT in the PS-co-PMMA copolymer matrix.

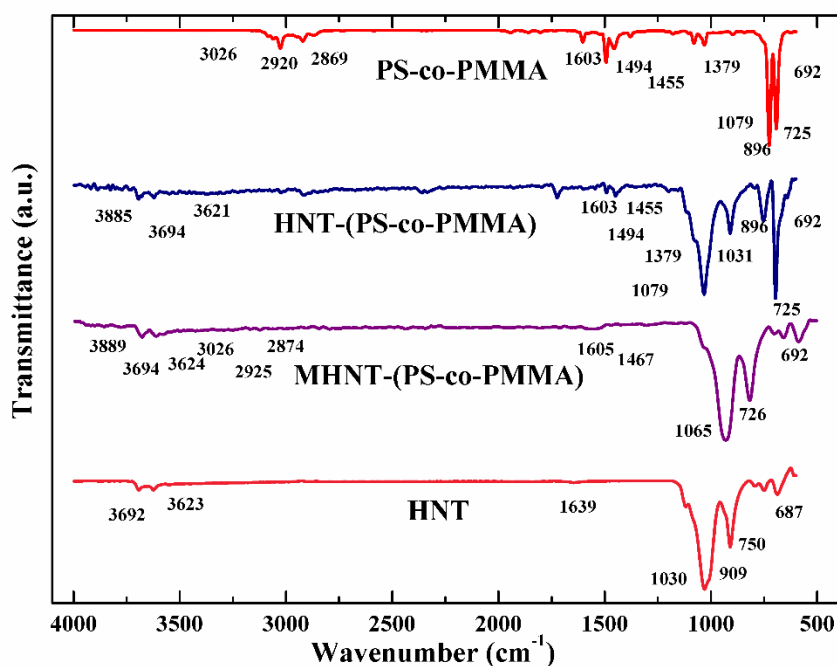


Figure 7.13 FT-IR spectrum of nanocomposites synthesized on using HNT and MHNT by ultrasound-assisted miniemulsion polymerization

#### 7.4.4 Studies on thermal stability of [HNT-(PS-co-PMMA)], and [MHNT-(PS-co-PMMA)] nanocomposites synthesized by ultrasound-assisted miniemulsion polymerization

Figure 7.14 shows DSC traces of (PS-co-PMMA), [HNT-(PS-co-PMMA)] and [MHNT-(PS-co-PMMA)] nanocomposites. It can be observed [HNT-(PS-co-PMMA)] nanocomposites showed higher  $T_g$  than that of prepared without HNT thereby indicating better thermal stability. On incorporation of 3 wt% HNTs, the  $T_g$  evidently improves and is believed to restrict the movement of intercalated polymer chains between the interlayers of the HNTs which restricts the segmental motions of the polymer chains.  $T_g$  improved significantly upto 5 wt% HNTs,  $T_g$  did not increase appreciably with further increase in amount of HNTs, which confirms that 5 wt % itself

can be effective on improving the  $T_g$  and hence thermal stability. Incorporation of higher HNT content resulted in non-uniform dispersion and hence  $T_g$  did not increase appreciably. The increase in thermal stability may result due to dispersion of layers into the polymer chain. The layered structure of the clay can retard heat-transfer and also strengthen the polymer chain to resist heat degradation. Modification of HNTs further caused appreciable increment in the thermal properties of HNTs due to improvement in dispersability of MHNTs in the polymer matrix. This signifies the modification of HNTs.

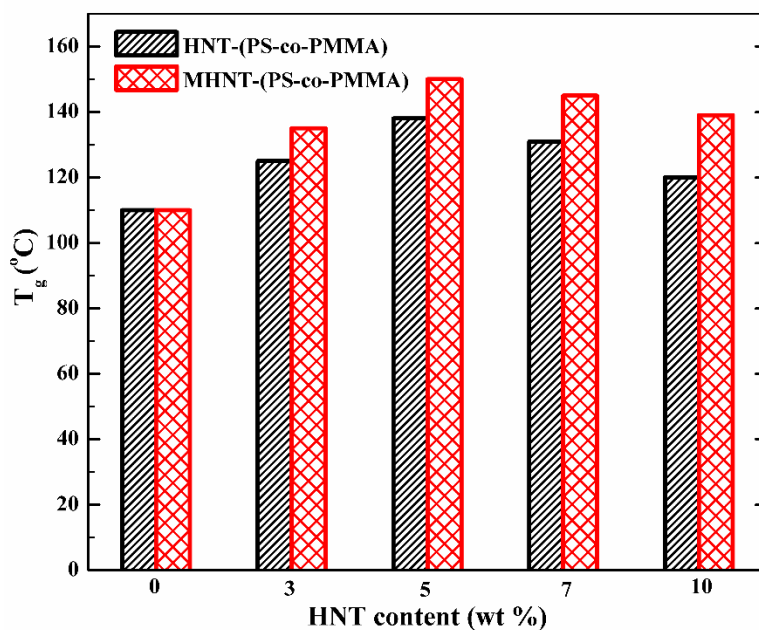


Figure 7.14 DSC thermograms of [HNT-(PS-co-PMMA)] and [MHNT-(PS-co-PMMA)] nanocomposites with different HNT loading (wt%)

## 7.5 SUMMARY

Nanocomposites of PS, PMMA and PS-co-PMMA was synthesized using HNTs and MHNTs by ultrasound-assisted miniemulsion polymerization. The surface of HNTs was favorably modified by  $\gamma$ -MPS. The resulting MHNTs were used to fill a PMMA nanocomposite synthesized by miniemulsion polymerization assisted by ultrasound. FT-IR confirmed the modification of the HNTs and presence of MHNTs in the polymer. XRD results showed that there was no prominent shift in the basal spacing, indicating that a very small amount of  $\gamma$ -MPS intercalated into the interlayers of HNTs,

while the surface of HNTs was modified completely. SEM analyses showed a reduction in aggregates of HNTs after surface modification. DSC analysis showed enhancement in thermal stability in terms of  $T_g$  of the MHNT–PMMA nanocomposite as a result of modification of HNTs. Improvement in the properties of nanocomposite was observed on utilizing ultrasound for carrying out the synthesis. Additionally, surface modification of HNTs caused considerable improvement in exfoliation of HNTs into the polymer matrix and hence, thermal stability. Therefore, surface treatment of HNTs using  $\gamma$ -MPS together with miniemulsion polymerization assisted by ultrasound proves to be a promising technique to achieve better dispersion of HNTs in the polymer and obtain nanocomposites with enhanced properties.

## CHAPTER 8

### APPLICATION OF HNT-BASED PS, PMMA AND PS-co-PMMA NANOCOMPOSITES FOR COATING SODA LIME GLASSES

*This chapter reports the application of HNT-polymer nanocomposites for coating the surface of soda-lime glass. The coating was deposited on the surface of glass by dip-coating, and spin coating methods. The spectral properties of the glass, morphology, surface-wettability, and thermo-mechanical properties of the nanocomposite coatings were investigated and presented here.*

#### 8.1 INTRODUCTION

Organic-inorganic coatings on glass substrates have gained considerable attention of researchers since these coatings prevent the glass substrates from physical damage; protect them from environmental degradation and improve their mechanical, barrier and thermal properties. Hence, in this chapter, the potential use of HNT-based polymethylmethacrylate (PMMA) and polystyrene (PS) nanocomposites prepared by ultrasound-assisted solution blending method for coating glass surfaces is reported. The HNT-polymer (PS or PMMA) nanocomposite coatings were applied by dip-coating technique on four different types of soda-lime glass, namely, clear (C), bronze (Br), green (G) and grey (Gr) with an ultimate objective of protecting the glass surface against abrasion and to improve its thermo-mechanical properties without sacrificing their inherent spectral properties. The spectral, surface, thermal and mechanical properties of HNT-polymer nanocomposites coated glasses were investigated in detail and reported. Transparent hydrophobic coatings on glass can find potential applications in commercial products like building windows, lens and optical devices, solar panels, etc. These HNT-based polymer nanocomposite coatings can be used for automobiles, building materials, household products, high performance fabrics, and food packaging. Also, developing a copolymer of both these polymers can remunerate their drawbacks as copolymers holds potential to combine the properties of two or more polymers into a single polymer and the resulting composite can be used for various applications. The copolymer of PS and PMMA possess the properties which are intermediate between those of the corresponding individual polymers and will display synergically enhanced

physical, chemical, and biological properties. Hence, herein the the synergetic effect of both PS and PMMA copolymer incorporated with HNTs on two types of glass, i.e., Bronze (Bz) and Green (GG) glass. [HNT-(PS-co-PMMA)] nanocomposites were synthesized by solution casting method assisted by ultrasound. PS-co-PMMA was spin coated onto different soda lime glasses and their behavior was investigated in detail and reported in this chapter. All the results are explained in form of tables and figures.

## **8.2 HNT-BASED PS AND HNT-BASED PMMA COATINGS USING DIP COATING**

### **8.2.1 Spectral properties of polymer coated glass substrate**

The effect of applying HNT-filled polymer nanocomposite coatings on spectral properties of glass samples was assessed. The spectral properties were measured with 0° tilt angle of incidence in the ultraviolet (UV), visible (V) and infrared region (IR) regions of light between 300 *and* 2500 *nm* wavelengths. UV region lies below 380 *nm* which is comprised of short waves; visible light lies between 380 *and* 780 *nm*, and the rest represents the IR region which is composed of long waves. Figs.8.1 and 8.2 show the percentage transmittance, reflectance and absorptance of glass samples coated with HNT-PS and HNT-PMMA nanocomposites, respectively. The decrease in transmittance (Figs. 8.1a, 8.1d, 8.2a and 8.2d) and reflection (Figs. 8.1b, 8.1e, 8.2b, and 8.2e) values around 400 *to* 600 *nm* can be attributed to increase in the absorption of radiation into glass (Figs. 8.1c, 8.1f, 8.2c, and 8.2f). It can be seen that clear glass has the highest transmittance and grey glass has the least transmittance because of their varying refractive indices. The uncoated glasses also exhibited the same spectral behavior. Hence, the inherent spectral behavior of glasses was not affected by applying HNT-based polymer coatings.

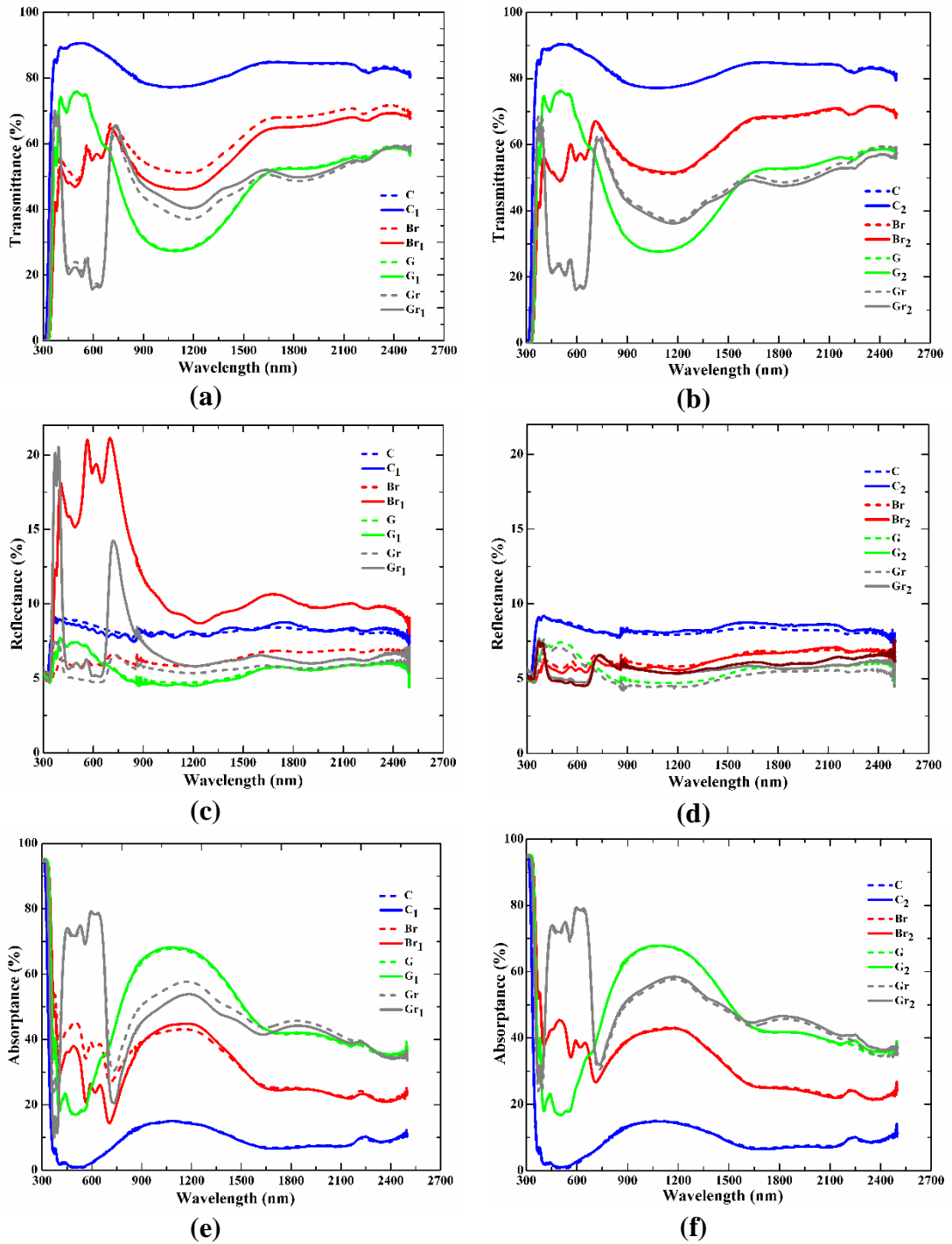
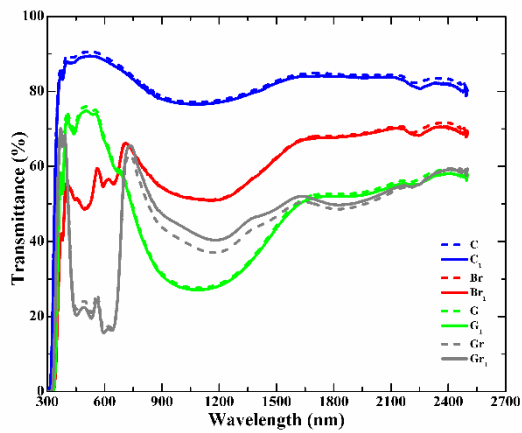
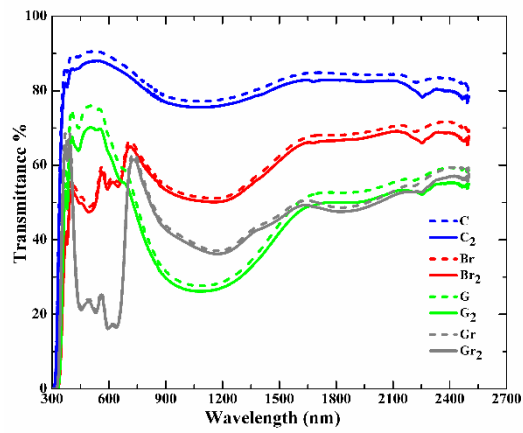


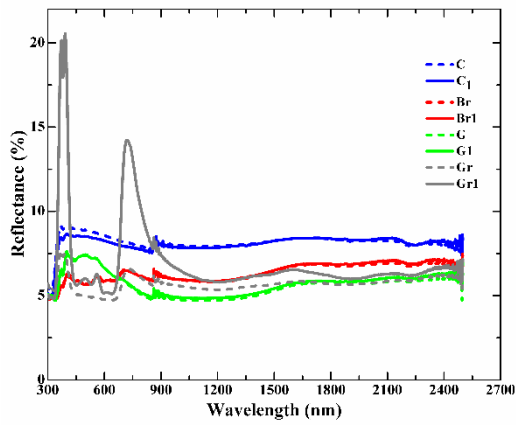
**Figure 8.1 Spectral properties of HNT-PS coated glass samples:(a) transmittance (b) reflectance and (c) absorptance of single side coated glass samples, and (d) transmittance (e) reflectance and (f) absorptance of double side coated glass samples. Suffixes 1 and 2 indicate single side and double side coated glasses, respectively. The dotted lines represent the corresponding properties of uncoated glass samples**



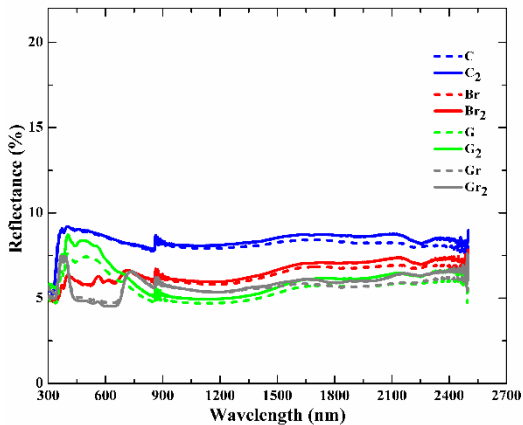
(a)



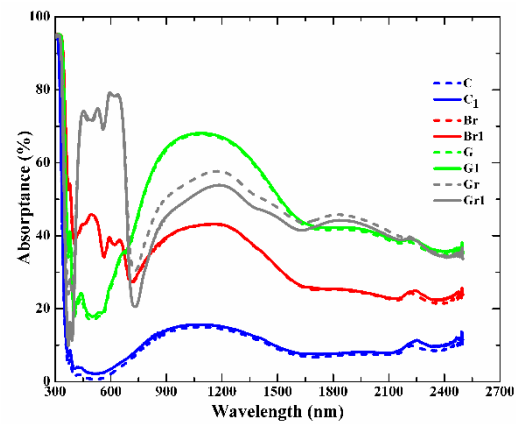
(b)



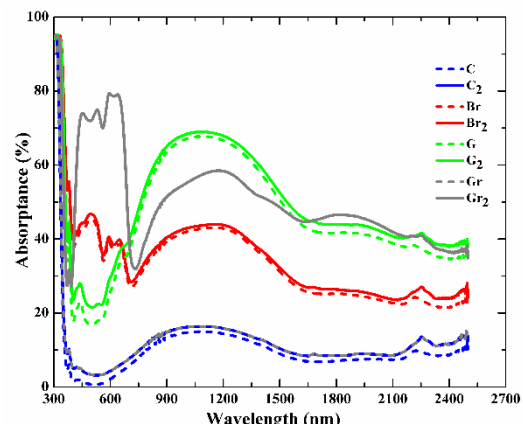
(c)



(d)

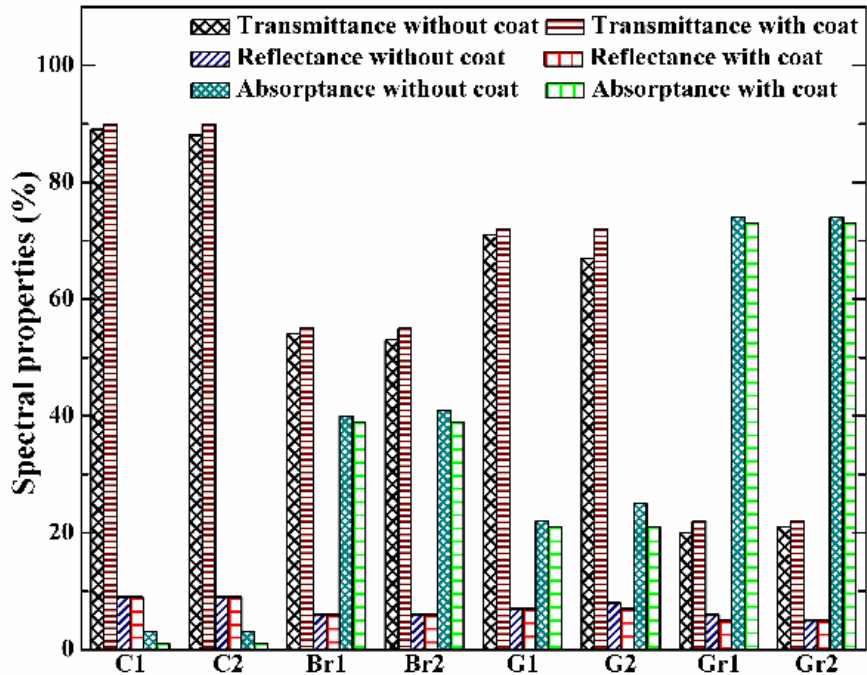


(e)

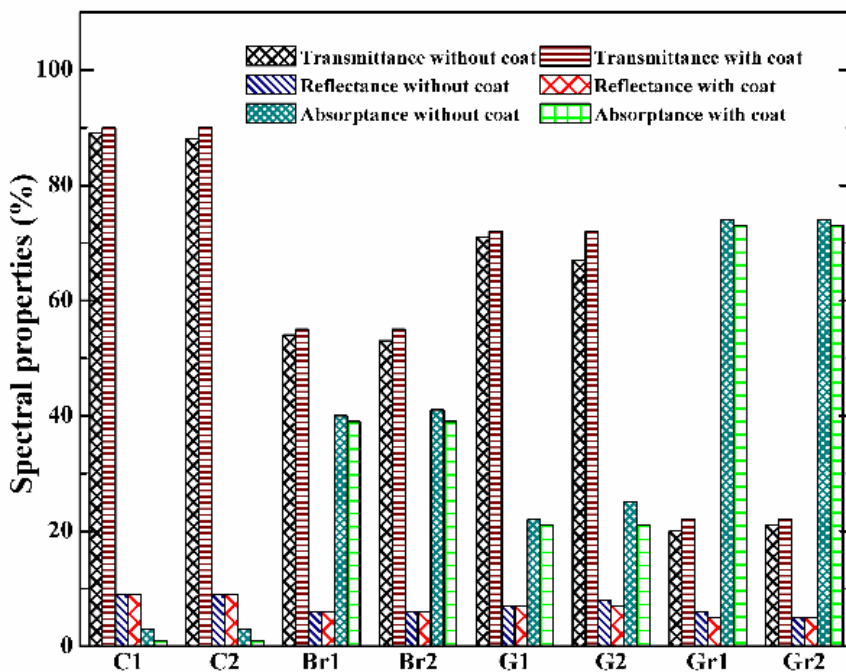


(f)

**Figure 8.2 Spectral properties of HNT-PMMA coated glass samples: (a) transmittance (b) reflectance and (c) absorbance of single side coated glass samples, and (d) transmittance (e) reflectance and (f) absorbance of double side coated glass samples. Suffixes 1 and 2 indicate single and double side coated glasses, respectively. The dotted lines represent the corresponding properties of uncoated glass samples**



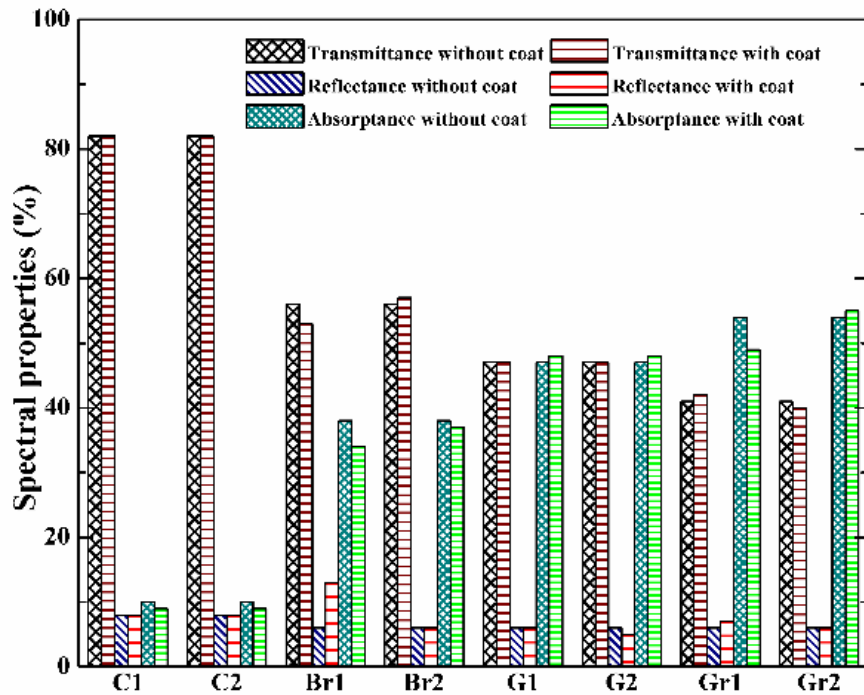
(a)



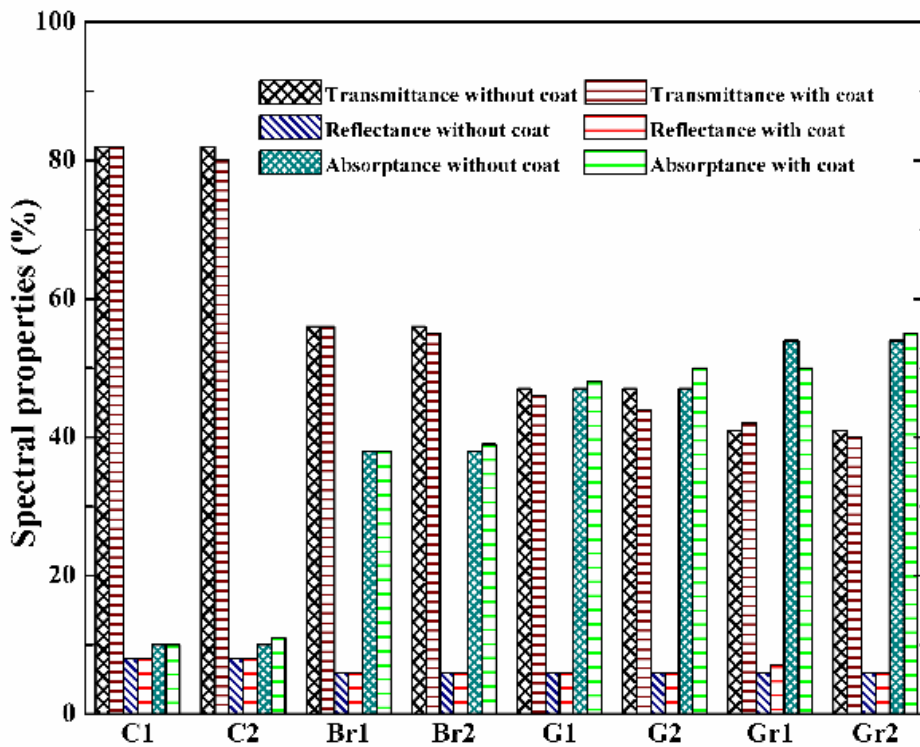
(b)

Figure 8.3 Spectral properties of (a) HNT-PS coated and (b) HNT-PMMA coated glass samples in UV and visible regions. Suffixes 1 and 2 represent single and double side coated glasses, respectively





(a)



(b)

Figure 8.4 Spectral properties of (a) HNT-PS coated and (b) HNT-PMMA coated glass samples in IR region. Suffixes 1 and 2 represent single and double side coated glasses, respectively

In order to understand the spectral behavior in different regions of wavelength of radiation, the percentage transmittance, reflectance and absorptance of glasses coated with HNT-based polymer nanocomposites as well as without coatings in UV<sub>a</sub> plus visible and infrared ranges are calculated separately using equations (1) to (3) and the results are presented in Figs. 8.3 and 8.4, respectively. It can be clearly found that there are no significant changes in the transmittance and reflectance properties of glasses after coating. It reveals the fact that the polymer coating did not affect the inherent spectral properties of the glasses in any of the UV, visible and IR regimes. Basically, light-scattering is a function of refractive and diffractive mechanisms. The clay particles do not diffract light enough since they are too small. Also, the refractive index of clay is very close to the refractive index of polymers and glasses (Beall and Powell 2011). Hence, the presence of HNTs in coatings did not alter the transmittance of light. It is important not to alter the inherent spectral properties of the glass upon coating and HNT-based polymer nanocomposite coatings satisfy this requirement.

The calculated values of SSPF and SMPF using equations (7) to (10) for different glasses with and without coatings are listed in Table 8.1. There was no significant increase in SSPF and SMPF values upon coating the glasses. This might be due to the fact that the coating thickness is only 5 *mm* and HNT content in polymer is 5 *wt %*. If coating thickness or the HNT content in polymer is increased, it might show a positive impact on these factors. A uniform dispersion of HNTs in the polymer matrix is responsible for providing protection for materials as well as skin; further, HNTs also stabilize the polymer and protect them against photo-degradation and increases its photo-resistance (Hoang-Minh T et al. 2010; Woo et al. 2007). The protection factors may also increase due to creation of tortuous path by HNTs in the polymer matrix which obstructs the passage of radiations across the glass. It can be seen from Figs. 8.1 and 8.2 that there was a decrease in transmission and reflection curves in the region between 320 and 400 *nm* which explains an increase in absorbance in this region. This suggests that UV<sub>a</sub> radiations and some part of UV<sub>b</sub> radiations were absorbed by the coated nanocomposites which is a reason for slight changes in SMPF and SSPF values observed in Br, G, Gr glass samples except clear glass (**Refer Appendix**). The SEM image of dip-coated polymer thin film on glass substrate is shown in Fig. 8.5. The

thickness of the coating is measured as 5  $\mu\text{m}$  and it is also clear that the coating was evenly applied on the glass substrate. Due care was taken to achieve the same thickness of coating in all test samples.

Table 8.1 SSPF and SMPF values of coated and uncoated glasses

Sl. No	Glass type	SSPF			SMPF		
		Uncoated	HNT-PS coated	HNT-PMMA coated	Uncoated	HNT-PS coated	HNT-PMMA coated
1	Clear glass	0.89	0.89	0.89	0.50	0.50	0.50
2	Bronze glass	0.95	0.96	0.96	0.52	0.53	0.52
3	Green glass	0.93	0.94	0.95	0.32	0.33	0.38
4	Grey glass	0.90	0.92	0.93	0.71	0.73	0.73

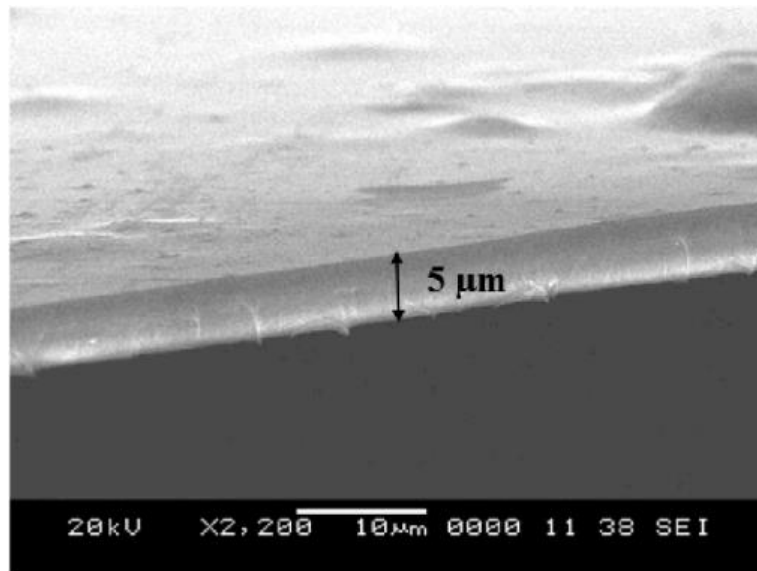


Figure 8.5 SEM image of HNT-PS coated glass portraying thickness of coating

## 8.2.2 Effect of sonication time on morphology of HNT-polymer coatings

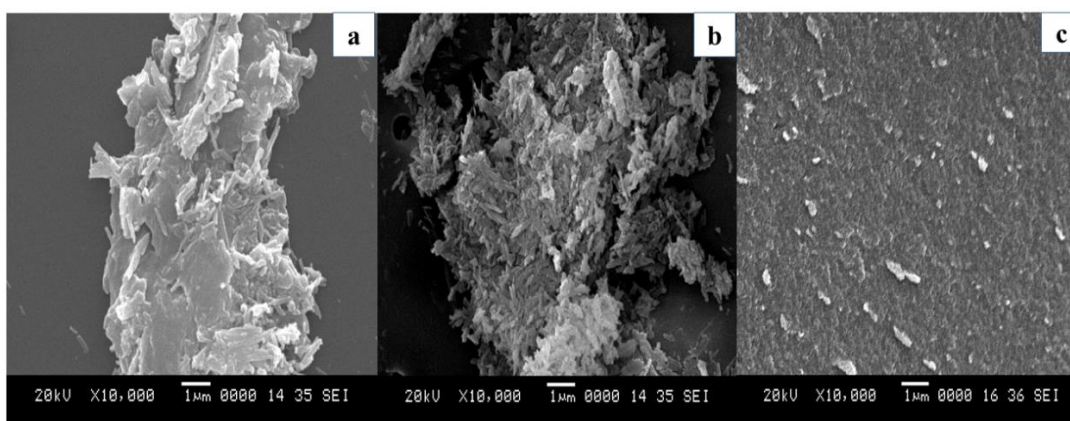


Figure 8.6 Morphology of a thin film of HNT-PS coatings obtained at different sonication times: (a) without sonication, (b) **30 min**, and (c) **60 min** of sonication

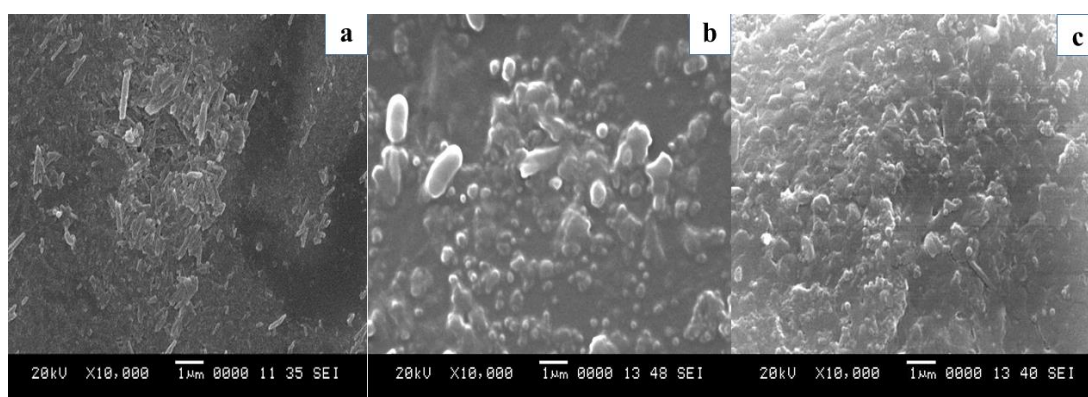


Figure 8.7 Morphology of a thin film of HNT-PMMA coatings obtained at different sonication times: (a) without sonication, (b) **30 min**, and (c) **60 min** of sonication

Sonication time plays an important role in determining the properties of the resulting nanocomposites. A series of nanocomposite samples were collected at different sonication times and were used to coat the glass. These experiments were performed to find out an optimal sonication time that gives a coating material with better properties. The SEM images displaying the morphology of HNT-PS and HNT-PMMA coated glass substrates with different ultrasonic blending times (**0, 30 and 60 min**) are shown in Figs. 8.6 and 8.7, respectively.

Cavitation collapse (implosions) results in shock waves, and localized high temperatures (up to approx. **5000 K**) and pressures (**up to 100 atm**) (Suslick 1990b).

These shock waves are responsible for the disintegration of the neighboring solids, leading to the generation of shear forces and eddies which, in turn, lead to an increase in turbulent energy dissipation. It was observed that HNTs were in the form of agglomerates for unsonicated cases (Figs. 8.6a and 8.7a). After **30 min** of sonication, the attractive forces between the strong particle agglomerates weakened and resulted in looser agglomerates as shown in Figs. 8.6b and 8.7b. Finally, **60 min** of sonication facilitated a good dispersion of HNTs in polymer solution which is responsible for the enhanced properties of the nanocomposite coatings. The corresponding SEM images are shown in Figs. 8.6c and 8.7c. There are also numerous unfilled regions (surface roughness) in coatings which were observed on the coated glass surfaces and they facilitate the enhanced hydrophobic nature.

### **8.2.3 Surface wetting behavior of coated and uncoated glass substrates**

Surface wetting is a characteristic feature of all glass surfaces and depends on the chemical composition and topography of the surface. Surface free energy depends on the variation in surface orientation which influences the surface wettability. The morphology of the HNT based polymer coatings (Figs. 8.6c and 8.7c) indicates that the surface contact area that is accessible to water is very low and as a result, these surfaces exhibit hydrophobic properties. Hydrophobicity of a material surface is mainly controlled by the intrinsic chemical properties and surface microstructures. By addition of surface roughness on the coating, the hydrophobicity of a surface can be further enhanced (Zhang et al. 2016). Surface roughness traps air in its irregularities which directs water droplets to reside on the outthrust and prevents surface wetting. To confirm the hydrophobic nature of the surface, the contact angles were measured using the sessile drop technique. Approximately 0.5 ml drop of distilled water was placed on the coated and uncoated glass surfaces using a syringe and contact angle was measured. In general, higher the contact angle, better is the hydrophobic nature of the surface.

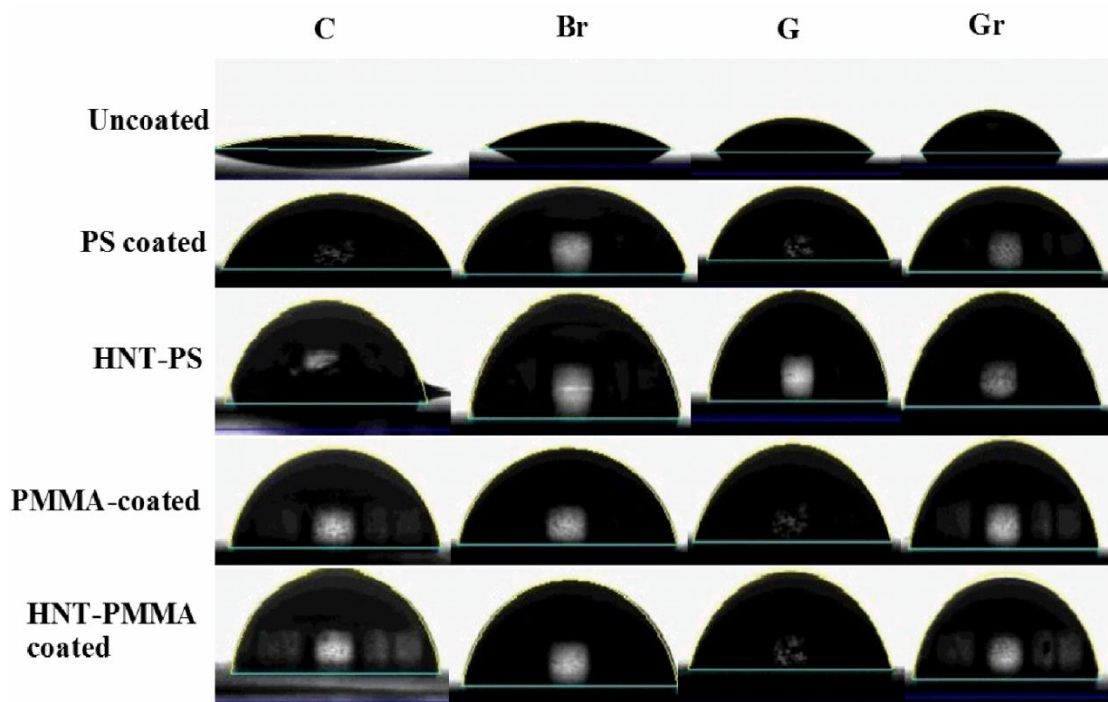


Figure 8.8 Images show contact angles of Clear (C), Bronze (Br), Green (G) and Grey (Gr) glass samples without coat, with only PS coat, HNT-PS coat with PMMA coat, and with HNT-PMMA coat

It is very clear from Table 8.2 that the coated glass samples show drastic increase in contact angles in comparison with uncoated glasses. The hydrophobicity is enhanced upon addition of HNTs into the polymer matrix, and thereby HNT-polymer nanocomposite coatings facilitate converting relatively hydrophilic surface of glass to hydrophobic. In addition, the glasses coated with HNT-PMMA nanocomposite exhibits higher hydrophobicity than HNT-PS nanocomposite. This is due to higher surface roughness of HNT-PMMA coated glasses (**157.6 nm**) compared to HNT-PS coated samples (**127 nm**) (Burton and Bhushan 2005). The surface roughness values were calculated using Gwyddion 2.48 software. Fig. 8.8 visualizes the water droplet on four types of glass samples without coating, with neat polymer coating and with HNT based polymer (PS and PMMA) coatings. It is observed that the spreading of the water droplets increases gradually on moving from the HNT-polymer nanocomposite coated glass samples to coated with neat polymers ones and then to the uncoated ones, which

indicates the HNT-polymer nanocomposite coating provide better hydrophobicity to the surface. This is a desirable quality of coatings for preventing water stains on glasses.

Table 8.2 Contact angles of coated and uncoated glasses

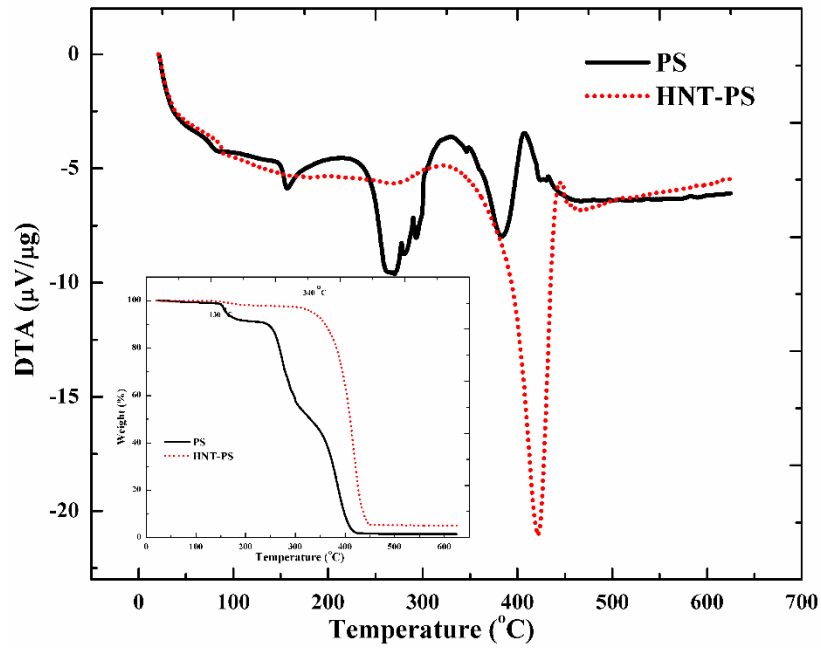
Sl. No.	Glass substrates	Contact angle, $\theta$				
		Uncoated	PS coated	HNT-PS coated	PMMA coated	HNT-PMMA coated
1	Clear glass	6.36	68.74	90.31	77.68	95.80
2	Bronze glass	24.24	74.33	91.58	75.37	93.85
3	Green glass	32.60	79.55	95.50	68.74	90.89
4	Grey glass	48.68	68.97	89.83	76.57	91.57

#### 8.2.4 Thermal behavior of HNT-PS and HNT-PMMA nanocomposites

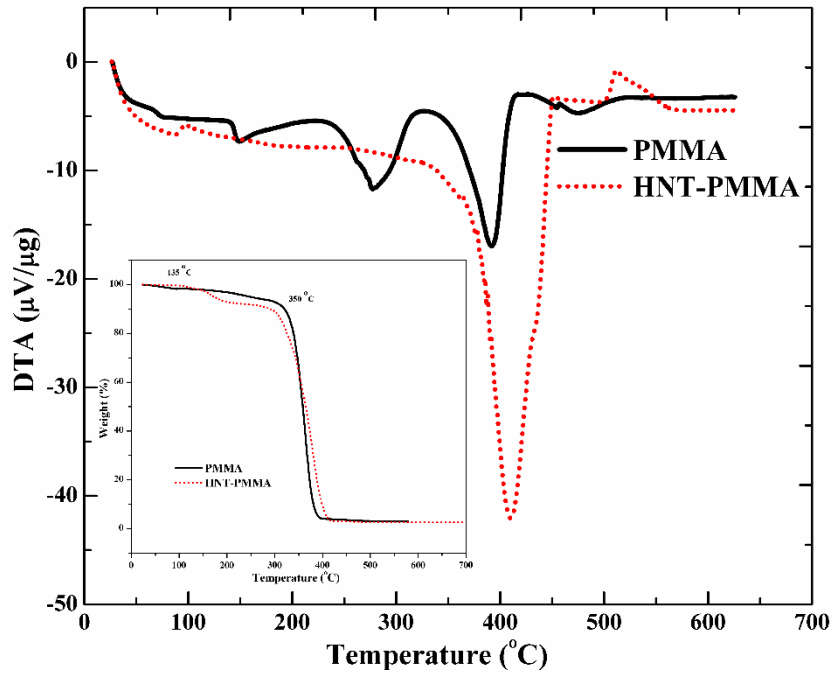
It is important to test the thermal behavior of the HNT-based polymer nanocomposites to assure the extent of the thermal degradation of the coating material while it is exposed to high temperature environment. The integral (TGA) and derivative (DTG) thermogravimetric curves render knowledge on the extent of polymer degradation and thermal stability. Differential temperature analysis (DTA) is a technique which records temperature difference between a specimen and a reference material against time or temperature when both the specimen and the reference materials are subjected to identical temperature in an environment which is heated or cooled at a controlled rate.

##### 8.2.4.1 Thermo-gravimetric analysis (TGA)

The integral (TGA) and derivative (DTG) thermo-gravimetric analyses have been carried out using coated samples and the results are shown in Figs. 8.9a (neat PS and HNT-PS) and 8.9b (neat PMMA and HNT-PMMA).



(a)



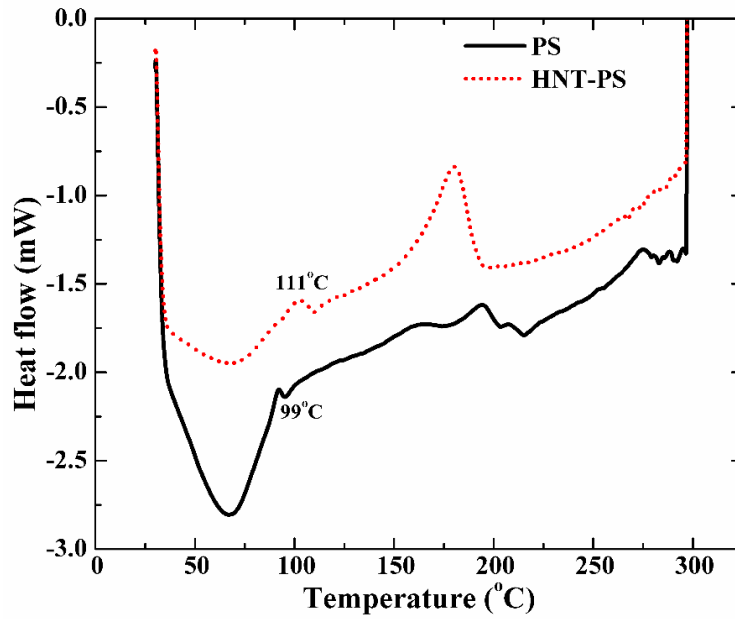
(b)

Figure 8.9 Thermogravimetric (TGA) plots of (a) HNT-PS and (b) HNT-PMMA nanocomposites. The corresponding TGA curves of respective neat polymers are presented for comparison

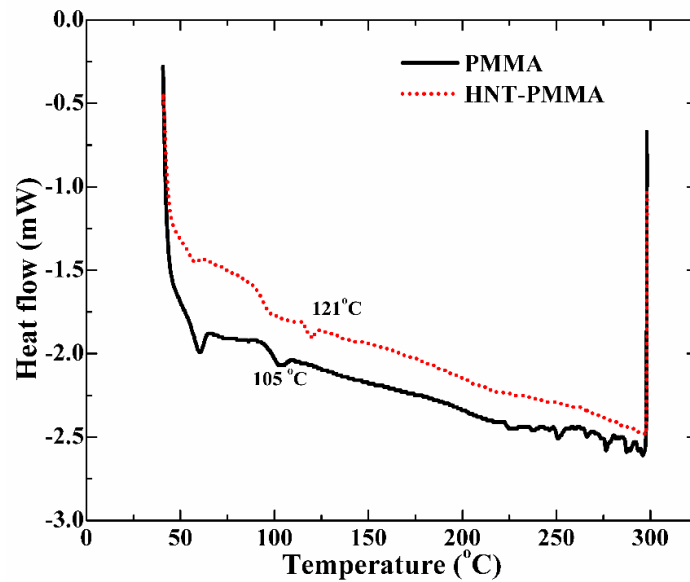


There is no change in the mass of the nanocomposite till 320 °C (Fig. 8.9a) which indicates the synthesized nanocomposite was thermally stable till 320 °C whereas the coatings without HNT (only PS) was stable only till 142 °C. In addition, the DTG curve shows the similar trends for both the cases. Hence, addition of HNTs in the polymer enhances the thermal stability of the coatings. The onset temperature ( $T_{onset}$ ) and maximum degradation temperature ( $T_{max}$ ) of HNTs reinforced polymers increased drastically when compared to neat polymers. It can also be seen from the DTA curve that the endothermic feature at around 390 °C for pure PS is shifted to relatively higher temperatures; this further indicates enhanced thermal stability of nanocomposites synthesized using HNTs and delay in the degradation process. Likewise, the onset temperature of pure PMMA is 170 °C, whereas on inclusion of HNTs, the onset temperature shifted to 378 °C (Fig. 8.9b). In addition, the DTA curve showed delay in the degradation process due to presence of HNTs. The increase in the thermal stability on reinforcing the polymer with HNTs is associated with the morphological changes in the nanocomposites due to the formation of intercalated as well as exfoliated structure between the polymer and clay as a result of sonication. Another reason is that clay forms char and its formation obstructs the diffusion of the volatile decomposition products, which causes a decrease in permeability, and consequently, promotes the thermal stability of the nanocomposites (Parija et al. 2004).

The thermal behavior of HNT-PS and HNT-PMMA coatings on glass were also analyzed by DSC (Fig. 8.10). The observed glass transition temperature of both PS and PMMA were increased due to the presence of HNT fillers. The increase in  $T_g$  (DTG) of HNT-PS and HNT-PMMA nanocomposites over neat polymer was found to be 12 and 16 °C, respectively. The reason for the increase in  $T_g$  of nanocomposites is due to limited mobility of interfacial polymers that are present in the interlayer spaces of HNTs, and also due to the presence of a tortuous paths among HNTs through which polymer must relax. Hence, the thermal stability of the nanocomposite coatings was greatly enhanced upon addition of HNTs to the polymer.



(a)



(b)

Figure 8.10 Glass transition temperature of (a) HNT-PS and (b) HNT-PMMA nanocomposites. The corresponding  $T_g$  values of respective neat polymers are given for comparison

### 8.2.5 Mechanical behavior of HNT-PS and HNT-PMMA nanocomposites

Evaluation of the mechanical behavior of glass before and after coating with HNT-based polymer nanocomposites is important in order to understand the effect of coating on the mechanical stability of surface. Hence, the tensile and scratch tests were performed to study the mechanical behavior of the nanocomposite coatings.

#### 8.2.5.1 Tensile tests

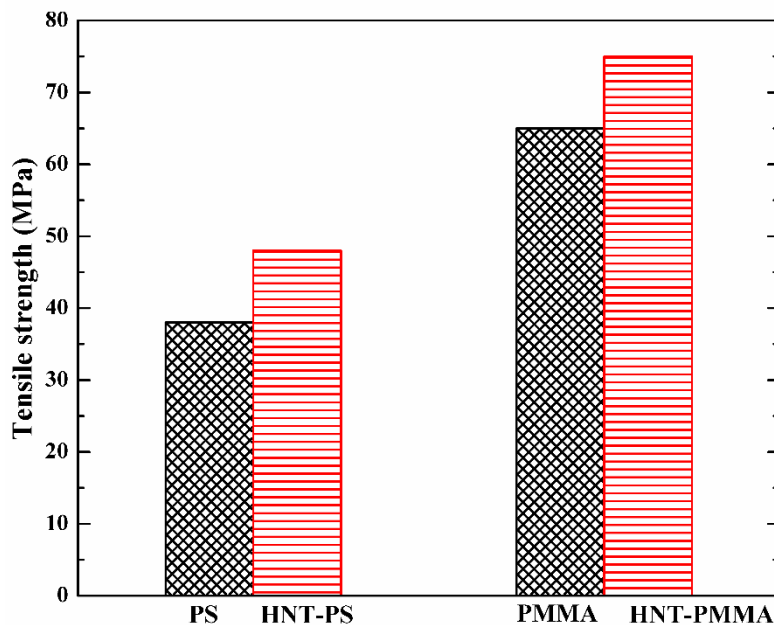


Figure 8.11 Tensile strength HNT-PS and HNT-PMMA nanocomposites along with their corresponding neat polymer values

Figure 8.11 shows the effect of addition of HNTs on the tensile strength of PS and PMMA nanocomposites. Addition of HNTs in polymer improves the tensile strength of nanocomposite in both cases. This behavior can be attributed to the large aspect ratio of HNT which act as efficient stress transfer agents in the nanocomposites. This induces plastic deformation in the polymer matrix and consequently enhances the tensile strength. Another possible reason for an increase in tensile strength of HNT-polymer nanocomposites is due to formation of numerous intermolecular hydrogen bonds between the polymers and HNT which facilitates 3D network and the negative charges on the HNT surface makes it readily interacting with the polymers through electrostatic attraction (Huang et al. 2012).

### 8.2.5.2 Scratch tests

All four types (C, Br, G, and Gr) of both coated and uncoated glass samples were subjected to scratch tests to analyze the scratch resistance of the coatings. Scratch test was performed using HB pencils. Pencil hardness test is a simple and effective method to analyze the scratch resistance of the coatings (Bhanvase et al. 2012a). The pencil was sharpened and used to scratch the surface of the glass samples. Pencil hardness from 6B to 9H were used for this study. The scratch test results are provided in Table 8.3. The glass substrates without coatings could not maintain their scratch resistance beyond F pencil hardness. Neat polymer coatings without HNTs on glass samples could resist scratches upto 2B. But the samples coated with both HNT-PS and HNT-PMMA nanocomposite coatings were able to withstand without any scratch against upto 6H and 5H pencils, respectively. PS generally possesses a better scratch resistance compared to PMMA due to its relatively higher molecular weight. Hence, HNT-PS coated glass samples exhibited a better scratch resistance in comparison with HNT-PMMA coated glass samples (Moghbelli et al. 2008). The enhancement in scratch resistance of the HNT-based coatings can be ascribed to the presence of hard HNTs.

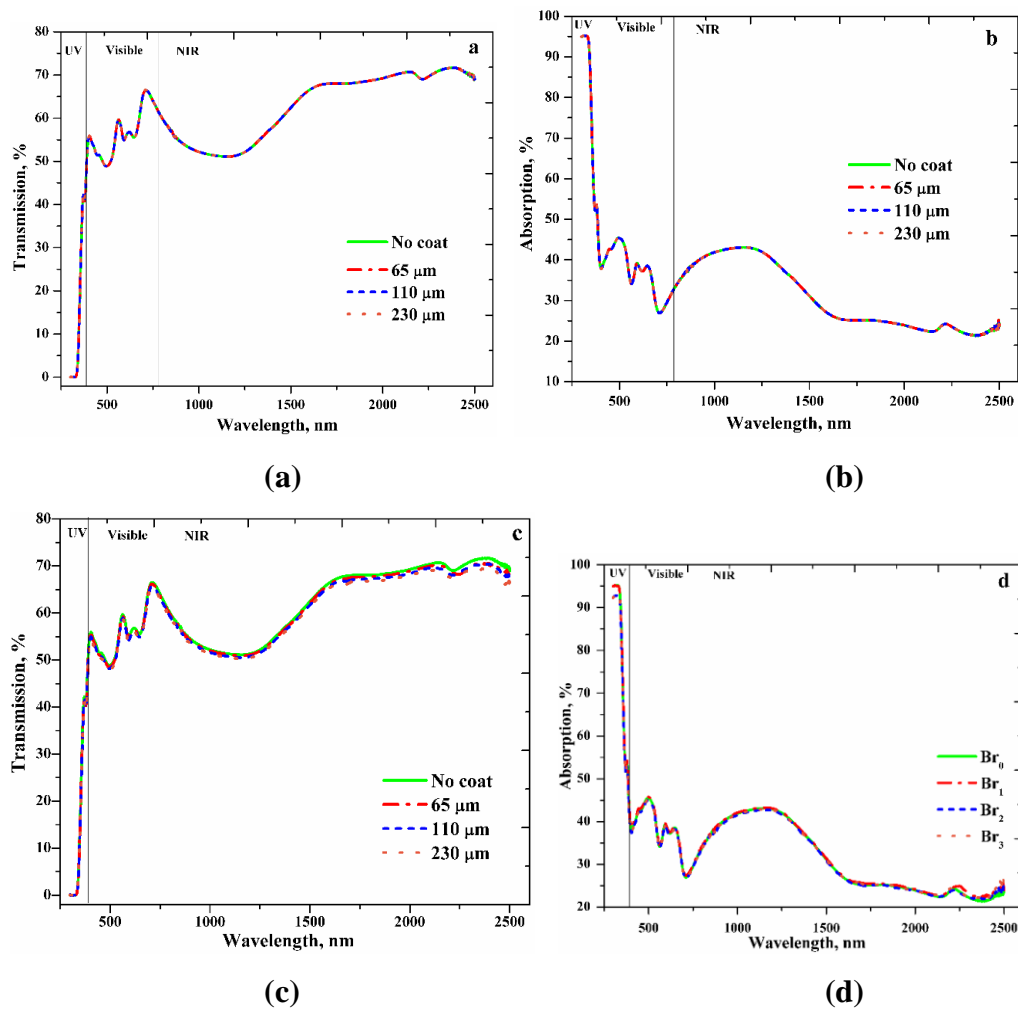
Table 8.3 Scratch test results of all four types of glass samples

<b>Sl. No.</b>	<b>Pencil Hardness</b>	<b>Without coating</b>	<b>Neat polymer (PS/PMMA) coating without HNTs</b>	<b>HNT-PS coated</b>	<b>HNT-PMMA coated</b>
1.	6B	Pass	Pass	Pass	Pass
2.	5B	Pass	Pass	Pass	Pass
3.	4B	Pass	Pass	Pass	Pass
4.	3B	Pass	Pass	Pass	Pass
5.	2B	Pass	Pass	Pass	Pass
6.	B	Pass	Fail	Pass	Pass
7.	HB	Pass	Fail	Pass	Pass
8.	F	Pass	Fail	Pass	Pass
9.	H	Fail	Fail	Pass	Pass
10.	2H	Fail	Fail	Pass	Pass
11.	3H	Fail	Fail	Pass	Pass
12.	4H	Fail	Fail	Pass	Pass
13.	5H	Fail	Fail	Pass	Pass
14.	6H	Fail	Fail	Pass	Fail
15.	7H	Fail	Fail	Fail	Fail
16.	8H	Fail	Fail	Fail	Fail
17.	9H	Fail	Fail	Fail	Fail

### 8.3 HNT BASED PS-co-PMMA COATINGS USING SPIN COATING

#### 8.3.1 Spectral properties of HNT based co-polymer coated glass substrate

The spectral properties of glasses play a vital role in deciding its usage, and hence, they must be evaluated to analyze the effect of coating materials on them. Herein, an attempt to assess the potential use of [HNT-(PS-co-PMMA)] nanocomposites for coating soda-lime glass is performed. The spectral properties were examined at 0° tilt angle of incidence in near-ultraviolet (UV, 300 – 380 nm), visible (380 – 780 nm) and near-infrared (NIR, 780 – 2500 nm) regions of light. UV region is further divided into UV<sub>a</sub> with wavelengths ranging between 315 and 380 nm, UV<sub>b</sub> between 280 and 315 nm, and UV<sub>c</sub> between 100 and 280 nm.



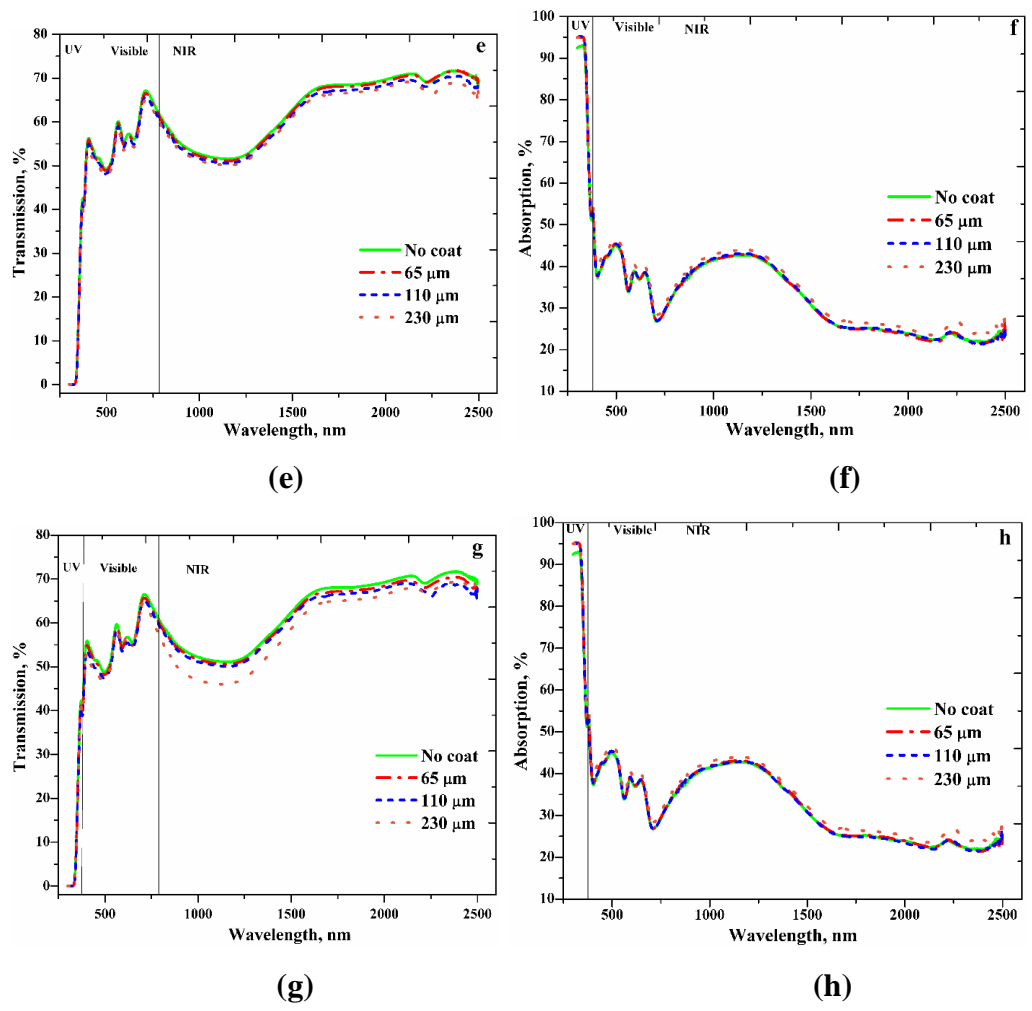
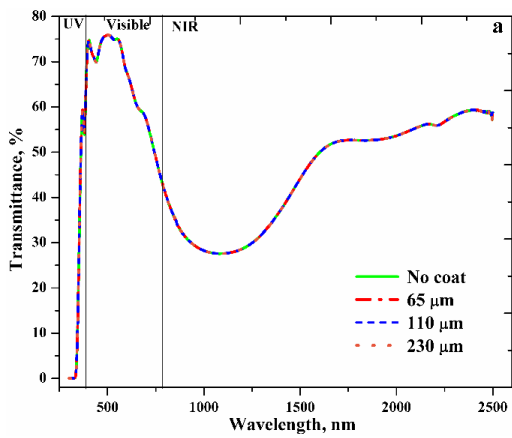
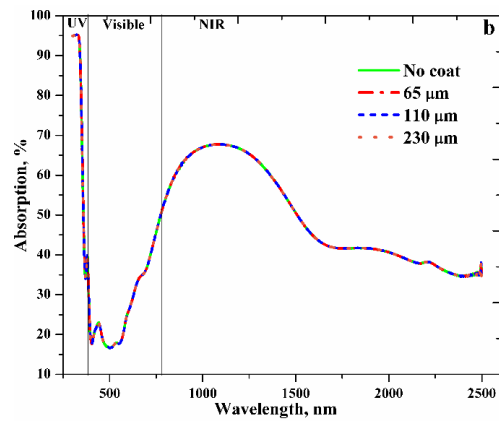


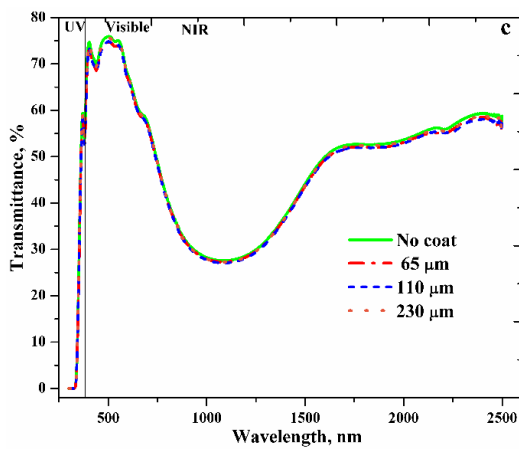
**Figure 8.12** Spectral behavior of [HNT-(PS-co-PMMA)] coated Bronze glass. (a) transmission (b) absorption of 3 wt% HNT content coating coated glass; (c) transmission (d) absorption of 5 wt% HNT content coating coated glass; (e) transmission (f) absorption of 7 wt% HNT content coating coated glass; (g) transmission (h) absorption of 10 wt% HNT content coating coated glass; Different coating thicknesses of samples are indicated by different colors ( $Bz_0$  – uncoated,  $Bz_1$  – 65  $\mu\text{m}$ ,  $Bz_2$  – 110  $\mu\text{m}$ ,  $Bz_3$ –230  $\mu\text{m}$ )



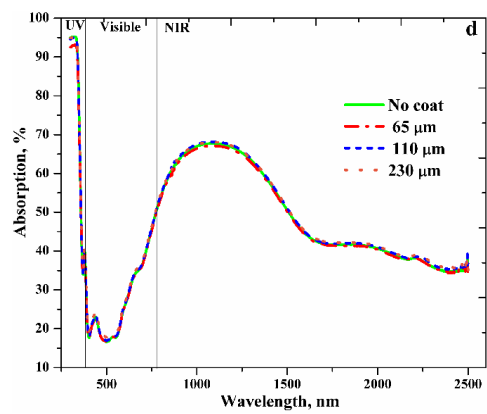
(a)



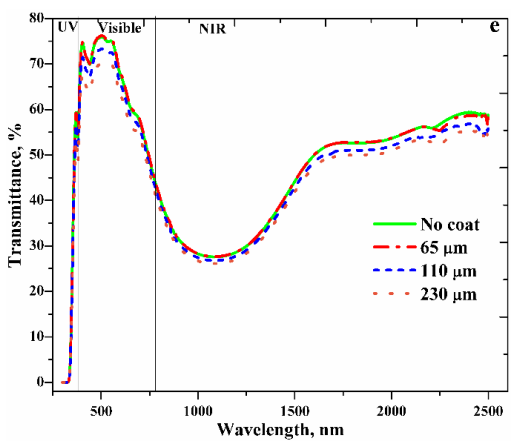
(b)



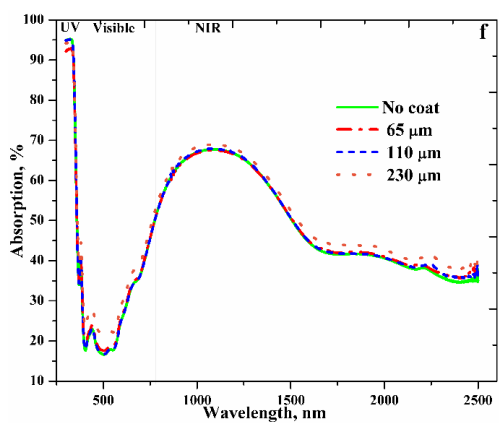
(c)



(d)



(e)



(f)



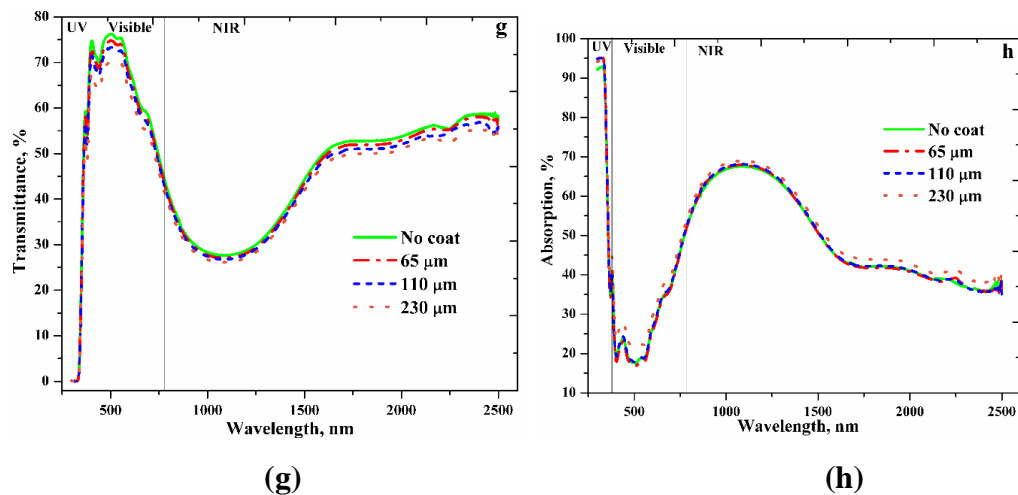
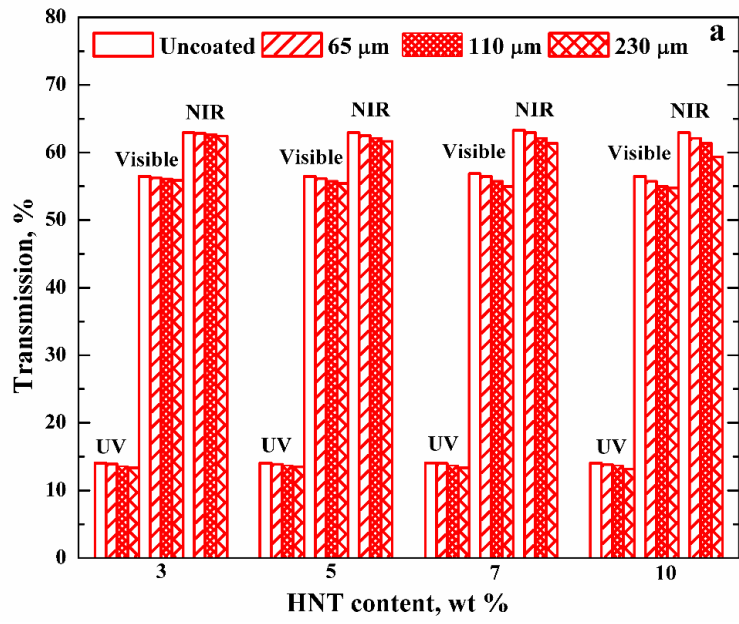


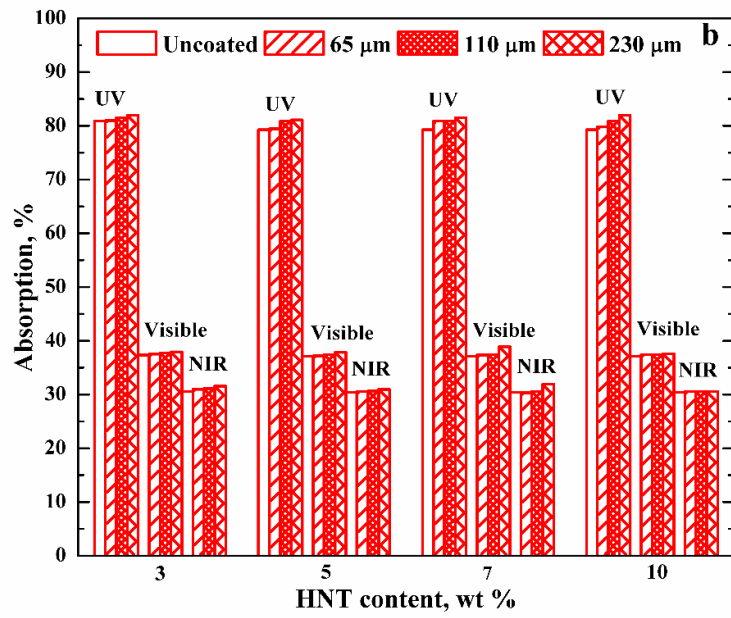
Figure 8.13 Spectral behavior of [HNT-(PS-co-PMMA)] coated Green glass. (a) transmission (b) absorption of 3 wt% HNT content coating coated glass; (c) transmission (d) absorption of 5 wt% HNT content coating coated glass; (e) transmission (f) absorption of 7 wt% HNT content coating coated glass; (g) transmission (h) absorption of 10 wt% HNT content coating coated glass; Different coating thicknesses of samples are indicated by different colors ( $GG_0$  – *uncoated*,  $GG_1$  – 65  $\mu\text{m}$ ,  $GG_2$  – 110  $\mu\text{m}$ ,  $GG_3$  – 230  $\mu\text{m}$ )

The spectral characteristics of coated glass samples in UV, visible and near infrared regions (NIR) were calculated and presented in Figs. 8.12 and 8.13 to have a detailed understanding of the spectral behaviour of these coatings in different regions of wavelength. The transmission and absorption of uncoated and coated Bz and GG glass coupons in UV, visible and NIR regions were reported as a function of HNT content in coatings and coating thickness in Fig. 8.14. It can be observed that there were no significant changes in the spectral properties of both Bz and GG glasses due to the applied coatings containing 3 – 5 wt % HNT content. On increasing the HNT content of coatings further, a slight decrease in the transmission and increase in absorption was noticed for both Bz and GG glasses. It indicates that increase in HNT content beyond 5 wt % could slightly obstruct the passage of light through the glasses. It is mainly because some of the radiations are absorbed by the coating which contributes to the reduction in transmission. However, since there was no drastic change in the spectral behaviour of glasses, the transparency and optical clarity of glasses were retained. A similar kind of result was observed in the case of HNT based PS and PMMA

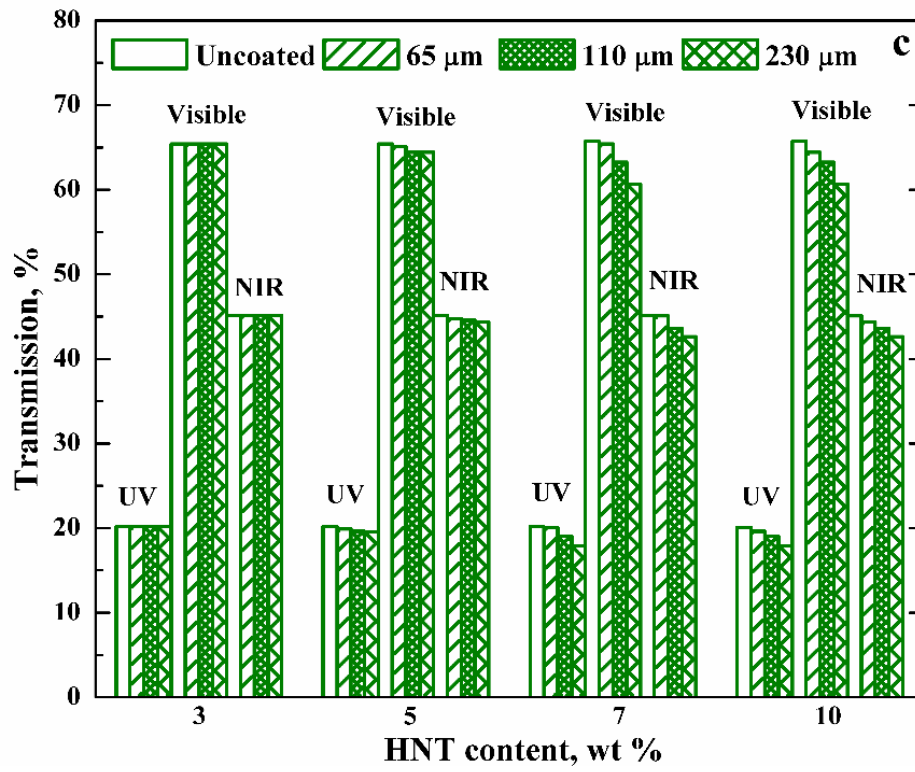
nanocomposite coatings as seen in section 8.2. The capability of glass to protect indoor materials and human skin from solar radiation is quantified in terms of solar material protection factor (SMPF) and solar skin protection factor (SSPF). Jelle et al. (2007) reported solar radiations, in particular, ultraviolet rays damage materials as well as human skin and hence there is a need to protect them. Else, it may result in photo-damage of materials whose intensity ranges from discoloration of material to loss in its mechanical integrity. Human skin may undergo light sun tanning or sun burning, thereby resulting in loss of skin integrity. The wavelength of solar radiations that reach the surface of the earth can range approximately between 295 *and* 2500 nm. The solar radiation classified as UV<sub>a</sub> (315 – 400 nm) has the energy between 389 *and* 300 kJ.mol<sup>-1</sup>. Whereas UV<sub>b</sub> (280 – 315 nm) has the highest energy around 426 – 380 kJ.mol<sup>-1</sup> but fortunately the highest energetic part of UV<sub>b</sub> (280 – 295 nm) is filtered by the stratosphere and does not reach the surface of the earth (Pospisil and Nespurek 2000). The effects of solar irradiation can be predicted by calculating SMPF and SSPF values of glass (ISO 1992). Higher values of SMPF and SSPF means better protection of material and skin, respectively. The SSPF and SMPF are plotted as a function of HNT content and coating thickness in Fig. 8.14e and f. The PS-co-PMMA nanocomposite coating on glass improves the protection to materials and skin against solar radiations. It can be observed that there is considerable improvement in the SMPF values on increasing the HNT content in coatings. It is due to the uniform distribution of HNTs in the copolymer achieved by sonication. Also, HNTs aid in stabilizing and conserving the polymers from photo-degradation and improve the photo-resistance of polymers (Hoang-Minh T et al. 2010). The improvement in protection factors can also be attributed to the formation of the tortuous paths by HNTs in the copolymer matrix. This obstructs the passage of radiations across the glass. The transmission of light decreased for both the glasses (Bz and GG) in the UV region between 300 *and* 400 nm and absorption increased slightly in this region. It suggests that UV<sub>a</sub> radiations and some part of UV<sub>b</sub> radiations were absorbed by the coatings which resulted in a higher SMPF. It is also evident from



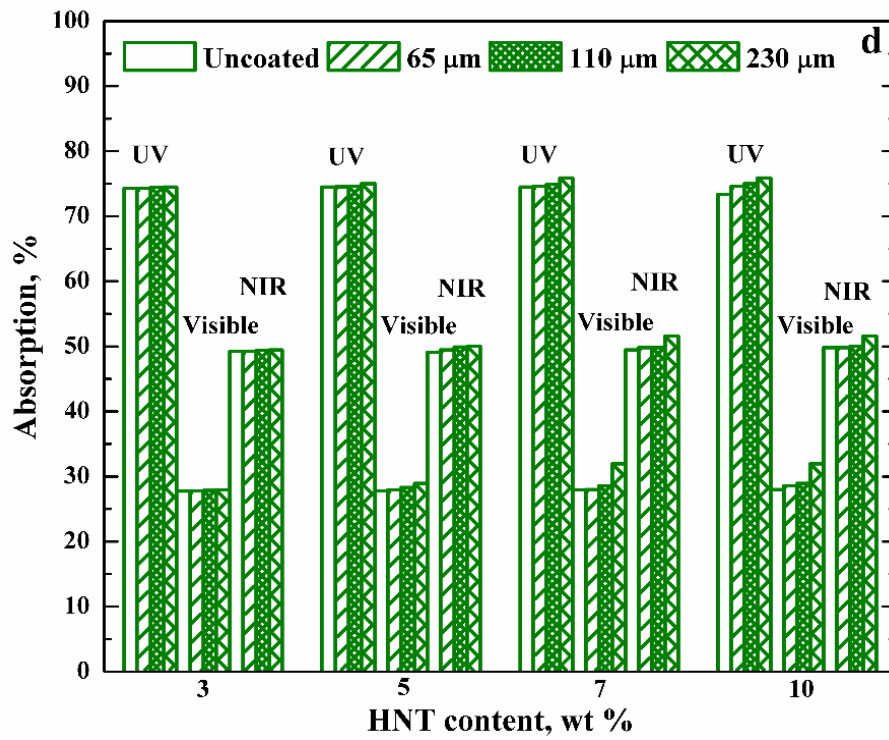
(a)



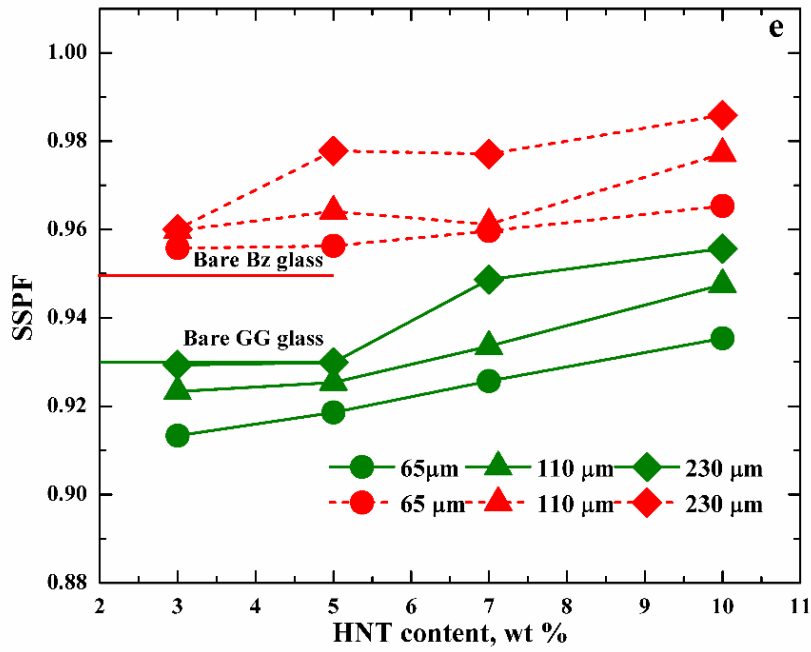
(b)



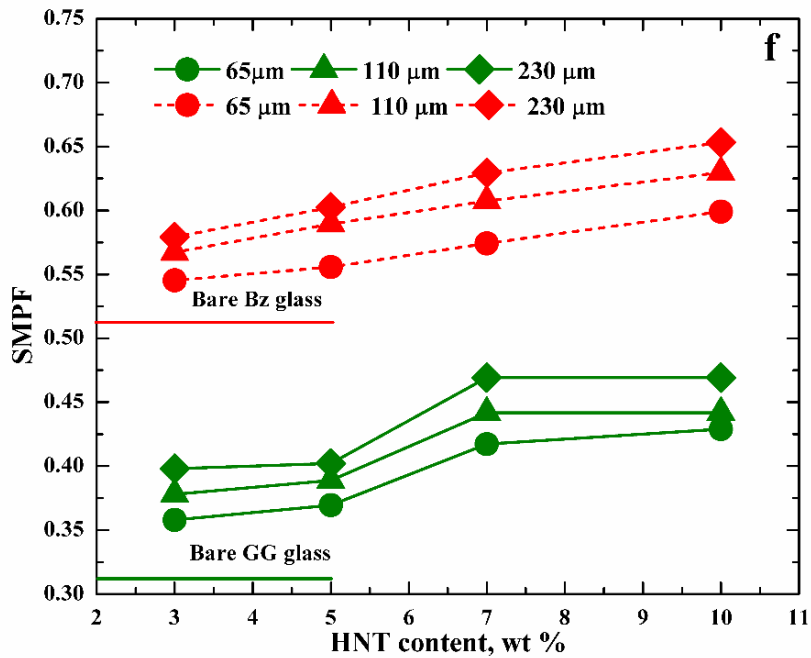
(c)



(d)



(e)

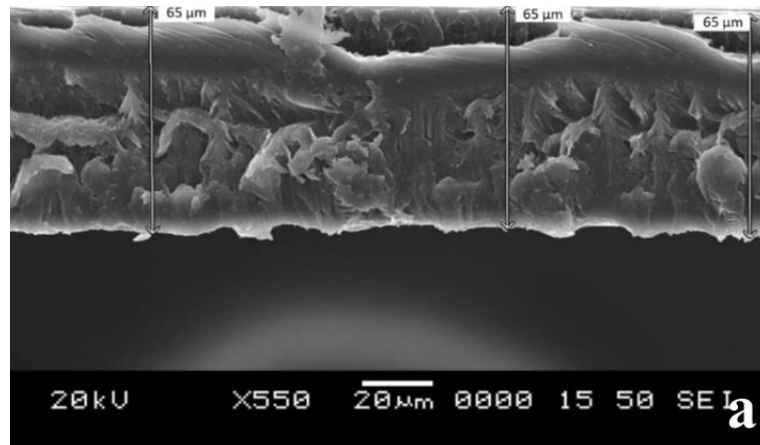


(f)

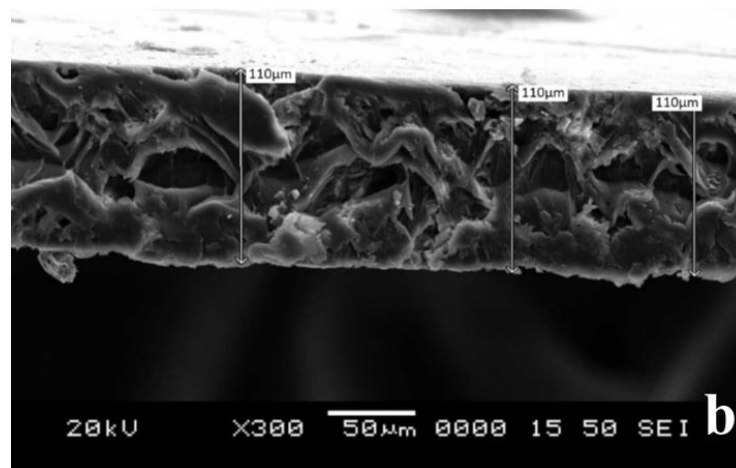
Figure 8.14 Effect of different HNT content and coating thickness on (a) Transmission of bronze glass (b) Absorption of bronze glass (c) Transmission of bronze glass (d) Absorption of green glass (e) SSPF of bronze and green glass (f) SMPF of bronze and green glass

Fig.8.14e and f that higher values of SSPF and SMPF can be obtained by increasing the thickness of the coating. It is also that due to the capability of HNTs to resisting photo-oxidation, the [HNT-(PS-co-PMMA)] coatings can retain their mechanical properties in extreme conditions, and hence they provide better protection factors (Scarfato et al. 2015). Also, in comparison with HNT-PS and HNT-PMMA coatings, [HNT-(PS-co-PMMA)] coatings display a notable increase in SMPF value due to the increased content of HNTs and the synergetic effects of PS and PMMA in a copolymer.

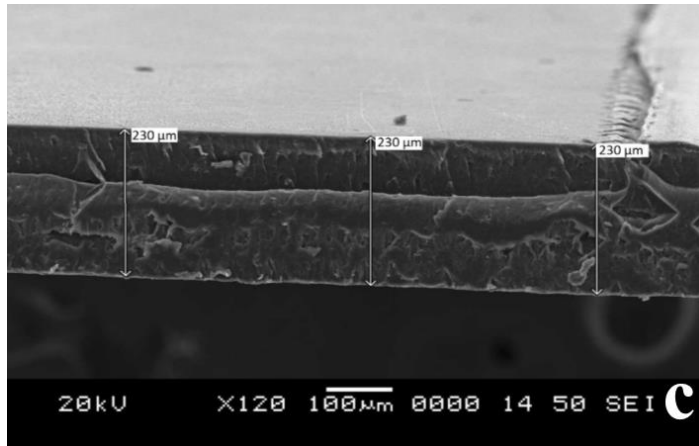
### 8.3.2 Morphology of HNT-based co-polymer coatings



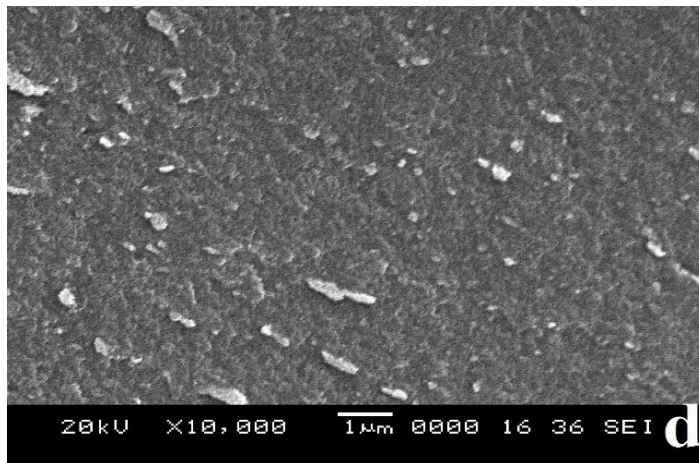
(a)



(b)

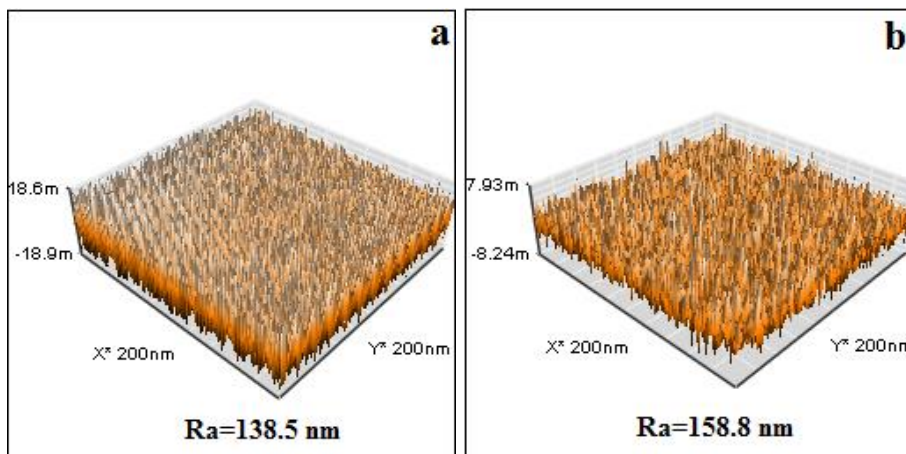


(c)



(d)

**Figure 8.15 SEM images of cross-section of 5 wt% [HNT-(PS-co-PMMA)] nanocomposite coatings on Bronze (Bz) glass having different coating thickness: (a) 65  $\mu\text{m}$ , (b) 110  $\mu\text{m}$ , (c) 230  $\mu\text{m}$**



(a)

(b)

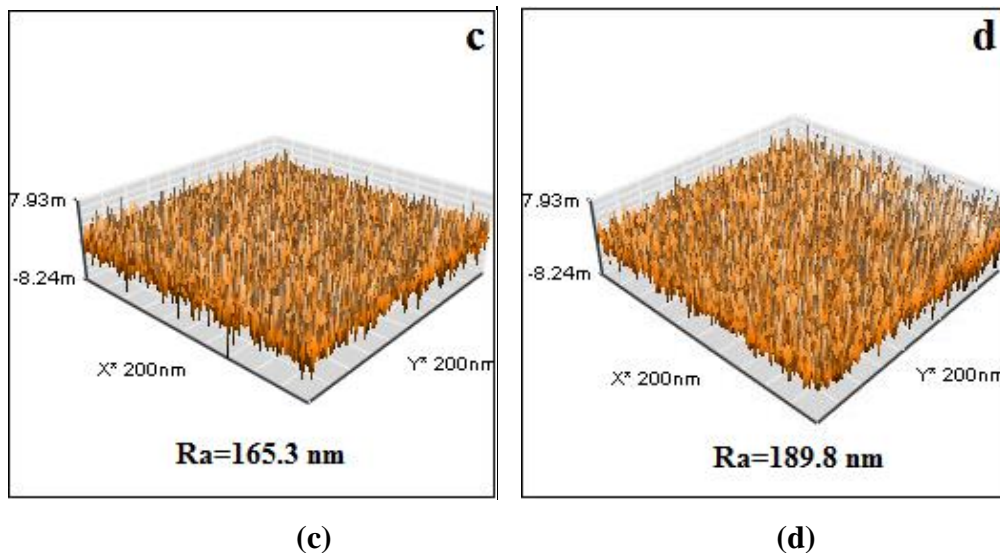


Figure 8.16 Atomic Force Microscope images of surface of coated bronze glass with a thickness of **110  $\mu\text{m}$** . The content of HNTs in the coatings are **(a) 3 wt%** **(b) 5 wt%** **(c) 7 wt%** **and (d) 10 wt%**

Fig. 8.15 shows the cross-section and thickness of coating containing 5 wt% of HNTs on glass coupons obtained from SEM analysis. The thickness of the coating was calculated from SEM images by taking an average of different values measured at multiple locations. Three different coating thicknesses, i.e., 65  $\mu\text{m}$ , 110  $\mu\text{m}$ , 230  $\mu\text{m}$ , were achieved. The uniform distribution of HNTs in the polymer matrix is crucial in getting the enhanced properties of the nanocomposites. The distribution of HNTs in the polymer matrix can be seen in Fig. 8.15d. It can be observed that the particles are distributed evenly in the polymer matrix. 60 min of sonication time was good enough for achieving better dispersion. Sonication produces acoustic cavitation and streaming, in a polymer solution containing HNTs, which greatly aid in achieving a uniform distribution of HNTs in the polymer matrix. The implosion of cavitation bubbles results in the production of high pressure and temperatures and high shear which led to a reduction in agglomerates of the HNT particles. There is a presence of outthrusters which provided necessary surface roughness. The surface roughness of coatings with different HNT content was calculated from AFM analysis and plotted in Fig. 8.16. It can be seen that the surface roughness of coatings increases with the HNT content in coatings. SEM



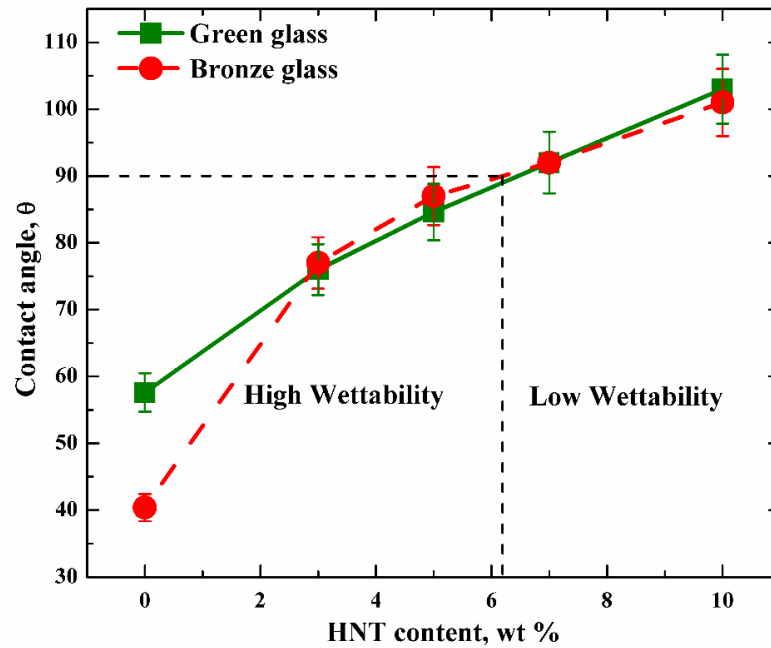
images also reveal that the coating has a uniform distribution of HNTs in the polymer which is responsible for the enhanced hydrophobic behavior of the coatings.

### **8.3.3 Surface wetting behavior of coated and uncoated glass substrates**

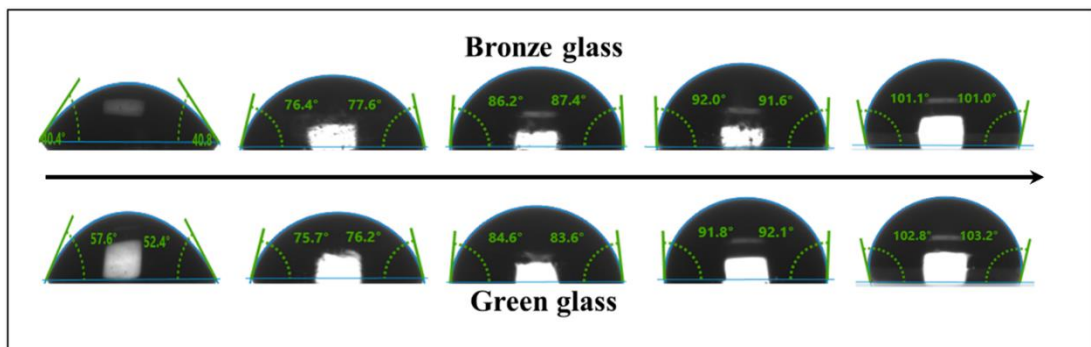
Surface wetting is another interesting behavior of the coating materials. The application of hydrophobic coatings on glasses may improve their self-cleaning and antifouling properties. Since the surface energy of glass is generally high, most of the liquids, completely wet the glass surface which restricts its application in various fields. Thus, altering this nature of glass by applying hydrophobic coatings, i.e., making the surface as relatively hydrophobic can broaden its applications. Addition of surface roughness to the hydrophobic coatings on the surface of glass is one way to improve the hydrophobicity (reducing wettability) of coated glass (Zhang et al. 2016).

Surface roughness traps air in its irregularities which directs water droplets to reside on the outthrust and prevents complete surface wetting. AFM analysis reveals that the surface roughness ( $Ra$ ) of the 110  $\mu m$  thickness HNT (5 wt%)-PS-co-PMMA coating is 158.8 nm. The value lies close to that of HNT (5 wt%)-PMMA coating (157.6 nm) but higher than that of HNT (5 wt%)-PS coating (127 nm). Whereas, there is a significant improvement in surface roughness of [HNT-(PS-co-PMMA)] nanocomposite coatings with increasing HNT content (Fig. 8.16), which majorly contributes to the hydrophobic behavior of coatings. The surface roughness of the coatings with 3, 5, 7 and 10 wt% of HNTs was measured as 138.5, 158.8, 165.3, and 189.8 nm, respectively. It can be observed the surface roughness of coatings increases with HNT content owing to decrease in wettability. It emphasizes that the contact area on the surface that is available to interact with water is very low which enhances the hydrophobicity of the coatings. To further investigate the surface wettability of coatings on glass, contact angle measurements were made, and the results are presented in Fig. 8.17. Generally, surfaces with higher contact angle exhibit better hydrophobicity. The contact angle images of glass specimens coated with coatings containing different HNT content are provided for visualization in Fig. 8.17b. It can be seen that increase in HNTs content in coatings resulted in a drastic increase in contact angles of the coatings. Also, in comparison with HNT based PS and PMMA

nanocomposites coatings (section 8.2), [HNT-(PS-co-PMMA)] nanocomposite coatings exhibited better hydrophobicity.



(a)



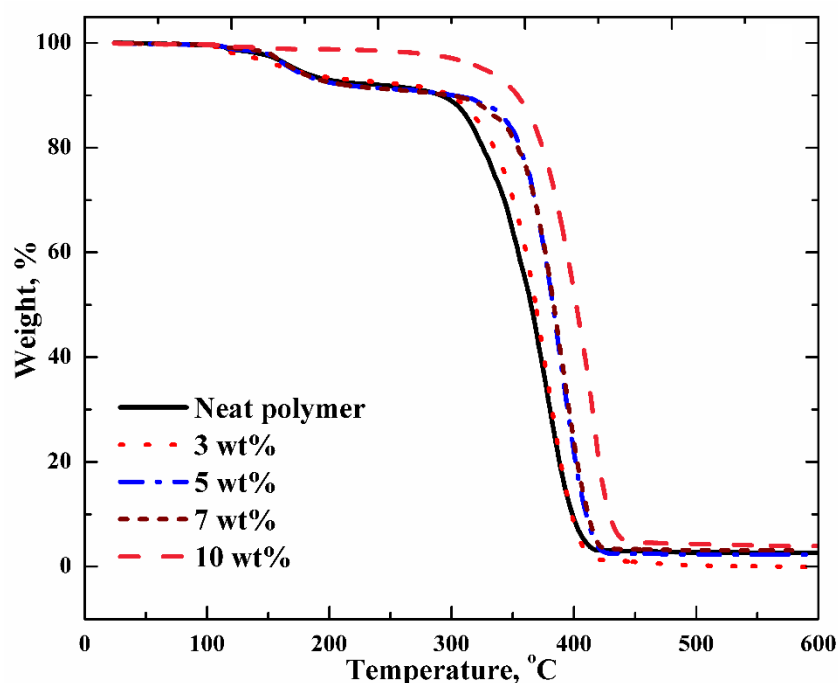
(b)

**Figure 8.17 (a)** Effect of HNT content of coatings on contact angles measured with water droplet coated glass with coating thickness of  $110 \mu m$ . Contact angle value at  $0 \text{ wt}\%$  HNT is measured using a neat PS-co-PMMA coated glass, and (b) Images of a water droplet on glass samples coated with neat PS-co-PMMA and [HNT-(PS-co-PMMA)] nanocomposite coatings containing 3, 5, 7, and 10 wt% HNTs, respectively. The direction of the arrow indicates the increasing content of HNTs in coatings

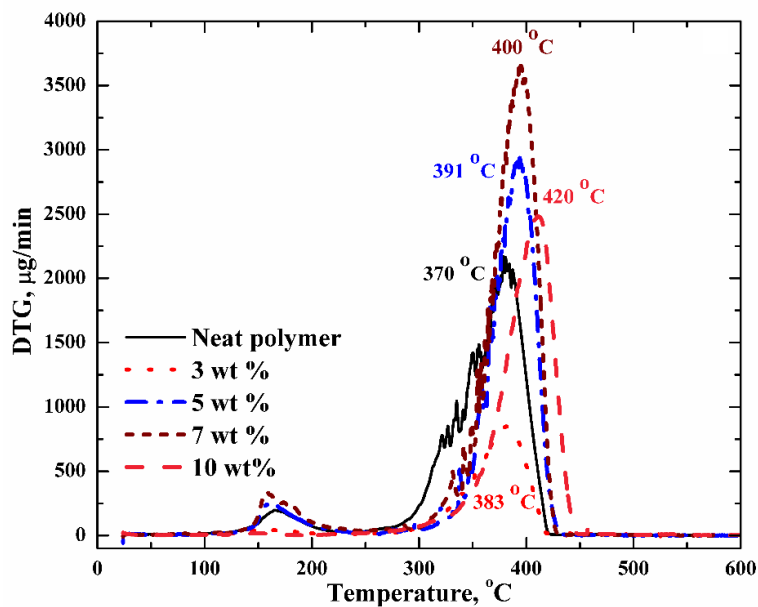
### 8.3.4 Thermal behavior of HNT based PS-co-PMMA nanocomposites

Thermal behavior of [HNT-(PS-co-PMMA)] nanocomposite coatings was investigated to understand the exposure of coatings to high temperatures. The thermogravimetric analysis (TGA) and derivatized thermal gravimetric analysis (DTG) of [HNT-(PS-co-PMMA)] coatings containing different HNTs content (0, 3, 5, 7 and 10 wt%) was carried out. The thermal stability of coatings becomes high when HNT content increases as shown in TGA and DTG curves (Fig. 8.18). The DTG curve (Fig. 8.18b) shows a delay in the degradation of the copolymer with the highest HNT content signifying the role of HNTs in increasing the stability of the copolymer. This is due to the intercalated and exfoliated morphology formed between HNT and polymer. Also, HNTs form char and obstruct diffusion of volatile decomposition products causing a decrease in permeability and promotes thermal stability (Parija et al. 2004). In comparison with HNT based PS and PMMA nanocomposites, [HNT-(PS-co-PMMA)] nanocomposite shows better thermal stability. It can be explained as follows. Generally, the thermal degradation of polystyrene occurs by breaking of polymer chain followed by a depropagation process as a result of competition between the three different reaction mechanisms, i.e., unzipping, intramolecular and intermolecular hydrogen transfer. Hence, the typical end products of polystyrene include styrene monomer, the dimer and the trimer (styrene monomer was the major product and oligomers present in traces) (McNeill et al. 1990). On the other hand, degradation of the poly(methyl methacrylate) occurs as per the usual mechanistic scheme consisting of chain end and random chain scission initiation, depropagation and termination (Holland and Hay 2001). Hence thermal degradation of PS-co-PMMA would take more time because it involves decomposition of both PS and PMMA. This is the reason for the better thermal stability of the copolymer. It can be observed from the DTG curves that the decomposition of the PS-co-PMMA copolymer containing 5 wt% HNT occurs between 300 and 430 °C. To further understand the degradation, FT-IR analysis was carried out at four temperatures before degradation, at maximum degradation and after degradation, i.e., at 300, 390, 430, and 500 °C, respectively. The results are presented in Fig. 8.18c. At initial degradation, i.e., at 300 °C the IR bands at 1300 to 1800  $cm^{-1}$  represents the evolution of water and unsaturated aromatic compounds, the bands around wavenumber 2300  $cm^{-1}$  represents CO<sub>2</sub> emissions, the bands at 3020  $cm^{-1}$  can

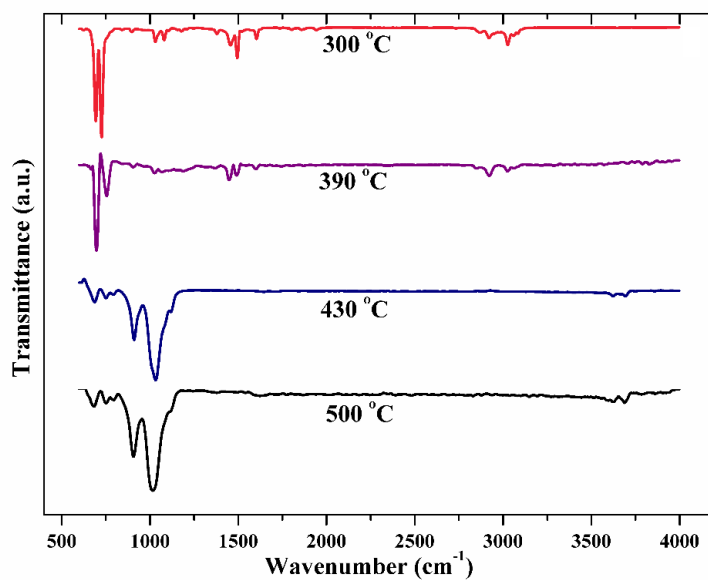
be attributed to C-H vibrations. These bands suggest that the [HNT-(PS-co-PMMA)] nanocomposites degrade via unzipping depolymerization leading to the formation of monomers or evolution of volatiles. Thus, a considerable decrease in all the bands can be seen. At 390 °C, all these species were detected in the IR spectra for 5 wt% HNT-PS-co- PMMA nanocomposite. It confirms the maximum decomposition temperature as observed in the TGA analysis. The evolution of gaseous products initiates at around 320 °C, gradually it increases to a maximum at 430 °C and then decreases. The major evolution of gases will subside around 500 °C, later only traces of gases appear. The major degradation product is CO<sub>2</sub> (2300, and 1700 cm<sup>-1</sup>) in all cases. This evolution of CO<sub>2</sub> was mainly due to cleavage of C-N amide bond and also from the alkyl chain oxidation. Hence the degradation of the copolymer is evident from Fig. 8.18c (Achhammer et al. 1951; Celina et al. 1997; Kandare et al. 2006).



(a)



(b)



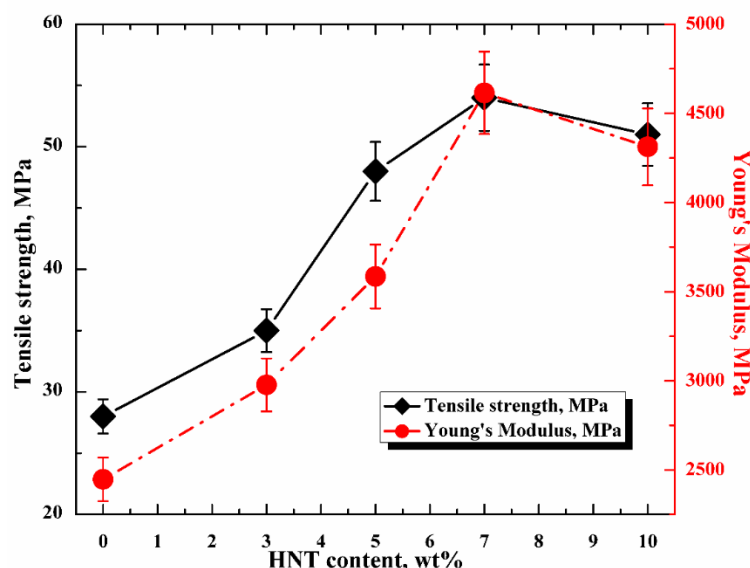
(c)

Figure 8.18 Thermal stability of [HNT-(PS-co-PMMA)] nanocomposite containing different amounts of HNT (a) The solid black line represents the TGA curve of neat PS-co-PMMA polymer and it is given for comparison to show the enhanced thermal stability. The corresponding DTG curves are presented in (b) FT-IR spectra of PS-co-PMMA copolymer with **5 wt %** HNT at different temperatures (c)

### 8.3.5 Mechanical properties of HNT based PS-co-PMMA nanocomposites

Mechanical properties and wear resistance of coatings play a major role in determining the durability of coatings. Hence, the effect of HNT content in coatings on tensile strength and Young's modulus of nanocomposite coatings were evaluated.

#### 8.3.5.1 Tensile tests



**Figure 8.19** Effect of HNT content on mechanical properties [HNT-(PS-co-PMMA)] nanocomposite. The values at 0 wt% of HNT correspond to neat PS-co-PMMA polymer

The tensile properties of coatings were measured at room temperature. The strain rate was 5 mm/min under a load of 1 kN. Three measurements were made for each composite to maintain accuracy. Fig. 8.19 portrays the tensile strength and Young's modulus of coatings with different HNT contents. It can be observed that the inclusion of HNTs in the copolymer matrix up to 7 wt% HNT content greatly enhances tensile strength and Young's modulus. This improvement is due to the large aspect ratio of HNTs which behaves as competent stress transfer agents in the polymer matrix. This induces a plastic deformation in the polymer matrix and consequently enhances the tensile strength. In addition, many intermolecular hydrogen bonds formed between copolymer and HNTs facilitate 3D network as well as the negative charges on HNT which increase the compatibility between polymer and HNTs. This results in the

increased tensile strength of the [HNT-(PS-co-PMMA)] nanocomposites (Huang et al. 2012).

Increase in HNT content beyond 7 wt%, *i.e.*, 10 wt% resulted in the brittle sample, and a decrease in mechanical strength was observed. Therefore 7 wt % of HNT content was optimum for composites with the best mechanical properties for coatings. The mechanical strength of [HNT-(PS-co-PMMA)] coatings was found to be significantly higher than that of HNT based PS and PMMA coatings. Generally, PMMA is a transparent and brittle polymer, and the toughness of PMMA can be improved by combining it with PS. Therefore, the PS-co-PMMA copolymer becomes ductile which ultimately improves the tensile strength and Young's modulus. Thus the copolymer of PS and PMMA exhibits combined effects of both polymers into a single polymer which would contribute to the improved mechanical properties of the coatings.

#### **8.3.5.2 Scratch tests**

A simple scratch test was performed on coated glass samples to understand the effect of thickness of coating and content of HNTs on scratch resistance of the coated surface. Scratch test was carried out using HB pencils from 6B to 9H. If the tip of the pencil makes a scratch on the surface, the resistance is poor, and the test result is fail (F). Otherwise, the result is pass (P). The scratch resistance results of coatings are presented in Table 8.4. Increase in the HNT content resulted in enhanced scratch resistance of the coatings. HNT-based PS and PMMA nanocomposite coatings could resist scratch up to pencil hardness of 6B and 5B respectively, whereas [HNT-(PS-co-PMMA)] could resist scratch up to 7H hardness. This was due to the combined effects of PS and PMMA in a copolymer present in coatings.

Table 8.4 Effect of HNT content present in coatings on scratch resistance of [HNT-(PS-co-PMMA)] nanocomposite coatings on soda-lime glass

Sl. No.	Pencil Hardness	Glass substrate					
		No coat	0 wt%	3 wt%	5 wt%	7 wt%	10 wt%
1.	6B	Pass	Pass	Pass	Pass	Pass	Pass
2.	5B	Pass	Pass	Pass	Pass	Pass	Pass
3.	4B	Pass	Pass	Pass	Pass	Pass	Pass
4.	3B	Pass	Pass	Pass	Pass	Pass	Pass
5.	2B	Pass	Pass	Pass	Pass	Pass	Pass
6.	B	Pass	Fail	Pass	Pass	Pass	Pass
7.	HB	Pass	Fail	Pass	Pass	Pass	Pass
8.	F	Pass	Fail	Pass	Pass	Pass	Pass
9.	H	Pass	Fail	Pass	Pass	Pass	Pass
10.	2H	Fail	Fail	Pass	Pass	Pass	Pass
11.	3H	Fail	Fail	Pass	Pass	Pass	Pass
12.	4H	Fail	Fail	Pass	Pass	Pass	Pass
13.	5H	Fail	Fail	Fail	Pass	Pass	Pass
14.	6H	Fail	Fail	Fail	Fail	Pass	Pass
15.	7H	Fail	Fail	Fail	Fail	Pass	Pass
16.	8H	Fail	Fail	Fail	Fail	Fail	Fail
17.	9H	Fail	Fail	Fail	Fail	Fail	Fail



## 8.4 SUMMARY

In this work, halloysite (HNT)-based polystyrene (HNT-PS) and polymethylmethacrylate (HNT-PMMA) nanocomposites were synthesized by ultrasound-assisted blending and the characteristics of nanocomposite coatings over four different types of soda-lime glass were investigated. Good dispersion of HNTs in the polymer matrix is crucial for the enhancement of properties in nanocomposites. SEM analysis revealed that 60 *min* of sonication facilitates a good dispersion of HNTs in polymer. The DSC and TGA results indicated that there is a significant improvement in the thermal stability of coatings upon inclusion of HNTs in the polymer matrix. From the spectral analysis of coated glass samples, a negligible change in the absorbance, transmittance and reflectance properties was observed when compared to uncoated glasses. Hence, HNT-based PS and PMMA nanocomposites can be potentially used as protective surface coatings for glass substrates without altering their inherent spectral properties. Further, the coated glasses exhibit better hydrophobic behavior which is the prime requirement in most of the applications. Finally, the mechanical behavior like tensile strength and scratch resistance of coatings were also found to be higher for nanocomposites compared to their neat counterparts. Therefore, it was demonstrated that both the HNT-based PS and PMMA nanocomposites can be effectively used as protective coatings for the soda-lime glass. [HNT-(PS-co-PMMA)] copolymer nanocomposites were prepared by ultrasound-assisted solution blending technique and applied as coatings for the soda-lime glass. Two types of glass, i.e., bronze (Bz) and green (GG), were coated using a spin coater. The effect of HNT content and thickness on the characteristics of coatings were investigated. The spectral analysis demonstrated a negligible change in the transmission and absorption of both glasses on applying coatings with HNT content of 5 *wt%*. The increase in HNTs content beyond 5 *wt%* slightly obstructed the passage of light through the glasses. However, there were no drastic changes in the spectral properties of glasses and the transparency and optical clarity of glasses were retained. Hence, [HNT-(PS-co-PMMA)] nanocomposite coatings can be used as a potential coating material for the soda-lime glass. The SSPF and SMPF values can be made higher by increasing the content of HNTs and thickness of coating. SEM analysis confirmed the uniform distribution of HNTs in the copolymer

matrix which is crucial for the enhancement of nanocomposite's properties. The surface roughness and the contact angles of coatings on glass increased with HNT content. Contact angle measurements were in concert with surface roughness results from AFM analysis. A notable improvement in the thermal stability as well as mechanical properties of the [HNT-(PS-co-PMMA)] nanocomposite coatings compared to their neat counterparts was confirmed from TGA and tensile tests. [HNT-(PS-co-PMMA)] nanocomposite coatings exhibited better hydrophobicity, thermal, and mechanical properties compared with HNT-PS or HNT-PMMA nanocomposites due to the synergetic effect of both the polymers. It is evident that the [HNT-(PS-co-PMMA)] nanocomposite coatings possess good thermal stability, mechanical strength, and hydrophobicity. They ensure the better protection of the surface and the increased durability of the soda-lime glass.

## **CHAPTER 9**

### **APPLICATION OF HNT-BASED PS MEMBRANES FOR WATER PURIFICATION**

*This chapter presents the technical feasibility of HNT-polymer composite membranes, fabricated by an ultrasound-assisted solution casting method, for water purification. To this end, the effects of various solvents on the structure, morphology, thermal, and mechanical properties of HNT-PS membranes were investigated. The results of water samples after treatment by passing through these membranes are reported.*

#### **9.1 INTRODUCTION**

Membrane technologies are a sustainable solution for treatment of water and wastewater. In this chapter the technical feasibility of halloysite nanotube-polystyrene (HNT-PS) membranes, fabricated by an ultrasound-assisted solution casting method, for water purification is explored. The fabricated HNT nanocomposites were first characterized in order to assess the structural, morphological, mechanical, and thermal properties of the membranes. A detailed investigation on the formation of pores filled with HNTs was carried out using different solvents. Also, the effects of various solvents on the structure, morphology, thermal, and mechanical properties of HNT-PS membranes were investigated. The basic properties of the membranes were then assessed in terms of percent solvent content, porosity, pure water flux, shrinkage ratio, rejection, and recovery. The actual performance of these membranes was tested against effluent wastewater samples collected from pulp and paper plant. These samples were subjected to the water purification procedures, and the water quality of the treated samples was then assessed in terms of changes in a list of key variables (e.g., turbidity, pH, conductivity, total suspended solids (TSS), total dissolved solids (TDS), biological oxygen demand (BOD), chemical oxygen demand (COD), dissolved oxygen (DO), and heavy metals) before and after the filtration. These membranes were overall useful enough to purify real wastewater collected from pulp and paper mill.

## 9.2 HNT-PS MEMBRANES FOR WATER PURIFICATION

### 9.2.1 Morphology of HNT-PS membranes by SEM and EDAX

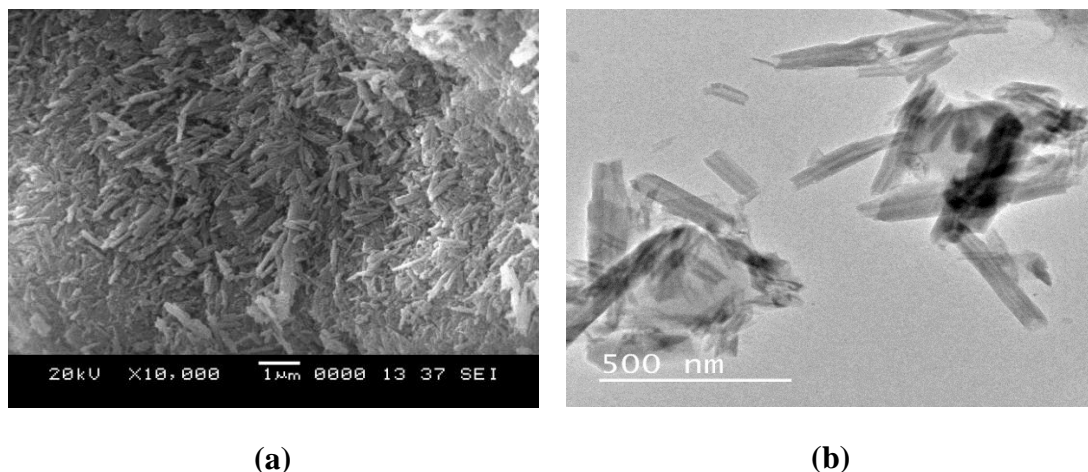


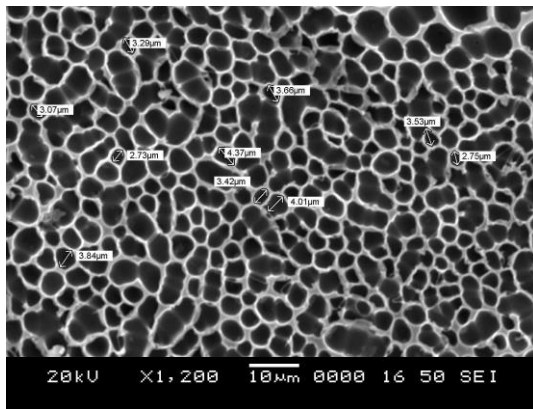
Figure 9.1 Results of the HNT image analysis: (a) SEM and (b) TEM

The SEM and TEM portraits of HNTs as received can be seen from Fig. 9.1 (a and b). It can be observed that the HNTs had nanoscale structure and were cylindrical in shape. The dispersion of inorganic filler in the polymer matrix is important in improving the overall properties of the membrane, as its properties depend upon how well and uniformly the filler is distributed in the polymer matrix. Uniform dispersion of HNTs in polymer matrix mainly depends on the selection of solvent and technique adopted for synthesis of membrane. Initial screening experiments were conducted using various aromatic and non-aromatic solvents which were reported to dissolve PS. Hence, 0.15 g of clay was added to different test-tubes, and 5 ml of various solvents were added subsequently. This mixture was then stirred for 1 h and allowed to sit for 24 h (e.g., to observe settling). As tetrahydrofuran (THF) and N-methyl-2-pyrrolidone (NMP) provided better dispersion of clay (e.g., without causing precipitation even after 24 h), they were chosen for the solvents in this study. In order to achieve uniform dispersion of HNTs in the solvent, ultrasound-assisted technique was used. A 13 mm stainless steel probe connected to an ultrasonic generator with frequency of 20 kHz (Sonics Vibra-cell, USA) was used for this study. Acoustic cavitations were effectively induced by coupling ultrasound with liquid medium for dispersion of filler

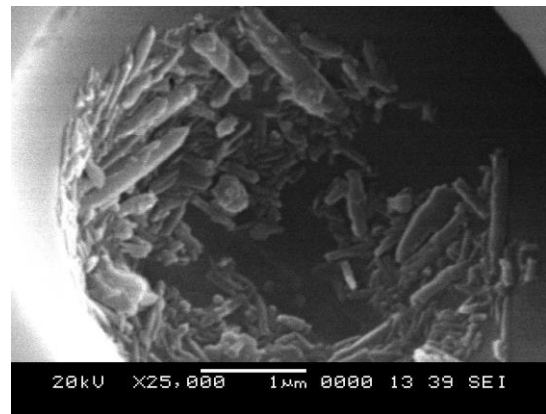
and quality control. This resulted in uniform and ordered distribution of filler in the matrix.

### **9.2.2 HNT-PS nanocomposites synthesized using tetrahydrofuran (THF) and N-methyl-2-pyrrolidone (NMP) as solvents**

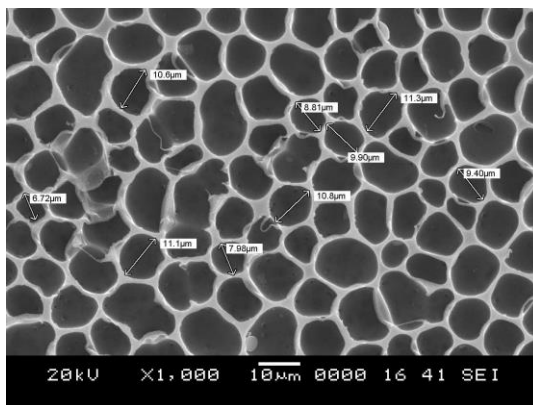
HNT-PS membrane was synthesized using THF as the solvent and was de-moisturized in an oven at 40 °C (refer to Fig. 9.2a and b). It was observed that the pore size varied roughly between 2–5  $\mu\text{m}$ . Further magnification indicated that the pores were filled with HNTs that were dispersed uniformly in the solvent after sonication. The solvent escaped from the polymer via evaporation to form pores and leave HNTs behind. These HNT-filled pores assisted in purifying water as it percolated through the pores. Due to the nanoscale dimensions of HNTs, water is purified when impurities are trapped on the membrane. During the phase inversion, an interchange between solvent and non-solvent took place due to the diffusion which caused the casting solution to undergo the phase transition for the formation of the membrane. Pore formation in the membrane depends on the mass transfer properties as well as the thermodynamics of the solution (Young and Chen 1995). The interaction between solvent and non-solvent is very significant with respect to pore formation. Due to the strong interaction between THF and water, THF in the casting solution was rapidly desolvated into the water bath. Then, the water diffused into the casting solution as it is non-solvent for the polymer. Subsequently, casting solution directly entered the solidification region to form a dense top layer. The diffusion of THF and water is hampered by the dense top layer. Hence, only some water molecules diffuse into the interior portion of the casting solution to initiate the formation of nuclei. Since the density of THF is less than water, the water droplets could sink into the polymer solution. These pores may further grow rapidly as THF diffuses into pores with a large driving force for THF and water which should lead to the formation of micropores in the polymer membrane.



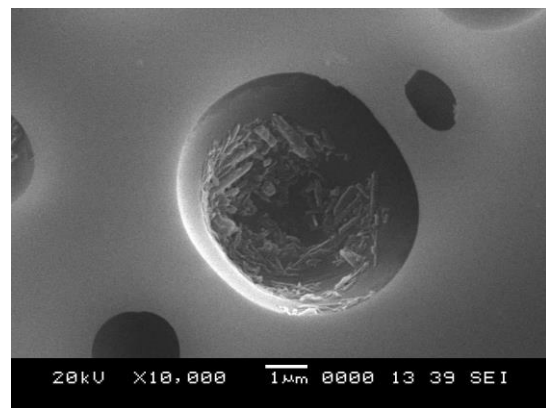
(a)



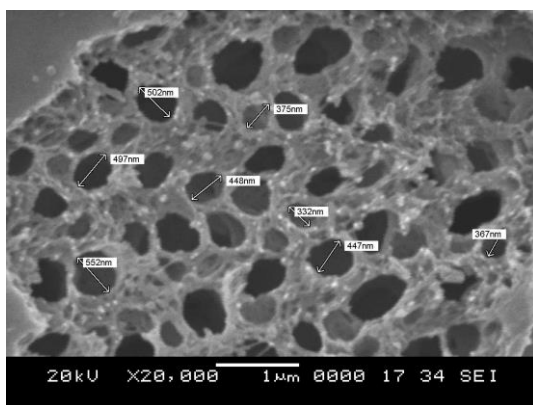
(b)



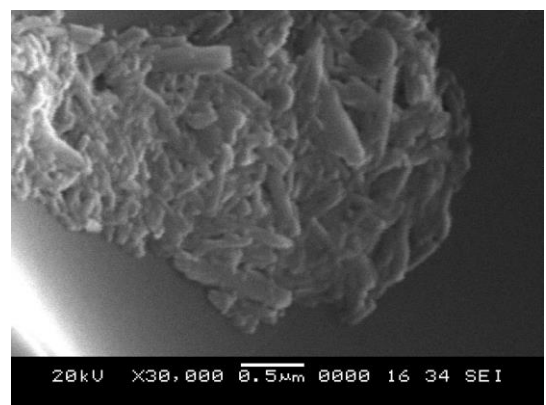
(c)



(d)



(e)



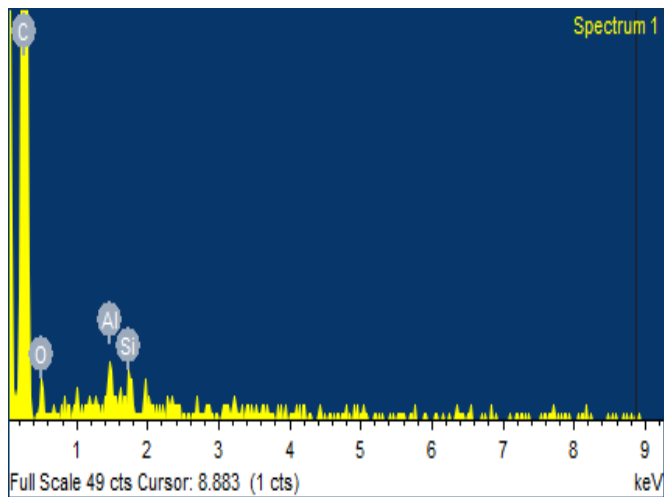
(f)

**Figure 9.2** HNT-PS microporous membrane (a) dried in an oven at 40 oC for 24 h (b) 25, 000x magnification (to view the structure inside the pore) (c) dried at room temperature for 24 h (d) 10, 000x magnification and (e) HNT-PS nanoporous synthesized using NMP as a solvent membrane (f) 20, 000x magnification (to view the structure inside the pore)

HNT-PS nanocomposites synthesized using THF and then dried at room temperature are shown in Fig. 9.2c. The same morphology was observed, although the structure has slightly larger pores. The different pore sizes might have occurred due to changes in temperature during the day and night and changes in atmospheric pressure on the surface of the membrane during evaporation. Hence, to overcome the limitations related to the formation of uneven pore sizes, the membranes were initially dried in an oven at a uniform temperature and were used for further experimentation.

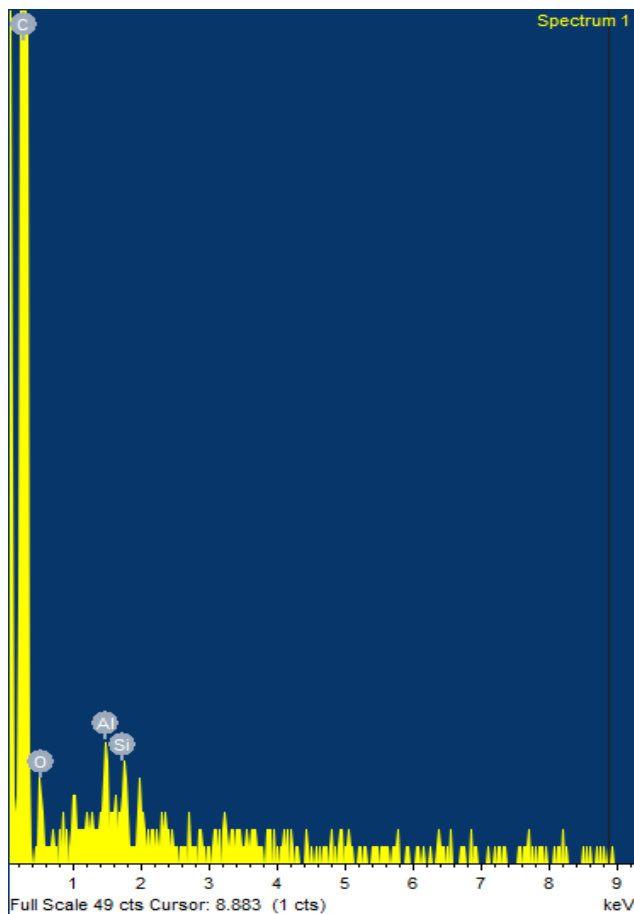
HNT-PS nanocomposites synthesized using NMP as solvent, are shown in Fig. 9.2e. Membranes synthesized using NMP possessed nanosized pores. Further magnification showed the presence of HNTs in the pores. This might reflect the relatively low evaporation rate of NMP caused by its higher density and boiling point relative to THF. Morphological investigations of the fabricated membranes confirmed the presence of two different morphologies in the produced nanocomposites. The use of different solvents (THF and NMP) led to the formation of micropore and nanopore membranes, respectively. Hence, two-stage filtration units were designed. A microporous membrane was placed in the first stage to aid the separation of micron-sized contaminants, while a nanoporous membrane in the second stage for purifying nano-sized impurities.

The EDAX analysis (Fig. 9.3 a and b) further confirmed the presence of aluminum, silicon, and oxygen in the pores of membranes. As such, these results proved the presence of HNTs in the pores. In order to understand the systematic arrangement of pores in the polymer matrix, the statistical analysis of SEM images was made for both microporous and nanoporous membrane using ImageJ as plotted in Fig. 9.4 (a and d).



Element	Weight %	Atomic %
C K	93.09	94.97
O K	6.08	4.66
Al K	0.43	0.19
Si K	0.41	0.18
Totals	100.00	

(a)



Element	Weight %	Atomic %
C K	92.70	94.69
O K	6.37	4.89
Al K	0.78	0.36
Si K	0.15	0.06
Totals	100.00	

(b)

**Figure 9.3 EDAX of HNT-PS: (a) Microporous membrane and (b) Nanoporous membrane**



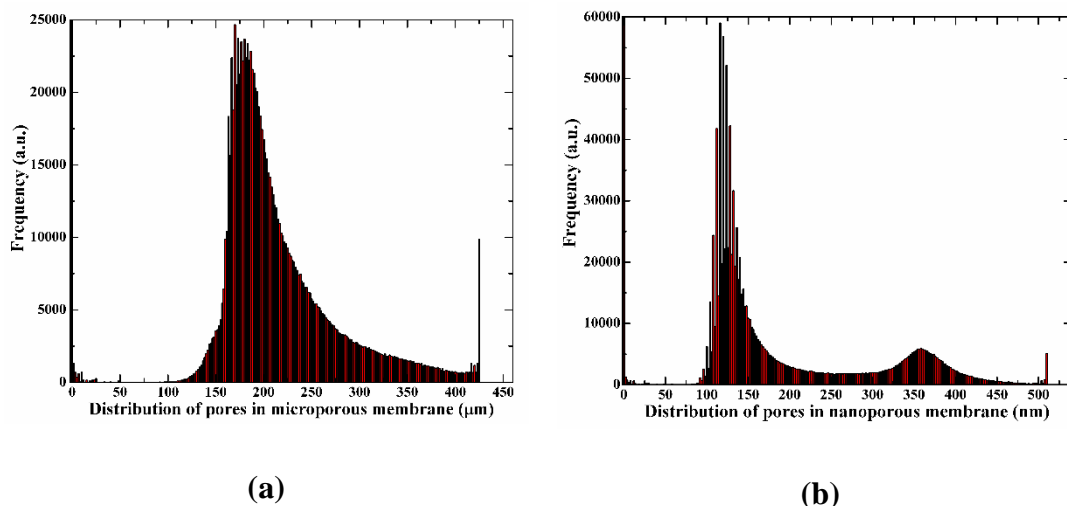
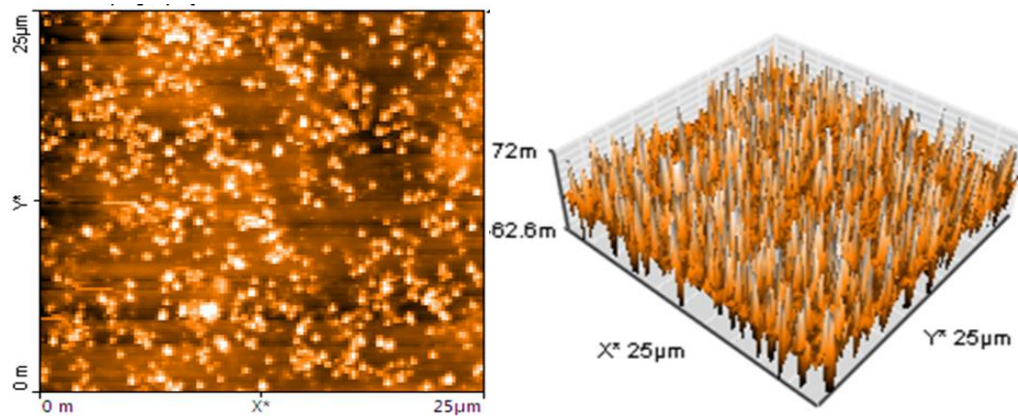


Figure 9.3 Statistical approach to assess the distribution of pore size: (a) microporous and (b) nanoporous membranes

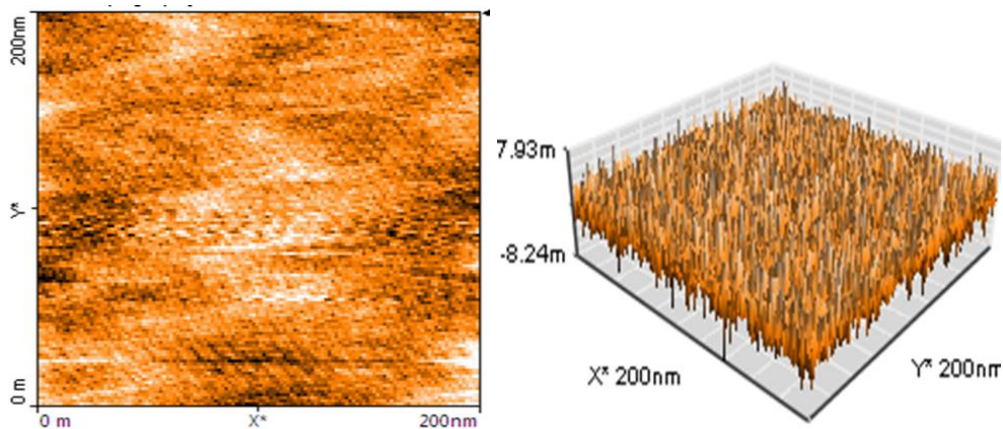
### 9.2.3 Morphology of HNT-PS membranes by atomic force microscopy (AFM)

The morphologies of microporous and nanoporous membranes were investigated further by AFM. Fig. 9.5a shows  $25 \times 25 \mu\text{m}$  of microporous membranes and Fig. 9.5b shows the  $200 \times 200 \text{ nm}$  of nanoporous membrane. The brightest area represents the highest points of the membrane surface while the dark points for the membrane pores. The impact of the addition of HNTs on pore formation and surface roughness of membrane can be demonstrated as follows. During the phase inversion, the hydrophilic HNTs migrated towards the membrane/water interface to lead to the formation of pores. Further, during the drying stage, the solvent became evaporated through these pores so that the HNTs remain deposited in the pores. The mean roughness ( $R_a$ ) for microporous and nanoporous membranes was  $38.42 \pm 0.5$  and  $45.38 \pm 0.7 \text{ nm}$ , respectively. It was observed that the number of grains present in a selected area in nanoporous membrane are more than that of microporous membrane. Hence, it led to the creation of more uneven surface on nanoporous membrane. Additionally, as nanoporous membrane has higher surface to volume ratio than microporous membrane, the former has more roughness of membrane than the latter. These results were consistent with qualitative SEM observations.



**Ra= 38.42**

**(a)**



**Ra=45.38**

**(b)**

Figure 9.4 AFM image of HNT-PS (a) microporous membrane 2D (left) and 3D (right) and (b) nanoporous membrane 2D (left) and 3D (right)

Water purification membranes can be contaminated by various physical or biological media over time (e.g., bacteria, viruses, proteins, dirt, and fungi). These contaminants adhere to the surface to block the pores, as their growth or agglomeration may be observed on the surface. This reduces the quality of permeate and membrane permeability, while increasing the energy costs for separation. This drawback can be resolved by developing antifouling membranes which will increase membrane efficiency and usability of membranes. The membranes synthesized in this work displayed antifouling property mainly due to the following reasons: firstly, the charges present in the HNTs can help suppress the growth of microbes. HNTs can thus

efficiently aid the enhancement of antimicrobial activity. Secondly, HNTs possess porous structures with various surface functional groups (hydroxyl groups) making them hydrophilic. These hydrophilic HNTs reduces the interface energy at the membrane/water interface and improves membrane hydrophilicity. This mechanism confirms the improvement in antifouling property. Additionally, membranes with low roughness and surface energy were reported to display good anti-fouling abilities (Vatanpour et al. 2012). Likewise, AFM results demonstrated low roughness for both microporous and nanoporous membranes to support their enhanced antifouling properties. This activity was further supported by contact angle analysis (Fig. 10.6) which showed favorable hydrophilicity.

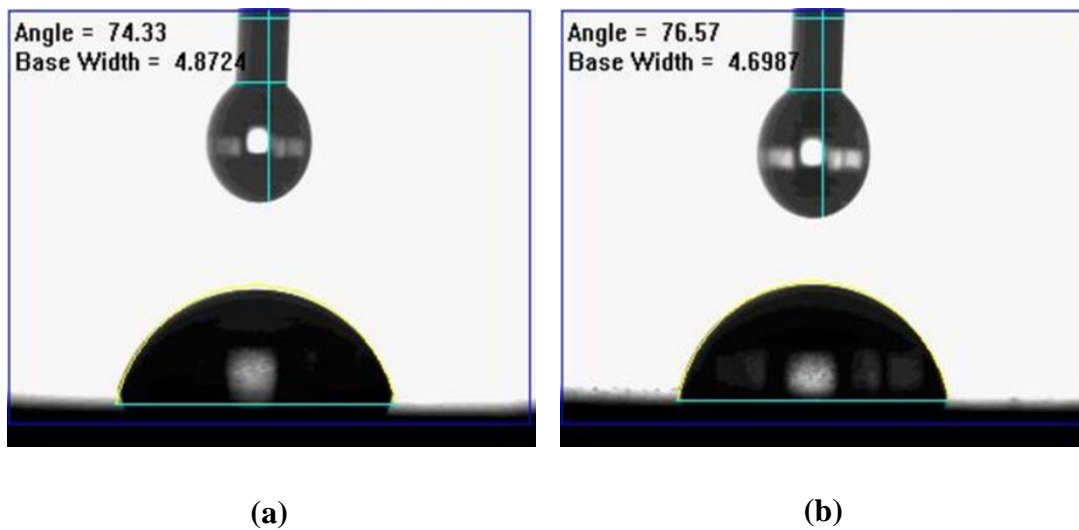
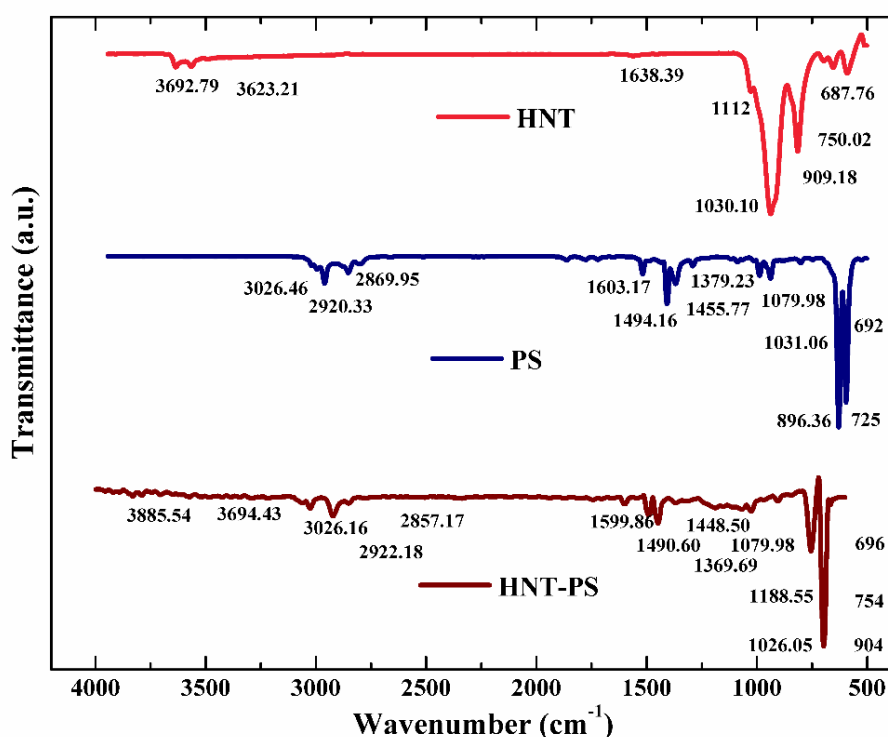


Figure 9.5 Contact angle of HNT-PS: (a) Microporous membrane and (b) Nanoporous membrane

#### 9.2.4 Studying the functional groups of HNT-PS membranes

As shown in Fig. 9.7 for, HNT, the peaks at  $3692.79$  and  $3623.21$   $cm^{-1}$  are associated to the stretching vibrations of lumen space Al-OH. Water in the interlayer is indicated by the frequency of bending vibration at  $1638.39$   $cm^{-1}$ . The peak at  $1030.10$   $cm^{-1}$  is associated to the stretching mode of the Si-O apical. Note that, in contrast to previous work (Yuan et al. 2008), a weak peak at  $1112.20$   $cm^{-1}$  in the pure HNT spectrum was observed; this can be attributed to Si-O perpendicular stretching. This quenching of the out-of-plane vibration in the clay layers might be the source of

the increased mechanical stability of HNTs and the composite (this will be discussed below). The peak at  $909.18\text{ cm}^{-1}$  is also attributed to a bending vibration of the inner-surface hydroxyl groups. Bending vibrations of Al-O-Si and Si-O-Si are observed at  $750.02$  and  $687.76\text{ cm}^{-1}$ , respectively. Fig. 9.7 for HNT-PS clearly demonstrates the existence of the major absorbance peaks of HNTs in the polystyrene spectrum, which proves the existence of clay inside the membrane pores. However, the peak at  $3692\text{ cm}^{-1}$  shifts to  $3694.43\text{ cm}^{-1}$  in the nanocomposite, which could reflect the interaction between the Al layers of HNTs and the polymer surface. The decreases in the frequencies related with O-H stretching and bending after formation of the composite might be the source of the increased chemical activity of HNTs. The strongest peak in HNTs (at  $1030.10\text{ cm}^{-1}$ ) basically originated due to asymmetric flexible vibration of O-Si bond in the presence of large O-Si-O groups on the exterior surface of HNTs. However, it was shifted slightly (i.e.,  $1040.01\text{ cm}^{-1}$ ) to reflect the interaction between Si-O and the polymer. Thus, on the basis of this FT-IR study, it can be inferred that HNTs have been incorporated successfully into the polymer matrix. These results were further supported by EDAX results.



**Figure 9.6** FT-IR spectra of PS, HNT-PS, and HNT

### 9.2.5 Studying the structure of HNT-PS membranes

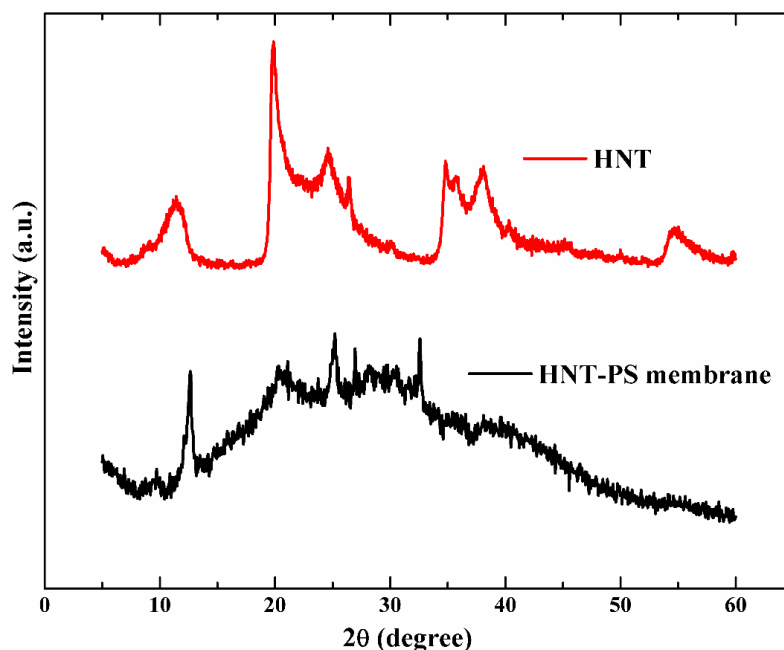


Figure 9.7 XRD data of HNT and HNT-PS membranes

XRD pattern of the membranes is presented in order to understand the structure of the membrane (Fig. 9.8), the peak at a  $2\theta$  value of 11.95 implies a  $d$  spacing value of 7.4 Å, as calculated using Bragg's law ( $\lambda = 2d \sin \theta$ ). This shows that the specimen is probably a mixture of the disordered 7 Å monoclinic form (creating a 14 Å cell) and the 10 Å form, which indicates the presence of water in the interlayers of HNTs. From XRD analysis of HNT-PS membrane, there was progressive disappearance of X-ray diffraction peaks; this implies the signal for the complete exfoliation of HNTs into the polymer matrix.

### 9.2.6 BET analysis of HNT-PS membranes

The BET analysis of the membranes is done as summarized in Table 9.1. The microporous membrane had pore diameter, pore volume and surface area of 358 nm, 0.229 cc/g, and 60.65 m<sup>2</sup>/g respectively. The nanoporous membranes had pore diameter, pore volume and surface area of 3.396 nm, 0.081 cc/g, and 53.60 m<sup>2</sup>/g respectively. The presence of relatively high surface areas and pore volumes suggests that electrostatic cross-linking points in the membrane are rigid enough to hamper the

structural collapse of the flexible polymer chains. The structure of pores in the membranes was also evaluated by nitrogen sorption isotherms (Fig. 9.9a). The pore sizes were determined by nonlinear density functional theory (NLDFT). As seen in Fig. 9.9b, the pore size distributions for microporous and nanoporous membrane were in the range of 123–1900 nm and 1.2–18.5 nm, respectively. The results were in agreement with the statistical analysis of SEM images. The contact angle of HNT-PS membranes. The surface hydrophilicity of the fabricated membranes was evaluated by water contact angle measurement. Basically, the low contact angle is associated with a number of factors and processes (e.g., higher surface energy, a greater tendency for water to wet the membrane, and higher surface hydrophilicity). It can be seen from Fig. 9.6 (a and b) that the microporous and nanoporous membranes were determined to be 74.33 and 76.57°, respectively to reflect the enhanced hydrophilicity of membranes. HNTs possess OH<sup>-</sup> polar groups on their inner lumen making them highly hydrophilic and have very few functional groups on their exterior structure, which aids them to separate from agglomerates and promotes their dispersion in the polymer, hence the membrane hydrophilicity is increased on addition of HNTs into polystyrene matrix.

Table 9.1 BET analysis of both microporous and nanoporous structures of HNT-PS membrane

Sl. No	Membrane	Pore diameter	Pore volume	Surface area
1	Microporous membrane	385 nm	0.229 cc/g	60.65 m <sup>2</sup> /g
2	Nanoporous membrane	3.396 nm	0.081 cc/g	53.60 m <sup>2</sup> /g

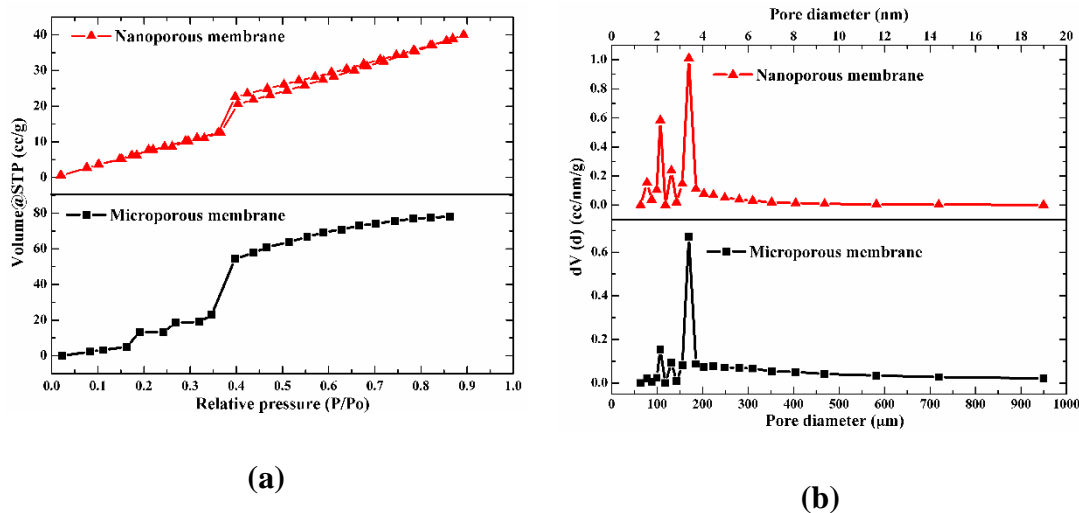


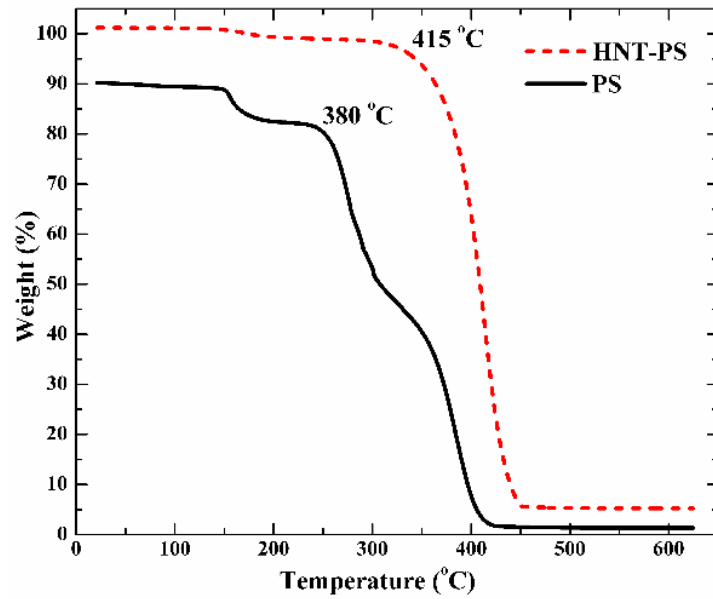
Figure 9.8 The structural analysis of microporous and nanoporous membranes (a) nitrogen adsorption–desorption isotherms at **77.4 K** and (b) their respective pore size distribution

## 9.2.7 Studying the thermal properties of HNT-PS membranes

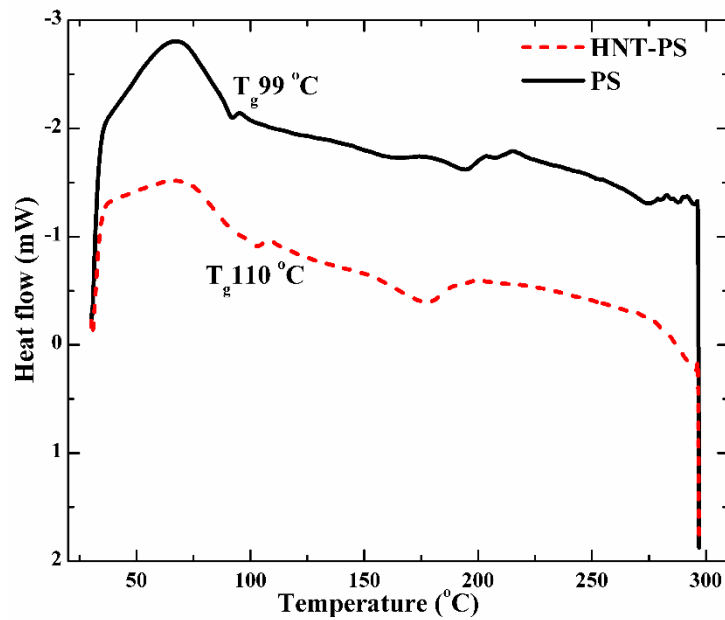
### 9.2.7.1 Glass transition temperature of HNT-PS membranes (DSC)

Glass transition temperature ( $T_g$ ) analysis was performed to further evaluate the properties of the membranes. HNTs were dispersed in the polymer matrix to interact with the polymer, where they played a vital role in improving the thermal properties of polymers. Fig. 9.10a shows a significant increase in the glass transition of PS after introducing HNTs into the polymer matrix. This phenomenon can be explained as follows. With a uniform dispersion of HNTs in the polymer matrix, the exfoliated structure of HNTs can help create a convoluted path for heat flow. This further delays its flow through the matrix, leading to an increase in  $T_g$ . This change in  $T_g$  also suggests that there are strong interactions between the HNTs and polymers. The interaction between polymer matrix and clay occurs at their interface. Generally, the interaction between polymer and clay takes either by intercalation, exfoliation, or combination of both structures. As seen from the SEM image (Fig. 9.1) and XRD analysis (Fig. 9.8), it can be concluded that the interaction between both polymer and HNT is combination of intercalation as well as exfoliation.

### 9.2.7.2 Thermal degradation and mass loss behavior of HNT-PS membranes (TGA)



(a)



(b)

**Figure 9.9 Thermal properties of PS and HNT-PS membranes: (a) Glass transition analysis and (b) Thermogravimetric analysis**

The degradation behavior of the membranes can be predicted based on the thermogravimetric analysis. Fig. 9.10b elucidates the increase in degradation



temperature of HNT-PS membranes. The hollow lumen space present in the HNT entraps and accommodates decomposition products, which act as barriers for heat transfer, thereby improving the thermal degradation of polymers (Du et al. 2006). The presence of aluminum and silicon in the HNTs also played a minor role in enhancing the thermal properties. Hence, the geometry and composition of HNTs both contributed to enhancing the thermal stability. Thermal stability is a significant factor to assess the feasibility of membranes because temperature and concentration affect their selectivity and flux through the alteration of the diffusion rate of water through the membrane. Consequently, the addition of HNT to the polymer greatly helped increase the thermal stability of the membrane. As such, it can further extend the application of these membranes for high-temperature performance.

### 9.2.8 Studying the tensile strength of HNT-PS membranes (tensile strength analysis)

Table 9.2 Mechanical properties on HNT-PS membranes with different HNT content

Sl. No.	HNT content (wt %)	Tensile strength (MPa)	Elongation (%)	Young's Modulus (MPa)
1	0	35	2.3	29.77
2	1	39	2.1	33.33
3	3	45	2.1	38.45
4	5	54	2	46.15
5	10	52	1.9	44.45

The mechanical properties of membranes were investigated to understand their durability. There was an enhancement in the tensile strength after the addition of HNTs (Table 9.2). Due to the strong interaction between polystyrene and HNTs, the addition of even 1% HNTs led to a drastic increase in the tensile strength and young's modulus of membrane in comparison to the neat PS membrane. However, there was slight reduction in the elongation which indicated the reinforcing benefits of halloysites

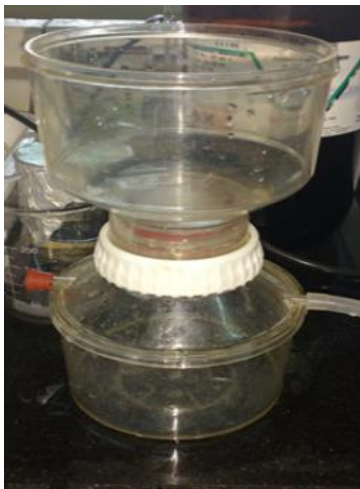
within PS matrix. Furthermore, on increasing the HNT loading beyond 5 wt% there was a slight decline in the tensile strength of the membrane with 10 wt % HNT content. This decrease in strength can be attributed to the aggregation of clay due to the uneven distribution of HNTs in the polymer matrix; these aggregates lead to stress concentrations at points in the polymer, which deteriorate the mechanical properties. However, the strength is still higher than that of the neat PS membrane. The effect of reinforcing HNTs in the polymer matrix greatly relies on the dispersion of HNTs in the matrix and their interfacial interactions (Okada and Usuki 2006). The reinforcing effect of HNTs in the polystyrene matrix can be understood by a combination of (a) the interactions between HNTs and the polystyrene, as seen in the FT-IR analysis, and (b) the uniform distribution of halloysite nanotubes in the polystyrene matrix, as seen from the SEM results. Hence, the HNTs exhibited good reinforcing ability with polystyrene in terms of the mechanical properties.

#### **9.2.9 Application of HNT-PS membranes for water treatment**

The experimental set up employed for water treatment testing in this study can be explained as follows (Fig. 9.11). The setup consists of a water purification apparatus connected to a vacuum pump. The water purification apparatus was equipped with a microporous membrane. The membrane was positioned to separate waste from the purified stream. The active filtration area was  $0.000176\text{ m}^2$ . The top compartment was filled with 100 mL of contaminated water. The vacuum pump was then turned on to create a vacuum pressure in the lower compartment so that water flowed through the membrane. Micro-purified water then began to accumulate in the lower compartment and was then passed through a nanoporous membrane for filtration of nano-sized contaminants. The water quality parameters were quantified before and after purification through both the microporous and nanoporous membranes. Fig. 9.12 depicts the cross-sectional area of the membrane and the membranes after passing pure water.



(a)



(b)



(c)



(d)

**Figure 9.10 Detailed description of the HNT-based water purification procedures: (a) Experimental setup for water treatment; (b) Compartments for water purification; (c) Purified water collected in the bottom compartment; and (d) HNT-PS membrane used for purifying water**

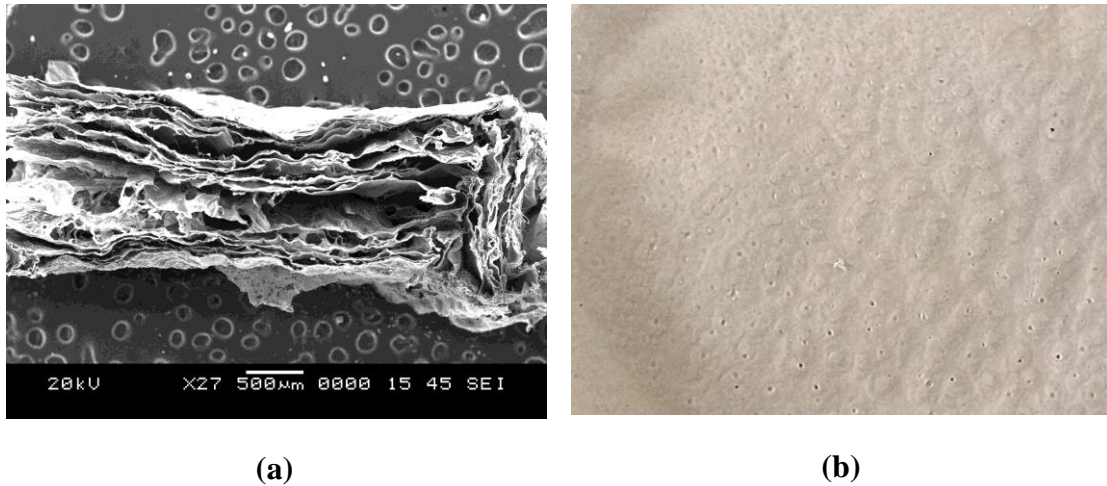


Figure 9.11 (a) Cross-sectional view of membrane and (b) Image of membrane after passing pure water

#### 9.2.10 Performance evaluation of this study

The efficiency of the fabricated membranes was determined by calculating % solvent content, porosity, shrinkage ratio, water flux, % rejection, and % recovery. Permeability, diffusion co-efficients, flux decline, rejection rate, and separation factors are the significant performance-related parameters. In contrast, various chemical and physical properties (pore size, pore size distribution, membrane thickness pore shape, adsorptive/absorptive properties, and charge density) are considered as morphology-related parameters. These parameters are discussed in detail to assess the performance of membranes. To determine the reusability of the membrane filter, it was cleaned with 0.2 wt% sodium hydroxide (NaOH) solution for 60 min and a 0.2 wt% nitric acid (HNO<sub>3</sub>) solution for 30 min twice. To confirm the cleanliness of the membranes, the percentage of regeneration for the membrane was determined. The clean water filtration was significant in identifying the regeneration percentage of the membrane at each stage and to estimate the state of its cleanliness after every experiment. In this work, the cleaning method showed almost complete regeneration of the membrane in most cases (94–99%) when tested repeatedly after cleaning the membrane after every three trials. The performance of membranes was tested for up to ten cycles.

**Percent solvent content:** For determining the water content of the membranes, the membranes were immersed in distilled water for 24 h, wiped with blotting paper to

remove any residual moisture present on the surface of membranes, and weighed using a weighing balance. The wet membranes were then de-moisturized at 100 oC for 24 h and reweighed. The % solvent content was estimated using the following equation:

$$\% \text{ Solvent content} = (W_1 - W_2) / W_2$$

here,  $W_1$  is the wet membrane weight (g), and  $W_2$  is the dry membrane weight (g).

**Porosity:** For determining the porosity of the membranes, the samples were immersed in distilled water for 24 h, wiped, and weighed. The membranes were then de-moisturized at 100 oC for 24 h and reweighed. The porosity was estimated using the following equation:

$$\text{Porosity} = (W_1 - W_2) / A$$

here,  $W_1$  is the wet membrane weight (g),  $W_2$  is the dry membrane weight (g), and A is the membrane area (cm<sup>2</sup>).

**Shrinkage ratio:** A small cross section of the wet membrane, immersed in a water bath, was cut. Both the length and width of the membrane were measured. The wet membrane was then heated at 100 oC for 24 h, and the measurements (length and width) of the dry membrane was noted. The following equation was used to calculate the shrinkage ratio:

$$\text{Shrinkage ratio} = [1 - (ab / a_1b_1)] * 100$$

here, a is the length of the dry membrane (m), b is the width of the dry membrane (m),  $a_1$  is the length of the wet membrane (m), and  $b_1$  is the width of the wet membrane (m).

**Water flux:** The cross-flow mode across the membrane was used for measuring the pure water flux of the membrane. Permeate was collected at intervals of 10 min for 1 h. Pure water flux estimation was done on the membrane at a transmembrane pressure of 345 kPa under steady-state flow. The following equation was used to calculate the pure water flux:

$$\text{Pure water flux, } J = q / (A * t)$$

here,  $q$  is the amount of permeate collected (L),  $J$  is the pure water flux ( $\text{mL}/\text{cm}^2 \text{ min}$ ),  $A$  is the membrane area ( $\text{cm}^2$ ), and  $t$  is the sampling time (min).

**Rejection:** Rejection is an estimation of the membrane efficiency, e.g., a number of components rejected by the membranes. It gives information about the separation efficiency of the components that is achieved by the membrane. The rejection is calculated by the following equation:

$$\text{Rejection} = 1 - (C_p/C_f)$$

here,  $C_p$  is the concentration of components in the permeate ( $\text{g}/\text{m}^3$ ), and  $C_f$  is the concentration of components in the feed water ( $\text{g}/\text{m}^3$ ).

**Recovery:** The efficiency of the membrane can be measured in terms of recovery. A membrane in cross-flow mode was used in this case. According to the mass balance relationship, the flow of the feed is equal to the sum of the concentrate flow and the permeate flow. Thus, recovery can be calculated by the following equation:

$$\text{Recovery} = (Q_p/Q_f) * 100$$

here,  $Q_p$  is the permeate flow ( $\text{m}^3/\text{h}$ ), and  $Q_f$  is the feed flow ( $\text{m}^3/\text{h}$ ).

Table 9.3 presents the % solvent content of the microporous and nanoporous membranes with different HNT content in different solvents. Accordingly, there was an increase in the % solvent content with increased loading of HNT. This is because the HNTs generally increase the hydrophilicity of the membranes, which ultimately increases the % solvent content of membranes. It can also be observed that the solvent hydrophobicity caused a decrease in the % solvent content with the change from water to less polar solvents. Also, the transport of water and other ions within the membrane was influenced by the polymer membrane structure; the microporous membrane had larger pores, allowing it to display better solvent retention than the nanoporous membrane.

Table 9.3 Evaluation of % solvent content of microporous and nanoporous membranes using different HNT content and solvents

HNT content (wt %)	% Solvent content							
	Microporous membrane				Nanoporous Membrane			
	W	E	M	P	W	E	M	P
0	1	0.008	0.006	0.001	0.5	0.008	0.006	0.001
1	1.4	1.25	1.01	0.09	1.1	0.7	0.4	0.1
3	2.67	2.2	1.97	1	2.0	1.5	0.9	0.5
5	3.46	2.98	2.44	1.34	3.1	2.2	2.1	1.2
10	5.97	4.95	3.54	2.58	5.3	4.5	3.0	2.1

\*Water-W, Ethanol-E, Methanol-M, Propanol-P

Table 9.4 displays the porosity values of micro and nanoporous membranes prepared using 1, 3, 5, and 10 wt % HNT content in different solvents with decreasing hydrophilicity. The porosity of the membrane is defined as the ratio of the volume of the pores to the total volume of the membrane. A higher porosity indicates higher permeability of water in the membrane, as water can more easily flow through more porous media. Virgin polystyrene had the lowest porosity in all of the solvents. There was an enhancement in the porosity of the membrane after the addition of HNTs. Also, these pores were filled with HNTs, as seen in the SEM results, to aid in the purification of water as it flows through the pores. It was also noted that the porosity of the membrane was reduced by using different solvents due to the inherent hydrophilicity of the solvents. The reason behind this can be due to the fact that HNTs increase the hydrophilic nature of the polymer membrane. The porosity of the membrane was highest in water and lowest in propanol. This suggests that the porosity and percent solvent content are greatly dependent on solvent hydrophilicity. Hence, it can be

concluded that the membrane with 10 wt% HNTs gives the maximum efficiency for water purification. However, membranes with 5 wt% HNTs led to better thermal and mechanical properties and so were used for the water purification studies.

Table 9.4 Evaluation of porosity of microporous and nanoporous membranes using different HNT content and solvents

HNT content (wt %)	% Porosity							
	Microporous membrane				Nanoporous Membrane			
	W	E	M	P	W	E	M	P
0	0.001	0.001	0.001	0.001	0.001	0.001	0.001	0.001
1	0.082	0.065	0.056	0.028	0.15	0.09	0.07	0.04
3	0.106	0.097	0.085	0.06	0.25	0.15	0.11	0.089
5	0.244	0.178	0.155	0.1	0.35	0.24	0.20	0.154
10	0.512	0.315	0.296	0.23	0.54	0.36	0.35	0.235

\*Water-W, Ethanol-E, Methanol-M, Propanol-P

Membrane shrinkage measurements were also carried out to accurately assess the area of the membrane. This provides an approximation of the decrease in the film dimensions after it is submerged in a solvent bath. This parameter plays a crucial role in the scaling-up step. Higher membrane shrinkage exerts tension within the membrane, which affects the mechanical properties of the resultant membrane. Table 9.5 shows the shrinkage ratio of both microporous and nanoporous membranes with different HNT content in different solvents. The virgin PS was seen to maintain the highest shrinkage ratio due to polymer contraction in a solvent bath. In contrast, the addition of clay to the polymer matrix reduced the shrinkage ratio because the additives resulted in dissimilar polymer contraction, leading to different degrees of shrinkage (Susanto and



Ulbricht 2009). Another reason for the reduced shrinkage of membranes is due to the increase in pore size upon the addition of HNTs to the polymer matrix; clay loading enhances the porosity of membranes. Hence, it can be noted that decreased membrane shrinkage occurred when the clay loading was increased. The membrane with 10 wt% clay loading had the smallest shrinkage ratio. In order to investigate the performance efficiency of HNT-PS microporous and nanoporous membranes, these membranes were tested for the treatment of actual wastewater samples.

Table 9.5 Evaluation of shrinkage ratio using different HNT content and solvents

HNT content (wt %)	Shrinkage ratio							
	Microporous membrane				Nanoporous Membrane			
	W	E	M	P	W	E	M	P
0	11.40	10.40	9.50	8.80	10.8	10.0	9.40	8.10
1	8.5	7.45	6.49	6.02	7.9	7.05	6.00	5.80
3	7.65	7.00	6.95	5.04	7.0	6.40	5.45	4.92
5	7.05	6.50	6.04	4.98	6.7	5.84	5.06	4.50
10	6.25	5.50	4.90	4.45	6.0	4.80	4.50	4.15

\*Water-W, Ethanol-E, Methanol-M, Propanol-P

In the first stage, a microporous membrane was employed for removal of micron-sized contaminants. Then, the water samples containing nano-sized impurities were purified in the second stage by passing them through nanoporous membranes. Nano filtration combines ejection of uncharged components on the nanoscale with charge effects between the membrane and solution, the rejection of uncharged components results due to size exclusion or due to differences in diffusion rates in a non-porous structure, which depends also on molecular size (Van Der Bruggen and Vandecasteele 2003). The results are presented in Fig. 9.13. The pure water flux is an

important property of the membrane and is a critical factor in determining the selection of membranes for real-world applications. The pure water flux for virgin PS was very low because of the low membrane porosity. However, the addition of HNTs to the polymer matrix increased the water flux in both the microporous and nanoporous membranes due to the increased membrane porosity. Moreover, increasing the HNT content further increased the water flux.

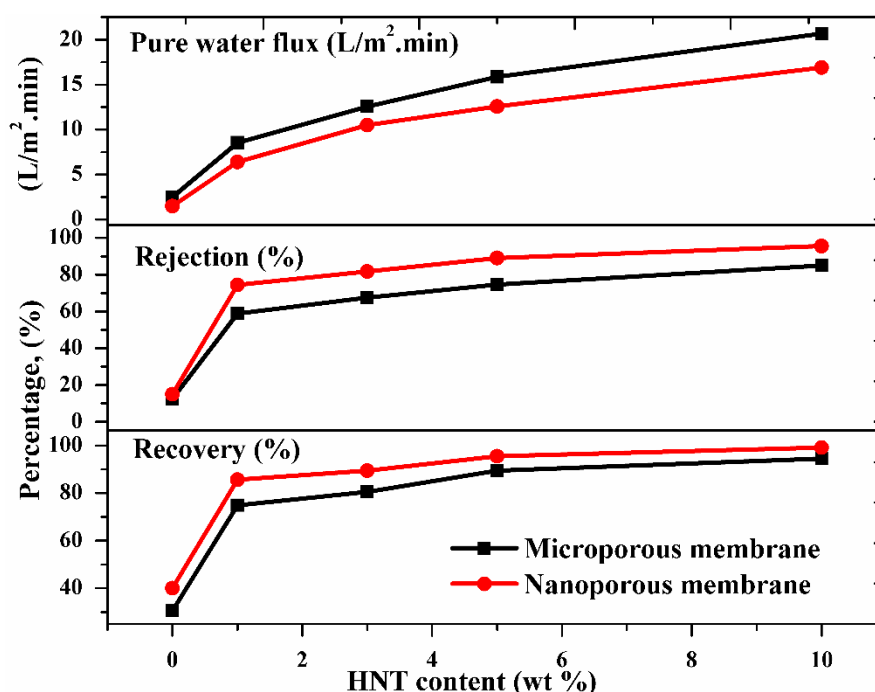


Figure 9.12 Evaluation of the performance efficiency of Pure water flux, Rejection %, and Recovery % of HNT-PS membranes

The increase in pure water flux of the membranes as seen in Fig. 9.13a can be attributed to the following facts, firstly, the addition of hydrophilic HNTs into the PS matrix enhanced phase separation and resulted in the formation of pores which in-turn enhanced the hydrophilicity of the membranes as demonstrated by contact angle analysis. Due to the increase in the hydrophilicity of membranes, they could attract water molecules inside the pores of membrane matrix and promote water to pass through the membrane and enhance permeability accordingly (Yan et al. 2006). Secondly, HNTs possess hollow nano tubular structure in the submicrometer range, which causes water molecules to permeate through them (Liao et al. 2011). Next, the addition of HNTs to polymer matrix resulted in an increase in solubilization and

diffusion of water molecules into the membrane matrix, which facilitated the permeation of water into the membranes. Further, the formation of voids at the interface of embedded HNTs and the presence of lumen of HNTs provided more reduced pathways for the permeation of water molecules.

Despite the differences in pore size and porosity, there is not much difference in the flux of micro and nanoporous membrane; this can be explained as follows, water with concentrated contaminants take more time to process than diluted contaminants. In this study, water with concentrated contaminants are first passed through microporous membrane which ejects more contaminants and demands more time for purification. Afterwards, the water containing only nanosized impurities was allowed to pass through nanoporous membrane which also took comparatively short time (e.g., comparably to micropores); hence, there is not much difference in fluxes determined from both pore sizes. Also, both the size and number of pores were seen to play the major role in enhancing the water flux. As seen from the AFM image (Fig. 9.5) and by statistical analysis (Fig. 9.4), the number of pores present in the given area in nanoporous membrane is more than that in microporous membrane. Additionally, an important factor affecting water flux is the hydrophilicity of the membranes. It can be seen from Fig. 9.6 that there is not much difference in the contact angle of both the membranes; hence, there is no discernible difference in the flux of both membranes.

The rejection efficiency of a membrane greatly relies on its structure and morphology as well as on the characteristics of the feed solution (Geise et al. 2010). It is clear from Fig. 9.13b that the neat PS membrane could not satisfactorily reject contaminants, whereas the addition of HNTs to the membrane increased the rate of rejection. This is attributed to the presence of HNTs in the pores, which aids in the rejection of impurities. Increasing the HNT content led to an increase in the % rejection. Similarly, the recovery % values were derived from the HNT-PS microporous and nanoporous membranes (Fig. 9.13c). The incorporation of HNTs into the fabricated polymer matrix elucidated led to an increase in the recovery %. Also, there was a considerable increase in the rate of recovery as the HNT content was increased. This clearly explains the role of clay in the purification of water as well as the increase in efficiency of the membrane after the addition of clay.

Basically, clays have inherent properties to capture and filter water as it flows through by physical, chemical, and biological processes. The texture and structure of clays play a vital role in water purification as they determine how easily water will move through clay for filtration. Physical filtration is directly analogous to passing water through the screen. HNTs contain small pores which act as a sieve to hold back particles that are large to pass through. As the pollutants are caught up by HNTs, they can become cleaned physically. Moreover, the efficiency of such capturing may become enhanced further by the tortuous path that water takes to move through clay. As such, HNT structure provides multiple opportunities to capture contaminants (sediments and bacteria). Also, as HNTs possess positively charged lumen and negatively charged surface, they can capture chemicals with opposite charge and hold them tightly for the effective purification. Unlike other clays with only one charge, HNTs are bestowed with both positive and negative charges. For example, positively charged ammonium ions can be attracted by and deposited on the lumens, while negatively charged nitrates are attached to the surface of HNTs. Likewise, various forms of pollutants (e.g., heavy metals, salts, organic chemicals, and pesticides) can be uptake as well. As such, HNTs can form covalent bonds (sharing of electrons) to help retain both organic and inorganic pollutants for the filtration of water.

It is recognized that various physical and chemical processes can impart antibacterial/antimicrobial activity to clays. Physical bactericide can take place due to the surface attraction between clay minerals and bacteria. However, such interaction can affect the passive and active uptake of essential nutrients, muddle cell envelopes, or damage efflux of metabolites (Ferris et al. 1987). The charges present on the HNTs, are not favorable for growth of microbes and bacteria may not grow further or will be killed. HNTs can thus efficiently aid the enhancement of antimicrobial activity. The difference in antibacterial properties thus suggests that the bactericidal mechanism should not be physical (e.g., pull between clay and bacteria) but rather a chemical transfer or reaction. It is observed that the pore size of the membrane is in nanoscale which is smaller than the microbes; hence, the microbes can be caught up inside the filtration module. The performance of the synthesized HNT-PS membranes was compared with membranes synthesized using other clays. Accordingly they were found

to possess better mechanical, thermal, hydrophilicity, and flux (Anadão et al. 2010; Lai et al. 2011, 2014; Monticelli et al. 2007).

The membrane which is reported in this work has been compared with other polymer-clay membranes and can be seen in Table 9.6. It gives the details about properties and performance of few polymer-clay membranes. It can be observed that HNT-PS membranes shows good mechanical strength, thermal properties as well as performance in comparison with other membranes.

**Table 9.6 Comparison of membrane properties with previous reports**

Sl. No	Membrane details	Mechanical Properties			Thermal properties (°C)	Water Flux (L/m <sup>2</sup> .h)	Author and Year
		TS (MPa)	YM (MPa)	E (%)			
1	HNT-PS	39	33.33	11	415	230	(Buruga et al. 2018)
2	PVDF-Closite B	4.5	17	75	350	-	(Lai et al. 2011)
3	PVDF-nanoclay	-	-	-	-	20	(Daraei et al. 2013)
4	Polyethersulfone-Ag-HNT	-	-	-	300	375	(Chen et al. 2013)
5	PES-HNT	-	-	-	230	80	(Zhu et al. 2014)
6	PES-Dextran HNT	-	-	-	350	18	(Yu et al. 2014)
7	Polyetherimide/Bentonite	-	-	-	-	186	(Hebbar et al. 2014)
8	Chitosan-Montmorillonite	4.6	-	30.6	-	2	(Zhu et al. 2015)

9	Polyethersulfone-HNT	-	-	-	350	1.2	(Wang et al. 2015)
10	Polysulfone-HNT	-	-	-	-	2.5	(Ghanbari et al. 2015)
11	Polysulfone-organoclay	7	-	-	-	4	(Shokri et al. 2016)
12	Polyacrylonitrile-mHNT	-	-	-	-	1	(Qin et al. 2016)
13	Polysulfone/polymer-grafted bentonite	-	-	-	350	135	(Kumar et al. 2016)
14	PVDF-mHNT	-	-	-	420	42	(Zeng et al. 2017b)
15	PVDF-HNT	-	-	-	-	150	(Guo et al. 2019)

\*TS-Tensile strength, YM-Young's Modulus, E- Elongation

### 9.2.11 Characterization of wastewater

According to the analysis of the mechanical properties, thermal properties, and performance efficiency of HNT-PS membranes, 5 wt % clay loading was the optimum amount for purification. Hence, these membranes were used for purification of wastewater. The characterization results of wastewater before and after passing through the membrane are presented in Table 9.7. It can be seen that there was a considerable increase in the purification of water after it passed through the membranes.

Table 9.7 Comparison of wastewater properties between before and after passing through HNT-PS membrane filters

Sl. No	Parameter	Standard acceptable value	Before treatment	Microfiltration membrane	Nanofiltration membrane
1	pH	6-10	9.56	8	7
2	Turbidity	FTU	1.9	1	0.5
3	Conductivity, mS/cm	50-800	1300	900	450
4	Hardness, mg/L	60	280	146	53
3	DO, mg/L	0-18	15.2	11.5	12.0
4	TDS, mg/L	3500	2950	1800	985
5	TSS, mg/L	150	1120	870	490
6	COD, mg/L	150	1860	1280	980
7	BOD, mg/L	80	380	190	62

\* Dissolved oxygen-DO, Total dissolved solids-TDS, Total suspended solids-TSS, Chemical oxygen demand-COD, Biological oxygen demand-BOD.

### 9.3 HNT-PS MEMBRANES FOR TREATING WATER RECEIVED FROM VARIOUS SOURCES

The membranes synthesized were further used to purify water collected from three different sources i.e., Sea water, Tap water and Effluent water.

#### 9.3.1 HNT-PS membranes for treating water collected from Sea

For treatment and characterization of sea water, sea water is passed through membranes synthesized using 1, 5, 10 wt% HNT-PS nanotube membrane. Among them water purified through 5 wt% membrane is showing appropriate values resulting in low levels of turbidity, conductivity, dissolve oxygen, Biological Oxygen Demand,

Ferrous, Zinc, dissolved solids and high level of alkalinity as seen in Table 9.9. The purified water from this membrane showed wide range of difference compared with the characteristics of water determined before purification. It is due to even distribution of HNT in the membrane which allows water to pass through it by stopping foreign particles above the membrane.

**Table 9.8 Characterization of Sample – 1 (Sea Water)**

Sl. No	Parameter	Sample-I	1 wt %	5 wt %	10 wt %
			HNT-PS	HNT-PS	HNT-PS
1	pH	8.35	8.41	8.37	8.39
2	Conductivity (mS)	51.3	50.8	50.3	51.3
3	Turbidity (NTU)	3.8	0	0.09	1.4
4	Total Solids (g/L)	39.5	----	----	----
5	TSS (g/L)	----	0.1333	0.25	0.115
6	TDS (g/L)	----	38.5	38	39
7	DO (mg/L)	31	17.2	20.6	19.8
8	BOD(mg/L)	17	13.4	3.6	7.6
9	Zinc (mg/L)	0.187	0.019	0.102	0.009
10	Ferrous (mg/L)	3.194	2.762	2.095	2.264

\* Dissolved oxygen-DO, Total dissolved solids-TDS, Total suspended solids-TSS, Chemical oxygen demand-COD, Biological oxygen demand-BOD.

### 9.3.2 HNT-PS membranes for treating Tap water

For treatment and characterization of tap water, water is passed through membranes synthesized using synthesized 1, 5, 10 wt% HNT-PS nanocomposite membranes. Among them water purified through 10 wt% membrane is showing



appropriate values resulting in low levels of turbidity, conductivity, dissolved oxygen, Biological Oxygen Demand, Ferrous, Zinc, dissolved solids and alkalinity as seen from Table 9.10. The purified water from this membrane showed wide range of difference compared with the characteristics of water determined before purification.

### 9.3.3 HNT-PS membranes for treating water from effluent

Table 9.9 Characterization of Sample -II (Tap water)

S. No	Parameter	Sample-II	1 wt %	5 wt %	10 wt %
			HNT-PS	HNT-PS	HNT-PS
1	pH	8.35	8.41	8.37	8.39
2	Conductivity (mS)	51.3	50.8	50.3	51.3
3	Turbidity (NTU)	3.8	0	0.09	1.4
4	Total Solids (g/L)	39.5	----	----	----
5	TSS (g/L)	----	0.1333	0.25	0.115
6	TDS (g/L)	----	38.5	38	39
7	DO (mg/L)	31	17.2	20.6	19.8
8	BOD(mg/L)	17	13.4	3.6	7.6
9	Zinc (mg/L)	0.187	0.019	0.102	0.009
10	Ferrous (mg/L)	3.194	2.762	2.095	2.264

\* Dissolved oxygen-DO, Total dissolved solids-TDS, Total suspended solids-TSS, Chemical oxygen demand-COD, Biological oxygen demand-BOD.

Table 9.10 Characterization of Sample – III (Effluent water)

Sl. No	Parameter	Sample-II	1 wt %	5 wt %	10 wt %
			HNT-PS	HNT-PS	HNT-PS
1	pH	8.10	7.80	7.85	7.70
2	Conductivity (mS)	0.151	0.217	0.177	0.176
3	Turbidity (NTU)	0.7	0.2	0.5	0.1
4	Total Solids (g/L)	0.35	----	----	----
5	TSS (g/L)	----	0.04	0.026	0.084
6	TDS (g/L)	----	0.27	0.225	0.23
7	DO (mg/L)	15.2	11.6	13.2	13.6
8	BOD(mg/L)	2.2	1.6	1.6	2
9	Ferrous (mg/L)	1.797	1.785	Nd	Nd

\* Dissolved oxygen-DO, Total dissolved solids-TDS, Total suspended solids-TSS, Chemical oxygen demand-COD, Biological oxygen demand-BOD.

Characterization of effluent water has been done using synthesized 1, 5, 10 wt% HNT-PS membranes. Among them water purified through 10 wt% membrane is showing appropriate values resulting in low levels of turbidity, conductivity, dissolve oxygen, Biological oxygen demand, Ferrous, Zinc, dissolved solids and alkalinity. The purified water from this membrane showed wide range of difference compared with the characteristics of water determined before purification.

The water is purified due to high agglomeration of HNTs where the high concentration of HNTs is favorable in purifying soft water to differentiate very small particles also.

#### **9.4 SUMMARY**

HNT-PS membranes were fabricated using two types of solvents to inspect the effect of solvents on the physical, mechanical, and thermal aspects of membranes. The SEM results demonstrated the formation of pores with different sizes, which were influenced by the inherent properties of the solvents (e.g., density, boiling point, and rate of evaporation). It was also seen that HNTs were deposited in the pores of the membranes by EDAX after evaporation of the solvent, which aided in the purification of water. AFM and contact angle analysis showed that the membranes possessed favorable roughness and hydrophilicity. BET analysis explained the pore size and its distribution in the polymer matrix. The treatment of wastewater with these membranes can be performed in two stages based on pore size. In the first stage, it was favorable to carry out micro filtration (1000–104 Å) and remove suspended solids with the micropore membrane synthesized using THF. In the second stage, ultrafiltration (10–1000 Å) was carried out to remove oil droplets (less than 10 ppm in the feed) or microorganisms with the nanopore membrane synthesized using NMP. The performance evaluation of these membranes, tested in terms of pure water flux, rejection, and recovery, confirmed the excellent performance of these membranes. When they were tested for the purification of wastewater, they exhibited excellent results. The fabricated membranes displayed high water flux, great solute rejection, long-term stability of water flux, good rejection, and excellent mechanical and thermal properties. Hence, these membranes are promising candidates for use in the field of water purification. The performance of water purification units developed based on these membranes should also be investigated further to maximize their effectiveness at varying scales. The fabricated membranes containing HNTs were endowed with excellent morphological, mechanical, and thermal properties along with a number of merits like good hydrophilicity, antifouling properties, good water flux, and rejection/recovery rates. The superiority of the HNT-PS membrane is expected to be useful to establish a profitable approach for water purification. Hence, the results of this study were meaningful to evidence the fact that these membranes can be proposed

as potential candidates to open a propitious future in the field of water purification. HNT-PS nanocomposite membranes with 1, 3, 10 wt % nanofiller have been fabricated by solution intercalation method assisted by sonication. Solvent plays a very significant role in enhancing properties on nanocomposite, THF was found suitable for dispersion of clay as well as dissolving polymer. The nanocomposite membranes with 3 wt % nanofiller was effective for the purification of hard water as it is having equal distribution of HNTs favorable for separation of large particles and allow water to pass through it. The nanocomposite membranes with 10 wt % nanofiller was effective in purifying soft water due to agglomeration of HNTs which helps in separating very small particles.

## CHAPTER 10

### CONCLUSIONS

The present work focused on synthesis of HNT-polymer nanocomposites by solution blending, emulsion polymerization and miniemulsion polymerization methods with an objective to study the effect of synthesis methods on properties of composites. These synthesized nanocomposites were used for two applications i.e., coating the surface of soda-lime glass and as membranes for water purification.

To begin with, HNTs are very hydrophilic in nature and they agglomerate causing hindrance to uniform distribution in polymer matrix. Therefore the surface of HNTs were modified to make them organophilic and aid in better dispersion. Surfactant CTAB and silane compound  $\gamma$ -MPS was employed to modify the surface of HNTs. Modification of HNTs using CTAB was successful and CTAB was intercalated into the clay gallery as observed by XRD analysis. The increase in  $d$  – *spacing* for HNT and CHNT was from 7.3 to 7.5 Å. FT-IR results confirmed successful adsorption of CTAB onto the surface of HNTs. The surface of HNTs was also favorably modified by silane  $\gamma$ -MPS. Studies on functional groups of HNTs and MHNTs by FT-IR confirmed the successful modification of the HNTs. XRD results showed that there was no prominent shift in the basal spacing, indicating that a very small amount of  $\gamma$ -MPS intercalated into the interlayers of HNTs, while the surface of HNTs was modified completely.

Next focus was on incorporation of modified HNTs (CHNT and MNHT) into polymer matrix using different methods to study the effect of HNTs modification of polymer properties. In solution casting method the solvent plays a very important role in enhancing the overall properties of nanocomposites and hence, the effect of solvent of the structure, morphology and thermal stability of nanocomposites was investigated. Although nanocomposites could be propitiously synthesized using various solvents, toluene revealed good exfoliation, uniformly dispersed morphology and good  $T_g$  in comparison with other solvents, hence proving it to be the best solvent for HNT-polymer nanocomposite synthesis. Toluene was observe to be the best solvent as it was capable of over-ruling polymer-polymer interactions in order to dissolve polymer

segments. It had favorable interaction with the polymer segments. Additionally, polystyrene, as well as polymethylmethacrylate, exhibits strong polarizable side groups that can be dissolved by toluene. Thus toluene was suitable solvent for dissolving polystyrene and polymethylmethacrylate. Also, toluene had the potential for dispersing HNTs, further ultrasound aided in uniform dispersion of HNTs into the polymer matrix and also caused sufficient increase in basal spacing of nanocomposites for polymer to enter the interlayers of clay which resulted in intercalated as well as exfoliated morphology thereby enhancing polymer properties for potential applications. HNT-PS and HNT-PMMA nanocomposites were fabricated using pristine HNTs, CHNT and MHNT with 0, 3, 5, and 10 wt % HNT content. XRD analysis showed progressive disappearance of significant peaks which explains the good interaction between polymer and HNTs. Surface modification of HNTs further aided the formation of ordered structure. The presence of a broad peak in the XRD structure showed amorphous nature of composites. Sonication time of 1 h was sufficient to achieve good miscibility between HNT and polymer matrix. Ultrasonic treatment produced a rapid interaction of HNTs inside the polymer matrix. This is supported by SEM analysis showing a homogenous dispersion of HNTs. Surface modification of HNTs further aided in uniform dispersion of HNTs in the polymer matrix. FT-IR analysis of the nanocomposites revealed the presence of characteristic peaks of HNTs, CHNT, and MHNT in the polymer matrix. This confirms the reinforcement of HNTs in polymer matrix. DSC analysis of HNTs displayed a notable increase in the glass transition temperature of nanocomposites on the addition of HNTs into the polymer matrix. Improvement in the  $T_g$  was observed on addition of HNTs up to 5 wt%; further addition caused a decrease in  $T_g$  due to dispersion difficulties.

Ultrasound-assisted emulsion polymerization was successfully carried out for synthesis of HNT-PS, HNT-PMMA and [HNT-(PS-co-PMMA)] using pristine and modified HNT. It was found that the polarity and hydrophilicity of the monomers greatly affect dispersion of the HNT in polymer matrix. In comparison with conventional emulsion polymerization technique, ultrasound-assisted polymerization resulted in generation of free radical due to cavitation and also aided in fast dissociation of initiator to free radicals. Additionally, on use of ultrasound for the process, HNT particles are

dispersed more uniformly. During sonication, it was observed that there was increase in the viscosity of the monomer/HNT mixture and gelation occurred which indicated network formation by the disruption and dispersion of clay aggregates. Modification of HNTs showed improvement in dispersion of HNT in the polymer matrix thereby improving thermal properties of nanocomposites. Barrier properties showed increasing trend in improvement with the increase in HNT content. And better dispersion of HNT due to modification improved barrier properties to a significant extent. Also, the addition of 5 wt% HNT content was optimum, and higher HNT content resulted in agglomeration. XRD results showed a slight increase in the basal spacing, and the composite was a mixture of intercalated as well as exfoliated structure for all polymers. The modification of HNTs results in better HNTs separation and a more disordered intercalated nanocomposite. This is because of favorable interactions of the HNTs with the monomer. Introducing polymerizable groups onto the HNTs surface improves the dispersion of clay significantly and mixed (intercalated and exfoliated) HNT-polymer nanocomposites were obtained. The presence of HNTs can substantially improve the dimensional stability of the polymer matrix in an exfoliated nanocomposite with uniform mesoscale clay dispersion. CTAB has been employed for surface modification of clays as it has long hydrophobic alkyl chain which shows good compatibility towards organophilic polymer. Also, along with long alkyl chain structure, sonication also plays a great role in increasing the gallery space between the HNT interlayers.. There are apparently two steps of dispersion and distribution of HNTs in the polymer matrix. The first step is nanoscale dispersion, which involves layer separation of the HNTs. Here, the physical interaction, as well as chemical compatibility among modified HNT surface and intercalated compound, determines the degree of increase in layer spacing. The second step involves the mesoscale distribution of HNTs where the disruption of HNT aggregates and primary particles take place. This requires interaction of HNTs with the polymer matrix which depends on the mixing strength. The CTAB modified clay was more effective in promoting mixed structure in polymer. This depicts the role of ammonium salt (modifier) on the structure of nanocomposites.

Nanocomposites of PS, PMMA and PS-co-PMMA was synthesized using HNTs and MHNTs by ultrasound-assisted miniemulsion polymerization. FT-IR confirmed the modification of the HNTs and presence of MHNTs in the polymer. XRD results showed that there was no prominent shift in the basal spacing, indicating that a very small amount of  $\gamma$ -MPS intercalated into the interlayers of HNTs, while the surface of HNTs was modified completely. SEM analyses showed a reduction in aggregates of HNTs after surface modification. DSC analysis showed enhancement in thermal stability in terms of  $T_g$  of the MHNT-PMMA nanocomposite as a result of modification of HNTs. Improvement in the properties of nanocomposite was observed on utilizing ultrasound for carrying out the synthesis. Additionally, surface modification of HNTs caused considerable improvement in exfoliation of HNTs into the polymer matrix and hence, thermal stability. Therefore, surface treatment of HNTs using  $\gamma$ -MPS together with miniemulsion polymerization assisted by ultrasound proves to be a promising technique to achieve better dispersion of HNTs in the polymer and obtain nanocomposites with enhanced properties.

Next, the application of synthesised nanocomposites were investigated. HNT based polystyrene (HNT-PS) and polymethylmethacrylate (HNT-PMMA) nanocomposites were synthesized by ultrasound-assisted blending and the characteristics of nanocomposite coatings over four different types of soda-lime glass were investigated. Good dispersion of HNTs in the polymer matrix is crucial for the enhancement of properties in nanocomposites. SEM analysis revealed that 60 min of sonication facilitates a good dispersion of HNTs in polymer. The DSC and TGA results indicated that there is a significant improvement in the thermal stability of coatings upon inclusion of HNTs in the polymer matrix. From the spectral analysis of coated glass samples, a negligible change in the absorbance, transmittance and reflectance properties was observed when compared to uncoated glasses. Hence, HNT-based PS and PMMA nanocomposites can be potentially used as protective surface coatings for glass substrates without altering their inherent spectral properties. Further, the coated glasses exhibit better hydrophobic behavior which is the prime requirement in most of the applications. Finally, the mechanical behavior like tensile strength and scratch resistance of coatings were also found to be higher for nanocomposites compared to



their neat counterparts. Therefore, it was demonstrated that both the HNT-based PS and PMMA nanocomposites can be effectively used as protective coatings for the soda-lime glass. [HNT-(PS-co-PMMA)] copolymer nanocomposites were prepared by ultrasound-assisted solution blending technique and applied as coatings for the soda-lime glass. Two types of glass, i.e., bronze (Bz) and green (GG), were coated using a spin coater. The effect of HNT content and thickness on the characteristics of coatings were investigated. The spectral analysis demonstrated a negligible change in the transmission and absorption of both glasses on applying coatings with HNT content of 5 wt%. The increase in HNTs content beyond 5 wt% slightly obstructed the passage of light through the glasses. However, there were no drastic changes in the spectral properties of glasses and the transparency and optical clarity of glasses were retained. Hence, [HNT-(PS-co-PMMA)] nanocomposite coatings can be used as a potential coating material for the soda-lime glass. The SSPF and SMPF values can be made higher by increasing the content of HNTs and thickness of coating. SEM analysis confirmed the uniform distribution of HNTs in the copolymer matrix which is crucial for the enhancement of nanocomposite's properties. The surface roughness and the contact angles of coatings on glass increased with HNT content. Contact angle measurements were in concert with surface roughness results from AFM analysis. A notable improvement in the thermal stability as well as mechanical properties of the [HNT-(PS-co-PMMA)] nanocomposite coatings compared to their neat counterparts was confirmed from TGA and tensile tests. [HNT-(PS-co-PMMA)] nanocomposite coatings exhibited better hydrophobicity, thermal, and mechanical properties compared with HNT-PS or HNT-PMMA nanocomposites due to the synergetic effect of both the polymers. It is evident that the [HNT-(PS-co-PMMA)] nanocomposite coatings possess good thermal stability, mechanical strength, and hydrophobicity. They ensure the better protection of the surface and the increased durability of the soda-lime glass.

Next, HNT-PS membranes were fabricated using two types of solvents to inspect the effect of solvents on the physical, mechanical, and thermal aspects of membranes. The SEM results demonstrated the formation of pores with different sizes, which were influenced by the inherent properties of the solvents (e.g., density, boiling point, and rate of evaporation). It was also seen that HNTs were deposited in the pores of the membranes by EDAX after evaporation of the solvent, which aided in the purification

of water. AFM and contact angle analysis showed that the membranes possessed favorable roughness and hydrophilicity. BET analysis explained the pore size and its distribution in the polymer matrix. The treatment of wastewater with these membranes can be performed in two stages based on pore size. In the first stage, it was favorable to carry out micro filtration (1000–104 Å) and remove suspended solids with the micropore membrane synthesized using THF. In the second stage, ultrafiltration (10–1000 Å) was carried out to remove oil droplets (less than 10 ppm in the feed) or microorganisms with the nanopore membrane synthesized using NMP. The performance evaluation of these membranes, tested in terms of pure water flux, rejection, and recovery, confirmed the excellent performance of these membranes. When they were tested for the purification of wastewater, they exhibited excellent results. The fabricated membranes displayed high water flux, great solute rejection, long-term stability of water flux, good rejection, and excellent mechanical and thermal properties. Hence, these membranes are promising candidates for use in the field of water purification. The performance of water purification units developed based on these membranes should also be investigated further to maximize their effectiveness at varying scales. The fabricated membranes containing HNTs were endowed with excellent morphological, mechanical, and thermal properties along with a number of merits like good hydrophilicity, antifouling properties, good water flux, and rejection/recovery rates. The superiority of the HNT-PS membrane is expected to be useful to establish a profitable approach for water purification. Hence, the results of this study were meaningful to evidence the fact that these membranes can be proposed as potential candidates to open a propitious future in the field of water purification. HNT-PS nanocomposite membranes with 1, 3, 10 wt % nanofiller have been fabricated by solution intercalation method assisted by sonication. Solvent plays a very significant role in enhancing properties on nanocomposite, THF was found suitable for dispersion of clay as well as dissolving polymer. Different types of water were purified using these nanocomposite membranes. The nanocomposite membranes with 3 wt % nanofiller was effective for the purification of hard water as it is having equal distribution of HNTs favorable for separation of large particles and allow water to pass through it. The nanocomposite membranes with 10 wt % nanofiller was effective in

purifying soft water due to agglomeration of HNTs which helps in separating very small particles.

## **SCOPE FOR FURTHER RESEARCH**

In this work, CTAB and  $\gamma$ -MPS have been reported to successfully modify the surface of HNTs, future work can be focused on use of various other surfactants as well as silanes to modify the surface of HNTs. The modified HNTs can be reinforced into polymer and used as coating to improve performance of coatings. Also the surface functionalization of HNTs can be done to improve the properties of HNTs to make them capable of degrading dyes which can be reinforced into polymer matrix and can be used for dye degradation in textile wastewater.

## REFERENCES

- Achhammer, B. G., Reiney, M. J., and Reinhart, F. W. (1951). "Study of degradation of polystyrene, using infrared spectrophotometry." *J Res Natl Bur Stand (1934)*, 4(2), 116–125.
- Ahmadi, S. J., Huang, Y. D., and Li, W. (2004). "Synthetic routes, properties and future applications of polymer-layered silicate nanocomposites." *J Mater Sci*, 39(6), 1919–1925.
- Akita, H., and Hattori, T. (1999). "Studies on Molecular Composite. I. Processing of Molecular Composites Using a Precursor Polymer for Poly(p-phenylene benzobisthiazole)." *J Polym Sci Part B Polym Phys*, 37(3), 189–197.
- Alexandre, M., and Dubois, P. (2000). "Polymer-layered silicate nanocomposites: Preparation, properties and uses of a new class of materials." *Mater Sci Eng R Reports*, 28(1), 1–63.
- Anadão, P., Sato, L. F., Wiebeck, H., and Valenzuela-Díaz, F. R. (2010). "Montmorillonite as a component of polysulfone nanocomposite membranes." *Appl Clay Sci*, 48(1–2), 127–132.
- Aranda, P., and Ruiz-Hitzky, E. (1992). "Poly(ethylene oxide)-Silicate Intercalation Materials." *Chem Mater*, 4(6), 1395–1403.
- Arora, A., Choudhary, V., and Sharma, D. K. (2011). "Effect of clay content and clay/surfactant on the mechanical, thermal and barrier properties of polystyrene/organoclay nanocomposites." *J Polym Res*, 18(4), 843–857.
- Athawale, A. A., Bhagwat, S. V., Katre, P. P., Chandwadkar, A. J., and Karandikar, P. (2003). "Aniline as a stabilizer for metal nanoparticles." *Mater Lett*, 57(24–25), 3889–3894.
- Bansal, A., Yang, H., Li, C., Benicewicz, B. C., Kumar, S. K., and Schadler, L. S. (2006). "Controlling the thermomechanical properties of polymer nanocomposites by tailoring the polymer-particle interface." *J Polym Sci Part B Polym Phys*, 44(20), 2944–2950.

- Baral, S., Brandow, S., and Gaber, B. P. (1993). "Electroless Metalization of Halloysite, a Hollow Cylindrical 1:1 Aluminosilicate of Submicron Diameter." *Chem Mater*, 5(9), 1227–1232.
- Beall, G. W., and Powell, C. E. (2011). *Fundamentals of Polymer Clay Nanocomposites*.
- Berthier, P. (1826). "Analyse de l'halloysite." *Ann.Chim.Phys*, 32, 332–335.
- Bhanvase, B. A., Pinjari, D. V., Gogate, P. R., Sonawane, S. H., and Pandit, A. B. (2012a). "Synthesis of exfoliated poly(styrene-co-methyl methacrylate)/montmorillonite nanocomposite using ultrasound assisted in situ emulsion copolymerization." *Chem Eng J*, 770–778.
- Bhanvase, B. A., Pinjari, D. V., Sonawane, S. H., Gogate, P. R., and Pandit, A. B. (2012b). "Analysis of semibatch emulsion polymerization: Role of ultrasound and initiator." *Ultrason Sonochem*, 19(1), 97–103.
- Blumstein, A. (1965). "Polymerization of adsorbed monolayers. II. Thermal degradation of the inserted polymer." *J Polym Sci Part A Gen Pap*, 3(7), 2665–2672.
- Borthakur, L. J., Das, D., and Dolui, S. K. (2010). "Development of core-shell nano composite of poly (styrene-co-methyl acrylate) and bentonite clay by ultra sonic assisted mini-emulsion polymerization." *Mater Chem Phys*, 124(2–3), 1182–1187.
- Brindley, G. W., and Goodyear, J. (1948). "X-ray studies of halloysite and metahalloysite. Part II. The transition of halloysite to metalhalloysite in relation to relative humidity." *Mineral Mag*, 28, 407–422.
- Bruggen, B. Van Der, and Vandecasteele, C. (2003). "Removal of pollutants from surface water and groundwater by nanofiltration: Overview of possible applications in the drinking water industry." *Environ Pollut*, 122(3), 435–445.
- Burton, Z., and Bhushan, B. (2005). "Hydrophobicity, Adhesion, and Friction Properties of Nanopatterned Polymers and Scale Dependence for Micro- and Nanoelectromechanical Systems." *Nano Lett*, 5(8), 1607–1613.
- Buruga, K., Kalathi, J. T., Kim, K. H., Ok, Y. S., and Danil, B. (2018). "Polystyrene-halloysite nano tube membranes for water purification." *J Ind Eng Chem*, 61, 169–180.

- Camargo, P. H. C., Satyanarayana, K. G., and Wypych, F. (2009). "Nanocomposites: synthesis, structure, properties and new application opportunities." *Mater Res*, 12(1), 1–39.
- Cao, Y., Zheng, Y., and Pan, G. (2008). "Radical generation process studies of the cationic surfactants in ultrasonically irradiated emulsion polymerization." *Ultrason Sonochem*, 15(4), 320–325.
- Cao, Z., and Ziener, U. (2013). "Synthesis of nanostructured materials in inverse miniemulsions and their applications." *Nanoscale*, 5(21), 10093–10107.
- Capek, I. (2012). "On photoinduced miniemulsion polymerization of butyl acrylate with clay." *Des Monomers Polym*, 15(4), 345–355.
- Carastan, D. J., and Demarquette, N. R. (2007). "Polystyrene/clay nanocomposites." *Int Mater Rev*, 52(6), 345–380.
- Cavallaro, G., Donato, D. I., Lazzara, G., and Milioto, S. (2011). "Films of halloysite nanotubes sandwiched between two layers of biopolymer: From the morphology to the dielectric, thermal, transparency, and wettability properties." *J Phys Chem C*, 115(42), 20491–20498.
- Cavallaro, G., Lazzara, G., Milioto, S., and Parisi, F. (2015). "Hydrophobically Modified Halloysite Nanotubes as Reverse Micelles for Water-in-Oil Emulsion." *Langmuir*, 31(27), 7472–7478.
- Cavallaro, G., Lazzara, G., Milioto, S., Parisi, F., and Sanzillo, V. (2014). "Modified Halloysite Nanotubes: Nanoarchitectures for Enhancing the Capture of Oils from Vapor and Liquid Phases." *Appl Mater Interfaces*, 6, 606–612.
- Celina, M., Ottesen, D. K., Gillen, K. T., and Clough, R. L. (1997). "FTIR emission spectroscopy applied to polymer degradation." *Polym Degrad Stab*, 58, 15–31.
- Chen, Y., Zhang, Y., Liu, J., Zhang, H., and Wang, K. (2012). "Preparation and antibacterial property of polyethersulfone ultrafiltration hybrid membrane containing halloysite nanotubes loaded with copper ions." *Chem Eng J*, 210, 298–308.
- Chen, Y., Zhang, Y., Zhang, H., Liu, J., and Song, C. (2013). "Biofouling control of halloysite nanotubes-decorated polyethersulfone ultrafiltration membrane modified

with chitosan-silver nanoparticles.” *Chem Eng J*, 228, 12–20.

Chiang, C. L., and Ma, C. C. M. (2002). “Synthesis, characterization and thermal properties of novel epoxy containing silicon and phosphorus nanocomposites by sol-gel method.” *Eur Polym J*, 38(11), 2219–2224.

Choi, H. J., Kim, S. G., Hyun, Y. H., and Jhon, M. S. (2001). “Preparation and rheological characteristics of solvent-cast poly(ethylene oxide)/montmorillonite nanocomposites.” *Macromol Rapid Commun*, 22(5), 320–325.

Crespy, D., and Landfester, K. (2010). “Miniemulsion polymerization as a versatile tool for the synthesis of functionalized polymers.” *Beilstein J Org Chem*, 6, 1132–1148.

D. M. C. Macewan. (1946). “The Clay Minerals Halloysite and Meta-halloysite.” *Nature*, 157, 336–337.

Daraei, P., Madaeni, S. S., Salehi, E., Ghaemi, N., Ghari, H. S., Khadivi, M. A., and Rostami, E. (2013). “Novel thin film composite membrane fabricated by mixed matrix nanoclay/chitosan on PVDF microfiltration support: Preparation, characterization and performance in dye removal.” *J Memb Sci*, 436, 97–108.

Deen, I., and Zhitomirsky, I. (2014). “Electrophoretic deposition of composite halloysite nanotube-hydroxyapatite-hyaluronic acid films.” *J Alloys Compd*, 586, S531–S534.

Deng, S., Zhang, J., and Ye, L. (2009). “Halloysite–epoxy nanocomposites with improved particle dispersion through ball mill homogenisation and chemical treatments.” *Compos Sci Technol*, 69(14), 2497–2505.

Dogar, N. A., Nawaz, M., Majeed, M., and Saeed, A. Bin. (2013). “Characterization and Treatment of Wastewater from Sapphire Textile Industry, Pakistan.” *J Sci Innov Res*, 2(2), 351–371.

Doh, J. G., and Cho, I. (1998). “Synthesis and properties of polystyrene-organoammonium montmorillonite hybrid.” *Polym Bull*, 41(5), 511–518.

Douglas M C, M. M. A. (1947). “The nomenclature of the halloysite minerals.” *Mineral Mag*, (5), 36–44.

Du, M., Guo, B., and Jia, D. (2006). “Thermal stability and flame retardant effects of

- halloysite nanotubes on poly(propylene).” *Eur Polym J*, 42(6), 1362–1369.
- Du, M., Guo, B., and Jia, D. (2010). “Newly emerging applications of halloysite nanotubes: A review.” *Polym Int*, 59(5), 574–582.
- Erpek, C. E. Y., Ozkoc, G., and Yilmazer, U. (2017). “Comparison of natural halloysite with synthetic carbon nanotubes in poly(lactic acid) based composites.” *Polym Compos*, 38(11), 2337–2346.
- Ferris, F. G., Fyfe, W. S., and Beveridge, T. J. (1987). “Bacteria as nucleation sites for authigenic minerals in a metal-contaminated lake sediment.” *Chem Geol*, 63(3–4), 225–232.
- Fischer, H. (2003). “Polymer nanocomposites: From fundamental research to specific applications.” *Mater Sci Eng C*, 23(6–8), 763–772.
- Frost, R. L., Makó, É., Kristóf, J., Erzsébet Horváth, A., and Klopogge, J. T. (2001). “Modification of Kaolinite Surfaces by Mechanochemical Treatment.” *Langmuir*, 17, 4731–4738.
- Gao, L., and He, J. (2013). “A facile dip-coating approach based on three silica sols to fabrication of broadband antireflective superhydrophobic coatings.” *J Colloid Interface Sci*, 400, 24–30.
- Geise, G. M., Lee, H.-S., Miller, D. J., Freeman, B. D., McGrath, J. E., and Paul, D. R. (2010). “Water purification by membranes: The role of polymer science.” *J Polym Sci Part B Polym Phys*, 48(15), 1685–1718.
- Ghaemi, N., Madaeni, S. S., Alizadeh, A., Rajabi, H., and Daraei, P. (2011). “Preparation, characterization and performance of polyethersulfone/organically modified montmorillonite nanocomposite membranes in removal of pesticides.” *J Memb Sci*, 382(1–2), 135–147.
- Ghanbari, M., Emadzadeh, D., Lau, W. J., Lai, S. O., Matsuura, T., and Ismail, A. F. (2015). “Synthesis and characterization of novel thin film nanocomposite (TFN) membranes embedded with halloysite nanotubes (HNTs) for water desalination.” *Desalination*, 358, 33–41.
- Gilman, J. W. (1999). “Flammability and thermal stability studies of polymer layered-



silicate (clay) nanocomposites.” *Appl Clay Sci*, 15, 31–49.

Gogate, P. R. (2008). “Cavitation reactors for process intensification of chemical processing applications: A critical review.” *Chem Eng Process Process Intensif*, 47(4), 515–527.

Gopi, K. R., and Nagarajan, R. (2008). “Advances in Nanoalumina Ceramic Particle Fabrication Using Sonofragmentation.” *IEEE Trans Nanotechnol*, 7(5), 532–537.

“Guidelines for Drinking-water Quality Volume 1 Recommendations WHO Library Cataloguing-in-Publication Data.” (n.d.). .

Guo, B., Lei, Y., Chen, F., Liu, X., Du, M., and Jia, D. (2008). “Styrene – butadiene rubber / halloysite nanotubes nanocomposites modified by methacrylic acid.” *Appl Surf Sci*, 255, 2715–2722.

Guo, X., Fan, S., Hu, Y., Fu, X., Shao, H., and Zhou, Q. (2019). “A novel membrane biofouling mitigation strategy of D-amino acid supported by polydopamine and halloysite nanotube.” *J Memb Sci*.

Hasegawa, N., Okamoto, H., Kawasumi, M., and Usuki, A. (1999). “Preparation and mechanical properties of polystyrene-clay hybrids.” *J Appl Polym Sci*, 74(14), 3359–3364.

Hatami, L., Haddadi-Asl, V., Ahmadian-Alam, L., Roghani-Mamaqani, H., and Salami-Kalajahi, M. (2013). “Effect of nanoclay on styrene and butyl acrylate AGET ATRP in miniemulsion: Study of nucleation type, kinetics, and polymerization control.” *Int J Chem Kinet*, 45(4), 221–235.

Hebbar, R. S., Isloor, A. M., and Ismail, A. F. (2014). “Preparation and evaluation of heavy metal rejection properties of polyetherimide/porous activated bentonite clay nanocomposite membrane.” *RSC Adv*, 4(88), 47240–47248.

Hedicke-höchstötter, K., Lim, G. T., Altstädt, V., Teck, G., and Altstädt, V. (2009). “Novel polyamide nanocomposites based on silicate nanotubes of the mineral halloysite.” *Compos Sci Technol*, 69(3–4), 330–334.

Hendricks, S. B. (1938). “Crystal structures of the clay mineral hydrates [10].” *Nature*, 142(3583), 38.

Herk, A. M. van. (2010). "Historical Overview of (Mini)emulsion Polymerizations and Preparation of Hybrid Latex Particles." Springer, Berlin, Heidelberg, 1–18.

Hoang-Minh T, T L, Le, Kasbohm J, Giere R, Hoang-Minh, Le, T. L., Hoang-Minh, T., Le, T. L., Kasbohm, J., and Gieré, R. (2010). "UV-protection characteristics of some clays." *Appl Clay Sci*, 48(3), 349–357.

Holland, B. J., and Hay, J. N. (2001). "The kinetics and mechanisms of the thermal degradation of poly (methyl methacrylate) studied by thermal analysis-Fourier transform infrared spectroscopy." *Polymer (Guildf)*, 42, 4825–4835.

Hong, C. K., Kim, M. J., Oh, S. H., Lee, Y. S., and Nah, C. (2008). "Effects of polypropylene-g-(maleic anhydride/styrene) compatibilizer on mechanical and rheological properties of polypropylene/clay nanocomposites." *J Ind Eng Chem*, 14(2), 236–242.

Horst, C., Chen, Y.-S., Kunz, U., and Hoffmann, U. (1996). "Design, modeling and performance of a novel sonochemical reactor for heterogeneous reactions." *Chem Eng Sci*, 51(10), 1837–1846.

Hou, Q., Yan, K., Fan, R., Zhang, Z., Chen, M., Sun, K., and Cheng, C. (2015). "Experimental realization of tunable negative permittivity in percolative Fe<sub>78</sub>Si<sub>9</sub>B<sub>13</sub>/epoxy composites." *RSC Adv*, 5, 9472–9475.

Hu, J., Chen, M., and Wu, L. (2011). "Organic-inorganic nanocomposites synthesized via miniemulsion polymerization." *Polym Chem*, 2(4), 760–762.

Huang, D., Wang, W., Kang, Y., and Wang, A. (2012). "A chitosan/poly(vinyl alcohol) nanocomposite film reinforced with natural halloysite nanotubes." *Polym Compos*, 33(10), 1693–1699.

Huang, X., and Brittain, W. J. (2001). "Synthesis and characterization of PMMA nanocomposites by suspension and emulsion polymerization." *Macromolecules*, 34(10), 3255–3260.

Ismail, H., Pasbakhsh, P., Fauzi, M. N. A., and Abu Bakar, A. (2008). "Morphological, thermal and tensile properties of halloysite nanotubes filled ethylene propylene diene monomer (EPDM) nanocomposites." *Polym Test*, 27(7), 841–850.

Ismail, H., and Shaari, S. M. (2010). "Curing characteristics, tensile properties and morphology of palm ash/halloysite nanotubes/ethylene-propylene-diene monomer (EPDM) hybrid composites." *Polym Test*, 29(7), 872–878.

ISO. (1992). *ISO 9845-1:1992 Solar energy - Reference solar spectral irradiance at the ground at different receiving conditions - Part 1: Direct normal and hemispherical solar irradiance for air mass 1,5*. 14.

Jeon, H. G., Jung, H.-T., Lee, S. W., and Hudson, S. D. (1998). "Morphology of polymer/silicate nanocomposites." *Polym Bull*, 41(1), 107–113.

Jordan, J., Jacob, K. I., Tannenbaum, R., Sharaf, M. A., and Jasiuk, I. (2005). "Experimental trends in polymer nanocomposites - A review." *Mater Sci Eng A*, 393(1–2), 1–11.

Joshi, A. R., Null, R., Graham, S., Abdullayev, E., Mazurenko, V., and Lvov, Y. (2016). "Enhanced flame retardancy of latex coating doped with clay nanotubes." *J Coatings Technol Res*, 13(3), 535–541.

Joussein, E., Petit, S., Churchman, J., Theng, B., Righi, D., and Delvaux, B. (2005). "Halloysite clay minerals-a review." *Clay Miner*, 40(4), 383–426.

Kandare, E., Wang, D., Hossenlopp, J., and Kandare, E. (2006). "Thermal Stability and Degradation Kinetics of Poly ( methyl Methacrylate )/ Layered Copper Hydroxy Methacrylate Composites Thermal Stability and Degradation Kinetics of Poly ( methyl Methacrylate )/ Layered Copper Hydroxy Methacrylate Composites." *Polym Adv Technol*, 17(4), 312–319.

Kass, M. D., Kiggans, J., and Meek, T. T. (1996). "Ultrasonic modification of alumina powder during wet-ball milling." *Mater Lett*, 26(March), 241–243.

Kausar, A. (2014). "Novel Water Purification Membranes of Polystyrene/Multi-Walled Carbon Nanotube-grafted-Graphene Oxide Hybrids." *Am J Polym Sci*, 4(3), 63–72.

Ke, Z., and Yongping, B. (2005). "Improve the gas barrier property of PET film with montmorillonite by in situ interlayer polymerization." *Mater Lett*, 59, 3348–3351.

Khunova, V., Kristóf, J., Kelnar, I., and Dybal, J. (2013). "The effect of halloysite modification combined with in situ matrix modifications on the structure and properties

- of polypropylene/halloysite nanocomposites.” *Express Polym Lett*, 7(5), 471–479.
- Kickelbick, G. (2003). *Concepts for the incorporation of inorganic building blocks into organic polymers on a nanoscale*. *Prog Polym Sci*.
- Kim, T. H., Lim, S. T., Lee, C. H., Choi, H. J., and Jhon, M. S. (2003). “Preparation and rheological characterization of intercalated polystyrene/organophilic montmorillonite nanocomposite.” *J Appl Polym Sci*, 87(13), 2106–2112.
- Kong, Q., Lv, R., and Zhang, S. (2008). “Kong, Qinghong Lv, Ruibin Zhang, Shijun.” *J Polym Res*, 15(6), 453–458.
- Koo, C. M., Ham, H. T., Choi, M. H., Kim, S. O., and Chung, I. J. (2002). “Characteristics of polyvinylpyrrolidone-layered silicate nanocomposites prepared by attrition ball milling.” *Polymer (Guildf)*, 44(3), 681–689.
- Kruus, P. (1987). “Initiation of polymerization with ultrasound.” *Ultrasonics*, 25(1), 20–22.
- Kumar, S., Mandal, A., and Guria, C. (2016). “Synthesis, characterization and performance studies of polysulfone and polysulfone/polymer-grafted bentonite based ultrafiltration membranes for the efficient separation of oil field oily wastewater.” *Process Saf Environ Prot*, 102, 214–228.
- Lai, C. Y., Groth, A., Gray, S., and Duke, M. (2011). “Investigation of the dispersion of nanoclays into PVDF for enhancement of physical membrane properties.” *Desalin Water Treat*, 34(1–3), 251–256.
- Lai, C. Y., Groth, A., Gray, S., and Duke, M. (2014). “Enhanced abrasion resistant PVDF/nanoclay hollow fibre composite membranes for water treatment.” *J Memb Sci*, 449, 146–157.
- Lakshmi, M. S., Narmadha, B., and Reddy, B. S. R. (2008). “Enhanced thermal stability and structural characteristics of different MMT-Clay/epoxy-nanocomposite materials.” *Polym Degrad Stab*, 93(1), 201–213.
- Lan, T., and Pinnavaia, T. J. (1994). “Clay-Reinforced Epoxy Nanocomposites.” *Chem Mater*, 2219(20), 2216–2219.
- Landfester, K. (2006). “Synthesis of Colloidal Particles in Miniemulsions.” *Annu Rev*

*Mater Res*, 36(1), 231–279.

Landfester, K., Bechthold, N., Tiarks, F., and Antonietti, M. (1999). “Formulation and stability mechanisms of polymerizable miniemulsions.” *Macromolecules*, 32(16), 5222–5228.

Laus, M., Camerani, M., Lelli, M., Sparnacci, K., Sandrolini, F., Francescangeli, O. (1998). “Hybrid nanocomposites based on polystyrene and reactive organophilic clay.” *J Mater Sci*.

Lebaron, P. C., Wang, Z., and Pinnavaia, T. J. (1999). “Polymer-layered silicate nanocomposites: An overview.” *Appl Clay Sci*, 15(1–2), 11–29.

Lecouvet, B., Gutierrez, J. G., Sclavons, M., and Bailly, C. (2011). “Structure-property relationships in polyamide 12/halloysite nanotube nanocomposites.” *Polym Degrad Stab*, 96(2), 226–235.

Lee, J. W., Lim, Y. T., and Park, O. O. (2000). “Thermal characteristics of organoclay and their effects upon the formation of polypropylene / organoclay nanocomposites.” *Polym Bull* 45, 45, 191–192.

Leite, A. M. D., Maia, L. F., Pereira, O. D., Araujo, E. M., Lira, H. de L., and Castro, W. B. de. (2010). “Mechanical properties of nylon 6/Brazilian clay nanocomposites.” *J Alloys Compd*, 495(2), 596–597.

Levis, S. R., and Deasy, P. B. (2002). “Characterisation of halloysite for use as a microtubular drug delivery system.” *Int J Pharm*, 243(1–2), 125–134.

Li, Q., Yue, Q., Su, Y., and Gao, B. (2011). “Equilibrium and a two-stage batch adsorber design for reactive or disperse dye removal to minimize adsorbent amount.” *Bioresour Technol*, 102(9), 5290–5296.

Li, Y., and Ishida, H. (2003). “Solution intercalation of polystyrene and the comparison with poly(ethyl methacrylate).” *Polymer (Guildf)*, 44(21), 6571–6577.

Liao, C., Yu, P., Zhao, J., Wang, L., and Luo, Y. (2011). “Preparation and characterization of NaY/PVDF hybrid ultrafiltration membranes containing silver ions as antibacterial materials.” *Desalination*, 272(1–3), 59–65.

Lighthill, S. J. (1978). “Acoustic streaming.” *J Sound Vib*, 61(3), 391–418.

- Lii, C., Chen, C.-H., Yeh, A.-I., and Lai, V. M.-F. (1999). "Preliminary study on the degradation kinetics of agarose and carrageenans by ultrasound." *Food Hydrocoll*, 13(6), 477–481.
- Lin, M. C., and Otaduy, M. A. (2005). "Sensation-preserving haptic rendering." *IEEE Comput Graph Appl*, 25(4), 8–11.
- Lin, Y., Ng, K. M., Chan, C.-M. M., Sun, G., and Wu, J. (2011). "High-impact polystyrene/halloysite nanocomposites prepared by emulsion polymerization using sodium dodecyl sulfate as surfactant." *J Colloid Interface Sci*, 358(2), 423–429.
- Liu, L., Qi, Z., and Zhu, X. (1999). "Studies on nylon 6/clay nanocomposites by melt-intercalation process." *J Appl Polym Sci*, 71(7), 1133–1138.
- Liu, M., Guo, B., Du, M., Cai, X., and Jia, D. (2007). "Properties of halloysite nanotube-epoxy resin hybrids and the interfacial reactions in the systems." *Nanotechnology*, 18(45).
- Liu, M., Jia, Z., Jia, D., and Zhou, C. (2014). "Recent advance in research on halloysite nanotubes-polymer nanocomposite." *Prog Polym Sci*, 39(8), 1498–1525.
- Liu, M., Jia, Z., Liu, F., Jia, D., and Guo, B. (2010). "Tailoring the wettability of polypropylene surfaces with halloysite nanotubes." *J Colloid Interface Sci*, 350(1), 186–193.
- Liu, P., and Zhao, M. (2009). "Silver nanoparticle supported on halloysite nanotubes catalyzed reduction of 4-nitrophenol (4-NP)." *Appl Surf Sci*, 255(7), 3989–3993.
- Lvov, Y., and Abdullayev, E. (2013). "Functional polymer–clay nanotube composites with sustained release of chemical agents." *Prog Polym Sci*, 38(10–11), 1690–1719.
- Lvov, Y. M., and Price, R. R. (2008). "Halloysite Nanotubules, a Novel Substrate for the Controlled Delivery of Bioactive Molecules." *Bio-inorganic Hybrid Nanomater Strateg Synth Charact Appl*, Weinheim, Germany: Wiley-VCH Verlag GmbH & Co. KGaA, 419–441.
- Ma, H., Song, P., and Fang, Z. (2011). "Flame retarded polymer nanocomposites: Development, trend and future perspective." *Sci China Chem*, 54(2), 302–313.
- Macewan, D. M. C. (1946). "Halloysite-organic Complexes." *Nature*, 157, 336–337.

- Madaeni, S. S., and Mansourpanah, Y. (2004). "Chemical cleaning of reverse osmosis membranes fouled by whey." 161, 13–24.
- Madelin, G., Grucker, D., Franconi, J.-M., and Thiaudiere, E. (2006). "Magnetic resonance imaging of acoustic streaming: absorption coefficient and acoustic field shape estimation." *Ultrasonics*, 44(3), 272–8.
- Magaraphan, R., Lilayuthalert, W., Sirivat, A., and Schwank, J. W. (2001). "Preparation, structure, properties and thermal behavior of rigid-rod polyimide/montmorillonite nanocomposites." *Compos Sci Technol*, 61(9), 1253–1264.
- Mahdavian, A. R., Sarrafi, Y., and Shabankareh, M. (2009). "Nanocomposite particles with core-shell morphology III: Preparation and characterization of nano Al<sub>2</sub>O<sub>3</sub>-poly(styrene-methyl methacrylate) particles via miniemulsion polymerization." *Polym Bull*, 63(3), 329–340.
- Malas, A., and Das, C. K. (2017). "Influence of modified graphite flakes on the physical, thermo-mechanical and barrier properties of butyl rubber." *J Alloys Compd*, 699, 38–46.
- Maryan, A. S., and Montazer, M. (2015). "Natural and organo-montmorillonite as antibacterial nanoclays for cotton garment." *J Ind Eng Chem*, 22, 164–170.
- Mason, T. J., Collings, A., and Sumel, A. (2004). "Sonic and ultrasonic removal of chemical contaminants from soil in the laboratory and on a large scale." *Ultrason Sonochem*, 11(3–4), 205–210.
- McDowall, I., and Vose, W. (1952). "Sedimentation of halloysite." *Nature*, 170(4322), 368.
- McNeill, I. C., Zulfiqar, M., and Kousar, T. (1990). "A detailed investigation of the products of the thermal degradation of polystyrene." *Polym Degrad Stab*, 28(2), 131–151.
- Messersmith, P. B., and Giannelis, E. P. (1993). "Polymer-Layered Silicate Nanocomposites: In Situ Intercalative Polymerization of  $\epsilon$ -Caprolactone in Layered Silicates." *Chem Mater*, 5(8), 1064–1066.
- Messersmith, P. B., and Giannelis, E. P. (1995). "Synthesis and barrier properties of

poly( $\epsilon$ -caprolactone)-layered silicate nanocomposites.” *J Polym Sci Part A Polym Chem*, 33(7), 1047–1057.

Mirzataheri, M., Mahdavian, A. R., and Atai, M. (2009). “Nanocomposite particles with core-shell morphology IV: An efficient approach to the encapsulation of Cloisite 30B by poly (styrene-co-butyl acrylate) and preparation of its nanocomposite latex via miniemulsion polymerization.” *Colloid Polym Sci*, 287(6), 725–732.

Moghbelli, E., Browning, R. L., Boo, W.-J., Hahn, S. F., Feick, L. J. E., and Sue, H.-J. (2008). “Effects of molecular weight and thermal history on scratch behavior of polypropylene thin sheets.” *Tribol Int*, 41(5), 425–433.

Mohammad, R. K., and Yeum, J. H. (2008). “In Situ Intercalative polymerisation of conducting Polypyrrole/Montmorillonite Nanocomposites.” *J Polym Sci Part B Polym Phys*, 2279–2285.

Monticelli, O., Bottino, A., Scandale, I., Capannelli, G., and Russo, S. (2007). “Preparation and properties of polysulfone–clay composite membranes.” *J Appl Polym Sci*, 103(6), 3637–3644.

Moraes, R. P., Santos, A. M., Oliviera, P. C., Souza, F. C. T., Amoral, M. Do, Volera, T. S., and Demarquette, N. R. (2006). “Poly(styrene-co-butyl acrylate)-Brazilian montmorillonite nanocomposites, synthesis of hybrid latexes via miniemulsion polymerization.” *Macromol Symp*, 245–246, 106–115.

Morgan, A. B., and Harris, J. D. (2004). “Exfoliated polystyrene-clay nanocomposites synthesized by solvent blending with sonication.” *Polymer (Guildf)*, 45(26), 8695–8703.

Mu, B., Zhao, M., and Liu, P. (2008). “Halloysite nanotubes grafted hyperbranched (co) polymers via surface-initiated self-condensing vinyl (co) polymerization.” *J Nanopart Res*, 10, 831–838.

Nkeuwa, W. N., Riedl, B., and Landry, V. (2017). “Transparent UV-cured clay/UV-based nanocomposite coatings on wood substrates: surface roughness and effect of relative humidity on optical properties.” *J Coatings Technol Res*, 14(3), 555–569.

Noein, L., Haddadi-Asl, V., and Salami-Kalajahi, M. (2017). “Grafting of pH-sensitive



poly (N,N-dimethylaminoethyl methacrylate-co-2-hydroxyethyl methacrylate) onto HNTS via surface-initiated atom transfer radical polymerization for controllable drug release.” *Int J Polym Mater Polym Biomater*, 66(3), 123–131.

Noh, M. W., and Lee, D. C. (1999). “Synthesis and characterization of PS-clay nanocomposite by emulsion polymerization.” *Polym Bull*, 42(5), 619–626.

Novak, B. M. (1993). “Hybrid Nanocomposite Materials—between inorganic glasses and organic polymers.” *Adv Mater*, 5(6), 422–433.

Ogata, N., Jimenez, G., Kawai, H., and Ogihara, T. (1997). “Structure and Thermal / Mechanical Properties of Poly ( l-lactide ) -Clay Blend.” *J Polym Sci Part B Polym Phys*, 35, 389–396.

Ohtsuka, Y., Kawaguchi, H., and Sugi, Y. (1981). “Copolymerization of styrene with acrylamide in an emulsifier- free aqueous medium.” *J Appl Polym Sci*, 26(5), 1637–1647.

Okada, A., and Usuki, A. (2006). “Twenty years of polymer-clay nanocomposites.” *Macromol Mater Eng*, 291(12), 1449–1476.

Okitsu, K., Iwasaki, K., Yobiko, Y., Bandow, H., Nishimura, R., and Maeda, Y. (2005). “Sonochemical degradation of azo dyes in aqueous solution: A new heterogeneous kinetics model taking into account the local concentration of OH radicals and azo dyes.” *Ultrason Sonochem*, 12(4), 255–262.

Ooi, S. K., and Biggs, S. (2000). “Ultrasonic initiation of polystyrene latex synthesis.” *Ultrason Sonochem*, 7(3), 125–133.

Padhi, S., Achary, P. G. R., and Nayak, N. C. (2017). “Mechanical and morphological properties of halloysite nanotubes filled ethylene-vinyl acetate copolymer nanocomposites.” *J Polym Eng*, 24, 184–191.

Parija, S., Nayak, S. K., Verma, S. K., and Tripathy, S. S. (2004). “Studies on physico-mechanical properties and thermal characteristics of polypropylene/layered silicate nanocomposites.” *Polym Compos*, 25(6), 646–652.

Pasbakhsh, P., Ismail, H., Fauzi, M. N. A., and Bakar, A. A. (2010). “EPDM/modified halloysite nanocomposites.” *Appl Clay Sci*, 48(3), 405–413.

Petter Jelle, B., Gustavsen, A., Nilsen, T. N., and Jacobsen, T. (2007). "Solar material protection factor (SMPF) and solar skin protection factor (SSPF) for window panes and other glass structures in buildings." *Sol Energy Mater Sol Cells*, 91, 342–354.

Pooria Pasbakhsh, and G. J. C. (2015). *Natural mineral nanotubes*.

Pospisil, J., and Nespurek, S. (2000). "Photostabilization of coatings. Mechanisms and performance." *Prog Polym Sci*, 25(9), 1261–1335.

Price, G. J. (1996). "Ultrasonically enhanced polymer synthesis." *Ultrason Sonochem*, 3(3), S229–S238.

Price, G. J., Norris, D. J., and West, P. J. (1992). "Polymerization of Methyl methacrylate Initiated by Ultrasound." *Macromolecules*, 25(24), 6447–6454.

Qin, L., Zhao, Y., Liu, J., Hou, J., Zhang, Y., Wang, J., Zhu, J., Zhang, B., Lvov, Y., and Bruggen, B. Van Der. (2016). "Oriented Clay Nanotube Membrane Assembled on Microporous Polymeric Substrates." *ACS Appl Mater Interfaces*, 8(50), 34914–34923.

Qutubuddin, S., Fu, X. a., and Tajuddin, Y. (2002). "Synthesis of polystyrene-clay nanocomposites via emulsion polymerization using a reactive surfactant." *Polym Bull*, 48(2), 143–149.

R. Price, B. P. Gaber, Y. Lvov, R., Price, R. R., Gaber, B. P., and Lvov, Y. (2001). "In-vitro release characteristics of tetracycline HCl, khellin and nicotinamide adenine dinucleotide from halloysite; a cylindrical mineral." *J Microencapsul*, 18(6), 713–722.

Ray, S. S., and Bousmina, M. (2005). "Biodegradable polymers and their layered silicate nanocomposites: In greening the 21st century materials world." *Prog Mater Sci*, 50(8), 962–1079.

Rezaei, H., Ashtiani, F. Z., and Fouladitajar, A. (2011). "Effects of operating parameters on fouling mechanism and membrane flux in cross- flow micro filtration of whey." *DES*, 274(1–3), 262–271.

Richards, W. T., and Loomis, A. L. (1927). "The chemical effects of high frequency sound waves I. A preliminary survey." *J Am Chem Soc*, 49(12), 3086–3100.

Roy, R., Roy, R. A., and Roy, D. M. (1986). "Alternative perspectives on 'quasi-crystallinity': Non-uniformity and nanocomposites." *Mater Lett*, 4(8–9), 323–328.

Ryu, J. G., Park, S. W., Kim, H., and Lee, J. W. (2004). "Power ultrasound effects for in situ compatibilization of polymer-clay nanocomposites." *Mater Sci Eng C*, 24(1–2), 285–288.

Sarat K. Swain, A. I. I. (2013). "PA6/Clay Nanocomposites by Continuous Sonication Process." *Polym Polym Compos*, 21(7), 449–456.

Scarfato, P., Acierno, D., and Russo, P. (2015). "Photooxidative weathering of biodegradable nanocomposite films containing halloysite." *Polym Compos*, 36(6), 1169–1175.

Sedláková, Z., Pleštil, J., Baldrian, J., Šlouf, M., and Holub, P. (2009). "Polymer-clay nanocomposites prepared via in situ emulsion polymerization." *Polym Bull*, 63(3), 365–384.

Shchukin, D. G., Lamaka, S. V., Yasakau, K. A., Zheludkevich, M. L., Ferreira, M. G. S., and Möhwald, H. (2008). "Active anticorrosion coatings with halloysite nanocontainers." *J Phys Chem C*, 112(4), 958–964.

Shchukin, D. G., and Möhwald, H. (2007). "Self-repairing coatings containing active nanoreservoirs." *Small*, 3(6), 926–943.

Shchukin, D. G., Sukhorukov, G. B., Price, R. R., and Lvov, Y. M. (2005). "Halloysite nanotubes as biomimetic nanoreactors." *Small*, 1(5), 510–513.

She, J., Inoue, T., Suzuki, M., Sodeoka, S., and Ueno, K. (2000). "Mechanical properties and fracture behavior of  $\alpha$ -brous  $\text{Al}_2\text{O}_3$  / SiC ceramics." *J Eur Ceram Soc*, 20, 1–5.

Shokri, E., Yegani, R., Pourabbas, B., and Kazemian, N. (2016). "Preparation and characterization of polysulfone/organoclay adsorptive nanocomposite membrane for arsenic removal from contaminated water." *Appl Clay Sci*, 132–133, 611–620.

Silva, A. A., Dahmouche, K., and Soares, B. G. (2010). "The effect of addition of acrylic acid and thioglycolic acid on the nanostructure and thermal stability of PMMA-montmorillonite nanocomposites." *Appl Clay Sci*, 47(3–4), 414–420.

Singla, P., Mehta, R., and Upadhyay, S. N. (2012). "Clay Modification by the Use of Organic Cations." *Green Sustain Chem*, 02(01), 21–25.

- Sinha Ray, S., and Okamoto, M. (2003). "Polymer/layered silicate nanocomposites: A review from preparation to processing." *Prog Polym Sci*, 28(11), 1539–1641.
- Suh, Y. J., Kil, D. S., Chung, K. S., Abdullayev, E., Lvov, Y. M., and Mongayt, D. (2011). "Natural Nanocontainer for the Controlled Delivery of Glycerol as a Moisturizing Agent." *J Nanosci Nanotechnol*, 11(1), 661–665.
- Sun, K., Xie, P., Wang, Z., Su, T., Shao, Q., Ryu, J. E., Zhang, X., Guo, J., Shankar, A., Li, J., Fan, R., Cao, D., and Guo, Z. (2017). "Flexible polydimethylsiloxane/multi-walled carbon nanotubes membranous metacomposites with negative permittivity." *Polymer (Guildf)*, 125, 50–57.
- Sun, Q., Deng, Y., and Wang, Z. L. (2004). "Synthesis and characterization of polystyrene-encapsulated laponite composites via miniemulsion polymerization." *Macromol Mater Eng*, 289(3), 288–295.
- Sur, G. ., Sun, H. ., Lyu, S. ., and Mark, J. . (2001). "Synthesis, structure, mechanical properties, and thermal stability of some polysulfone/organoclay nanocomposites." *Polymer (Guildf)*, 42(24), 9783–9789.
- Susanto, H., and Ulbricht, M. (2009). "Characteristics, performance and stability of polyethersulfone ultrafiltration membranes prepared by phase separation method using different macromolecular additives." *J Memb Sci*, 327(1–2), 125–135.
- Suslick, K. S. (1990a). "Ultrasound: its chemical, physical, and biological effects." *J Acoust Soc Am*, 82, 919–920.
- Suslick, K. S. (1990b). "Sonochemistry." *Science (80- )*, 247(4949), 1439–1445.
- Tang, Y., Deng, S., Ye, L., Yang, C., Yuan, Q., Zhang, J., and Zhao, C. (2011). "Effects of unfolded and intercalated halloysites on mechanical properties of halloysite-epoxy nanocomposites." *Compos Part A Appl Sci Manuf*, 42(4), 345–354.
- Tang, Y., Ye, L., Deng, S., Yang, C., and Yuan, W. (2012). "Influences of processing methods and chemical treatments on fracture toughness of halloysite-epoxy composites." *Mater Des*, 42, 471–477.
- Teo, B. M., Prescott, S. W., Ashokkumar, M., and Grieser, F. (2008). "Ultrasound initiated miniemulsion polymerization of methacrylate monomers." *Ultrason*

*Sonochem*, 15(1), 89–94.

Tierrablanca, E., Romero-García, J., Roman, P., and Cruz-Silva, R. (2010). “Biomimetic polymerization of aniline using hematin supported on halloysite nanotubes.” *Appl Catal A Gen*, 381(1–2), 267–273.

Tjong, S. C., Wang, G. S., and Mai, Y. W. (2005). “High cycle fatigue response of in-situ Al-based composites containing TiB<sub>2</sub> and Al<sub>2</sub>O<sub>3</sub> submicron particles.” *Compos Sci Technol*, 65(10), 1537–1546.

Tong, Z., and Deng, Y. (2013). “The formation of asymmetric polystyrene/saponite composite nanoparticles via miniemulsion polymerization.” *J Appl Polym Sci*, 127(5), 3916–3922.

Tseng, C. R., Lee, H. Y., and Chang, F. C. (2001). “Crystallization kinetics and crystallization behavior of syndiotactic polystyrene/clay nanocomposites.” *J Polym Sci Part B Polym Phys*, 39(17), 2097–2107.

Vatanpour, V., Madaeni, S. S., Rajabi, L., Zinadini, S., and Derakhshan, A. A. (2012). “Boehmite nanoparticles as a new nanofiller for preparation of antifouling mixed matrix membranes.” *J Memb Sci*, 401–402, 132–143.

Wang, C., Wang, Q., and Chen, X. (2005a). “Intercalated PS/Na<sup>+</sup>-MMT nanocomposites prepared by ultrasonically initiated in situ emulsion polymerization.” *Macromol Mater Eng*, 290(9), 920–926.

Wang, J., Du, J., Zhu, J., and Wilkie, C. A. (2002). “An XPS study of the thermal degradation and flame retardant mechanism of polystyrene-clay nanocomposites.” *Polym Degrad Stab*, 77(2), 249–252.

Wang, J., Hu, Y., Wang, S., and Chen, Z. (2005b). “Sonochemical one-directional growth of montmorillonite-polystyrene nanocomposite.” *Ultrason Sonochem*, 12(3), 165–168.

Wang, J., Shi, Z., Mao, F., Chen, S., and Wang, X. (2017). “Bilayer Polymer Metacomposites Containing Negative Permittivity Layer for New High-*k* Materials.” *ACS Appl Mater Interfaces*, 9(2), 1793–1800.

Wang, R., Jiang, G., Ding, Y., Wang, Y., Sun, X., Wang, X., and Chen, W. (2011).

“Photocatalytic activity of heterostructures based on TiO<sub>2</sub> and halloysite nanotubes.” *ACS Appl Mater Interfaces*, 3(10), 4154–4158.

Wang, S., Long, C., Wang, X., Li, Q., and Qi, Z. (1998). “Synthesis and properties of silicone rubber/organomontmorillonite hybrid nanocomposites.” *J Appl Polym Sci*, 69(8), 1557–1561.

Wang, Y., Zhu, J., Dong, G., Zhang, Y., Guo, N., and Liu, J. (2015). “Sulfonated halloysite nanotubes/polyethersulfone nanocomposite membrane for efficient dye purification.” *Sep Purif Technol*, 150, 243–251.

Webster, A. J., and Cates, M. E. (1998). “Stabilization of Emulsions by Trapped Species.” *Langmuir*, 14(8), 2068–2079.

Woo, R. S. C., Chen, Y., Zhu, H., Li, J., Kim, J. K., and Leung, C. K. Y. (2007). “Environmental degradation of epoxy-organoclay nanocomposites due to UV exposure. Part I: Photo-degradation.” *Compos Sci Technol*, 67(15–16), 3448–3456.

Wu, J., and Lerner, M. M. (1993). “Structural, thermal, and electrical characterization of layered nanocomposites derived from sodium-montmorillonite and polyethers.” *Chem Mater*, 5(6), 835–838.

Xie, W., Gao, Z., Liu, K., Pan, W. P., Vaia, R., Hunter, D., and Singh, a. (2001). “Thermal characterization of organically modified montmorillonite.” *Thermochim Acta*, 367–368, 339–350.

Yan, L., Shui, Y., Bao, C., and Xianda, S. (2006). “Effect of nano-sized Al<sub>2</sub>O<sub>3</sub> -particle addition on PVDF ultrafiltration membrane performance.” *J Memb Sci*, 276, 162–167.

Yang, Y. (2017). “Recent Advances on Surface Modification of Halloysite Nanotubes for Multifunctional Applications.” *Appl Sci*, 7(12), 1215.

Yano, K., Usuki, A., and Okada, A. (1997). “Synthesis and properties of polyimide-clay hybrid films.” *J Polym Sci Part A Polym Chem*, 35(11), 2289–2294.

Yin, N., and Chen, K. (2004). “Ultrasonically initiated emulsifier-free emulsion copolymerization of n-butyl acrylate and acrylamide. Part I: Polymerization mechanism.” *Polymer (Guildf)*, 45(11), 3587–3594.

Young, T. H., and Chen, L. W. (1995). “Pore formation mechanism of membranes from

phase inversion process.” *Desalination*, 103(3), 233–247.

Yu, H., Zhang, Y., Sun, X., Liu, J., and Zhang, H. (2014). “Improving the antifouling property of polyethersulfone ultrafiltration membrane by incorporation of dextran grafted halloysite nanotubes.” *Chem Eng J*, 237, 322–328.

Yuan, P., Southon, P. D., Liu, Z., Green, M. E. R., Hook, J. M., Antill, S. J., and Kepert, C. J. (2008). “Functionalization of halloysite clay nanotubes by grafting with  $\gamma$ -aminopropyltriethoxysilane.” *J Phys Chem C*, 112(40), 15742–15751.

Zanetti, M., Camino, G., Thomann, R., and Èlhaupt, R. M. (2001). “Synthesis and thermal behaviour of layered silicate-EVA nanocomposites.” *Polymer (Guildf)*, 42, 4501–4507.

Zatta, L., Gardolinski, J. E. F. da C., and Wypych, F. (2011). “Raw halloysite as reusable heterogeneous catalyst for esterification of lauric acid.” *Appl Clay Sci*, 51(1–2), 165–169.

Zeng, C., and Lee, L. J. (2001). “Poly(methyl methacrylate) and polystyrene/clay nanocomposites prepared by in-situ polymerization.” *Macromolecules*, 34(12), 4098–4103.

Zeng, G., Ye, Z., He, Y., Yang, X., Ma, J., Shi, H., and Feng, Z. (2017a). “Application of dopamine-modified halloysite nanotubes/PVDF blend membranes for direct dyes removal from wastewater.” *Chem Eng J*, 323, 572–583.

Zeng, G., Ye, Z., He, Y., Yang, X., Ma, J., Shi, H., and Feng, Z. (2017b). “Application of dopamine-modified halloysite nanotubes/PVDF blend membranes for direct dyes removal from wastewater.” *Chem Eng J*, 323, 572–583.

Zengeni, E., Hartmann, P. C., and Pasch, H. (2012). “Encapsulation of clay by Ad-miniemulsion polymerization: The influence of clay size and modifier reactivity on latex morphology and physical properties.” *ACS Appl Mater Interfaces*, 4(12), 6957–6968.

Zhang, D., Wang, L., Qian, H., and Li, X. (2016). “Superhydrophobic surfaces for corrosion protection: a review of recent progresses and future directions.” *J Coatings Technol Res*, 13(1), 11–29.

Zhang, K., Li, G. H., Feng, L. M., Wang, N., Guo, J., Sun, K., Yu, K. X., Zeng, J. B., Li, T., Guo, Z., and Wang, M. (2017). “Ultralow percolation threshold and enhanced electromagnetic interference shielding in poly(l-lactide)/multi-walled carbon nanotube nanocomposites with electrically conductive segregated networks.” *J Mater Chem C*, 5(36), 9359–9369.

Zhang, K., Park, B. J., Fang, F. F., and Choi, H. J. (2009). “Sonochemical preparation of polymer nanocomposites.” *Molecules*, 14(6), 2095–2110.

Zhang, Y., and Yang, H. (2012). “Halloysite nanotubes coated with magnetic nanoparticles.” *Appl Clay Sci*, 56, 97–102.

Zhao, M., and Liu, P. (2008). “Halloysite nanotubes/polystyrene (HNTs/PS) nanocomposites via in situ bulk polymerization.” *J Therm Anal Calorim*, 94(1), 103–107.

Zhu, J., Guo, N., Zhang, Y., Yu, L., and Liu, J. (2014). “Preparation and characterization of negatively charged PES nanofiltration membrane by blending with halloysite nanotubes grafted with poly (sodium 4-styrenesulfonate) via surface-initiated ATRP.” *J Memb Sci*, 465, 91–99.

Zhu, J., Morgan, A. B., Lamelas, F. J., and Wilkie, C. A. (2001). “Fire properties of polystyrene-clay nanocomposites.” *Chem Mater*, 13(10), 3774–3780.

Zhu, J., Tian, M., Zhang, Y., Zhang, H., and Liu, J. (2015). “Fabrication of a novel ‘loose’ nanofiltration membrane by facile blending with Chitosan-Montmorillonite nanosheets for dyes purification.” *Chem Eng J*, 265, 184–193.



## APPENDIX

The light transmittance, light reflectance and light absorptance values can be computed using equations (1) to (3) in the visible range wavelength of 380-780 nm. The solar direct transmittance, solar direct reflectance and solar direct absorptance values can be computed using equations (4) to (5) in the total solar spectrum range of 300-2500 nm wavelength. The interval wave length of 2 nm is used in calculations.

$$\tau_v = \frac{\sum_{\lambda=380}^{\lambda=780} D_{\lambda} \tau(\lambda) V(\lambda) \Delta\lambda}{\sum_{\lambda=380}^{\lambda=780} D_{\lambda} V(\lambda) \Delta\lambda} \quad (1)$$

$$\rho_v = \frac{\sum_{\lambda=380}^{\lambda=780} D_{\lambda} \rho(\lambda) V(\lambda) \Delta\lambda}{\sum_{\lambda=380}^{\lambda=780} D_{\lambda} V(\lambda) \Delta\lambda} \quad (2)$$

$$\alpha_v = 1 - (\tau_v + \rho_v) \quad (3)$$

$$\tau_s = \frac{\sum_{\lambda=300}^{\lambda=2500} S_{\lambda} \tau(\lambda) \Delta\lambda}{\sum_{\lambda=300}^{\lambda=2500} S_{\lambda} \Delta\lambda} \quad (4)$$

$$\rho_s = \frac{\sum_{\lambda=300}^{\lambda=2500} S_{\lambda} \rho(\lambda) \Delta\lambda}{\sum_{\lambda=300}^{\lambda=2500} S_{\lambda} \Delta\lambda} \quad (5)$$

$$\alpha_s = 1 - \frac{\sum_{\lambda=300}^{\lambda=2500} S_{\lambda} \tau(\lambda) \Delta\lambda}{\sum_{\lambda=300}^{\lambda=2500} S_{\lambda} \Delta\lambda} - \frac{\sum_{\lambda=300}^{\lambda=2500} S_{\lambda} \rho(\lambda) \Delta\lambda}{\sum_{\lambda=300}^{\lambda=2500} S_{\lambda} \Delta\lambda} \quad (6)$$

where,  $\tau_v$  is the visible transmittance;  $\rho_v$  is the visible reflectance;  $\alpha_v$  is the visible absorptance;  $D_{\lambda}$  is the relative spectral distribution of the illuminant;  $V(\lambda)$  is the spectral luminous efficiency for photopic vision;  $\tau_s$  is the solar direct transmittance;  $\rho_s$  is the solar direct reflectance;  $\alpha_s$  is the solar direct absorptance;  $S_{\lambda}$  is the relative spectral distribution of the solar radiation;  $\tau(\lambda)$  is the measured spectral transmittance of the glass;  $\rho(\lambda)$  is the measured spectral reflectance of the glass;  $\Delta\lambda$  is the wave length interval.

**Solar skin protection factor (SSPF):** Solar skin protection factor value can be computed near ultra-violet region ranging from 300-400nm. The value of solar skin protection value lies between 0 and 1. The skin protection increases with increasing

value of SSPF. The calculation of SSPF value for various glass materials were computed using equations (7) and (8) as per standard procedure.

$$F_{SD} = \frac{\sum_{\lambda=300}^{\lambda=400} E_{\lambda} \tau(\lambda) S_{\lambda} \Delta\lambda}{\sum_{\lambda=300}^{\lambda=400} E_{\lambda} S_{\lambda} \Delta\lambda} \quad (7)$$

$$SSPF = 1 - F_{SD} \quad (8)$$

where,  $E_{\lambda}$  is the CIE erythemal effectiveness spectrum;  $F_{SD}$  is the skin damage factor

**Solar material protection factor (SMPF):** The solar material protection factor can be computed in the solar spectrum wave length range of 300-600 nm and earlier it was done in wavelength range of 300-500 nm. The SMPF lies between 0 and 1. SMPF values tending to zero indicates poor protection and values closer to 1 indicates better protection. The SMPF values for various glass materials with and without coatings were computed by using equations (9) and (10) as per standard procedure.

$$F_{CIE} = \frac{\sum_{\lambda=300}^{\lambda=600} C_{\lambda} \tau(\lambda) S_{\lambda} \Delta\lambda}{\sum_{\lambda=300}^{\lambda=600} C_{\lambda} S_{\lambda} \Delta\lambda} \quad (9)$$

$$SMPF = 1 - F_{CIE} \quad (10)$$

where,  $C_{\lambda} = e^{-0.012\lambda}$  ( $\lambda$  in nm);  $F_{CIE}$  is the CIE damage factor.

## RESEARCH PUBLICATIONS

### (A) Research Papers in National and International Journals

1. **Kezia Buruga**, and Jagannathan T. K. (2018). "Performance of halloysite nanotube/poly(styrene-comethylmethacrylate) nanocomposite coatings for the protection of soda-lime glass" *J. Alloys Compd*, 774, 370-377. <https://doi.org/10.1016/j.jallcom.2018.09.284>. (IF-3.77)
2. **Kezia Buruga**, and Jagannathan T. K. (2018). "A facile synthesis of halloysite nanotubes based polymer nanocomposites for glass coating application." *J. Alloys Compd*, 735, 1807–1817. [doi.org/10.1016/j.jallcom.2017.11.211](https://doi.org/10.1016/j.jallcom.2017.11.211). (IF-3.77)
3. **Kezia Buruga.**, Jagannathan T. K., Kim, K. H., Ok, Y. S., and Danil, B. (2018). "Polystyrene-halloysite nanotube membranes for water purification." *J. Ind. Eng. Chem*, 61, 169–180. [doi.org/10.1016/j.jiec.2017.12.014](https://doi.org/10.1016/j.jiec.2017.12.014). (IF-4.8)
4. **Kezia Buruga**, and Jagannathan T.K. (2018). "Fabrication of  $\gamma$ -MPS-Modified HNT-PMMA Nanocomposites by Ultrasound-Assisted Miniemulsion Polymerization." *The Minerals, Metals & Materials Society*, [doi.org/10.1007/s11837-018-2829-9](https://doi.org/10.1007/s11837-018-2829-9). (IF-2.125)
5. **Kezia Buruga**, and Jagannathan T.K. (2017). "Sonochemical Synthesis of CTAB modified HNT-polystyrene nanocomposites by solution casting method" *Asian J. Chem.*, 29 (1), 199-202. [doi.org/10.14233/ajchem.2017.20377](https://doi.org/10.14233/ajchem.2017.20377). (IF-0.45)
6. Kishore K. M. J., **Kezia Buruga.**, Jagannathan T. K. (2016). "Sonochemical Synthesis of Polymethylmethacrylate-Halloysite Nanotube by Solution Casting Method." *Indian Journal of Advances in Chemical Science* S1 (2016) 213-216.
7. **Kezia Buruga.**, Jagannathan T. K., and Kim. K. H. (2018). "Functional polymer-clay membranes for water treatment" (Revisions submitted to *Journal of Hazardous Materials*)

## **(B) Papers Presented in International Conferences**

1. **Kezia Buruga**, and Jagannathan T.K. (2017). “Ultrasound-assisted synthesis of  $\gamma$ -MPS modified HNTs-Polystyrene Nanocomposites by Miniemulsion Polymerization.” 6<sup>th</sup> International Engineering symposium (IES-17). 1-3<sup>rd</sup> March 2017. Kumamoto University, Japan
2. **Kezia Buruga**, and Jagannathan T.K. (2017). “Ultrasound-assisted Synthesis of Poly (styrene-co-methylmethacrylate)-HNT’s Nanocomposites by In-Situ Emulsion Copolymerization and its Characterization.” *Mater Today Proc*, 4(8), 7467–7475.” doi:10.1016/j.matpr.2017.07.078.
3. **Kezia Buruga**, and Jagannathan T.K. (2017). “Effects of Solvents on Structure, Morphology and Thermal Stability of Polystyrene-HNTs Nanocomposites by Ultrasound Assisted Solution Casting Method.” *Mater Today Proc*, 4(9), 9434–9439. doi:10.1016/j.matpr.2017.06.199.
4. **Kezia Buruga**, and Jagannathan T.K. (2015). “Sonochemical Synthesis of Poly (Styrene-co-Methylmethacrylate)-HNT’s Nanocomposites by Mini-emulsion Polymerisation.” International Conference on Advances in Chemical Engineering (ICACE-2015). 20-22<sup>nd</sup> December 2015. National Institute of Technology Karnataka, Surathkal, India.
5. **Kezia Buruga**, and Jagannathan T.K. (2015). “Synthesis of Polystyrene-HNT Nanocomposites by Ultrasound Assisted Solution Casting Method” International Conference on Direct Digital Manufacturing and Polymers (ICDDMAP). 28-31<sup>st</sup> October 2015. Karnataka University Dharwad (KUD), Dharwad, India.

## **(C) Papers Presented in National Conferences**

1. **Kezia Buruga**, and Jagannathan T.K. (2016). “Synthesis of Polymethylmethacrylate-HNTs Nanocomposites by Ultrasound Assisted Miniemulsion Polymerization” 69<sup>th</sup> Annual Session of the Indian Institute of Chemical Engineers (CHEMCON-2016). 27-30<sup>th</sup> December 2016. (Received Best Paper award)

**BIO-DATA**  
**KEZIA BURUGA**

Email ID: kezia.nitk@gmail.com and Contact no: +91-8884089882

**Personal Details:**

Fathers Name: B.Y.Krupadas

Date of Birth: 19 June, 1988

**Gender:** Female

**Nationality:** Indian

**Permanent Address:** H.No. 17, Pacific Park, Kusugal Road, Hubli-580020,  
Karnataka

**Educational qualification:**

- Ph.D. (Pursuing) in Chemical Engineering, 2013-2019 (Expected)  
Department of Chemical Engineering,  
National Institute of Technology Karnataka Surathkal, Mangalore, Karnataka, India
- M.Tech in Industrial Pollution Control, 2011-2013  
Department of Chemical Engineering,  
National Institute of Technology Karnataka Surathkal, Mangalore, Karnataka, India
- B.E. in Chemical Engineering, 2006-2010  
Department of Chemical Engineering  
KLE's College of Engineering and Technology, Belgaum, Karnataka, India

**Declaration:**

I hereby declare that the above-written particulars are true to the best of my knowledge.

Place: Surathkal, India

( )

Date:

**KEZIA BURUGA**